EXCITATION SOURCES FOR STRUCTURAL HEALTH MONITORING OF BRIDGES

A Thesis

Submitted to the College of Graduate Studies and Research

In Partial Fulfillment of the Requirements

for the

Degree of Doctor of Philosophy

in the

Department of Civil Engineering and Geological Engineering

University of Saskatchewan

Saskatoon

by

Mazin B. Alwash

PERMISSION TO USE

In presenting this thesis in partial fulfillment of the requirements for a Postgraduate degree from the University of Saskatchewan, I agree that the Libraries of this University may make it freely available for inspection. I further agree that permission for copying this thesis in any manner, in whole or in part, for scholarly purposes may be granted by the professors who supervised my thesis work or, in their absence, by the Head of the Department or the Dean of the College in which my thesis work was done. It is understood that any copying or publication or use of this thesis or parts thereof for financial gain shall not be allowed without my written permission. It is also understood that due recognition shall be given to me and to the University of Saskatchewan in any scholarly use which may be made of any material in my thesis.

Requests for permission to copy or to make other use of material in this thesis in whole or part should be addressed to:

Head of the Department of Civil and Geological Engineering
University of Saskatchewan
57 Campus Drive
Saskatoon, Saskatchewan, S7N 5A9

ABSTRACT

Vibration-based damage detection (VBDD) methods are structural health monitoring techniques that utilize changes to the dynamic characteristics of a structure (i.e. its natural frequencies, mode shapes, and damping properties) as indicators of damage. While conceptually simple, considerable research is still required before VBDD methods can be applied reliably to complex structures such as bridges. VBDD methods require reliable estimates of modal parameters (notably natural frequencies and mode shapes) in order to assess changes in the condition of a structure. This thesis presents the results of experimental and numerical studies investigating a number of issues related to the potential use of VBDD techniques in the structural health monitoring of bridges, the primary issue being the influence of the excitation source.

Two bridges were investigated as part of this study. One is located on Provincial Highway No. 9 over the Red Deer River south of Hudson Bay, Saskatchewan. The other is located near the Town of Broadview, Saskatchewan, off Trans-Canada Highway No. 1, 150 km east of the City of Regina. Field tests and numerical simulations were conducted using different types of excitation to evaluate the quality of the modal properties (natural frequencies and mode shapes) calculated using these excitation types, and thus to evaluate the performance of VBDD techniques implemented using the resulting modal data.

Field tests were conducted using different sources of dynamic excitation: ambient, traffic excitation, and impact excitation. The purpose of field testing was to study the characteristics and repeatability of the modal parameters derived using the different types of dynamic excitation, and to acquire data that could be used to update a FE model for further numerical simulation.

A FE model of the Red Deer River bridge, calibrated to match the field measured dynamic properties, was subjected to different types of numerically simulated dynamic excitation with different noise (random variations) levels added to them. The types of dynamic excitation considered included harmonic forced excitation, random forced excitation and the subsequent free vibration decay, impact excitation, and different

models of truck excitation. The bridge model was subjected to four different damage scenarios; in addition, six VBDD methods were implemented to evaluate their ability to identify and localize damage. The effects of uncertainty in the definition of controlled-force excitation sources and variation in measurement of the bridge response were also investigated.

Field tests on the Hudson Bay bridge showed that excitation induced by large trucks generally produced more reliable data than that of smaller vehicles due to higher signal-to-noise ratios in the measured response. It was also found that considering only the free vibration phase of the response after the vehicle left the bridge gave more reliable data. Impact excitation implemented the on Hudson Bay bridge using a spring-hammer yielded repeatable and high quality results, while using a heavy weight delectometer for impact excitation on the Broadview bridge produced results of lesser quality due to the occurrence of multiple strikes of the impact hammer. In general, wind induced vibration measurements taken from both bridges were less effective for defining modal properties than large vehicle loading or impact excitation.

All of the VBDD methods examined in this study could detect damage if the comparison was made between modal parameters acquired by eigenvalue analyses of two FE models of the bridge, before and after damage. However, the performance of VBDD methods declined when the dynamic properties were calculated from response time histories and noise was introduced. In general, the damage index method performed better than other damage detection methods considered.

Numerical simulation results showed that harmonic excitation, impact excitation, and the free decay phase after random excitation yielded results that were consistent enough to be used for the identification of damage. The reliability of VBDD methods in detecting damage dropped once noise was introduced. Noise superimposed on the excitation force had little effect on the estimated modal properties and the performance of VBDD methods. On the other hand, noise superimposed on the “measured” dynamic response had a pronounced negative influence on the performance of the VBDD methods.

ACKNOWLEDGEMENTS

I wish to express my profound gratitude to my supervisors: Professor Leon Wegner and Professor Bruce Sparling. Throughout the duration of the present study, they have given me invaluable guidance, criticism, suggestions, and encouragement.

Also, I would like to extend my appreciation to other members of my advisory committee: Professor Ian Fleming, Professor Gordon Sparks, Professor Mohamed Boulfiza, and Professor Reza Fotouhi for their advice during the whole process.

The financial support from the ISIS Canada Network of Centres of Excellence, and the Department of Civil and Geological Engineering is greatly appreciated.

This project would not have been possible without the financial assistance of Saskatchewan Highways and Transportation, and field support that was provided by their personnel.

A special thanks goes to Mr. Dale Pavier, Mr. Brennan Bokoyoway, Mr. Alan Duffy, and David Messner, the structural laboratory technicians, for their constant assistance in the experimental work for this thesis.

Finally, I would like to thank Professor Don Gendzwill of the Department of Geology at the University of Saskatchewan for providing us with the spring-actuated impact hammer, and Professor Curtis Berthelot of the Department if Civil and Geological Engineering for letting us use the heavy weight deflectometer (HWD) machine in this research.

TABLE OF CONTENTS

PERMISSION TO USE……i

ABSTRACT……ii

ACKNOWLEDGEMENTS……iv

TABLE OF CONTENTS……v

LIST OF TABLES……x

LIST OF FIGURES……xii

NOMENCLATURE……xxi

LIST OF ABBREVIATIONS……xxiii

1 INTRODUCTION 1
1.1 BACKGROUND 1
1.2 OBJECTIVES 3
1.3 METHODOLOGY 4
1.4 THESIS LAYOUT 5

2 LITERATURE REVIEW 7
2.1 OVERVIEW 7
2.2 MODAL ANALYSIS 9
2.2.1 Overview 9
2.2.2 Frequency Domain Methods 10
2.2.3 Time Domain Methods 12
2.3 VBDD METHODS 15
2.3.1 Overview 15
2.3.2 Change in Mode Shape Method 16
2.3.3 Change in Mode Shape Curvature Method 16
2.3.4 Damage Index Method 17
2.3.5 Change in Measured Modal Flexibility Method 18
2.3.6 Change in Uniform Load Surface Curvature Method 19
2.4 APPLICATION OF VBDD METHODS ON BRIDGE STRUCTURES 20
2.5 TYPES OF DYNAMIC EXCITATION 22
2.6 COMPARISON OF DIFFERENT DYNAMIC EXCITATION METHODS 24
2.7 NOISE AND VARIABILITY IN DYNAMIC TESTING 26
2.8 VBDD RESEARCH AT THE UNIVERSITY OF SASKATCHEWAN 28
2.9 SUMMARY 30

3 RESEARCH METHODOLOGY 33
3.1 OVERVIEW 33
3.2 HUDSON BAY BRIDGE DESCRIPTION 33
3.3 FINITE ELEMENT MODEL OF HUDSON BAY BRIDGE 35
3.4 ISTRUMENTATION 38
3.4.1 Overview 38

3.4.2 Strain Gauges 38
3.4.3 Accelerometers 41
3.4.4 Data Acquisition System 43
3.5 DATA ACQUISITION AND POST PROCESSING CONSIDERATIONS 44
3.6 FIELD TESTING 48
3.6.1 Overview 48
3.6.2 Field Testing on the Hudson Bay Bridge 49
3.6.2.1 Uncontrolled Truck Excitation for the Hudson Bay Bridge 49
3.6.2.2 Ambient Excitation for the Hudson Bay Bridge 50
3.6.2.3 Impact Excitation for the Hudson Bay Bridge 50
3.6.2.4 Static (Controlled) Load Testing on Hudson Bay Bridge 53
3.6.3 Field Testing on the Broadview Bridge 54
3.6.3.1 Bridge Description and testing overview 54
3.6.3.2 Impact Test Equipment 55
3.6.3.3 Test Setup and Procedure 57
3.7 EXCITATION FOR NUMERICAL DYNAMIC SIMULATION 58
3.7.1 Overview 58
3.7.2 Harmonic Excitation 60
3.7.3 Random Excitation 61
3.7.4 Impact Excitation 62
3.7.5 Truck Excitation 63
3.7.6 Road roughness 67
3.8 MODAL ANALYSIS TECHNIQUES 70
3.9 PREPROCESSING FOR NUMERICAL SIMULATION 70
3.10 DAMAGE SCENARIOS 71
3.11 VBDD METHODS 72
3.12 VARIABILITY IN MEASUREMENT 72
3.13 ADDITIONAL TESTS 74
3.13.1 Strain Gauge Environmental Test 74
3.13.2 Rebound Hammer Test 76

4 EXPERIMENTAL RESULTS 78
4.1 OVERVIEW 78
4.2 MODAL TESTING AT THE HUDSON BAY BRIDGE 78
4.2.1 Truck Excitation 78
4.2.2 Ambient Environmental Excitation 83
4.2.3 Variability of Modal Properties Measured Using Truck Excitation and Ambient Excitation 85
4.2.4 Impact Excitation Test at the Hudson Bay Bridge 88
4.2.5 Variability of Modal Properties Measured Using Impact Excitation and Ambient Excitation 91
4.2.6 Evaluating Noise Levels in Field Readings 95
4.3 STATIC LOAD TEST 96
4.4 RESULTS OF THE IMPACT EXCITATION TEST AT THE BROADVIEW BRIDGE 101

5 NUMERICAL SIMULATION OF DYNAMIC EXCITATIONS 108
5.1 OVERVIEW 108
5.2 FE MODEL UPDATING OF HUDSON BAY BRIDGE 108
5.3 COMPARISON OF DIFFERENT EXCITATION METHODS AND THE EFFECT OF UNCERTAINTY 112
5.3.1 Forced Harmonic Excitation 112
5.3.2 Random Excitation 114
5.3.3 Impact Excitation 116
5.3.4 Truck Excitation 119
5.3.4.1 Simplified truck model 119
5.3.4.2 Dynamic truck model 122
5.3.5 Modal Variability Due to Different Types of Excitation 127

6 NUMERICAL SIMULATION of VBDD 131
6.1 OVERVIEW 131
6.2 VBDD METHODS USING ERROR FREE MODE SHAPES 131
6.2.1 Overview 131
6.2.2 First damage scenario - External reinforcing bars cut at the centre of all girders of the middle span 132
6.2.3 Second damage scenario - External reinforcing bars cut on the middle of one girder within the centre span 137
6.2.4 Third damage scenario - External reinforcing bars cut from the middle of all girders in an end span 142
6.2.5 Fourth damage scenario - External reinforcing bars removed from the girders in the middle span and replaced by steel plates 146
6.2.6 Discussion 151
6.3 COMPARING THE FOURTH DAMAGE SCENARIO TO SITE MEASUREMENTS DUE TO IMPACT EXCITATION ON HUDSON BAY BRIDGE 153
6.4 EFFECT OF DYNAMIC EXCITATION ON THE PERFORMANCE OF VBDD METHODS 155
6.4.1 Overview 155
6.4.2 Harmonic excitation 155
6.4.3 Impact excitation 160
6.4.4 Free decay of random excitation 163
6.4.5 Conclusions 164
6.5 EFFECT OF NOISE ON THE APPLICABILITY OF VBDD 168
6.5.1 Effect of noise on VBDD when harmonic excitation is used 168
6.5.2 Effect of noise on VBDD when impact excitation is used 171
6.5.3 Effect of averaging of readings on improving VBDD 175
6.5.4 Conclusions 176
6.6 STOCHASTIC CONFIDENCE OF DETECTED DAMAGE 178

7 SUMMARY AND CONCLUSIONS 186
7.1 SUMMARY 186
7.2 CONCLUSIONS 188

7.3 RECOMMENDATIONS FOR FUTURE WORK 192

REFERENCES 193

APPENDIX A: HUDSON BAY BRIDGE DETAILED ELEVATIONS AND SECTIONS 204

APPENDIX B: EXPERIMENTAL TRUCK TESTS ON HUDSON BAY BRIDGE . 206
B.1 Introduction 206
B.2 Trucks listing during site test on August 26, 2003 206
B.3 Trucks listing during site test on June 24, 2004 208
B.4 Trucks listing during site test on August 26, 2004 210
B.5 Trucks listing during site test on September 17, 2004 210
B.6 Trucks listing during site test on September 29-30, 2005 212

APPENDIX C: DYNAMIC TRUCK SIMULATION 217
C.1 Properties of QS-600 truck 217

APPENDIX D: RESULTS OF FIELD TESTS ON HUDSON BAY BRIDGE 218
D.1 Results of rebound hammer test 218
D.2 Variability of modal parameters calculated from site measurement on Hudson Bay Bridge 219

APPENDIX E: HDUSON BAY BRIDGE IMPACT TEST RESULTS 220
E.1 Locations of Impact Hammer and Accelerometers 220
E.2 Modal Amplitude and Statistical Characteristics of Mode 1 (2.640 Hz) Calculated From Spring Hammer Excitation, with rubber pad 220
E.3 Modal Amplitude and Statistical Characteristics of Mode 1 (2.641 Hz) Calculated From Spring Hammer Excitation, without rubber pad 221
E.4 Modal Amplitude of Mode 1 (2.625 Hz) Calculated From Ambient Excitation 222

APPENDIX F: BROADVIEW BRIDGE TEST RESULTS 223
F.1 Locations of Accelerometer Measured Response 223
F.2 Modal Amplitude and Statistical Characteristics of Mode 1 (9.967 Hz) Calculated From 50 kN Impact Excitation 223
F.3 Modal Amplitude and Statistical Characteristics of Mode 2 (11.17 Hz) Calculated From 25 kN Impact Excitation 225
F.4 Modal Amplitude of Mode 1 (9.526 Hz) Calculated From Ambient Excitation 226

APPENDIX G: EFFECT OF NOISE ON THE APPLICABILITY of VBDD 227
G.1 OVERVIEW 227
G.2 First damage scenario - cutting the external rebars from the middle of all girders at the centre span 228
G.2.1 Harmonic excitation (input noise) 228

G.2.1.1 Change in mode shape method 228
G.2.1.2 Change in mode shape curvature method 229
G.2.1.3 Damage index method..... 230
G.2.1.4 Change in modal flexibility method..... 231
G.2.1.5 Change in uniform load surface curvature method 232
G.2.1.6 Change in unit load surface curvature method..... 233
G.2.2 Harmonic excitation (output noise)..... 234
G.2.2.1 Change in mode shape method 234
G.2.2.2 Change in mode shape curvature method 235
G.2.2.3 Damage index method..... 236
G.2.2.4 Change in modal flexibility method..... 237
G.2.2.5 Change in uniform load surface curvature method 238
G.2.2.6 Unit load surface curvature method 239
G.2.3 Impact excitation (input noise)..... 240
G.2.3.1 Change in mode shape method 240
G.2.3.2 Change in mode shape curvature method 241
G.2.3.3 Damage index method..... 242
G.2.3.4 Change in modal flexibility method..... 243
G.2.3.5 Change in uniform load surface curvature method 244
G.2.3.6 Change in unit load surface curvature method..... 245
G.2.4 Impact excitation (output noise)..... 246
G.2.4.1 Change in mode shape method 246
G.2.4.2 Change in mode shape curvature method 247
G.2.4.3 Damage index method..... 248
G.2.4.4 Change in modal flexibility method..... 249
G.2.4.5 Change in uniform load surface curvature method 250
G.2.4.6 Change in unit load surface curvature method..... 251

APPENDIX H: MATLAB ROUTINES FOR VBDD 252
H.1 OVERVIEW..... 252
H.2 MATLAB ROUTINE FOR THE CHANGE IN MODE SHAPE METHOD, THE CHANGE IN MODE SHAPE CURVATURE METHOD, AND THE DAMAGE INDEX METHOD..... 252
H.3 MATTLAB ROUTINE FOR THE CHANGE IN MEASURED MODAL FLEXIBILITY METHOD, AND THE CHANGE IN UNIFORM LOAD SURFACE CURVATURE METHOD 257
H.4 MATTLAB ROUTINE FOR THE CHANGE IN UNIT LOAD SURFACE CURVATURE METHOD 260
H.5 SAMPLE OF INPUT FILES..... 263

LIST OF TABLES

Table 3.1 Values for $S_u(\kappa_0)$ (Cebon 2000) 68

Table 4.1 Statistical characteristics of measured natural frequencies for Hudson Bay bridge, calculated from truck excitation..... 86

Table 4.2 Statistical characteristics of measured natural frequencies for Hudson Bay bridge, calculated from impact and ambient excitations..... 93

Table 4.3 Statistical characteristics of measured natural frequencies for the Broadview bridge..... 104

Table 5.1 Comparison of field measured natural frequencies to those calculated from a calibrated FE model, for Hudson Bay bridge. 110

Table 5.2 MAC values for 1st mode shape derived from harmonic loading (noise in input). 113

Table 5.3 MAC values for 1st mode shape derived from harmonic loading (noise in output). 114

Table 5.4 Natural frequencies using random dynamic excitation..... 115

Table 5.5 MAC values of random excitation. 116

Table 5.6 Natural frequencies and MAC values from impact excitation..... 117

Table 5.7 Natural frequencies and standard deviations from impact excitation with random noise in measured output. 118

Table 5.8 MAC values from Impact excitation with random noise in measured output. 118

Table 5.9 Natural frequencies and mode shape MAC values from simplified truck excitation model. 120

Table 5.10 Natural frequencies and mode shape MAC values from simplified truck excitation model plus sinusoid. 121

Table 5.11 Dynamic load allowance resulting from dynamic truck loading model. 124

Table 5.12 Natural frequencies and mode shape MAC values from dynamic truck model excitation. 126

Table 5.13 Averaged coefficient of variation of modal amplitudes due to different types of excitation..... 128

Table 6.1 Comparison of the natural frequencies from FE model of the Hudson Bay bridge for the fourth damage scenario to measured ones after the rehabilitation work. 154

Table 6.2 Comparison of the t value calculated from different types of excitation, output noise levels, and number of trials..... 186

Table B.1. Truck description for east side setup. 206

Table B.2. Truck description for west side setup. 207
Table B.3. Truck description for east side setup. 208
Table B.4. Truck description for west side setup. 208
Table B.5. Truck description for west side setup. 210
Table B.6. Truck description for east side setup. 210
Table B.7. Truck description for west side setup. 211
Table B.8. Truck description for west side setup on September 29, 2005. 212
Table B.9. Truck description for east side setup on September 29, 2005. 213
Table B.10. Truck description for west side setup on September 30, 2005. 214
Table B.11. Truck description for east side setup on September 30, 2005. 215
Table C.1. Properties of QS-600 trcuk (Fafard et al. 1998). 217
Table D.1. Field test rebound hammer readings. 218
Table D.2. Standard deviation of the normalised amplitudes of the first mode in the middle span due to free decaying truck excitation. 219
Table D.3. Standard deviation of the normalised amplitudes of the first mode in the middle span due to ambient excitation. 219
Table E.1. Modal amplitudes and statistical characteristics of Mode 1 Spring Hammer Excitation, with rubber pad 220
Table E.2. Modal amplitudes and statistical characteristics of Mode 1 Spring Hammer Excitation, without rubber pad 221
Table E.3. Modal amplitudes and statistical characteristics of mode 1 induced by ambient excitation 222
Table F.1. Modal amplitudes and statistical characteristics of Mode 1 induced by 50 kN impact excitation 224
Table F.2. Modal amplitudes and statistical characteristics of Mode 2 induced by 25 kN impact excitation 225
Table F.3. Modal amplitudes and statistical characteristics of mode 1 induced by ambient excitation 226

LIST OF FIGURES

Figure 2.1. State-space system (Van Overschee and De Moor 1996). 14

Figure 2.2. Graphical representation of an (output-only) Stochastic State-space system (Van Overschee and De Moor 1996). 15

Figure 3.1 Bridge elevation (redrawn from Earth Tech 2001)..... 34

Figure 3.2 Bridge photograph showing external positive moment reinforcement..... 34

Figure 3.3 Schematic of the finite element model for Hudson Bay brigdge: (a) isometric view of entire model; and (b) close-up view of south end showing meshing details. 37

Figure 3.4 FLM-60-11-2LT strain gauge. 39

Figure 3.5 Plan view of Hudson Bay bridge showing strain gauge layout. 39

Figure 3.6 Typical sensor locations on Hudson Bay bridge cross section (looking north). 40

Figure 3.7. A group of strain gauges as installed on Hudson Bay bridge. 40

Figure 3.8 Snooper truck used to install the strain gauges on Hudson Bay bridge..... 41

Figure 3.9. Lead wire compensation using a three-wire hookup. 41

Figure 3.10 EpiSensor FBA ES-U accelerometer. 42

Figure 3.11 Accelerometers locations on the Hudson Bay bridge. 43

Figure 3.12 Data acquisition system. 44

Figure 3.13 Window functions used in signal processing of forced excitation: a) Tukey window; and b) exponential window. 46

Figure 3.14 Hanning window function, used in signal processing of ambient excitation. 47

Figure 3.15 Summary of procedure for estimating the modal parameters of a bridge. .. 48

Figure 3.16 Spring actuated impact hammer mounted on the back of a truck..... 51

Figure 3.17 Steel plate strengthening of Hudson Bay bridge during installation. 52

Figure 3.18 Steel plate strengthening of Hudson Bay bridge after completion. 52

Figure 3.19 A plan view showing instrumentation locations for impact testing at the Hudson Bay Bridge. 53

Figure 3.20 Test truck used for static load test. 54

Figure 3.21 Photograph showing the Broadview bridge (looking north). 55

Figure 3.22 Heavy Weight Deflectometer (HWD). 56

Figure 3.23 Impact hammer of the HWD. 56

Figure 3.24 Schematic plan view showing test setup for Broadview bridge. 57

Figure 3.25 Locations of nodes used for data extraction from the FEM model of Hudson Bay bridge. 59

Figure 3.26 Harmonic excitation with no noise: a) example force time history; and b) force spectrum. 60

Figure 3.27 Harmonic excitation with 2% noise: a) example force time history; and b) force spectrum. 61

Figure 3.28 Random forced vibration: a) example force time history; b) force spectrum. 62

Figure 3.29 Impact excitation with no noise added: a) example force time history; and b) force spectrum. 63

Figure 3.30 Impact excitation with 2% noise: a), example force time history; and b) force spectrum. 63

Figure 3.31 Schematic of truck configurations for simplified truck model. 65

Figure 3.32 Truck excitation: a) example forced time history; b) response acceleration spectrum. 65

Figure 3.33 Schematic of QS-660 truck for dynamic truck model. 66

Figure 3.34 Truck wheel modelled as a two degree of freedom system: m', k' and c' are the mass, stiffness and damping of wheel system; k and c are the stiffness and damping of the suspension system; m is the portion of the truck mass supported by a specific wheel. 67

Figure 3.35 Spectral density plots of simulated road roughness profiles. 68

Figure 3.36 Simulated road roughness profiles..... 69

Figure 3.37 Strain gauge attached to concrete prism. 75

Figure 3.38 Load-strain relationship for environmental test of strain gauge. 75

Figure 3.39 Relationship between rebound hammer number and concrete compressive strength. 77

Figure 4.1 Example of Hudson Bay bridge response to a large truck: (a) acceleration time history; and (b) acceleration spectrum. 79

Figure 4.2 Decaying (free vibration) portion of Hudson Bay bridge response to a large truck: (a) acceleration time history; and (b) acceleration spectrum. 79

Figure 4.3 Hudson Bay bridge response to a small truck: (a) acceleration time history; and (b) acceleration spectrum. 80

Figure 4.4 Decaying (free vibration) portion of Hudson Bay bridge response to a small truck: (a) acceleration time history; and (b) acceleration spectrum. 80

Figure 4.5 Hudson Bay bridge response to a large timber haul truck: (a) acceleration time history; and (b) acceleration spectrum of free decay. 81

Figure 4.6 Hudson Bay bridge response to a large truck followed by a passenger car. . 82

Figure 4.7 Hudson Bay bridge response to two large trucks crossing the bridge in succession. 83

Figure 4.8 Auto power spectrum of the reference accelerometer due to ambient excitation. 84

Figure 4.9 Auto power spectrum of the reference accelerometer produced by ambient excitation for: a) a single 30 s event, and b) a 140s time record divided into 30 s segments overlapping by 60%. 85

Figure 4.10 Standard deviations (shown as error bars) of the normalised amplitudes of the first mode in the middle span due to free decaying truck excitation, for the Hudson Bay bridge. 86

Figure 4.11 Standard deviations (shown as error bars) of the normalised amplitudes of the first mode in the middle span due to ambient excitation, for the Hudson Bay bridge. 87

Figure 4.12 Hudson Bay bridge response to impact excitation: (a) acceleration time history; and (b) acceleration spectrum, for the reference accelerometer. 90

Figure 4.13 Lowest four vibration mode shapes calculated from the spring hammer excitation at the Hudson Bay bridge: a) mode 1 (2.640 Hz), b) mode 2 (4.253 Hz), c) mode 4 (5.812 Hz), and d) mode 6 (8.156 Hz). 91

Figure 4.14 Auto Power Spectra of readings from 10 impact events measured by the reference accelerometer, for the Hudson Bay bridge. 92

Figure 4.15 Standard deviation (shown as error bars) of the normalised amplitudes of the first mode due to impact excitation with rubber pad for the Hudson Bay bridge. 94

Figure 4.16 Typical strain gauge reading from truck static load test: a) before smoothing, and b) after smoothing. 98

Figure 4.17 Strain signals from the bottom strain gauge of the second strain gauge cluster from the north on the east side of the bridge, obtained from four repeated tests. 99

Figure 4.18 Readings of a cluster of strain gauges near the bridge north pier support... 99

Figure 4.19 Readings of a cluster of strain gauges near the bridge midspan. 100

Figure 4.20 Strain gauge readings showing relative response of the bridge girders..... 100

Figure 4.21 Acceleration-time history of reference accelerometer on the Broadview bridge due to HWD tests: a) 50 kN drop weight, and b) 25 kN drop weight. 102

Figure 4.22 Superimposed normalised auto power spectra of readings from 10 impact events measured by the reference accelerometer on the Broadview bridge. 103

Figure 4.23 First mode of the Broadview Bridge (9.967 Hz) calculated from 50 kN impact excitation. 106

Figure 4.24 Second mode of the Broadview Bridge (11.17 Hz) calculated from 25 kN impact excitation. 106

Figure 4.25 First mode of the Broadview Bridge (9.526 Hz) calculated from ambient excitation. 106

Figure 5.1 Lowest six vibration mode shapes generated from the FE model. 110

Figure 5.2 Comparison between strains calculated from FE analysis and a corresponding set of measured strains on the bridge using a test truck; strain gauge locations are near the soffit of the girders, on the (a) east girder, (b) middle girder, and (c) west girder.. 111

Figure 5.3 Bridge response acceleration spectrum due to harmonic excitation at the location of the reference accelerometer: a) excitation without noise, and b) excitation with 2% noise. 112

Figure 5.4 Bridge response acceleration spectrum due to random excitation: a) during forced excitation phase, and b) free vibration phase. 115

Figure 5.5 Bridge response acceleration spectrum due to impact excitation: a) excitation without noise, and b) with 2% noise. 117

Figure 5.6 Bridge response to simulated truck PV4 crossing the bridge at 81km/h: (a) acceleration time history; and (b) normalized acceleration spectrum. 119

Figure 5.7 Bridge response to simulated truck PV4 plus sinusoid crossing the bridge at 81km/hr: (a) acceleration time history; and (b) normalized acceleration spectrum..... 121

Figure 5.8 Bridge response to simulated truck QS-660 crossing the bridge at 81km/h, with road roughness, Su(κ0), values of 64*10-6 m3/cycle: (a) acceleration time history; and (b) normalized acceleration spectrum. 123

Figure 5.9 Frequency spectrum for QS-660 truck wheel forces. 125

Figure 5.10 Variability of the first mode for the middle girder of the bridge calculated by a) random forced excitation, b) free vibration decay after random excitation. 130

Figure 6.1 Distribution of the change in mode shape caused by cutting the external rebars from the middle of all the girders in the centre span. 134

Figure 6.2 Distribution of the change in mode shape curvature caused by cutting the external rebars from the middle of all the girders in the centre span. 135

Figure 6.3.Distribution of the damage index caused by cutting the external rebars from the middle of all the girders in the centre span. 135

Figure 6.4 Distribution of the change in modal flexibility caused by cutting the external rebars from the middle of all the girders in the centre span. 136

Figure 6.5 Distribution of the change in uniform load surface curvature caused by cutting the external rebars from the middle of all the girders at the centre span. 136

Figure 6.6 Distribution of the change in unit load surface curvature caused by cutting the external rebars from the middle of all the girders at the centre span. 137

Figure 6.7 Distribution of the change in mode shape caused by cutting the external rebars from the west girder in the centre span. 139

Figure 6.8 Distribution of the change in mode shape curvature caused by cutting the external rebars from the west girder in the centre span. 139

Figure 6.9 Distribution of the damage index caused by cutting the external rebars from the west girder in the centre span. 140

Figure 6.10 Distribution of the change in modal flexibility caused by cutting the external rebars from the west girder in the centre span. 140

Figure 6.11 Distribution of the change in uniform load surface curvature caused by cutting the external rebars from the west girder in the centre span. 141

Figure 6.12 Distribution of the change in unit load surface curvature caused by cutting the external rebars from the west girder in the centre span..... 141

Figure 6.13 Distribution of the change in mode shape caused by cutting the external rebars from girders in the end span. 143

Figure 6.14 Distribution of the change in mode shape curvature caused by cutting the external rebars from girders in the end span. 144

Figure 6.15 Distribution of damage index caused by cutting the external rebars from girders in the end span..... 144

Figure 6.16 Distribution of change in modal flexibility caused by cutting the external rebars from girder in the end span..... 145

Figure 6.17 Distribution of the change in uniform load surface curvature caused by cutting the external rebars from girders in the end span. 145

Figure 6.18 Distribution of the change in unit load surface curvature caused by cutting the external rebars from girders in the end span. 146

Figure 6.19 Distribution of the change in mode shape caused by replacing the external rebars from the girders in the centre span by steel plates. 148

Figure 6.20 Distribution of the change in mode shape curvature caused by replacing the external rebars from the girders in the centre span by steel plates..... 149

Figure 6.21 Distribution of the damage index caused by replacing the external rebars from the girders in the centre span by steel plates. 149

Figure 6.22 Distribution of the change in modal flexibility caused by replacing the external rebars from the girders in the centre span by steel plates..... 150

Figure 6.23 Distribution of the change in uniform load surface curvature caused by replacing the external rebars from the girders in the centre span by steel plates. 150

Figure 6.24 Distribution of the change in unit load surface curvature method caused by replacing the external rebars from the girders in the centre span by steel plates. 151

Figure 6.25 Comparison of the modal amplitudes for the 1st mode of the middle girder before and after damage: a) 1st damage scenario, and b) 4th damage scenario. 151

Figure 6.26 Distribution of the change in mode shape caused by first damage scenario using harmonic excitation. 157

Figure 6.27 Distribution of the change in mode shape curvature caused by first damage scenario using harmonic excitation. 157

Figure 6.28 Distribution of the damage index caused by first damage scenario using harmonic excitation. 158

Figure 6.29 Distribution of the change in modal flexibility caused by first damage scenario using harmonic excitation. 158

Figure 6.30 Distribution of the change in uniform load surface curvature caused by first damage scenario using harmonic excitation. 159

Figure 6.31 Distribution of the change in unit load surface curvature caused by first damage scenario using harmonic excitation. 159

Figure 6.32 Distribution of the change in mode shape caused by first damage scenario using impact excitation. 160

Figure 6.33 Distribution of the change in mode shape curvature caused by first damage scenario using impact excitation. 161

Figure 6.34 Distribution of the damage index method caused by first damage scenario using impact excitation. 161

Figure 6.35 Distribution of the change in modal flexibility caused by first damage scenario using impact excitation. 162

Figure 6.36 Distribution of the change in uniform load surface curvature caused by first damage scenario using impact excitation. 162

Figure 6.37 Distribution of the change in unit load surface curvature caused by first damage scenario using impact excitation. 163

Figure 6.38 Distribution of the change in mode shape caused by first damage scenario using free decay vibration. 165

Figure 6.39 Distribution of the change in mode shape curvature caused by first damage scenario using free decay vibration. 165

Figure 6.40 Distribution of the damage index caused by first damage scenario using free decay vibration. 166

Figure 6.41 Distribution of the change in modal flexibility caused by first damage scenario using free decay vibration. 166

Figure 6.42 Distribution of the change in uniform load surface curvature caused by first damage scenario using free decay vibration. 167

Figure 6.43 Distribution of the change in unit load surface curvature caused by first damage scenario using free decay vibration. 167

Figure 6.44 Distribution of the change in mode shape for the first damage scenario when harmonic excitation was used and noise was added to input force: a) 1% noise, b) 2% noise, c) 5% noise, d) 10% noise. 169

Figure 6.45 Distribution of the change in mode shape for the first damage scenario when harmonic excitation was used and noise was added to the output signal: a) 1% noise, b) 2% noise, c) 5% noise, d) 10% noise. 170

Figure 6.46 Distribution of the damage index for the first damage scenario when harmonic excitation was used and noise was added to input force: a) 1% noise, ... 171

Figure 6.47 Distribution of the damage index for the first damage scenario when harmonic excitation was used and noise was added to output signal: a) 1% noise, b) 2% noise, c) 5% noise, d) 10% noise. 172

Figure 6.48 Distribution of the change in mode shape for the first damage scenario when impact excitation was used and noise was added to input force: a) 1% noise, b) 2% noise, c) 5% noise. 173

Figure 6.49 Distribution of the change in mode shape for the first damage scenario when impact excitation was used and noise was added to the output signal: a) 1% noise, b) 2% noise, c) 5% noise. 174

Figure 6.50 Distribution of the damage index for the first damage scenario when impact excitation was used and noise was added to input force: a) 1% noise, b) 2% noise, c) 5% noise. 175

Figure 6.51 Distribution of the damage index for the first damage scenario when impact excitation was used and noise was added to output signal: a) 1% noise, b) 2% noise, c) 5% noise. 176

Figure 6.52 Distribution of the change in mode shape for the first damage scenario when harmonic excitation was used and 5% noise was added to output signal: a) 10 simulations, b) 20 simulations, c) 50 simulations, and d) 100 simulations. 177

Figure 6.53 Distribution of the damage index for the first damage scenario when impact excitation was used and 5% noise was added to output signal: a) 10 simulations, b) 20 simulations, c) 50 simulations, and d) 100 simulations. 178

Figure 6.54 Effect of noise on the t-test value using impact excitation and the change in mode shape: a) change in mode shape with 1% noise in the input signal, b) t values for 1% input noise, c) change in mode shape with 1% noise in the output signal, and d) t values for 1% output noise. 181

Figure 6.55 Effect of noise on the t-test value using harmonic excitation and change in mode shape curvature: a) change in mode shape with 1% noise in the input signal, b) t values for 1% input noise, c) change in mode shape with 1% noise in the output signal, and d) t values for 1% output noise. 182

Figure A.1. Typical bridge cross section. 204

Figure A.2. Bridge diaphragm. 204

Figure A.3. Hudson Bay Bridge plan and elevation. 205

Figure E.1. A plan view showing test setup for impact testing at Hudson Bay Bridge. 220

Figure F.1. Schematic plan showing nodes numbers of accelerometer response for Broadview Bridge. 223

Figure G.1. Distribution of the change in mode shape for the first damage scenario when harmonic excitation was used and noise was added to input force: a) 1% noise, ... 228

Figure G.2. Distribution of the change in mode shape curvature for the first damage scenario when harmonic excitation was used and noise was added to input force: 229

Figure G.3. Distribution of the damage index for the first damage scenario when harmonic excitation was used and noise was added to input force: a) 1% noise,..... 230

Figure G.4. Distribution of the change in modal flexibility for the first damage scenario when harmonic excitation was used and noise was added to input force: a) 1% noise, b) 2% noise, c) 5% noise, d) 10% noise..... 231

Figure G.5. Distribution of the change in uniform load surface curvature for the first damage scenario when harmonic excitation was used and noise was added to input force: a) 1% noise, b) 2% noise, c) 5% noise, d) 10% noise..... 232

Figure G.6. Distribution of the change in unit load surface curvature for the first damage scenario when harmonic excitation was used and noise was added to input force:..... 233

Figure G.7. Distribution of the change of mode shape for the first damage scenario when harmonic excitation was used and noise was added to the output signal: a) 1% noise, b) 2% noise, c) 5% noise, d) 10% noise..... 234

Figure G.8. Distribution of the change in mode shape curvature for the first damage scenario when harmonic excitation was used and noise was added to the output signal: a) 1% noise, b) 2% noise, c) 5% noise, d) 10% noise..... 235

Figure G.9. Distribution of the damage index for the first damage scenario when harmonic excitation was used and noise was added to the output signal: a) 1% noise, b) 2% noise, c) 5% noise, d) 10% noise..... 236

Figure G.10. Distribution of the change in modal flexibility for the first damage scenario when harmonic excitation was used and noise was added to the output signal: a) 1% noise, b) 2% noise, c) 5% noise, d) 10% noise..... 237

Figure G.11. Distribution of the change in uniform load surface curvature for the first damage scenario when harmonic excitation was used and noise was added to the output signal: a) 1% noise, b) 2% noise, c) 5% noise, d) 10% noise..... 238

Figure G.12. Distribution of the change unit load surface curvature for the first damage scenario when harmonic excitation was used and noise was added to the output signal: a) 1% noise, b) 2% noise, c) 5% noise, d) 10% noise..... 239

Figure G.13. Distribution of change in mode shape for the first damage scenario when impact excitation was used and noise was added to input force: a) 1% noise, b) 2% noise, c) 5% noise..... 240

Figure G.14. Distribution of change in mode shape curvature for the first damage scenario when impact excitation was used and noise was added to input force: a) 1% noise, b) 2% noise, c) 5% noise..... 241

Figure G.15. Distribution of damage index for the first damage scenario when impact excitation was used and noise was added to input force: a) 1% noise, b) 2% noise, c) 5% noise..... 242

Figure G.16. Distribution of change in modal flexibility for the first damage scenario when impact excitation was used and noise was added to input force: a) 1% noise, b) 2% noise, c) 5% noise..... 243

Figure G.17. Distribution of change in uniform load surface curvature for the first damage scenario when impact excitation was used and noise was added to input force: a) 1% noise, b) 2% noise, c) 5% noise. 244

Figure G.18. Distribution of change in unit load surface curvature for the first damage scenario when impact excitation was used and noise was added to input force: a) 1% noise, b) 2% noise, c) 5% noise. 245

Figure G.19. Distribution of change in mode shape for the first damage scenario when impact excitation was used and noise was added to output signal: a) 1% noise, b) 2% noise, c) 5% noise. 246

Figure G.20. Distribution of change in mode shape curvature for the first damage scenario when impact excitation was used and noise was added to output signal: a) 1% noise, b) 2% noise, c) 5% noise. 247

Figure G.21. Distribution of damage index for the first damage scenario when impact excitation was used and noise was added to output signal: a) 1% noise, b) 2% noise, c) 5% noise. 248

Figure G.22. Distribution of change in modal flexibility for the first damage scenario when impact excitation was used and noise was added to output signal: a) 1% noise, b) 2% noise, c) 5% noise. 249

Figure G.23. Distribution of change in uniform load surface curvature for the first damage scenario when impact excitation was used and noise was added to output signal: a) 1% noise, b) 2% noise, c) 5% noise. 250

Figure G.24. Distribution of change in unit load surface curvature for the first damage scenario when impact excitation was used and noise was added to output signal: a) 1% noise, b) 2% noise, c) 5% noise. 251

NOMENCLATURE

f'', $f_j''^*$	The curvatures of the uniform load surface vectors before and after damage respectively
$\Delta f_j''$	A vector representing the change in the uniform load surface curvature
h	Distance between measurement points
n_1, n_2	Constants used in calculating the displacement spectral density
s	Standard deviation of a sample
t	time, student's (t-distribution) variable
$u(t)$	Input vector
w_k, v_k	Disturbance and measurement noise respectively
$x(t)$	time series
$\bar{x}$	Sample mean
$y(t)$	Output vector
A_c	State matrix
B_c	Input influence matrix
C	Damping matrix
C_c	Output matrix
D_c	Output Control matrix
E	Modulus of elasticity
E_c	Modulus of elasticity of concrete
[F]	Flexibility matrix
[ΔF]	Change in flexibility matrix
$F(t)$	Force vector
$H(f)$	Frequency response function
I	Moment of inertia
K	Stiffness matrix
L	Length
M	Mass matrix
$M(x)$	Bending moment at location x
P	Probability

$Su(\kappa)$	Displacement spectral density
$U(t)$	Displacement vector
$\dot{U}$,$\ddot{U}$	First and second derivatives of displacement with respect to time
$X(f)$	Fourier transform of $x(t)$
Z_j	Normalized damage indicator for location j
β_{ij}	The damage index for location j for the ith mode
γ_c	Concrete density
δ_{ij}	An element of the matrix [ΔF]
Δ	Distance interval between successive ordinates of the surface profile
θ	Random phase angle
κ	Wave number
κ_0	Datum wave number
$v''(x)$	Curvature at a location x
μ, σ	Mean and standard deviation respectively
ϕ_j, ϕ_j^*	Amplitude of the pre- and post damage mode shape at node j respectively
$\Delta\phi_j$	Absolute difference between the pre- and post-damage mode shapes at node j
ϕ''_j, ϕ''^*_j	Pre- and post-damage mode shape curvatures at node j respectively
$\Delta\phi''_j$	The difference in mode shape curvature between the pre- and post-damage mode shape curvatures at node j
$\{\phi_i\}$	The ith identity-matrix normalised mode shape
ω_i	The ith natural frequency of a structure

LIST OF ABBREVIATIONS

APS	Auto Power Spectrum
ASTM	American Standards for Testing and Materials
CFRP	Carbon fibre reinforced polymer
COMAC	Coordinate Modal Assurance Criterion
COV	Coefficient of variation
CPS	Cross Power Spectrum
CSA	Canadian Standards Association
DAQ	Data acquisition system
DC	Direct current
DNL	Dynamic Nodal Load
ENL	Equivalent nodal load
ERA	Eigen Realisation Algorithm
FE	Finite Element
FFT	Fast Fourier Transform
FRF	Frequency response function FRF
HWD	Heavy Weight Deflectometer
LVDT	Linear variable displacement transducer
MAC	Modal Assurance Criterion
MACEC	A MATLAB Toolbox for Experimental and Operational Modal Analysis
NExT	Natural Excitation Technique
SHM	Structural health monitoring
SSI	Stochastic Subspace Identification
SVD	Singular Value Decomposition
VBDD	Vibration-based Damage Detection

1 INTRODUCTION

1.1 BACKGROUND

Countries around the world make large investments in the construction, operation, maintenance and rehabilitation of various types of infrastructure, such as bridges, roads, dams, power stations, buildings, etc. It is of utmost importance to have good asset management policies for the efficient utilisation of the usually limited funding available for management of the infrastructure inventory. Accurate and detailed condition information is essential for the infrastructure owner to come up with good decisions regarding the utilisation of the funding available for their infrastructure. Structural health monitoring (SHM) is one way of providing the essential information required for the proper implementation of asset management systems.

SHM comprises a wide range of techniques for condition and damage assessment of an existing structure. In the current study, a class of SHM methods known as vibration-based damage detection (VBDD) techniques was employed on a bridge that has undergone structural rehabilitation and upgrading using steel plates, as well as on a second bridge that was decommissioned.

Vibration-based assessment methods utilise changes in the global dynamic characteristics of the structure (i.e., natural frequencies, mode shapes and damping characteristics) as an indicator of structural damage. Since these dynamic modal characteristics are directly related to specific physical properties of the structure, measured changes in the modal characteristics can be used to detect and quantify damage.

VBDD is implemented by performing modal testing on the bridge or structure under consideration. Modal testing, as used in the context of VBDD, is an experimental testing technique that employs vibration tests and analytical methods to extract the modal

parameters of a structure (natural frequencies, mode shapes and damping ratios) from measurements of its responses due to dynamic excitation.

Different sources of dynamic excitation are available, including forced excitation induced by a shaker, impact excitation by dropping a weight, releasing a force or impact from a hammer, forced excitation due to traffic, or ambient excitation due to wind and river flow. Regardless of the excitation source, the computed dynamic response characteristics are distorted to some extent by measurement errors and approximations introduced during numerical processing of the measured data. For the case of traffic and ambient excitation, however, additional uncertainty is induced due to the random nature of the force itself. The accumulated uncertainty is then reflected in the reliability of the extracted modal properties and, ultimately, in the ability to successfully detect small-scale damage using VBDD methods.

One issue yet to be resolved is the influence that the character of the dynamic excitation has on the effectiveness of VBDD techniques. In practice, the most readily accessible sources of dynamic excitation for bridges are traffic and/or wind loading, both of which are random in nature and difficult to quantify, introducing considerable uncertainty into the identification of the required vibration mode parameters. On the other hand, controlled harmonic excitation or impact excitation, although more difficult to achieve in field applications, appear to be a more reliable method for generating the prerequisite vibration (Wegner et al. 2004). However, the extent of differences between the various excitation types has not been adequately quantified.

In the present study, two bridges were investigated. One is located on Provincial Highway No. 9 over the Red Deer River south of the town of Hudson Bay, Saskatchewan. The second bridge is located near the Town of Broadview, Saskatchewan, on an abandoned stretch of Trans-Canada Highway No. 1, 150 km east of the City of Regina. Field tests and numerical simulations were conducted using different types of excitation to determine the influence that the type of excitation had on the reliability of modal properties (natural frequencies and mode shapes), and thus on the implementation of VBDD.

Field tests were conducted using different sources of dynamic excitation: ambient, traffic excitation, and impact excitation. The purpose of field testing was to study the accuracy and repeatability of different types of dynamic excitation, in addition to using the results of field tests to update the finite element (FE) model of the bridge for further numerical simulation.

1.2 OBJECTIVES

The primary objective of this research was to study the influence of the character of the dynamic excitation on the effectiveness of modal parameter estimation and, therefore, on the likelihood of successfully applying VBDD techniques.

More specific objectives for this study are detailed below:

- To investigate the influence of uncertainty in the forcing function (system input) and measurements (system output) on the reliability of extracted modal properties;
- To investigate the implementation of VBDD techniques on a real structure as it underwent structural rehabilitation. In the process, the feasibility of some VBDD techniques and their ability to locate and quantify damage (in this case, the structural rehabilitation) was assessed;
- To compare the characteristics and relative reliability of modal properties extracted from measured responses to various forms of excitation, including harmonic forced excitation, random forced excitation, excitation from different configurations and models of trucks, free vibration of the bridge after random and truck excitation, impact forced excitation and ambient excitation;
- To establish typical statistical characteristics of modal parameters obtained using different types of excitation;
- To investigate the influence of using various numerical models to simulate truck loading excitation on the reliability of extracted modal properties; and
- To investigate the assumption that the response of a dynamically calibrated FE model of the bridge is representative of the actual bridge response.

1.3 METHODOLOGY

In the present study, two bridges were investigated. The first one was located on Provincial Highway No. 9 over the Red Deer River south of Hudson Bay, Saskatchewan. This bridge underwent structural rehabilitation to its middle span to increase its load carrying capacity. The second bridge was located near the Town of Broadview, Saskatchewan, off Trans-Canada Highway No. 1, 150 km east of the City of Regina. This bridge was decommissioned due to realignment of the highway, and was scheduled for demolition.

Field tests were conducted using different sources of dynamic excitation, including ambient (wind and river flow), traffic excitation, and impact excitation. The bridge response under the different dynamic excitation types was recorded using accelerometers that were attached to the bridge deck. The purpose of this type of field tests was to assess the different types of dynamic excitation in terms of their suitability for VBDD application, and to calibrate an FE model of the bridge that was used in further simulations.

In addition, strain gauges were installed on the girders of Hudson Bay bridge to record the bridge strains under different loading conditions (static and dynamic truck loading).

In addition to field tests, a calibrated FE model of the Hudson Bay bridge was generated and subjected to different types of dynamic forced excitation; including harmonic, random (white noise), impact and different types of model of truck excitation. In addition, different levels of noise (random variations) were superimposed on this excitation or on the bridge response to simulate the uncertainty that is inherent in field tests. The modal properties calculated from each of these tests were evaluated statistically and compared to evaluate the relative accuracy and reliability of results using various excitation methods.

The FE model was subjected to different damage scenarios by removing the external steel reinforcement from different locations on the bridge. This reinforcement was added to the soffit of the bridge girders in a previous rehabilitation to increase the bridge loading capacity. Different types of dynamic excitation were then applied to the FE model; the bridge modal properties were then calculated accordingly. Six VBDD

methods were used to evaluate the feasibility of detecting different types of damage using the above mentioned types of dynamic excitation with different levels of induced uncertainty.

The results of the different VBDD methods were examined and evaluated. Statistical evaluation was also performed to see whether the damage indicators suggested by the different VBDD methods were statistically significant or not.

1.4 THESIS LAYOUT

The thesis is organized in seven chapters, with additional information provided in the appendices. This thesis consists of experimental and numerical studies, which are described separately in subsequent chapters. The contents of the different chapters in the thesis are described below.

An overview for the study is presented in Chapter 1, including a background section that establishes the need for structural health monitoring and VBDD, in addition to the objectives and methodology of the present study.

In Chapter 2, a literature review including the theoretical background of modal analysis techniques, vibration-based damage detection methods, and dynamic excitation forces is presented.

Chapter 3 introduces the methodology used in this study. This chapter describes the general procedures and steps that were implemented; it starts with describing the Hudson Bay bridge and the FE model that was developed for that bridge. The instrumentation, sensor installation, field tests, data acquisition and processing are described next. In addition to the experimental phase of this study, Chapter 3 details the numerical simulation which includes the numerical modelling of the different dynamic excitation forces, simulated damage scenarios and the implementation of different VBDD methods. Statistical methods, such as the student t-test, that were used in assessing the variability of modal properties are also detailed. The experimental procedures and setups for conducting the impact test on the Broadview bridge are also discussed in Chapter 3.

The experimental results and discussion are presented in Chapter 4. The experimental programme included dynamic testing of the bridge using ambient vibration, traffic excitation, and impact using a spring hammer and a Heavy Weight Deflectometer (HWD). The FE model updating using field data is described as well. Strain gauge readings recorded during the crawl speed truck test are presented and discussed. Results of the impact excitation test that was conducted on the Broadview bridge are also discussed in Chapter 4.

Chapter 5 presents the results of the numerical investigation (using the FE model) that examined the effect of different types of excitation on the accuracy of the calculated modal properties. In this chapter, the variability of extracted modal properties using different dynamic excitation methods is presented and evaluated.

The performance of different VBDD methods under different damage cases is discussed in Chapter 6, as well as their performance in the presence of noise (random variation) in either the simulated dynamic excitation or in the bridge response.

Chapter 7 presents conclusions and recommendations for future research.

2 LITERATURE REVIEW

2.1 OVERVIEW

Civil infrastructure, in general, and bridges in particular, inevitably age and deteriorate over time. In Canada, over 40% of the bridges in use were built more than 30 years ago (Mufti 2001). Many of these bridges are deficient due, in large part, to the corrosion of reinforcement as a result of using de-icing salts in winter. In addition, due to evolving traffic loads and design standards, many of these bridges are deficient in strength or geometric layout and require strengthening, widening or replacement (Mufti 2001). This situation has led bridge owners to look for efficient ways of using their limited resources to inspect, maintain and rehabilitate their infrastructure; this, in turn, has led to the development of structural health monitoring (SHM). One way to define SHM is by its objectives (Mufti 2001). In general terms, these objectives are: to monitor the behaviour of a structure accurately and efficiently, to detect damage and deterioration, and to determine the health or condition of a structure in order to assess its performance.

Structural health monitoring and damage detection are viewed by Wong (2001) as one component in a value chain, which he defines as "an end-to-end solution to a problem with the beneficiary constituting one end of the chain and the enabling technologies (or parties) making up the rest of the chain". He also looks at the subject holistically, suggesting that SHM can be part of risk management philosophy for which SHM can provide information to understand and quantify the risk. The owner would then take the risk information and select the most suitable option for risk mitigation.

Mufti et al. (2005) presented the argument that structural health monitoring can reduce the cost of maintenance for current structures. This could be done by providing the owners with the necessary information to allow them to accurately allocate resources to the most effective repair and rehabilitation strategies for their structures. SHM can help

bridge managers achieve this through enabling the monitoring and evaluation of the structure, thus improving safety and reliability. Mufti et al. (2005) also argued that the information provided by SHM will be useful to future projects as it will help in estimating the life cycle costs of the structures.

From the above discussion, it is easy to see that SHM is becoming a key component of modern asset management systems. By providing either a continuous or periodic condition assessment of the structure, SHM facilitates the detection of damage at an early stage when mitigation measures may be less extensive and less costly. The structural evaluation may be achieved to varying degrees by using one or more of the numerous available techniques, including detailed visual inspections, non-destructive evaluation (NDE) techniques such as ultrasonic or radiographic methods, and global methods that use changes in the overall response of a structure as indicators of damage. Of these, global methods have the advantage of generally being less labour intensive since they are capable of assessing the condition of an entire structure at once.

Vibration-based damage detection (VBDD) methods are global SHM techniques that utilize changes to the dynamic characteristics of a structure (i.e. its natural frequencies, mode shapes, and damping properties) as indicators of damage. Since damage will modify the physical properties of a system, most notably the structural stiffness, any deterioration in the main structural elements will also cause changes in a structure's global dynamic characteristics (Wolf and Richardson 1989). Since the dynamic characteristics are readily quantifiable, any measurable changes may be used to identify damage, even at an early stage before visible signs of distress are apparent. While conceptually simple, considerable research is still required before VBDD methods can be applied reliably to complex structures such as bridges.

In this chapter the main aspects of VBDD are listed and discussed. Among the different aspects of VBDD are the different methods used to induce vibration on a bridge, and the different analytical techniques required to analyse the bridge vibration data in order to determine the bridge dynamic properties. The bridge dynamic properties that are needed as input parameters in the different VBDD methods are also discussed in this chapter.

Finally, the effect of dynamic excitation and measurement variability on the accuracy of VBDD methods is examined.

2.2 MODAL ANALYSIS

2.2.1 Overview

Modal analysis, as used in the context of VBDD, is an experimental testing technique that employs vibration tests and analytical methods to extract the modal parameters of a structure (natural frequencies, mode shapes and damping ratios) from measurements of its responses to dynamic excitation (Maia and Silva 1997; Ewins 2000). Experimental modal analysis has many applications; for example, it is used for finite element model updating, where the results of the dynamic testing are used in updating and validating a finite element model of the structure, which would then be used for further analyses and simulations (Friswell and Mottershead 1995). Other applications include structural damage detection and structural health monitoring, where changes in the measured structure's modal properties are used to indicate damage (Doebling et al. 1996), as well as for seismic or condition evaluation, where the measured bridge dynamic properties would give an insight into the bridge response and aid in the selection of seismic retrofit procedures (Ventura et al. 1994).

Traditional modal analysis methods use the frequency response function (FRF), which is a transfer function that relates measured input, usually force, to measured output, which is usually acceleration (Ewins 2000). To calculate the FRF, sensor readings are transformed into spectra in the frequency domain using a Fast Fourier Transform (FFT). For civil engineering structures, the dynamic response that constitutes the output is measured by the sensors; however, measuring the excitation (input) of a real structure is often difficult and costly.

Modal analysis methods may be classified in many different ways. One system of classification is to separate approaches into frequency domain methods and time domain methods (Maia and Silva 1997); another approach is to classify them according to measured data, i.e. into input-output methods (the classical modal analysis methods) and output only methods, where the input force is not measured but assumed to be a white

noise with a uniform spectrum in the frequency range of interest (James et al. 1995; Peeters and De Roeck 2001).

2.2.2 Frequency Domain Methods

Frequency domain methods make use of the FFT spectra of measured signals to extract the modal properties. From the basic principles of structural dynamics, it is known that a structure will vibrate either at one or more of its own natural frequencies or at the frequencies induced as a result of forced vibrations. When a structure is excited by a force with a flat spectrum (i.e., a force with equal energy content at all frequencies in the frequency range of interest), then this structure will vibrate most vigorously at its own natural frequencies due to resonance. The resonant vibration will be manifested as peaks in the structure's response spectra that correspond to the structure's natural frequencies. It is therefore possible to look at the response spectra from an FFT analysis and check for peaks that correspond to the damped natural frequencies of the structure, a technique known as "peak picking". Once the natural frequencies are identified, the relative modal amplitudes at various measurement locations can be computed to estimate the vibration mode shapes (Bendat and Piersol 1993). Drawbacks of this method include the difficulty of distinguishing between peaks that represent natural frequencies and those due to excitation, as well as the difficulty in identifying closely spaced modes (Paultre et al. 1995; Farrar and James 1997). On the other hand, these methods are easy to implement and give acceptable results in many cases.

As mentioned above, traditional modal analysis uses the FRF in estimating the structure's modal properties. Mode shapes calculated using FRFs are properly scaled with respect to each other because the input force is measured; therefore, the ratio between the input excitation force and the output structural response (FRF) is known as well. In ambient vibration measurements (e.g., bridge vibration testing), it is not possible to measure the time history of the input force if it is due to ambient excitation such as that caused by traffic or wind loading. For this reason, only the spectra of bridge responses are measured and used to extract the structure's modal properties. The response of the structure at one location is then used as a reference to scale the responses at other locations in order to calculate the mode shape amplitudes.

For a more accurate estimate of modal properties, the Cross Power Spectrum (CPS) approach is often used, in which the CPS is a product of the spectra of a reference accelerometer and that of another accelerometer (James et al. 1995; Herman and Van Der Auweraer 1999; Farrar et al. 2000). From the definition of the CPS, which is a measure of the power that two signals have in common at specific frequencies (Stearns and David 1996), the two measured responses will be correlated only at frequencies common to both signals; therefore, the peaks retained in the CPS are those that are common to both signals and more likely to be true natural frequencies. The natural frequencies can then be estimated using visual inspection to locate peaks in the CPS. Mode shapes are subsequently estimated from the relative magnitudes of these peaks at different locations on the structure. Another enhancement to the peak picking method is to apply Singular Value Decomposition (SVD) to the cross spectral matrix, which reduces the influence of noise in the signal (Shih et al. 1988; Peeters and De Roeck 2001). These various signal processing techniques are described below.

For a time series *x(t)*, the Fourier Transform (Spectrum), *X(f)* is defined as:

$$X(f) = \int x(t) e^{i 2\pi f t} dt \qquad [2.\ 1]$$

where *t* and *f* are time and frequency variables, respectively.

The Auto Power Spectrum of *X(f)*, *APS(X)* is then:

$$APS(X) = X(f) X(f)^{*} \qquad [2.\ 2]$$

where * denotes the complex conjugate.

The Cross Power Spectrum of the time series *x(t)* and another time series *y(t)* is defined as:

$$CPS(X,Y) = Y(f) X(f)^{*} \qquad [2.\ 3]$$

where *Y(f)* is the Fourier Spectrum of *y(t)*. The Frequency Response Function, *H(f)* may then be defined as:

$$H(f) = \frac{X(f)}{F(f)} \qquad [2.\ 4]$$

where *F(f)* is considered to be the spectrum of the input force and *X(f)* the spectrum of the structure response (Maia and Silva 1997, Santamaria and Fratta 1998).

2.2.3 Time Domain Methods

Time domain methods are defined here as those in which modal properties are extracted from time histories (direct methods), or from impulse functions, which are the inverse Fourier transforms of the measured spectra (indirect methods) (Maia and Silva 1997).

The Eigen Realisation Algorithm (ERA) method utilizes the structure's vibration data to build a state-space system from which the modal parameters of the structure can be identified, thus "realizing" the experimental data. A state-space representation of a physical system is defined as a mathematical model of a set of input, output and state variables related by first-order differential equations. A state variable is an element of the set of variables that describe the state of a dynamical system. In ERA, a matrix containing the measured data is created; a Singular Value Decomposition is then performed on the data matrix to determine the rank of the system and rebuild the reduced matrix, which in turn is used to calculate the state-space matrices. Finally the eigenvalues and eigenvectors (modal properties) are calculated from the realized state-space matrices (Juang and Papa 1985).

James et al. (1992, 1995) developed the Natural Excitation Technique (NExT). In this technique, they have shown that, for an input which is not measured, but assumed to be white noise (broad-band random excitation with flat spectral density), the cross-correlation function between two response measurements (the inverse Fourier transform of the CPS) can be expressed as the sum of decaying sinusoids that have the same frequencies and damping ratios as the modes of the system. Therefore, the cross correlation function will have the same form as the system's impulse response function; hence, time domain methods such as the Eigen Realization Algorithm (ERA) can be applied to obtain the resonant frequencies.

Stochastic Subspace Identification (SSI) is a time domain method that works directly with the time data and is an output-only modal analysis method. SSI can be considered as an enhanced ERA, where the input is not measured but assumed to be a stochastic process (white noise) (Peeters and De Roeck 2001).

The dynamic model of a structure can be described by a set of linear second order differential equations (Van Overschee and De Moor 1996; De Roeck et al. 2000):

$$M\ddot{U}(t) + C\dot{U}(t) + KU(t) = F(t) \qquad [2.5]$$

where *M*, *C* and *K* are the mass, damping and stiffness matrices, *U(t)* and *F(t)* are the displacement and input force vectors; here, the superimposed dot notation ($\dot{U}$,$\ddot{U}$) is used to denote derivatives with respect to time. Eq. [2.5] can be re-written in a state-space representation as a set of first-order differential equations:

$$\dot{x}(t) = A_c x(t) + B_c u(t) \qquad [2.6a]$$

$$y(t) = C_c x(t) + D_c u(t) \qquad [2.6b]$$

where the state vector *x(t)* and force vectors *F(t)* are:

$$x(t) = \begin{Bmatrix} U(t) \\ \dot{U}(t) \end{Bmatrix} \qquad [2.7a]$$

$$F(t) = B_2 u(t) \qquad [2.7b]$$

The vectors *u(t)* and *y(t)* represent observations of the input and output of the process, respectively. A_c is the state matrix which represents the dynamic characteristics of the system; B_c is the input matrix which represents the input influence; C_c is the output matrix which specifies how system states are transformed to the output; D_c is the output control, or direct feed-through matrix; and the subscript c denotes continuous time. A discrete time state-space model becomes:

$$x_{k+1} = Ax_k + Bu_k \qquad [2.8a]$$

$$y_k = Cx_k + Du_k \qquad [2.8b]$$

where *k* is an index identifying a specific time increment.

In practice there is always noise (random uncontrolled variance) that can be divided into process and measurement noise. The process noise is due to disturbances in the input, whereas the measurement noise is due to noise and inaccuracy in sensor readings.

The state-space model can be extended to include these stochastic components, as follows:

$$x_{k+1} = Ax_k + Bu_k + w_k \quad [2.9a]$$

$$y_k = Cx_k + Du_k + v_k \quad [2.9b]$$

where w_k and v_k are the disturbance and measurement noise respectively, both of which are assumed to resemble white noise.

A graphical representation of the system in state-space terms is shown in Figure 2.1. The vector signals u_k and y_k are measurable (observed) while v_k and w_k are unknown disturbances (noise), and the symbol Δ represents a delay.

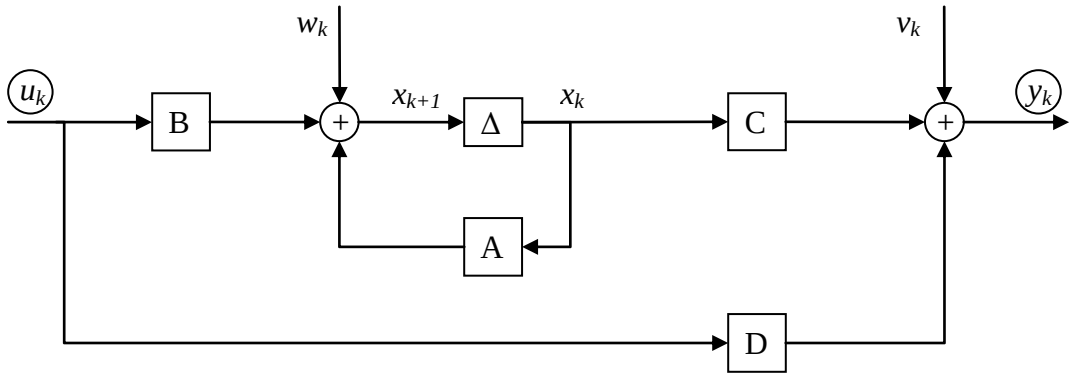

Figure 2.1. State-space system (Van Overschee and De Moor 1996).

In testing of civil engineering structures, only the response y_k of the structure is usually measured; therefore, it is impossible to distinguish the input term u_k from the noise term w_k in Eq. [2.9]. This results in the output- only stochastic system:

$$x_{k+1} = Ax_k + w_k \quad [2.10a]$$

$$y_k = Cx_k + v_k \quad [2.10b]$$

A graphical representation of the noisy system is show in Figure 2.2.

Eq. [2.10] constitutes the basis for a time-domain system identification, which can be realized (solved) by a stochastic subspace system identification (SSI) algorithm. The SSI algorithm uses several numerical techniques to identify the state space matrices *A* and *C*.

Once the state-space model of the structure is found, then it is easy to determine the modal parameters (natural frequencies, damping rations and modes shapes) by eigen-value decomposition. The SSI method, as implemented in the MACEC toolbox for MATLAB (Van den Branden et al. 1999), was adopted for use in this study.

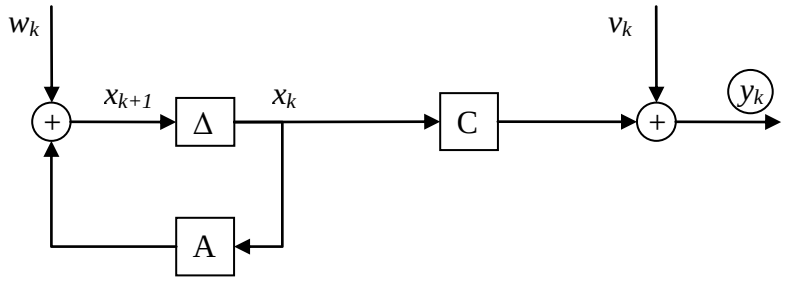

Figure 2.2. Graphical representation of an (output-only) Stochastic State-space system (Van Overschee and De Moor 1996).

2.3 VBDD METHODS

2.3.1 Overview

Currently used damage detection methods are either subjective, such as visual inspection which depends on the experience of the inspector, or localised in nature, such as ultrasonic and acoustic methods, magnetic field methods, thermal imaging, and radiographic methods. Many of these methods require that the damage location be known or guessed beforehand and that the location to be inspected be accessible; in addition, they are usually very time consuming. The need for an objective and global damage detection method that can be applied to real structures led to the development of methods that evaluate changes in the vibration characteristics of a structure.

The basic idea of vibration-based damage detection (VBDD) methods is that modal properties (natural frequencies, mode shapes and damping) are a function of the physical properties of the structure (mass, stiffness and boundary conditions). Therefore, changes in the physical properties of the structure will cause changes in the modal properties.

Detailed literature reviews of VBDD methods have been provided by Doebling et al. (1996) and Sohn et al. (2003). Early VBDD studies examined the changes in the dynamic properties during forced and ambient vibration. It was generally found that mode shapes were a more sensitive indicator of small damage than natural frequencies

or damping (Salane et al. 1981; Spyrakos et al.1990; Mazurek and DeWolf 1990; Farrar et al. 1994; Alampalli et al. 1997).

Other bridge damage detection methods have examined the changes in other vibration-based parameters, such as the frequency response function (FRF) (Samman and Biswas 1994a; 1994b), mechanical impedance function (Salane et al. 1981), modal assurance criterion (MAC) and coordinate modal assurance criterion (COMAC) (Fox 1992; Farrar et al. 1994; Salawu and Williams 1994), and finite element (FE) model updating methods (Beck and Katafygiotics 1992; Kaouk and Zimmerman 1993).

The methods examined in this study are based on changes in measured modes shapes or their derivatives, and, in some methods, the natural frequencies of the structure. These methods are: changes in mode shape values, changes in mode shape curvature, changes in measured modal flexibility, changes in uniform load surface curvature, changes in unit load surface curvature, and the damage index method (change in strain energy). These methods were chosen because they use modal properties that are readily available using site measurement and modal testing, and do not require additional steps such as the formulation and updating of an FE model.

2.3.2 Change in Mode Shape Method

The change in mode shape as an indicator of damage has been used by many researchers (Mazurek and DeWolf 1990; Srinivasan and Kot 1992). Due to its simplicity, the change in mode shape method can be considered as a basic method that other methods can be compared to. The mode difference can be defined as:

$$\Delta\phi_j = \left|\phi_j^* - \phi_j\right| \qquad [2.11]$$

where ϕ_j is the amplitude of the pre-damage mode shape at node j, ϕ^* is the amplitude of the post-damage mode shape at node j, and $\Delta\phi_j$ is the absolute difference between the pre- and post-damage mode shapes at node j.

2.3.3 Change in Mode Shape Curvature Method

Pandey et al. (1991) used the change in mode shape curvature as an indicator of damage, assuming that structural damage affected the structure's stiffness matrix. According to elementary beam theory, the curvature at a location x along a beam, $v''(x)$, is:

$$\nu''(x) = M(x)/(EI) \qquad [2.12]$$

where *M(x)* is the bending moment at location *x*, *E* is the modulus of elasticity and *I* is the moment of inertia of the cross section. It is evident from Eq. [2.12] that any reduction in flexural rigidity (*EI*) due to damage will lead to an increase in curvature, and that the difference between pre- and post-damage curvature mode shapes will be largest at the location of damage. The difference in mode shape curvature, $\Delta\phi''_j$, between the pre- and post-damage mode shape curvatures, ϕ''_j and ϕ''^*_j, respectively at location *j* may be expressed as:

$$\Delta\phi''_j = \left|\phi''^*_j - \phi''_j\right| \qquad [2.13]$$

Unless it is measured more directly, curvature of the mode shape can be estimated numerically using a central difference approximation as:

$$\phi''_j = \frac{\phi_{j+1} - 2\phi_j + \phi_{j-1}}{h^2} \qquad [2.14]$$

where ϕ_j is the mode shape amplitude at point *j* and *h* is the distance between measurement points.

2.3.4 Damage Index Method

The damage index method was developed by Stubbs et al. (1995). The damage index β is based on the change in the strain energy stored in a beam-like structure when it deforms in one of its mode shapes, where the change in modal strain energy can be related to the change in its curvature. The damage index β_{ij} for location *j* on the beam for the *i*th mode is:

$$\beta_{ij} = \frac{\left(\int_a^b \left[\phi''^*_i(x)\right]^2 dx + \int_0^L \left[\phi''^*_i(x)\right]^2 dx\right)}{\left(\int_a^b \left[\phi''_i(x)\right]^2 dx + \int_0^L \left[\phi''_i(x)\right]^2 dx\right)} \times \frac{\int_0^L \left[\phi''_i(x)\right]^2 dx}{\int_0^L \left[\phi''^*_i(x)\right]^2 dx} \qquad [2.15]$$

where $\phi''_i(x)$ and $\phi''^*_i(x)$ are the mode shape curvature functions of the *i*th mode for the undamaged and damaged structure, respectively, as a function of distance *x* along the

beam; here, L is the length of the beam, and a and b are the limits of the segment of the beam over which damage is being evaluated.

The damage index β can be written in a discrete form, assuming that the spacing between the points defining the mode shape is uniform, as follows:

$$\beta_{ij} = \frac{\left(\phi''^{*}_{ij}\right)^2 + \sum_{k=1}^{n}\left(\phi''^{*}_{ik}\right)^2}{\left(\phi''_{ij}\right)^2 + \sum_{k=1}^{n}\left(\phi''_{ik}\right)^2} \times \frac{\sum_{k=1}^{n}\left(\phi''_{ik}\right)^2}{\sum_{k=1}^{n}\left(\phi''^{*}_{ik}\right)^2} \qquad [2.16]$$

where n is the number of locations where modal curvature is calculated along the beam. Assuming that the damage indices are normally distributed, values falling two or more standard deviations from the mean are assumed to be indicative of damage, as calculated by:

$$Z_j = (\beta_j - \mu)/\sigma \geq 2.0 \qquad [2.17]$$

where Z_j is the normalized damage indicator, and μ and σ are the mean and standard deviation of damage indices for all locations. Two standard deviations from the mean correspond to a two sided confidence level of 95% (Wang et al. 2000).

2.3.5 Change in Measured Modal Flexibility Method

Pandey and Biswas (1994) showed that the flexibility matrix of a structure [**F**] can be approximated using the unit-mass normalised modal data as:

$$[\mathbf{F}] \approx \sum_{i=1}^{n} \frac{1}{\omega_i^2} \{\phi_i\}\{\phi_i\}^T \qquad [2.18]$$

where ω_i is the ith angular natural frequency, $\{\phi_i\}$ is the ith unit-mass normalised mode shape, and n is the number of measured modes. The flexibility matrix, [**F**], in Eq. [2.18] is an approximation because it is generally calculated using the lower measured modes only. The change in flexibility is then defined as:

$$[\mathbf{\Delta F}] = [\mathbf{F}]^{*} - [\mathbf{F}] \qquad [2.19]$$

where the asterisk means that the flexibility matrix corresponds to the damaged structure. If δ_{ij} is an element of the matrix [**ΔF**], then the absolute maximum value, $\overline{\delta}_j$, of the elements of each column in [**ΔF**] is defined as:

$$\overline{\delta}_j = \max\left|\delta_{ij}\right| \qquad i = 1,\ldots,n \qquad [2.20]$$

The position corresponding to the largest value of $\overline{\delta}_j$ is taken to indicate the probable location of damage.

2.3.6 Change in Uniform Load Surface Curvature Method

The elements of the *i*th column of the flexibility matrix represent the deflected shape of the structure when a unit load is applied at the *i*th degree of freedom. The sum of the corresponding elements in the columns of the flexibility matrix represents the deflected shape of the structure when a unit load is applied at every degree of freedom, which is referred to as the uniform load surface. The change in the curvature of the uniform load surface can be used to locate damage (Zhang and Aktan 1995) as follows:

$$\Delta f_j'' = \left| f_j''^{*} - f'' \right| \qquad [2.21]$$

where $\Delta f_j''$ is a vector representing the change in the uniform load surface curvature, f'' and $f_j''^{*}$ are the curvatures of the uniform load surface vectors, and the asterisk represents the damaged structure.

A variation of the change in uniform load surface curvature method was also used in this research. In this method, the curvature of the surface created by a unit load applied at the *i*th degree of freedom is calculated. This process is then repeated and the curvature is calculated with the unit load applied at all the other degrees of freedom individually. All unit load surface curvatures are then summed up and the absolute difference between the sums of unit load surface curvatures before and after damage is considered to be an indicator of damage (Farrar and Jauregui 1996). For the purpose of this research, this VBDD method is referred to as the change in unit load surface curvature method.

2.4 APPLICATION OF VBDD METHODS ON BRIDGE STRUCTURES

Numerous studies involving the development and application of VBDD methods on bridge structures have been published. These studies vary in their scope, implementation and type of bridge studied; as such, their methods and findings serve to highlight the common techniques and issues encountered when implementing VBDD in the field. Below is a brief review that highlights the application of the VBDD methods listed in Section 2.3 to bridge structures.

Mazurek and DeWolf (1990) tested the change in mode shape method on a two-span laboratory bridge model that was subjected to two types of structural deterioration: support failure and progressive cracking of the bridge girder at midspan. The test showed that the greatest change in mode shape occurred in the vicinity of the damage location.

From tests conducted on the I-40 bridge, which consisted of a concrete deck supported on two steel plate girders, in addition to stringers and floor beams, Farrar and Cone (1995) observed that changes in mode shapes were significant only at the most severe damage state, where the bottom flange and most of the web of one plate girder were cut, leaving the top part of the web and the top flange to carry the bridge load. They concluded that changes in mode shapes may not be sensitive enough indicators to detect damage at an early stage.

Stubbs et al. (1995) applied the damage index method to a three-span concrete deck on steel girder bridge (the same bridge that was studied by Farrar and Cone 1995). Eleven accelerometers were used to instrument the bridge, spaced at 4.9 m (16 ft) on average. The bridge response was interpolated at 160 locations using a spline function; these locations were spaced 0.3 m (1 ft) apart or 1/160 of the bridge length. It was concluded that the maximum damage localization error, or the difference between the actual and predicted damage location, was 2.5% of the span.

Wang et al. (2000) evaluated the numerical and experimental feasibility of using the damage index method to detect damage on a large span concrete box girder bridge. The severity of damage was modelled as a 10% to 50% reduction in the modulus of elasticity of different parts of the bridge. The study found that the method could correctly locate

damage states 70% of the time, and that the method was most successful when damage was located near the centre of the structure and less accurate when it was located near the supports.

A field verification study of the damage index method was conducted by Park et al. (2001). In that study, a two-span reinforced concrete box-girder bridge was monitored twice within a nine-month period, and its dynamic properties were compared for the two measurements using the damage index method. The damage index method was compared to a visual inspection conducted on the bridge which discovered surface cracks on the bridge. The results showed a good correlation between the crack locations predicted by the damage index method and the visual inspection, which showed the actual location of the cracks.

Aktan et al. (1994) found a good correlation between the deflections calculated using modal flexibility and that obtained from static load testing of a two-lane, three-span continuous, integral abutment, steel-stringer bridge. Also, they implemented the modal flexibility method on a steel truss bridge that was subjected to damage. Test results showed that the bridge became more flexible after the induced damage.

Toksoy and Aktan (1994) successfully implemented the change in modal flexibility method on a decommissioned bridge under different states of damage (removal of asphalt overlay). Mazurek (1997) examined the application of the change in modal flexibility method on a simply supported four-girder model bridge. Severe damage induced by cutting of one of the bridge girders was detected using this method.

Zhang and Aktan (1995) used the change in the curvature of the uniform load surface method to detect damage using a calibrated two-dimensional FE grid model. The model represented a three-span continuous steel stringer bridge. The model was calibrated using modal test results obtained from the actual bridge. The conclusion was that the sensitivity of the method was not large enough to distinguish between small damage states and experimental errors.

Farrar and Jauregui (1998a; 1998b) conducted a comparative study on a bridge where they examined five damage detection algorithms using experimental and numerical data. The damage detection methods examined in this study were: the damage index method,

mode shape curvature method, change in flexibility method, change in uniform load surface curvature method, and change in stiffness method. The bridge under consideration was a three-span bridge made up of a concrete deck supported by two steel plate girders and three stringers. Different levels of damage were implemented on the bridge to investigate the ability of each damage detection method to detect and locate the different levels of damage. The study concluded that all methods could accurately locate severe damage; however, these methods showed varying levels of success when the damage was small. Overall, it was concluded that the damage index method performed better than other methods in most cases.

It can be seen from this review that the published work varies in the type of bridge tested, the method of dynamic testing, and the implementation of the different VBDD techniques. This, in turn, makes it difficult to come up with a uniform conclusion regarding the feasibility of the different VBDD methods, or the effect of the different parameters that are involved in bridge testing on the accuracy of these methods.

2.5 TYPES OF DYNAMIC EXCITATION

Various devices are available to excite a structure for the purpose of dynamic testing. The dynamic exciter or shaker is widely used in modal testing. It can generate different types of dynamic excitations such as sinusoidal, random or chirp. There are different types of this device. The mechanical shaker uses a rotating out-of-balance mass to generate the prescribed force. There is little flexibility in the use of this shaker because the magnitude of the generated force is restricted by the configuration of the out-of-balance mechanism. The electromagnetic shaker converts the supplied input electrical signal to an alternating magnetic field around a coil that drives the shaker. The hydraulic shaker generates the dynamic force through the use of a hydraulic system which is often controlled by an electrical system. The hydraulic shaker has the advantage of providing long strokes, thus exciting the structure at larger amplitudes at low frequencies (Ewins 2000).

Another excitation method is through the use of hammer or impact excitation. The equipment consists of an impactor, usually with tips of varying stiffness to control its dynamic range, and with a load cell attached to it to measure the force imparted to the

test structure. The impactor can be in the shape of a hammer that can be operated by hand, a drop weight mechanism, or spring loaded device (Ewins 2000). Impact excitation is considered convenient because of its low cost, simplicity and speed of execution. Impact excitation has the advantage of producing a broadband excitation that has nearly constant energy over a predetermined frequency range (Pavic et al. 1997). The experimental setup and signal processing aspects for impact testing are detailed by Trethewey and Cafeo (1992) and ISO Standard 7626-5 (1994).

Another type of transient excitation is the step relaxation, in which a steady load is applied to the structure, usually by means of a steel cable or rope, and then released suddenly. This type of excitation is usually used for large structures (Ewins 2000).

A different method for dynamic testing is to measure the structure's response while it is in operation. In the case of a machine, the readings are taken while it is running, while for a bridge, readings are obtained while it is being subjected to wind or traffic excitation. This kind of testing is called operational or output-only modal testing, because only the structure's response (output) is measured, while the input is not measured.

While modal testing in mechanical and industrial engineering is well established, there are many challenges in implementing it on civil engineering structures. Pavic et al. (1997) outline the differences between modal testing in civil engineering compared to mechanical, automotive and aerospace engineering. These differences can be summarised as the requirement of using portable equipment in open space on a structure with large dimensions, low natural frequencies, closely spaced modes of vibration, and a limitation on testing time; in addition, the typically heavy weight of a civil engineering structure makes excitation difficult. All these factors require special consideration and the make modal testing more difficult.

Many researchers have used different methods to excite bridges for dynamic testing, in which the dynamic tests were done for different purposes. For example, Deger et al. (1994) used a hydraulic shaker to excite an arch bridge for the purpose of updating a finite element model; Rotter et al. (1994) used impact excitation on a railway bridge to determine its existing capacity; Anvar and Rahimian (1996) used ambient vibration

(wind and micro tremors) to estimate the dynamic characteristics of a concrete curved bridge; DeWolf et al. (1998) used a truck to excite a bridge in order to measure its lowest natural frequencies; Ventura et al. (2000) used ambient vibration on a steel-free-deck bridge to determine its dynamic properties, which were then used to update a finite element model of the bridge. Fanning et al. (2007) used ambient vibration and forced excitation with an electro-dynamic shaker to determine the fundamental natural frequency of a pedestrian bridge, to assist the designer in future modelling of similar bridges.

2.6 COMPARISON OF DIFFERENT DYNAMIC EXCITATION METHODS

By conducting an impact test and forced vibration test on a bridge, Zhang (1994) found that the modal data obtained from the impact test were of lower quality compared to those obtained using harmonic forced vibration. However, he could improve the results of the impact test and make them comparable to forced vibration test results by omitting the readings at the bridge boundaries (supports and abutments) where the signal-to-noise ratio was low.

A literature review regarding excitation methods for bridge structures was conducted by Farrar et al. (1999). In this literature review, the various methods that have been used to excite bridges during dynamic testing were summarized. They divided excitation methods into two categories: ambient excitation and measured input excitation methods. The ambient excitation methods listed were: test vehicle, traffic, wind and waves. They indicated that the frequencies observed from these types of excitation could be related to the truck or traffic excitation and not necessarily those of the bridge. The measured input excitations listed in the literature review were: impact, step relaxation, and a shaker with varying input waveforms. It was concluded that there was no agreement as to which method performed better, and that ambient excitation is the only practical method to excite large bridges.

Farrar et al. (2000) studied the variability in modal parameters related to the excitation source using statistical methods. Field results obtained from a hammer impact test were compared to those obtained from ambient vibration tests. Monte Carlo and Bootstrap methods were used to calculate the uncertainty bounds of the identified natural

frequencies and damping from measured FRFs. It was found that the uncertainty level of natural frequencies obtained using ambient vibration was higher than that due to hammer excitation. It was also determined that ambient excitation could not identify all the modes that the impact hammer could because of the deficiency of some frequency ranges in the input power spectrum.

Ndambi et al. (2000) compared different excitation methods and modal analysis techniques on concrete structures. They tested three concrete beams, each 6 m long. The beams were excited using three types of excitation: an instrumented hammer and an electromagnetic shaker using both pseudo-random and sine-sweep signals. The modal parameters were estimated by two different modal analysis techniques, curve fitting of the measured frequency response functions and the stochastic subspace identification method. It was concluded that the modal analysis methods had little effect on the estimated natural frequencies, while the type of excitation did affect estimation of the beam's natural frequencies. The measured natural frequencies produced by impact excitation were 2% different compared to those measured using shaker excitation. The difference was attributed to the influence of the shaker on the beam making it behave more rigidly. Only a qualitative assessment was presented regarding the nature of the calculated mode shapes of the concrete beam.

The effect of excitation sources and temperature on vibration-based health monitoring of civil engineering structures was studied by Peeters et al. (2001). Results obtained from the use of the following excitation types were compared: band-limited noise generated by a shaker, the impact from a drop weight, and ambient sources such as wind and traffic. Ambient and shaker excitations were logged for 11 minutes. Natural frequencies and MAC values of vibration modes estimated from the different excitation types were extracted and compared. Although there were differences in estimated parameters, they concluded that ambient excitation yielded comparable results to the use of shaker or impact excitation.

Brownjohn et al. (2003) examined the effect of different excitation methods on a bridge that had undergone upgrading to increase its load carrying capacity. Shaker excitation using a sine-sweep signal, vehicle induced response, and hammer impact were

employed to assess their viability in providing quality data for modal testing. It was found that the highest quality data were acquired when using a shaker.

It can be seen from the discussion above that different researchers came to different conclusions regarding which type of dynamic excitation would yield more accurate results; however, in general, it seems that forced excitation yields better results. This may be attributed, partially, to the fact that forced excitation would produce higher levels of excitation than ambient excitation, thus imparting more energy to excite the bridge.

2.7 NOISE AND VARIABILITY IN DYNAMIC TESTING

Different measurements taken at the same location and under the same excitation, but at different times, are known to vary to some extent due to random noise, errors in measurements, external interference, etc. Therefore, it is advisable to perform an averaging process involving several time history records (an ensemble) at the same measurement locations to increase the statistical reliability of modal parameters and mitigate the effect of random noise (Ewins 2000; Newland 1984).

Kim and Stubbs (1995) examined the impact of model uncertainty on the accuracy of damage detection applied to a model plate girder for which only a few modes were known. This plate girder was made up plates and angle sections. The uncertainties considered in their work included the type of FE model used to approximate the plate girder, uncertainty in the estimation of the stiffness parameters, and the uncertainty in the mode shape definition. It was found that the uncertainty in mode shapes had the strongest influence on damage detection accuracy, while the uncertainty in the stiffness parameters had little influence on damage detection accuracy.

Ruotolo and Surace (1997) showed how a statistical test using the t-distribution could be used to decide the statistical significance of changes in natural frequency shifts due to structural damage.

Alampalli et al. (1997) tested a one-sixth scale steel-girder bridge and a field bridge to study the feasibility of using measured modal properties for the detection of damage. The statistical properties of several modal parameters were evaluated and compared; in

addition, the effect of random variations of these measured properties on damage diagnosis was evaluated using a two-sample t-test. The bridges were excited by an instrumented impact hammer, and different damage scenarios were considered. The researchers used natural frequencies, modal amplitudes, MAC and COMAC values for damage detection. It was concluded that the damage was difficult to identify using the modal parameters considered in their study, and that random variation affected the sensitivity of damage detection.

Although their work was not specifically related to bridges, Cafeo et al. (1998) identified a number of different parameters that affect the variability of vehicle modal testing, such as the type, level and location of the excitation force, sensor calibration and method of attachment, and signal processing considerations.

A literature review done by Kirkegaard and Andersen (1998) investigating the use of statistical information for damage assessment concluded that the use of statistical information is the key to damage assessment of civil engineering structures using vibration based damage detection. The study noted also that few researchers have considered the problem of statistical evaluation of the modal parameters and its effect of damage detection.

Andersen and Brincker (1999) stated that modal parameters are often treated deterministically instead of stochastically. In applications where the change of modal parameters is of interest, such as in VBDD, the quality of these modal parameter estimates is essential. They stated also that statistical tests are required to evaluate the uncertainty in the estimated the modal parameters.

Farrar and Doebling (1997), in a literature review regarding modal-based damage identification methods, stated that "Very few modal based damage detection studies report statistical variations associated with the measured modal parameters used in the damage (identification) process."

Doebling et al. (1997) investigated the effects of statistical uncertainty of modal parameters on the detection of damage in a bridge structure. The uncertainties were calculated in the measured natural frequencies, modes shapes and mode shape curvatures using Monte Carlo simulation applied to FRFs measured from impact

excitation of the bridge. The results showed that the mode shape curvatures had the largest level of uncertainty, but also exhibited the largest change due to damage. It was concluded that the statistical significance of changes in modal parameters and not only the changes themselves, must be considered when using modal testing for damage detection.

Doebling and Farrar (1998) used the Monte Carlo method to define a normal probability distribution for the modal parameters of the I-40 Bridge calculated from the confidence intervals of the FRF data. This approach was used to examine the statistical significance of change in damage detection indicators, namely the change in natural frequency, the change in mode shape amplitude and the change in the flexibility matrix. An eccentric-mass shaker was used to excite the bridge. The result of their study indicated that the changes in both modal properties and damage indicators were statistically significant, but could not be used to accurately localise damage.

Ren and De Roeck (2002) examined the effect of measurement noise on a damage detection method that they developed based on stiffness matrix updating. They used an FE model of a beam with levels of noise of 1% and 2% of the original amplitude being added to its natural frequencies and mode shapes. It was found that damage identification was more sensitive to a perturbation of the mode shapes than to the variation of the natural frequencies. It was also determined that the effect of noise on damage identification depends strongly on the severity of damage, and that if damage and noise correspond to a comparable deviation of natural frequencies and mode shapes, then the damage can hardly be identified.

2.8 VBDD RESEARCH AT THE UNIVERSITY OF SASKATCHEWAN

This research is part of a comprehensive program at the University of Saskatchewan investigating different issues affecting the practical application of VBDD methods to bridges. The research program comprises two parts: the first part encompasses numerical- and laboratory-based experimental studies, while the second part consists of a field testing program where different parameters are studied to examine their effect on testing actual bridges under field conditions (Wegner et al. 2004). The issues that have been examined as part of this program include a comparison between different VBDD

methods, the effect of sensor type and spacing on damage detection, the number of mode shapes required to detect damage, the effect of temperature on dynamic testing and VBDD, the ability to detect small scale damage, the reliability of various types of measurements and the effect of the type of dynamic excitation. Wegner et al. (2004) identified measurement repeatability and uncertainty as the key issue that prevents VBDD from being applied to bridge structures in the field. They also found that measurement repeatability is affected by temperature changes, method of excitation, and the number, configuration, and type of sensors. The research concerning each of these issues is detailed below.

Zhou et al. (2004) applied several VBDD techniques to a full-scale prestressed concrete girder, while inducing small scale damage states. They found that as few as six accelerometers located along the span of the girder were sufficient for the detection of damage, and that only the first mode of vibration was required. The accuracy of the damage detection depended on the spacing of the sensors and the proximity of a sensor to the damage location. The study found that the change in mode shape method was the most robust method for detecting damage, followed by change in flexibility method.

Zhou et al. (2007) conducted a lab-based experiment and FE analysis to examine the ability of five VBDD methods to detect and localize small-scale damage on the deck of a scaled model of a two-girder, simply supported bridge. The research was focused on using a small number of sensors and only the fundamental mode of vibration of the bridge. The study showed that damage can be detected and localized in the longitudinal direction of the bridge within a distance equal to the spacing between sensors. This damage detection was achieved using only the fundamental mode shape before and after damage, defined by as few as five measurement points. The study also concluded that the resolution of the damage localization drops near the bridge supports, and increasing the number of measurement points improved the localization resolution. Using two additional modes did not significantly improve the resolution of damage localization

Siddique et al. (2007) investigated the use of VBDD methods to detect small scale damage on a two-span integral abutment bridge. They used a calibrated FE model to evaluate different VBDD methods and study the effect of sensor spacing, mode shape

normalisation and uncertainty in the measured mode shapes on VBDD. It was concluded that it was feasible to detect small scale damage on the bridge deck if sensors were located close enough to the location of the damage, and if uncertainty in the measured mode shapes was reduced by repeated and averaged measurements.

Pham et al. (2007) studied the effect of changes in ambient temperature on vibration-based damage detection of small scale damage on the deck of the same bridge studied by Siddique et al. (2007). The study found that variations in ambient temperature changed the bridge natural frequencies and mode shapes significantly. The pattern of changes in mode shapes due to damage was found to be different from that due to temperature changes, especially in the vicinity of damage; however, the temperature induced effects were found to be significantly larger for the studied case.

Wang et al. (2008) conducted an experimental study to investigate the reliability of VBDD methods using a 1/3rd scale bridge model. The study investigated the different variables that affect the reliability of VBDD, including the data recording period, data sampling rate, type of dynamic excitation, and sensor type and location. Both harmonic and random forcing was used to excite the bridge. The bridge response was measured using accelerometers and strain gauges both when it was in an undamaged state, as well as after several controlled damage scenarios were induced on the bridge. It was concluded that mode shapes derived from accelerometer readings were more accurate that those derived from strain gauge readings, and that harmonic excitation produced more repeatable mode shapes. Other findings from that study were that mode shape reliability increased with increasing the sampling period or increasing the degree of time averaging, that the structure's natural frequencies decreased with the progress of induced damage, and that damage detection assessment using change in mode shape measurements was influenced significantly by the manner in which the mode shapes were normalised.

2.9 SUMMARY

From the preceding literature review, it can be seen that the type of dynamic excitation used for modal testing affects the results of the test and the estimated modal properties due to the different response characteristics produced by each type of excitation.

Another factor that affects the quality of the estimated modal properties is the level of random uncertainty (noise) in measured signals. This noise can be characterized as input noise due to variation in the input excitation force, or output noise presenting itself as errors in the measured signal by the sensors that are used during the test. Output errors can be attributed to environmental effects, sensor limitations, limitations of the digitization process, or electromagnetic interference picked up along the connecting cables between different components of the data acquisition system.

Many researchers have compared different excitation methods. However, these comparisons were often limited to two or three different methods and focused on the effect of excitation on the extracted modal frequencies, and occasionally on mode shapes. Little research has been done to investigate the effect of excitation on modal properties in a quantitative manner that can be incorporated into a VBDD assessment, and to determine the influence of various types of excitation on the performance of different VBDD methods.

A number of researchers have drawn attention to the variability of estimated modal properties; nonetheless, the majority of work done so far is limited in nature and has addressed only specific aspects of the problem. For example, most of the work done to date was applied to measured data recorded using one type of excitation. Few attempts have been made to evaluate the level of uncertainty in the measured signal and its effect on estimated modal properties, and thus on the effectiveness of VBDD methods.

For a successful implementation of VBDD in the field that yields reliable results, it is important to identify the effect of different excitation methods on the structure's modal properties, and thus their effect on the different VBDD techniques. For VBDD to become a routine bridge testing procedure, it is crucial to choose a suitable dynamic excitation method that is not only easy to implement but also one that yields reliable results under field conditions. The variability of site measurements needs to be taken into account when implementing the different VBDD methods in order to provide a reliable damage evaluation for the bridge.

This research was designed to address this gap in the current knowledge base. A primary objective has been to examine the effect of different types of dynamic excitation on the

estimated modal properties. The types of excitation considered were: harmonic forced excitation, random forced excitation, truck excitation, and impact excitation. The influence of these excitation types on the estimated modal properties was evaluated, quantified and compared. The effect of uncertainty or variability in the input force, as well as in the measured signal, on the quality of estimated modal properties was examined.

The current research program also investigated the interaction between the excitation force, the level and source of uncertainty, and the effectiveness of VBDD techniques to determine which VBDD methods are more robust for practical applications. Statistical levels of confidence were also established to better understand the statistical significance of variability in VBDD indicators.

3 RESEARCH METHODOLOGY

3.1 OVERVIEW

The main aspects of the research methodology, along with its theoretical background, are described in this chapter, starting with a description of the Hudson Bay Bridge and the FE model used to simulate the bridge response under different conditions. This is followed by a description of the sensors and data acquisition system components used to measure and record the bridge response due to different types of excitation. Sensor layout and installation procedures are detailed, along with forced excitation methods implemented on site. Data acquisition, reduction and signal processing, in addition to modal analysis methods and procedures, are also detailed. In addition, several complementary tests regarding sensor durability and concrete property estimation are presented.

A study of impact excitation of a decommissioned bridge near the town of Broadview, SK is presented as a way of experimenting with different types of excitation and bridge configurations.

The implementation of different types of excitation within the numerical bridge model study, and the investigation of different levels of noise associated either with the input (excitation force) or output (sensor readings) are discussed.

Statistical tools needed to evaluate the variability in estimated modal properties, and the effect of that variability on the reliability of damage detection, are explained.

3.2 HUDSON BAY BRIDGE DESCRIPTION

The bridge under investigation is located on Provincial Highway No. 9 over the Red Deer River south of Hudson Bay, Saskatchewan. Built in 1957, the 100.5 m long continuous reinforced concrete bridge features three spans of 30.9 m, 38.7 m and 30.9 m,

respectively. Each span is supported by three arched beams braced with end diaphragms and intermediate diaphragms at quarter points of the span. The bridge is 8.9 m wide with two traffic lanes, one in each direction, and each lane is 3.66 m wide. The bridge is supported by rollers at all supports except for the south pier, where it is supported by hinged supports. Figure 3.1 shows an elevation of the bridge. Appendix A shows detailed bridge elevations and sections.

The bridge was strengthened in 1989 by rehabilitating the deck and adding reinforcement over the supports (regions of high negative moment), as well as by adding external reinforcing bars to the middle region of each spans (regions of high positive moment), as shown in Figure 3.2.

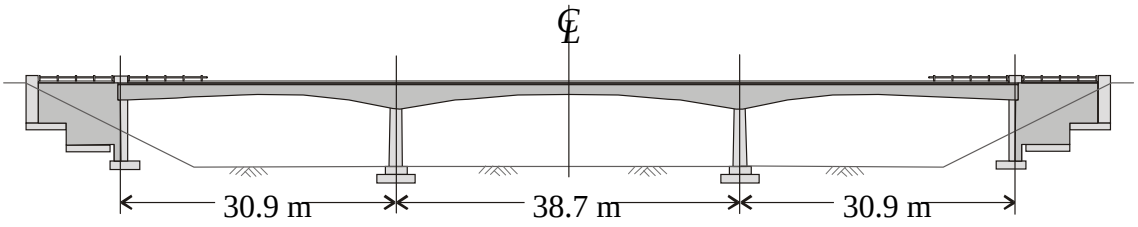

Figure 3.1 Bridge elevation (redrawn from Earth Tech 2001).

Figure 3.2 Bridge photograph showing external positive moment reinforcement.

In previous years, pressure from the forest industry to permit heavier timber haul trucks has led to the need for additional rehabilitation work to strengthen the bridge and increase its load carrying capacity. A structural consultant retained by Saskatchewan Ministry of Highways & Infrastructure recommended replacing the external steel reinforcement in the middle span with either carbon fibre reinforced polymer (CFRP) sheets or external steel plates to increase the positive moment capacity in this span (Earth Tech 2001). It was decided to strengthen the bridge with external steel plates and the rehabilitation work was performed in stages in November 2006, with the existing external reinforcement being removed from each of the three girders in turn and replaced by steel plates. In the course of the present study, field measurements were obtained both before and after the most recent rehabilitation.

3.3 FINITE ELEMENT MODEL OF HUDSON BAY BRIDGE

A preliminary finite element model was needed to determine the suitable type and locations of sensors to be used for the test. This model was based on engineering drawings and pre-existing data available for the bridge. Free vibration dynamic analyses were then used to determine the approximate natural frequencies and mode shapes of the system. The values of the calculated bridge natural frequencies were used to determine the range of frequencies likely to be required for the test, the resolution of readings in the case of closely spaced natural frequencies, and the data acquisition sampling rate. The estimated mode shapes were also used to determine the most suitable locations for the accelerometers to maximize the signal-to-noise ratio in the readings, and to avoid the nodal points of each mode where there is zero response. The preliminary finite element model of the bridge was built using the commercial analysis program ADINA (ADINA 2003). The FE model utilized quadratic shell elements to model both the concrete girders and the bridge deck.

A detailed finite element model of the bridge was required to perform further analyses to examine the effect of excitation force and noise on the quality of extracted modal properties and on the ability of VBDD methods to detect damage. The FE model was manually calibrated to reproduce the modal properties (natural frequencies and mode

shapes) extracted from site measurements, in order to be representative of the actual bridge under investigation.

For this more detailed study, a finite element model of the bridge was built using the commercial analysis program ANSYS (ANSYS 2005). As illustrated in Figure 3.3, the FE model used quadratic brick elements to model both the concrete girders and the deck; the brick elements were chosen because they would result in a more accurate geometrical representation of the bridge deck and girders, and to facilitate an investigation of simulated damage states in subsequent phases of the study. External reinforcing bars at the soffit of the girders were modelled as shell elements with a cross sectional area equal to the cross sectional area of the bars and with the same estimated material properties. The newly installed steel-plate reinforcement was modelled using shell elements that had the same geometric and material properties as the steel plates themselves. The guard rails along the edges of the bridge were modelled as beams, with the concrete posts supporting the guardrails modelled as rigid links between the bridge deck and the rails.

The bridge model behaviour was assumed to be linearly elastic. Initially, nominal values of material properties and ideal support conditions (frictionless pins and rollers) were assumed for the FE model. Subsequently, values of material properties and support conditions were calibrated manually by gradually varying them and comparing the resulting modal properties of the FE model to those that were calculated from dynamic tests conducted on the actual bridge. The FE model parameters (material properties and support conditions) were adjusted incrementally until the modal properties (natural frequencies and modes shapes) of the FE model were as close as possible to the modal properties of the actual bridge. The effective modulus of elasticity of the concrete was adjusted to allow for the presence of cracking and rebar, as well as the effect of axial compressive load in the girders due to the support restraint provided at the bridge piers and abutments. The concrete modulus of elasticity was calibrated to 35,200 MPa for the concrete girders and 25,000 MPa for the other parts of the bridge. These values of the modulus of elasticity are within the expected range for concrete giving the results of rebound hammer detailed in Section 3.13.2, which give a modulus of elasticity value of 30,950 MPa. The difference in the values of the modulus of elasticity can be attributed

to two factors. First, there is less cracking in the bridge girders due their curved shape, inducing some arching action that transfers loads to the support by compression rather than bending. Secondly, the girders are more heavily reinforced than the deck, and thus experiencing less cracking and a higher effective (composite) stiffness.

The mass value and distribution of the FE element model was considered to be known to a reasonable degree of accuracy based on the bridge geometry that was estimated from the available engineering drawings and the concrete density value of 2450 kg/m^3. The Poisson's ratio for concrete was taken to be 0.2.

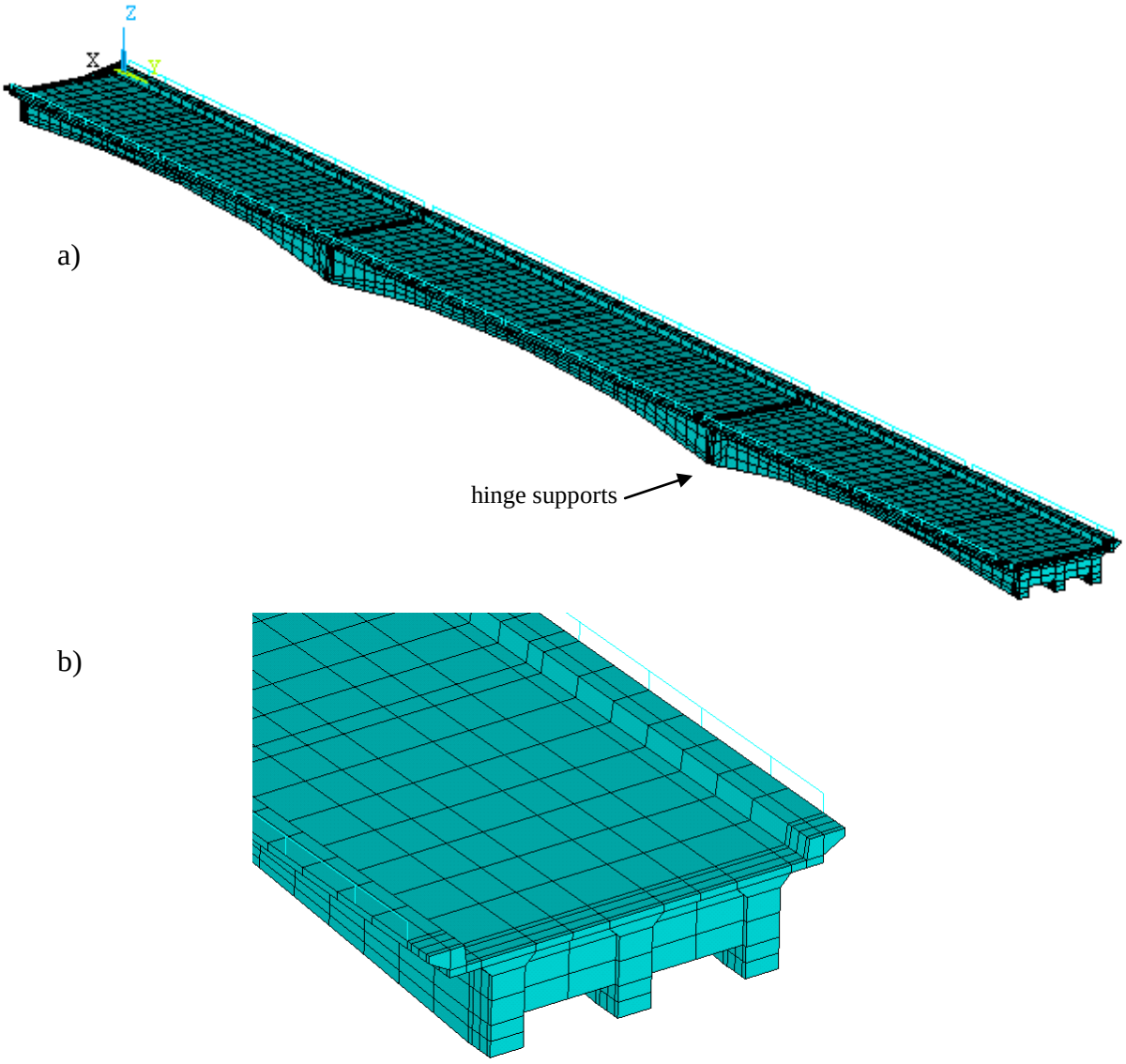

Figure 3.3 Schematic of the finite element model for Hudson Bay brigdge: (a) isometric view of entire model; and (b) close-up view of south end showing meshing details.

Properties of the steel that were used to model the external rebar or reinforcing plates included an elastic modulus of 200,000 MPa, and a Poisson's ratio of 0.3. A total of 26036 nodes and 4126 elements were used to model the bridge.

The bridge model supports were initially assumed to be hinged at the second interior support from the north (Figure 3.3a), and to act as pure rollers at the other supports, as indicated in the original design drawings of the bridge. Longitudinal and rotational springs were subsequently imposed on the supports to simulate the partial fixity that may have developed in these supports due to friction or support locking due to rusting or debris incursion. The calibrated values of the longitudinal and rotational springs were found to be 15,500 kN/m for longitudinal springs and 10,000 kNm/rad for rotational springs. Rotational springs were applied at all supports while longitudinal springs were applied at roller supports only. The results of the FE model updating are detailed in Section 4.4.

3.4 ISTRUMENTATION

3.4.1 Overview

Various types of sensors and instrumentation were used on the bridge to capture its response due to different types of excitation. The type, number, and layout of the sensor groups are detailed and explained in this section. Electrical wire strain gauges and accelerometers were used to capture the bridge response. The sensor readings were captured by a laptop computer-based dynamic data acquisition system.

3.4.2 Strain Gauges

Electrical resistance wire strain gauges of the type WFLM-60-11-2LT manufactured by TML Co. (Tokyo, Japan) were used for this research (Figure 3.4), being specifically designed for strain measurements on concrete surfaces. This type of gauge has a thin stainless-steel backing, preventing the penetration of moisture from the underside and providing good electrical insulation to the concrete surface, and a moisture proof over-coating, making it suitable for long-term outdoor applications. The gauges have a resistance of 120 Ω, feature an integral three-wire hook-up lead, and are 60 mm long with a backing length of 90 mm; this length made it suitable for measuring strains on

concrete surfaces because it can cross over multiple cracks, thus enabling average strain readings over the length of the strain gauge backing. The strain gauges were attached to the concrete surface using the polyester-based PS adhesive provided by the same manufacturer.

For the Hudson Bay bridge, the strain gauges were attached to the concrete girders in groups of three lined up vertically at each location, facilitating the measurement of the dynamic or static curvature of the girder; this was accomplished by fitting a straight line through the instantaneous strain readings, the slope of which represents the curvature. These strain gauge groups were placed at selected locations on each girder to capture the strain response of the bridge. A total of 45 electrical resistance strain gauges were placed on the bridge, at the locations shown in Figure 3.5. Figure 3.6 shows the placement of the strain gauges on a typical bridge cross section.

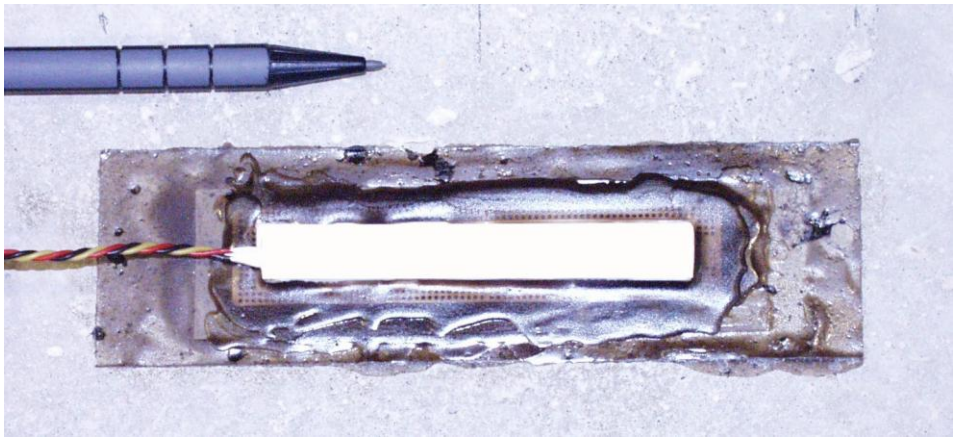

Figure 3.4 FLM-60-11-2LT strain gauge.

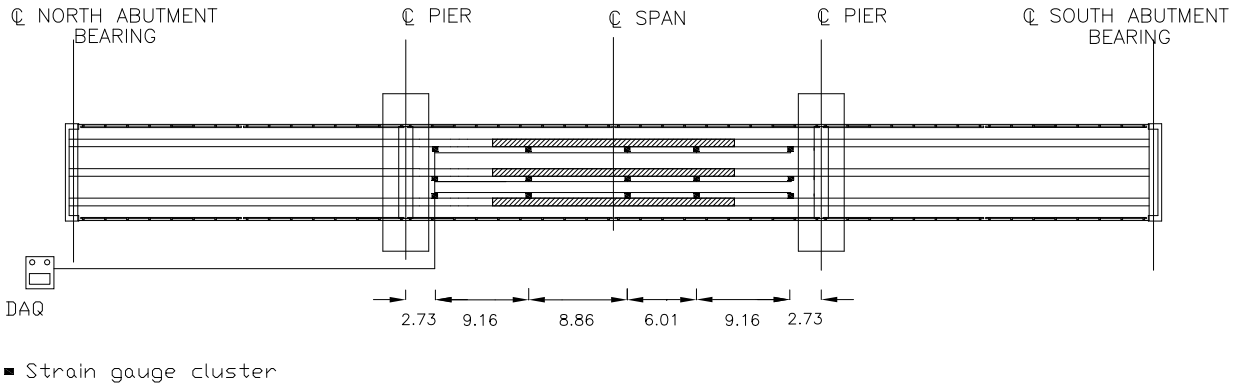

Figure 3.5 Plan view of Hudson Bay bridge showing strain gauge layout.

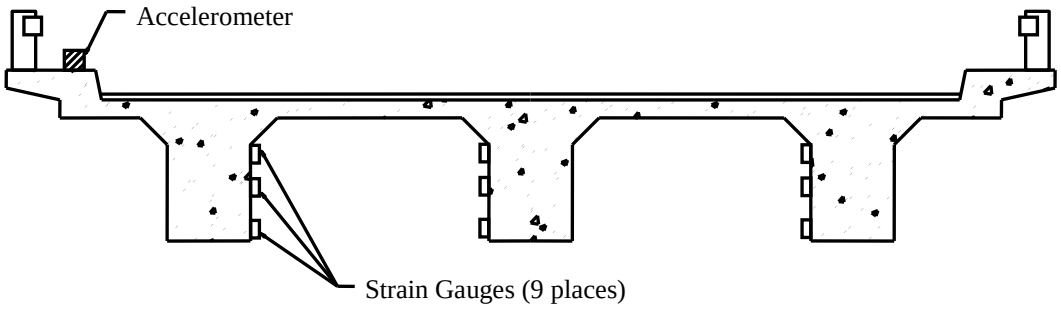

Figure 3.6 Typical sensor locations on Hudson Bay bridge cross section (looking north).

Due to the limited number of channels available on the data acquisition system (28 channels for strain measurement), only half of the strain gauges could be read at one time. A reference group of strain gauges on the middle girder, more specifically the second cluster in from the more northerly pier, was logged simultaneously with both halves to provide a common basis for combining the data. Figure 3.7 shows a group of strain gauges as installed on the bridge, while the snooper truck that was used to install the strain gauges is shown in Figure 3.8.

Figure 3.7. A group of strain gauges as installed on Hudson Bay bridge.

A three-wire hook-up, as shown in Figure 3.9, was used to connect the strain gauges to the data acquisition system to in order to compensate for lead wire resistance and temperature changes (Vishay 2007). The cables used were twisted-pair shielded cables

of gauge AWG 18; the heavier than usual wire gauge was chosen so as to reduce the lead wire resistance, thus improving the strain gauge sensitivity. Twisted-pair shielded cables have been also been recommended by others to reduce the noise picked up by the lead wires (Shah 1992, National Instruments 1998b). The lead wire resistance was taken into account by adding it to the strain gauge's own resistance when calculating the strains measured by the gauges.

Figure 3.8 Snooper truck used to install the strain gauges on Hudson Bay bridge.

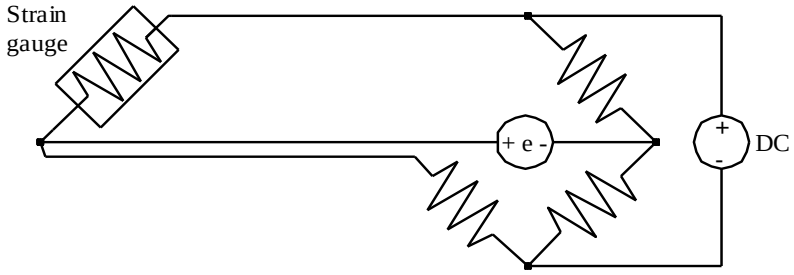

Figure 3.9. Lead wire compensation using a three-wire hookup.

3.4.3 Accelerometers

For large structures such as bridges, the first natural frequency of the structure is typically found to be in the order of 1 Hz, with most of the significant dynamic response occurring below 50 Hz (Ward 1984, Levi 1997); therefore, accelerometers with a

response bandwidth between 0 Hz (DC) and 100 Hz were required for the bridge instrumentation. In this research, seven EpiSensor FBA ES-U accelerometers, manufactured by Kinemetrics Inc. (California, USA), were used (Figure 3.10). These low-noise force-balance uniaxial accelerometers have a measurement range of 0-4 g and a response bandwidth from DC 0 Hz to 200 Hz, making them ideal for civil engineering applications where the structure's response is generally of small magnitude and whose natural frequencies are usually below 50 Hz. For this study, the accelerometers were configured for a maximum range of ± 0.25 g.

Figure 3.10 EpiSensor FBA ES-U accelerometer.

The bridge dynamic response was measured using the accelerometers, and recorded as a series of acceleration time histories. For the Hudson Bay bridge, when measuring truck excitation, the accelerometers were placed on the middle span of the bridge only due to the limited number of available sensors and to constraints on available access time to the bridge. The location of the sensors was chosen so as to avoid the nodal points of the first several modes, at which there is zero response. This location selection was based on results from the preliminary FE model of the bridge, as mentioned in Section 3.3.

One side of the bridge was instrumented at a time due to the limited number of accelerometers used. The same accelerometer layout was used for both sides of the bridge. The reference accelerometer, whose position is shown in Figure 3.11, was left in place and not moved, so that the readings of both sides of the bridge could be scaled in reference to it, and then 'glued' together to model the response of the whole bridge (Hermans & Van Der Auweraer 1999, Brownjohn et al. 2003).

The accelerometers were calibrated in the lab before each test. The calibration was done by securing all the accelerometers in a wooden jig then subjecting them to a gentle vibration manually. The accelerometer readings were then recorded and their maximum responses were compared. A calibration factor was calculated for each accelerometer in such a way that when each accelerometer calibration factor was multiplied by its readings that all accelerometers would have the same amplitude. This calibration process would ensure that the accelerometer readings on site were scaled correctly relative to each other.

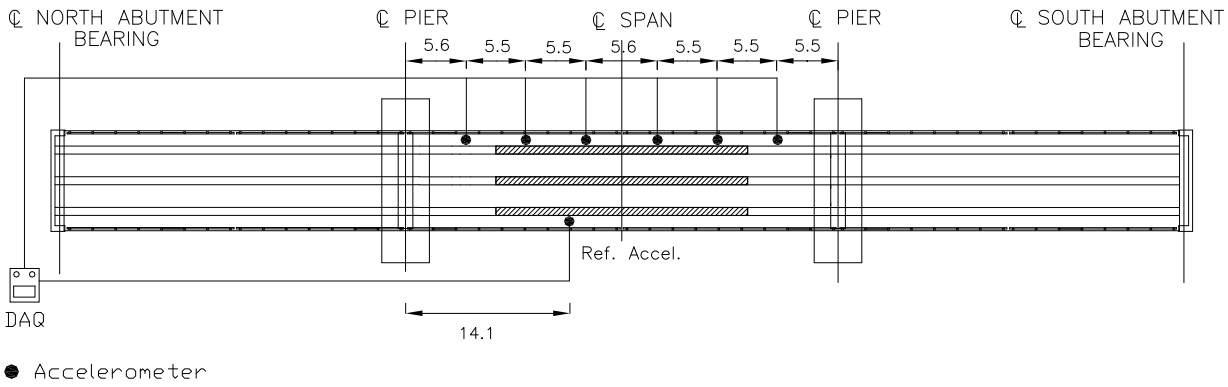

Figure 3.11 Accelerometers locations on the Hudson Bay bridge.

3.4.4 Data Acquisition System

The data acquisition system included a dynamic data acquisition PCMCIA card model NI DAQ Card-6036E from National Instruments, which was inserted into the PCMCIA slot of a laptop computer. This card had eight channels with a maximum sampling rate of 200,000 samples/sec and 16 bit accuracy (i.e. the range of the measured signal can be divided into 2^{16} or 65536 segments). The channel readings were multiplexed before being passed to the analogue to digital convertor (ADC). This high sampling rate reduces phase shift error when sampling multiple sensors, while the above-mentioned high resolution was necessary to distinguish small changes in the measured signals (for example, due to induced damage, if any was present). This card was connected to a data acquisition chassis model SCXI-1001 from the same manufacturer. To this chassis, several modules were connected to acquire and modulate sensor signals and prepare them to be digitised by the DAQ card (Figure 3.12).

3.5 DATA ACQUISITION AND POST PROCESSING CONSIDERATIONS

The signal measured by the sensors was digitised and stored on the computer for further analysis. There were several parameters which affected the quality of the digitised signal, such as the resolution, sampling rate and filtering procedures. The effect of these parameters was reflected in the measured signal in the form of quantization error (the difference between the actual analog value and quantized digital value), aliasing, phase shift, leakage and windowing, measurement noise and averaging of sensors' readings (Maguire 1990).

Figure 3.12 Data acquisition system.

Quantization error can be reduced by using a data acquisition system (DAQ) with high resolution. A DAQ with 16-bit resolution can digitize the signal into 2^{16}= 65,536 segments, while a 12-bit resolution can digitize the signal into 2^{12} = 4,096 segments only. The system used in this study had a 16-bit resolution.

The Nyquist (Shannon) sampling theorem states that the minimum permissible sampling frequency for data acquisition is twice the maximum frequency of interest. However, it is common practice to sample at least five times the maximum frequency of interest, to better represent the dynamic signal with good resolution. A sampling rate below the

minimum stated above would result in aliasing, which is the contamination of lower frequencies by higher frequency components (Maia and Silva 1997). A sampling rate of 300 Hz was used for site measurement, which satisfies the criteria discussed above, and prevents aliasing from happening as it is not expected for the measured signal to have frequency content above 150 Hz. In addition, the accelerometer's response bandwidth is 0-200 Hz with significant drop in sensitivity above 150 Hz. This sampling rate of 300 Hz gives a 60 Hz maximum frequency of interest.

The data acquisition system should be capable of reading the sensors at the appropriate sampling rate. For modal analysis, the sensors need to be read simultaneously; otherwise, there would be a phase difference (time delay) between successive readings. However, it is quite expensive to read the sensors simultaneously. The other alternative is to minimise the phase difference in the readings by choosing a high sampling rate compared to the natural frequencies of the structure. This reduces the distortion in reading due to phase lag or channel skew (Mathworks 2007). The sampling rate of the system used was 200,000 samples / second; therefore, by using the "sample and hold" feature of the DAQ system (sample all channels at the maximum sampling rate of the system then wait until the next time step in the defined sampling rate, 300 Hz or 0.00333 s in this case, to make another sampling cycle) the phase lag error was minimised.

If the measured signal is not periodic, or if the period is very long relative to the sampling period so that it must be truncated, then leakage may occur. Spectral leakage is defined as the spreading of the signal spectrum to adjacent frequency "bins", so that the spectral energy appears to spread (leak) to neighbouring frequencies. Tapered windows applied in the time domain that modify the signal to bring it smoothly to zero at both its beginning and end without significantly changing the shape of the resulting spectrum reduce the effect of spectral leakage (Maia and Silva 1997). In this study, a Tukey (tapered cosine) window was used with forced (truck induced) excitation (Figure 3.13a), while an exponential window was used with free-decay bridge response as shown in Figure 3.13b (Mathworks 2002). The Tukey window was selected to provide an approximate match to the shape of the signal envelope being windowed in order not to alter the signal significantly. The window flat top would match most of the bridge

response to truck excitation without much alteration to the signal. On the other hand, the exponential window matches the decaying shape of the bridge free vibration response after the truck leaves the bridge.

Different measurement segments taken at the same location and under the same excitation conditions but at different times would vary to some extent due to non-stationary properties of the excitation, random noise, errors in measurements, external interference, etc. Because measurement noise is considered random in nature, it is expected that this noise can be reduced by averaging multiple readings (Ewins 2000). For this study, modal results calculated from multiple site measurements were averaged to produce results with less noise and variation. The measurement segments considered were 30 seconds long, on average; up to ten segments were processed in each group of measurements from which the modal properties were calculated then averaged.

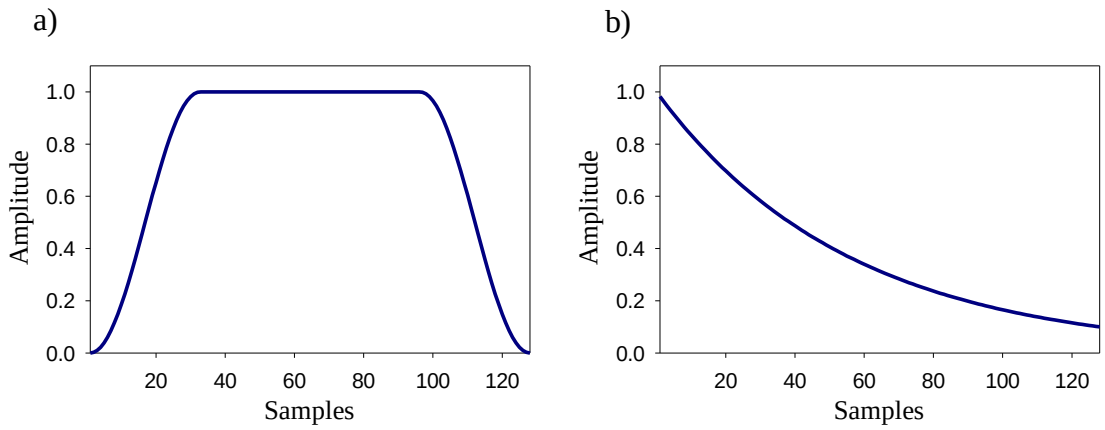

Figure 3.13 Window functions used in signal processing of forced excitation: a) Tukey window; and b) exponential window.

Similarly, a Hanning window (Figure 3.14) was used for averaging ambient vibration measurements (Mathworks 2002). Hanning window was used because of its smooth shape and its very low aliasing, which are useful features when working with continuous signal such as ambient vibration The ambient measurement records were divided into shorter segments that were windowed and averaged using a moving average with 60% overlap (Stearns and David 1996).

Figure 3.15 summarises the procedure with the various steps required for estimating the modal properties of a bridge.

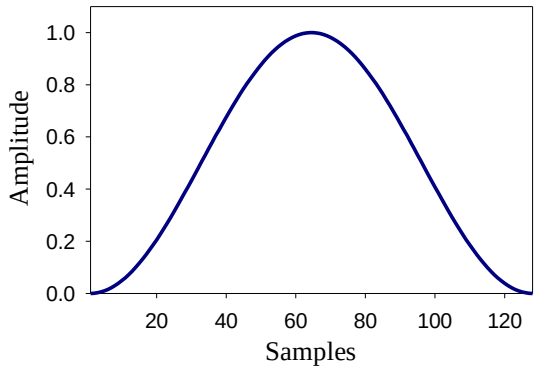

Figure 3.14 Hanning window function, used in signal processing of ambient excitation.

3.6 FIELD TESTING

3.6.1 Overview

Field testing was performed with two primary objectives. The first objective was to compare different dynamic excitation methods and their effect on estimated modal properties; for this purpose, the excitation generated by the passing of different types of trucks, ambient excitation by wind and river flow, and impact excitation applied by a heavy weight deflectometer (HWD) testing machine and a spring-loaded truck-mounted hammer were implemented on site and the results of these tests were evaluated and compared. Excitation generated by a hydraulic shaker was attempted on site, but resulted in numerous technical difficulties. The second objective was to evaluate the bridge strengthening scheme described in Section (3.2) and its effect of the bridge dynamic properties. In addition, field testing data provided an objective basis for numerical model calibration.

Dynamic tests were done at a sampling rate of 300 Hz, except for the impact test where the sampling rate was 1000 Hz in order to capture the transient nature of the excitation. On the other hand, the static tests were conducted at a 300 Hz sampling rate then down-sampled by a factor of 25, thus making the effective sampling rate equal to 12 Hz. This process was implemented to improve the quality of the readings and reduce noise.

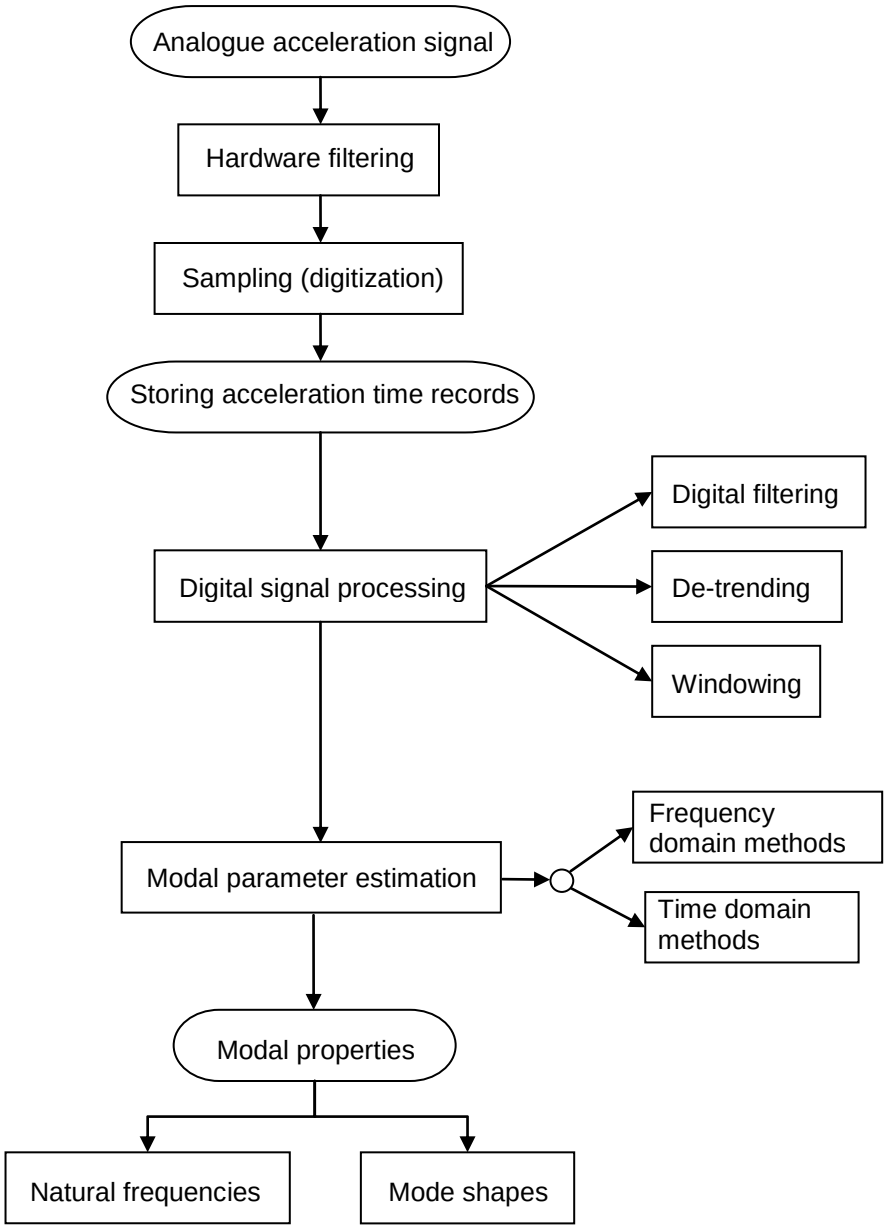

Figure 3.15 Summary of procedure for estimating the modal parameters of a bridge.

Several field tests were conducted over the span of six years. Each site visit lasted for one or two days. Seven site visits were made to Hudson Bay bridge, including two site visits to install the strain gauges and perform the static load test. Two site visits were also made to the Broadview bridge. Preliminary tests were conducted on the first visit, while a detailed impact excitation using a heavy weight deflectometer (HWD) machine, and ambient vibration test were conducted during the second site visit.

As expected in field tests, some of these site visits did not provide good results, and not all the readings recorded in each site visit were of good quality; therefore, an evaluation of the data collected was necessary before further processing. The quality of data can be affected by many site specific issues; for example, some of the sensors did not work and needed to be fixed on site before continuing the site test. Occasionally, some cables became disconnected or loose, thus affecting the sensor readings. In other cases, site restrictions affected the amount of collected data, because traffic control was made available only for several hours during the day up to a maximum of 8 to 10 hours, thus imposing a time limit on the test which, in turn, limited the amount of data that could be collected.

Both bridges are located in remote areas with limited traffic volumes. Broadview Bridge was actually decommissioned and traffic was rerouted away from the bridge. For this reason, it was possible to measure the bridge response to an isolated loading event due to a single truck passing over the bridge, to ambient (wind) excitation sources acting alone on the bridge, or impact excitation.

3.6.2 Field Testing on the Hudson Bay Bridge

3.6.2.1 Uncontrolled Truck Excitation for the Hudson Bay Bridge

The bridge response to truck excitation was measured as acceleration-time records, with excitation provided by different types of vehicles such as timber trucks, semi-trailers, passenger cars and pickup trucks. The bridge response to these vehicle types was then evaluated. Bridge modal properties were estimated from the response records, and used to update an FE model so it could better reflect the bridge response. The updated FE model was subsequently used for further numerical simulations, as described in Chapters 5 and 6. For each vehicle crossing over the bridge, the recording of the bridge response started before the truck entered the bridge and continued after the truck exited the bridge, allowing for extra time to monitor the decaying free-vibration response phase. Truck records were 30 s long, on average. The trucks usually travelled at highway speed, or roughly 60-90 km/hr; records from a nearby weigh scale indicated that the average weight of a loaded timber truck was 70 tonnes. All site tests were conducted during the summer season with ambient temperatures ranging from 10-25 °C.

Seven site visits were conducted for the Hudson Bay Bridge overall. Two site visits were needed to install the strain gauges on the bridge, and one site visit for measuring strains generated during both the controlled truck test and normal traffic. One site visit was conducted during the bridge rehabilitation but no useful data were collected due to the restriction on traffic at that time. One site visit was conducted to perform impact excitation with a spring hammer, and a hydraulic shaker. Only impact excitation measurements were recorded during that visit as the hydraulic shaker was found to exhibit multiple technical problems and could not be used. The remainder of the site visits were dedicated to measuring the bridge response due to truck excitation. Appendix B lists the number of site visits, and types of trucks encountered during each visit.

3.6.2.2 Ambient Excitation for the Hudson Bay Bridge

To study ambient excitation, accelerometer readings were taken when there was no traffic on the bridge. In this case, the bridge was excited solely by wind and river flow. During the several occasions that such measurements were taken on Hudson Bay Bridge, the flow in the river was estimated to be less than one metre deep. The same procedures that were followed when measuring truck excitation were applied for ambient vibration, except that ambient excitation measurements were taken for longer periods of time lasting several minutes, as compared to records lasting less that one minute for truck excitation.

Random variations in the response spectra could be attenuated significantly by averaging results obtained from multiple data segments (Stearns and David, 1996). For this reason, longer records were taken for ambient excitation to allow for signal averaging in order to reduce noise due to the low level of energy in ambient vibration as compared to truck loading. For ambient excitation, the bridge response was divided into 30 s or 60 s long segments (depending on the available record length), with 60% overlapping using a Hanning window, as detailed in Section 3.5.

3.6.2.3 Impact Excitation for the Hudson Bay Bridge

A spring-actuated, truck-mounted, damped-mass impact hammer was used to apply impact or pulse excitation on the bridge. The hammer was mounted on a vehicle using a standard trailer hitch (Figure 3.16). This hammer was developed by Prof. Don

Gendzwill in the Department of Geology at the University of Saskatchewan. The maximum energy output of the hammer was 750 Joules and its momentum output was up to 159 kgm/s. The spring-hammer is operated by a hydraulic system that loads the spring firing mechanism inside the hammer, and is connected to the hammer by hydraulic hoses. The hydraulic system remains at the back of the truck during the test.

The impact excitation test using the spring hammer was conducted on the Hudson Bay bridge after it underwent a rehabilitation process of replacing the external reinforcing bars on the middle span with steel plates attached to the soffits of each girder. The steel plate rehabilitation work on the bridge is shown in Figure 3.17 during the installation, and in Figure 3.18, after the installation had been completed.

Figure 3.16 Spring actuated impact hammer mounted on the back of a truck.

A sampling rate of 1000 Hz was used to measure the bridge response to the impact loads, in order to capture the transient nature of this excitation. The impact was applied within the middle span of the bridge, 18 m from the north pier, on top of the east girder, approximately opposite to the location of the reference accelerometer. Ten impact

events were applied for each accelerometer test setup; the results from the ten events were subsequently averaged. Two sets of impact events were conducted for each test setup; one set with the spring hammer contacting the bridge deck directly, and one set utilizing a rubber pad placed under the spring hammer to dampen its impact on the bridge.

Figure 3.17 Steel plate strengthening of Hudson Bay bridge during installation.

Figure 3.18 Steel plate strengthening of Hudson Bay bridge after completion.

Four accelerometer setups, allowing measurements to be taken on all three spans, were conducted on the Hudson Bay Bridge during the impact test, as opposed to only two setups on the middle span for the truck excitation tests. This arrangement was possible due to the speed at which the impact test could be conducted. Figure 3.19 shows the accelerometer locations used for the impact tests on the Hudson Bay Bridge. Impact excitation tests on the Broadview Bridge are detailed in Section 3.6.3.

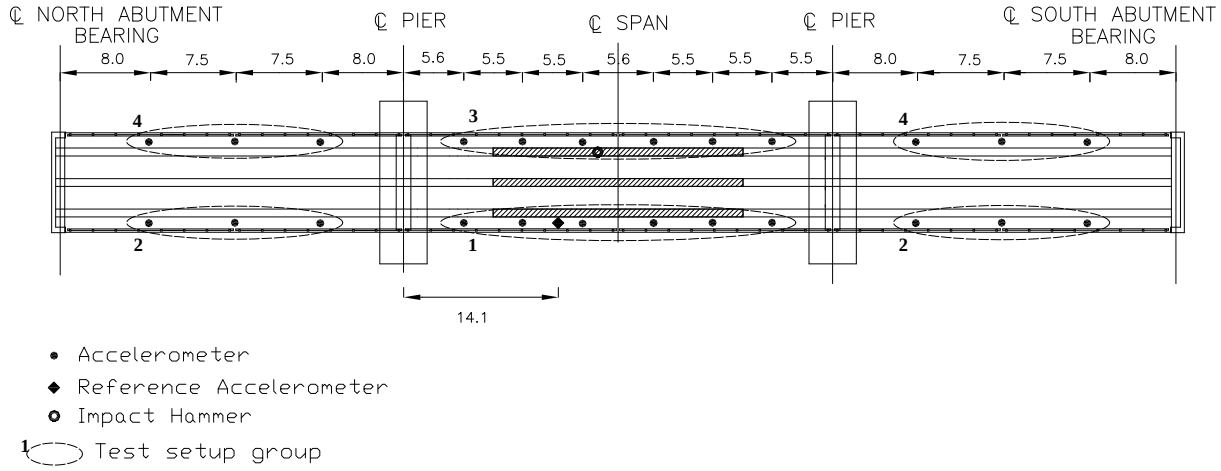

Figure 3.19 A plan view showing instrumentation locations for impact testing at the Hudson Bay Bridge.

3.6.2.4 Static (Controlled) Load Testing on Hudson Bay Bridge

Pseudo-static load tests were implemented on the Hudson Bay Bridge using a test truck of known weight and axle configuration. The tests were conducted in order to compare the response of the calibrated FE model of the bridge to site measurements to assess how accurately the dynamically calibrated FE model represented the bridge static response, as static load testing is a more conventional method for evaluating the bridge load capacity.

The static load test results were also used in a companion study (Jackson 2007) to evaluate various design-related response characteristics, including dynamic amplification factors and load-sharing behaviour.

The test truck had three axles and a total weight of 51.66 tonnes when loaded, divided into 4.8, 20.46 and 26.37 tonnes for the steer axle, drive axle and rear axle, respectively; the test truck is shown in Figure 3.20. The strain at selected locations on the bridge

girders was recorded while the truck was driven across the bridge at the crawl speed of approximately 10 km/hr, in both directions (northbound and southbound) on either of the two lanes on the bridge. A total of 33 crawl speed tests were conducted. The test truck was driven over the bridge at highway speed also; however, the quality of the data recorded was found to be insufficient to be used for further analyses.

The test results were also used to evaluate the repeatability of the static load test values, and the bridge response to the static loading.

Bridge response due to normal traffic was also recorded during this site visit. This test series was conducted over the span of two days in September 2005. Section B.6 in Appendix B lists the number of tests and types of trucks for each test encountered during this test.

Figure 3.20 Test truck used for static load test.

3.6.3 Field Testing on the Broadview Bridge

3.6.3.1 Bridge Description and testing overview

The Broadview Bridge is located near the town of Broadview, Saskatchewan, on Trans-Canada Highway No. 1, 150 km east of the city of Regina. The bridge was decommissioned due to realignment of the highway, and is no longer in service. The

bridge was 64 m long and 11.8 m wide. It had five spans, supported by straight abutments and internal piers that were skewed at 45° to the bridge. Each span was approximately 15 m long. The bridge was composed of a concrete deck supported by seven concrete beams spaced at 1.905 m on centre. The bridge is shown in Figure 3.21.

Two site visits were made to the Broadview Bridge. The first visit was to examine the bridge and obtain information regarding the bridge's general condition and its dynamic response. Preliminary ambient vibration measurements were taken during that visit, measuring bridge response to wind excitation, in addition to driving a passenger car over the bridge and measuring the bridge response due to this type of excitation. A detailed testing programme was conducted during the second visit, where the bridge response due to impact excitation from an HWD was measured at several locations along the bridge. The bridge response due to ambient excitation (wind) was also measured during this visit.

Figure 3.21 Photograph showing the Broadview bridge (looking north).

3.6.3.2 Impact Test Equipment

The impact test was conducted to evaluate the suitability of impact excitation for dynamic testing of bridges. The equipment used for the test was a Heavy Weight Deflectometer (HWD) test system model 8082 manufactured by Dynatest. This equipment is normally used to evaluate the properties of road pavement and is contained within a trailer that can be pulled by a truck. The HWD is designed to impart a pulse

load to the pavement surface, and subsequently, to evaluate the stiffness parameters of the pavement, such as Young's Modulus. The machine's ability to generate a controlled pulse load made it a good candidate for impact dynamic excitation. The HWD that was used in this research is shown in Figure 3.22; Figure 3.23 shows the impact hammer on the HWD.

Figure 3.22 Heavy Weight Deflectometer (HWD).

Figure 3.23 Impact hammer of the HWD.

3.6.3.3 Test Setup and Procedure

The truck used for towing and the HWD were positioned on the bridge such that the impact excitation was applied in the centre span of the bridge directly on top of the first interior beam at one third of the span length from the support. The mass of the truck and the HWD might have had an effect on the bridge dynamic response; however, this was difficult to assess without more in-depth investigations.

The reference accelerometer was placed within the same span, and on the same beam as the HWD, but at one third of the span length from the opposite support. The bridge response was recorded at 37 locations on the bridge using six different instrumentation setups. Figure 3.24 shows a schematic describing the various test setups. A high sampling rate of 1000 Hz was used in order to capture the transient nature of the impact excitation.

Ten impact events with a peak magnitude of 25 kN, as well as ten impact events with a peak magnitude 50 kN were applied for each test setup; the modal properties calculated for each event were then averaged. The impact events had a recorded duration of two seconds each. The two different force levels were used to examine the effect of force magnitude on the quality of calculated modal properties.

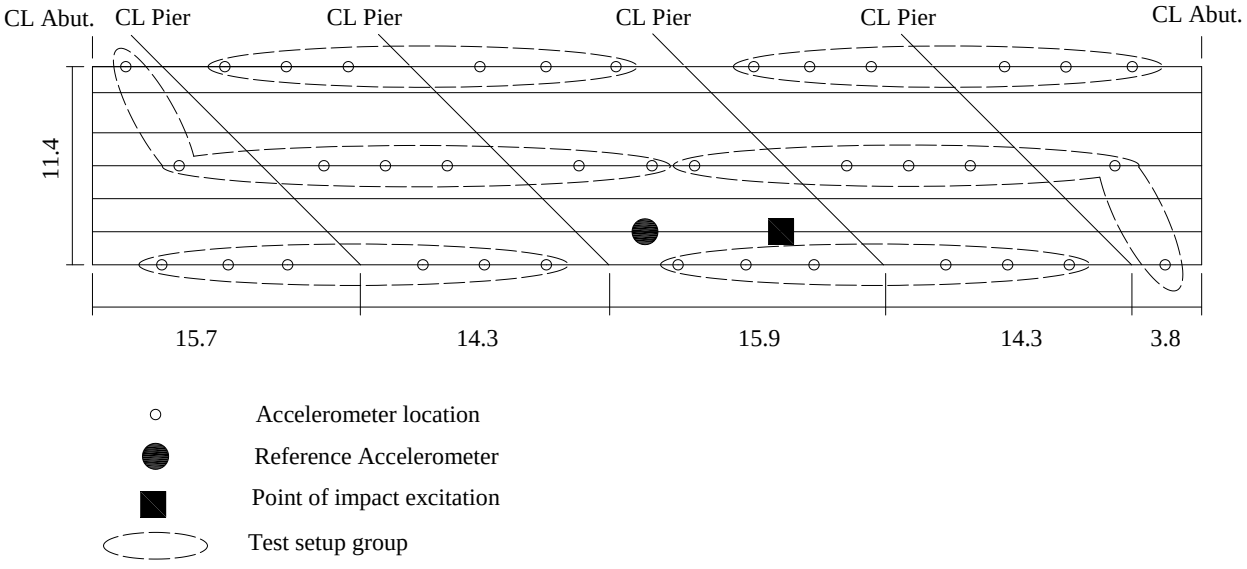

Figure 3.24 Schematic plan view showing test setup for Broadview bridge.

In addition, ambient vibration testing due to wind excitation was conducted for each test setup to complement the impact excitation test results. The sampling rate for ambient excitation was 100 Hz, and the bridge response was recorded for 6 minutes. The total record of the bridge response was then divided into segments that were 60 s long, featuring a 60% overlap between segments. After applying a Hanning window, the power spectra were calculated for each segment and subsequently averaged over all segments to produce a representative spectrum (Stearns and David 1996).

3.7 EXCITATION FOR NUMERICAL DYNAMIC SIMULATION

3.7.1 Overview

Using the calibrated FE model described in Section 3.3, the response of the Hudson Bay bridge to various forms of dynamic excitation was calculated in the time domain using Newmark's β method as the time marching scheme, assuming constant-average acceleration (Clough and Penzien 2003). To reduce computational requirements, the modal superposition approach was adopted, including contributions from the lowest seven vibration modes. Proportional damping equivalent to 2% of critical was assumed for all modes to reflect the behaviour of lightly cracked reinforced concrete (Chopra 1995); modal damping ratios in the order of 2% of critical were also extracted from measured data in the current study, although there was considerable variability in the field results depending, in large part, on the degree to which individual modes were excited by specific loading events.

To simulate the acquisition of data from a limited number of sensors in a field testing program, only the vertical displacement time histories from selected nodes on the FE model were extracted and stored for further analysis (see Figure 3.25). The longitudinal distribution of the simulated measurement points was similar to that used for site measurements, as shown in Figure 3.19. The response was calculated at uniform time increments of 0.005 s, simulating a sampling rate of 200 Hz, except for impact excitation where the sampling rate was 2000 Hz due to the short duration and transient nature of the excitation.

Modal properties of the bridge were then estimated from the time domain response at these "sensor" locations using the subspace stochastic identification method, as implemented in the commercially available software MACEC (Van den Branden et al. 1999). For the purposes of modal parameter estimation, it was assumed that the exciting force was not known exactly or measured, so that "output-only" modal extraction techniques were required, as detailed in Section 2.2.3. The extracted modal properties (natural frequencies and mode shapes) were compared to theoretically correct eigenvalue results generated from the same FE model.

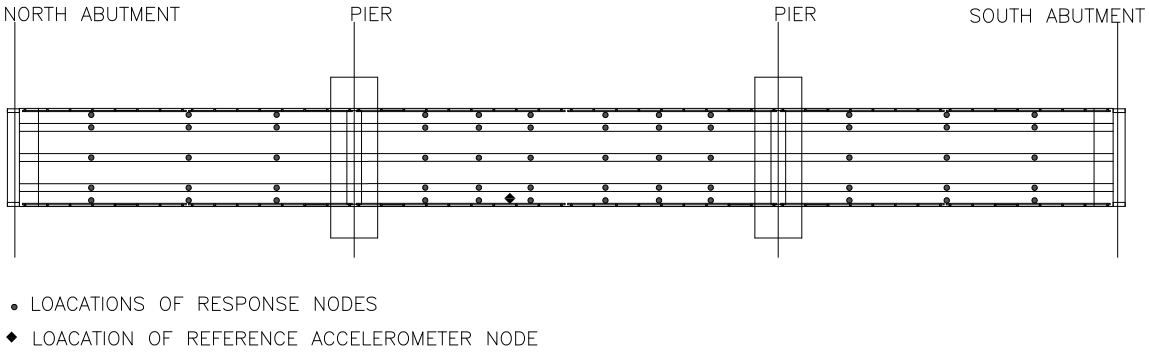

Figure 3.25 Locations of nodes used for data extraction from the FEM model of Hudson Bay bridge.

The forms of dynamic loading considered in the numerical study included harmonic, random, and impact forced excitation, as well as simulated truck loading time histories. The first three types of excitation were defined as a stationary vertical concentrated force applied at the node in the FE model corresponding to the location of the reference accelerometer in the field measurement study (see Figure 3.11). The truck excitation described the moving wheel loads for selected truck configurations as they passed over the bridge at a constant speed. Specific details regarding the various excitation types are presented in more detail below.

To evaluate the influence of uncertainty related to the excitation source, the analyses were repeated with random fluctuations (noise) superimposed upon the dynamic load time history. White noise with variances equal to 1%, 2%, 5% and 10% of that of the original force signal were used.

In addition, noise was superimposed upon the displacement time histories extracted from the FE analyses to simulate noise and errors in the measured signal due to random errors inherent in the data acquisition process. The analysis was repeated with random fluctuations (noise) superimposed upon the extracted displacement time histories of each response node, with different variance levels, similar to what was described in the previous paragraph.

3.7.2 Harmonic Excitation

In the numerical study, harmonic loading was used to simulate the excitation that would be induced by a mechanical shaker mounted on the bridge. A harmonic force with amplitude of 10 kN was applied at a location corresponding the location of the reference accelerometer in field tests, at frequencies corresponding to the first three natural frequencies of the bridge. Figure 3.26 shows an example force time history and spectrum of harmonic excitation with a forcing frequency equal to the first natural frequency of the structure. The force spectrum was calculated using Fourier transform applied to a 10 s long force time history.

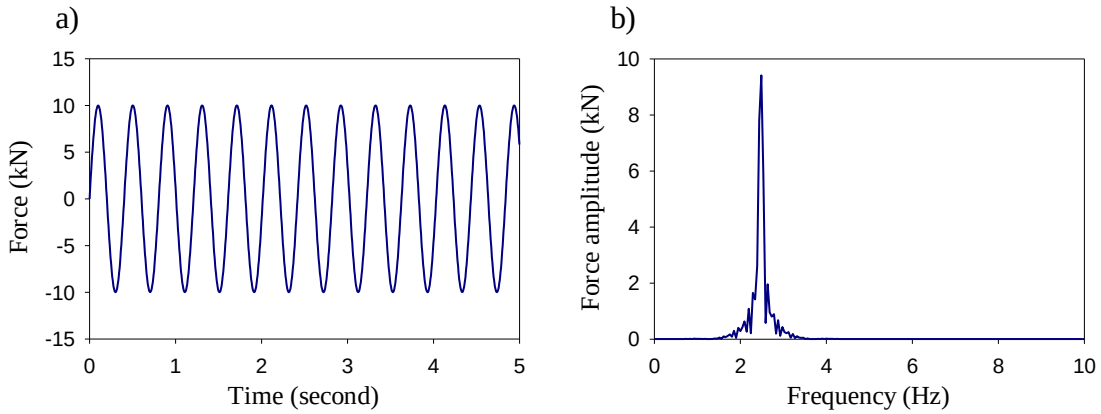

Figure 3.26 Harmonic excitation with no noise: a) example force time history; and b) force spectrum.

To evaluate the influence of uncertainty related to the excitation source, the analyses were repeated with random fluctuations (noise) superimposed upon the harmonic load time history. White noise with variance magnitudes equal to 1%, 2%, 5% and 10% of that of the original harmonic signal were used. White noise is defined as a random signal with a flat power spectrum. Ten loading events with durations of 10 seconds were

analysed for each level of noise; the modal properties for each event were extracted, averaged, and then compared to the eigenvalue results. Figure 3.27a shows a typical force time history of harmonic excitation with a forcing frequency equal to the first natural frequency of the structure and 2% added noise; Figure 3.27b shows the FFT spectrum of the noisy excitation force.

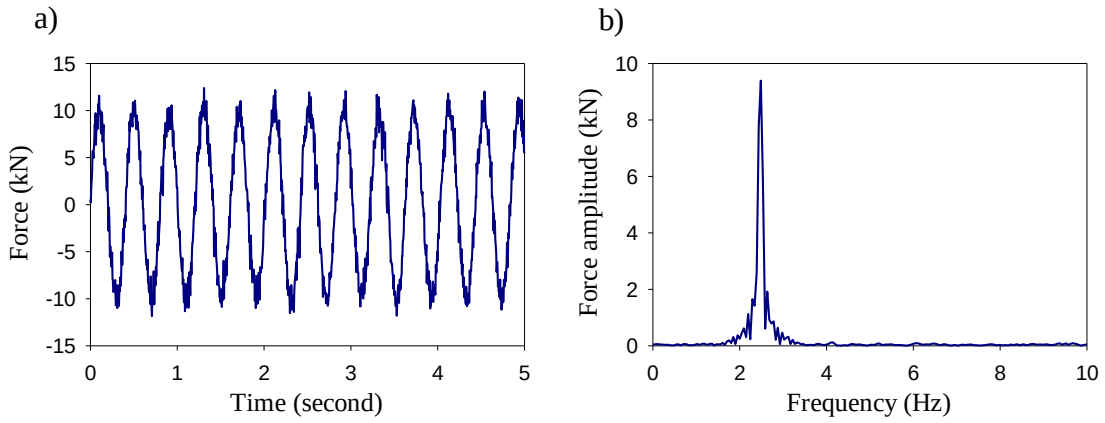

Figure 3.27 Harmonic excitation with 2% noise: a) example force time history; and b) force spectrum.

3.7.3 Random Excitation

Random excitation can be used to excite a bridge over a broad range of frequencies in order to measure the response in several vibration modes simultaneously. In practice, random excitation is typically achieved through the use of traffic or wind loading. For the current study, though, the random forced excitation was applied as a stationary concentrated load with a random time history defined such that the peak magnitude was 10 kN and the resulting force spectrum was approximately uniform over a broad band of frequencies, including the range of natural frequencies of interest for this bridge. The random force was applied at a location that corresponds to the location of the reference accelerometer in field tests.

In total, ten different random loading events were considered, each comprising a forced excitation phase lasting 10 s, followed by a 10 s free vibration phase during which the forced excitation was discontinued. For the purpose of extracting modal properties, responses in the forced and free vibration phases were considered separately. Figure 3.28a shows an example force time history of random excitation while Figure 3.28b

shows the corresponding force spectrum. Comparing Figure 3.28b to Figure 3.26b, it can be seen that, while the frequency content of the harmonic excitation is well defined and limited to the excitation frequency only, the frequency content of random vibration is spread out over a wide range of frequencies.

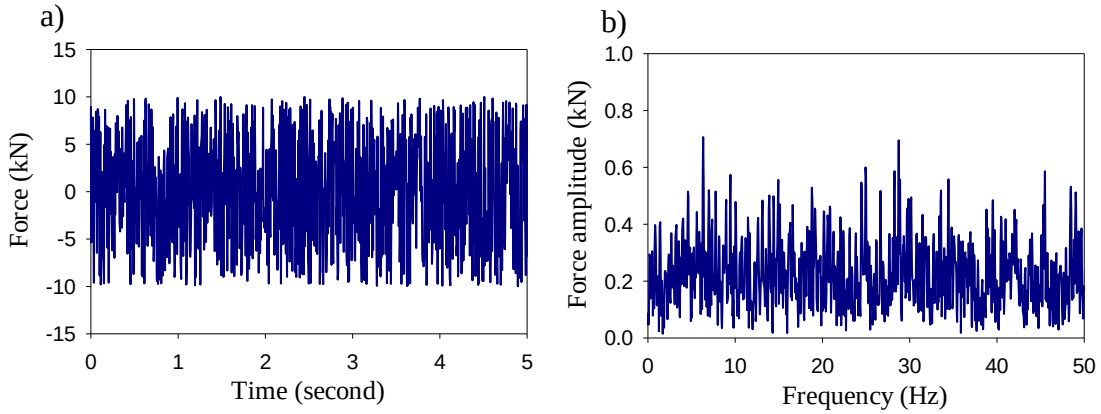

Figure 3.28 Random forced vibration: a) example force time history; b) force spectrum.

3.7.4 Impact Excitation

Simulating the effect of a drop-weight test in the field, excitation from a short duration impact was used to induce a force time history that had a relatively flat spectrum in the frequency range of interest. In the present numerical study, the impact load time history was defined as a half sine wave with a duration of 10 milliseconds and an amplitude of 10 kN (ISO 1994, Pavic et al. 1997). The impact force was applied at a location that corresponds to the location of the reference accelerometer in field tests. The subsequent bridge response was calculated over a 10 second interval. As with the harmonic forcing discussed previously, the effect of random fluctuations in the impact load time history was investigated. Figure 3.29a shows a typical force time history for impact excitation, while Figure 3.29b shows the corresponding force spectrum. Similarly, Figure 3.30a shows the force time history of impact excitation with 2% added noise and Figure 3.30b shows the corresponding force spectrum. It can be seen from comparing the force spectra in Figure 3.29b and Figure 3.30b that noise had little effect on the frequency content of the signal, except at frequencies above 150 Hz.

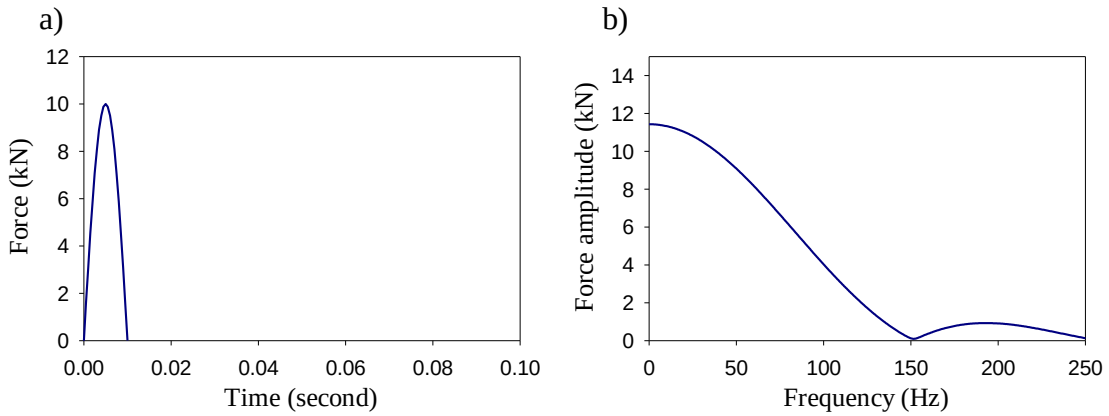

Figure 3.29 Impact excitation with no noise added: a) example force time history; and b) force spectrum.

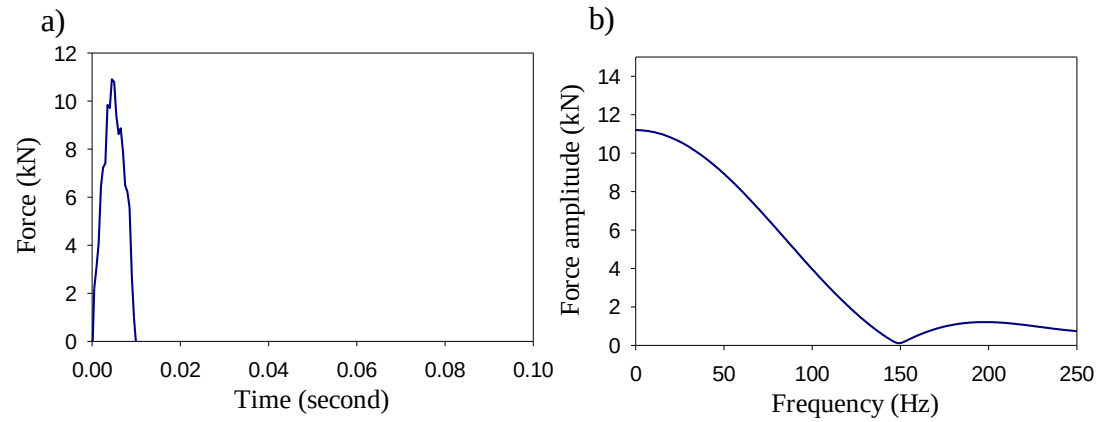

Figure 3.30 Impact excitation with 2% noise: a), example force time history; and b) force spectrum.

3.7.5 Truck Excitation

In this study, the bridge response, as opposed to the vehicle response, was of primary concern; therefore, it was reasonable to approximate the moving vehicles as a number of moving loads. This approach was further justified by the fact that the vehicle-to-bridge mass ratio could be considered small, making it possible to ignore the bridge-vehicle interaction. For example, the vehicle-to-bridge mass ratio of the QS-660 truck (Figure 3.33) to the Hudson Bay bridge was 4.7%. This type of simulation is referred to as a moving load model. With this model, the dynamic response of the bridge caused by a moving vehicle can be captured with sufficient accuracy (Yang et al. 2004), providing the mass ratio criterion mentioned above is satisfied.

Two truck models were used in this study to examine the suitability of truck-induced excitation for measuring modal properties. The first model was a simplified (moving quasi-static) truck loading, while the second model was a dynamic truck model where the dynamic properties of the truck where considered in the analysis of the bridge. In both cases, the truck loading was applied to the bridge using the dynamic nodal loading (DNL) method (Pan and Li, 2002). In the DNL method, the moving force is converted into a load history at each node along the wheel path in the finite element model based on the equivalent nodal loads (ENL) concept. In this way, the moving load problem is transformed into a time-history analysis which can be solved by most FE software. The wheel load in this approach is distributed proportionally to adjacent nodes in the longitudinal and transverse direction based on the relative distances from the adjacent nodes and the current position of the wheel at every time step (Chan and O'Conner 1990, Livingston et al. 2001, Marzougui et al. 2001, Nassif and Liu 2004).

The truck simulation began when the front axle of the truck entered the bridge and stopped when the rear axle exited the bridge. The simulated interval between successive time increments was 0.05 s (200 Hz). At each time interval, each wheel position was calculated using the truck speed and elapsed time.

Two different truck configurations were used in the conjunction with the simplified model, as illustrated in Figure 3.31. These two truck types are typical of the traffic experienced by the Red Deer River Bridge: a five-axle trailer (PV1) and a nine-axle trailer (PV4), with gross weights of 55.5 T and 94.5 T, respectively (Earth Tech 2001). The simulated trucks were "driven" across the bridge at speeds of 15 m/s (54 km/h) and 22.5 m/s (81 km/h). The resulting bridge response at the selected measurement points was recorded and analysed.

In the simplified truck loading model, vertical wheel loads representing the truck under consideration were moved across the bridge at specified speeds along a straight path. Figure 3.32a shows a typical force time history at a node on the bridge model for the case of a five-axle trailer (PV1) travelling at 54 km/hr, while Figure 3.32b shows the bridge vertical acceleration response spectrum due to this excitation.

Another simplified truck model was also investigated. In this second model, the effect of truck impact loading on the bridge was simulated by superimposing a sinusoidal varying load component acting at the first natural frequency of the bridge with a magnitude of 10% of the axle loading (Chan and O'Conner 1990).

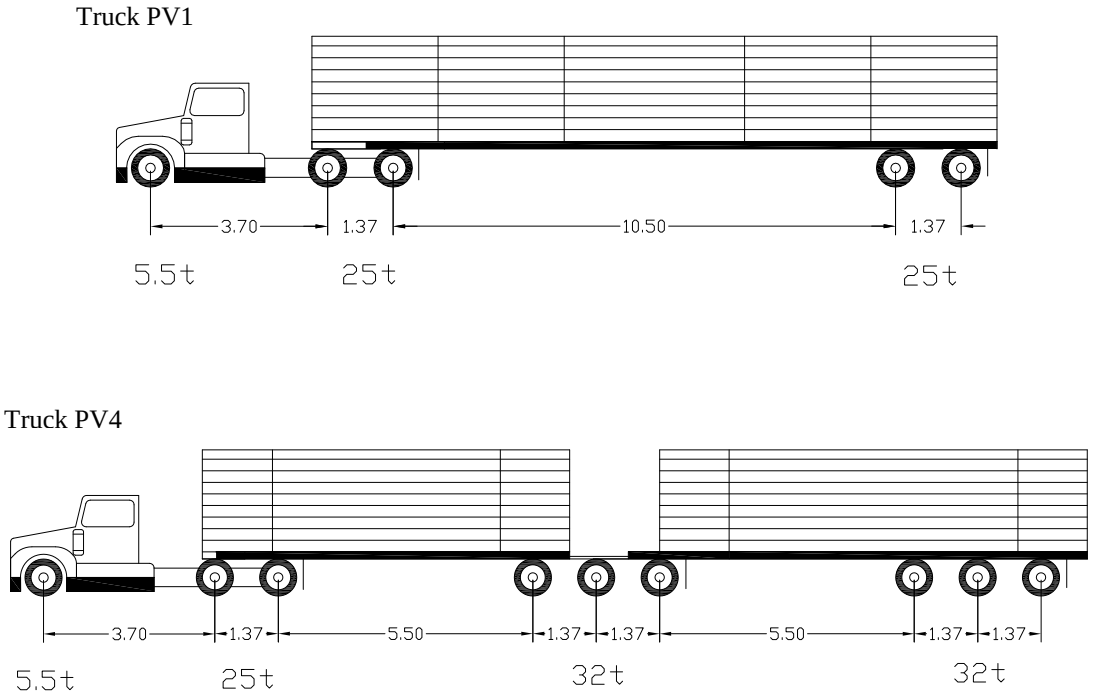

Figure 3.31 Schematic of truck configurations for simplified truck model.

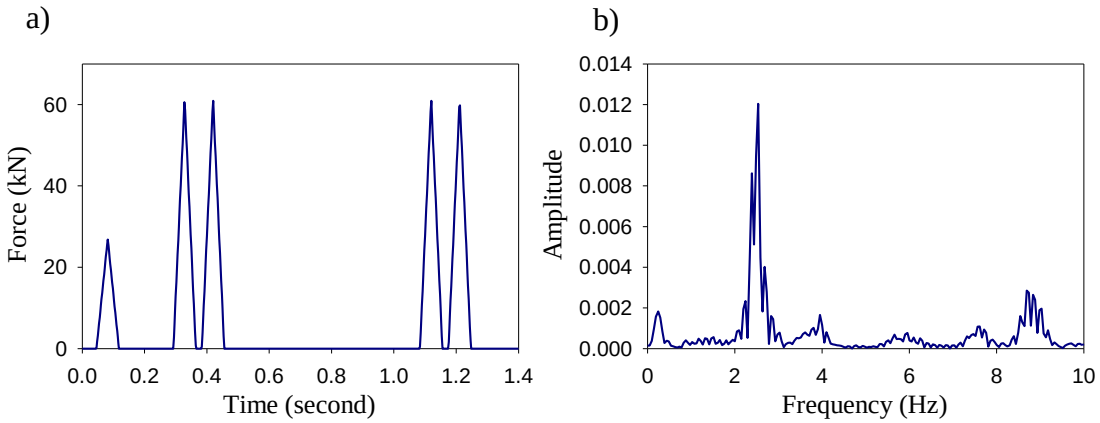

Figure 3.32 Truck excitation: a) example forced time history; b) response acceleration spectrum.

In addition to the simplified truck simulation, a dynamic truck model was also applied. For this model, the moving load model was further enhanced by considering the elastic and damping effects of the vehicle suspension system, thus introducing a spring-mass model, whereby a multiple-axle truck or tractor trailer can be modelled as a number of discrete masses, each supported by sets of springs and dashpots (Yang et al. 2004). In the case where the stiffness of the bridge is much larger than that of the vehicle, and the vehicle-bridge mass ratio is small, the vehicle dynamic response may be calculated ignoring the dynamic deflection of the supporting structure. The two systems of the vehicle and the bridge are thus treated as being decoupled (Pan and Li 2002).

The dynamic truck model used in this study was based on the QS-660 truck, a five-axle tractor trailer system that is the standard vehicle for evaluation and design of bridges in the province of Quebec. This vehicle has a total load of 660 kN (Figure 3.33), and was chosen because its dynamic properties have been documented in the published literature and can be used in the dynamic simulation (Fafard et al. 1998). In the truck dynamic model, each tire is modelled as a two-degree of freedom damped spring-mass system (Figure 3.34). The load on each tire is modelled as a mass supported on a set of springs representing the suspension system. The mass of the axles, wheels, drive shafts, and brakes is concentrated under the suspension system and over a set of linear springs representing the flexibility of each tire; dashpots are used to represent the damping produced by the tire and suspension system. The tire loading from the dynamic truck model was applied to the bridge using the DNL method. The dynamic properties of the QS-660 truck are listed in Table C.1 in Appendix C.

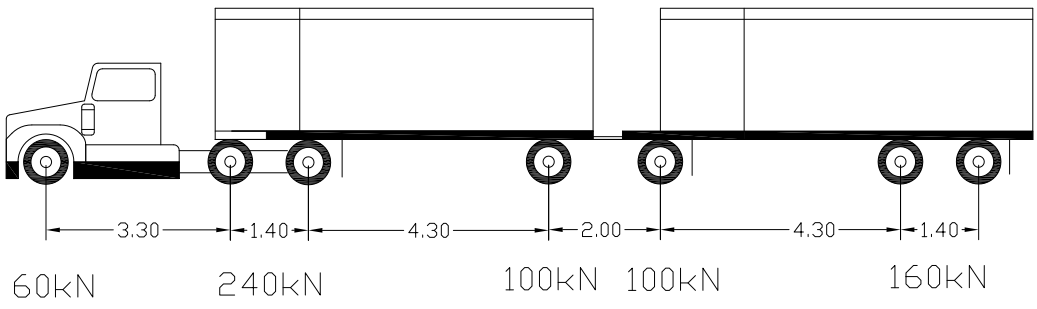

Figure 3.33 Schematic of QS-660 truck for dynamic truck model.

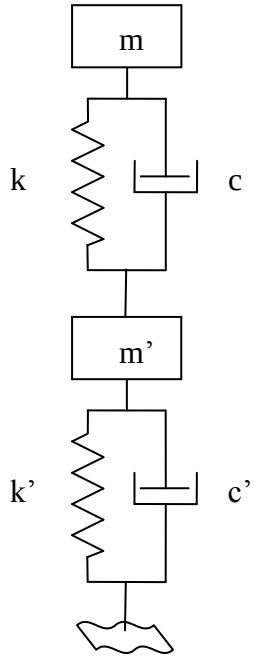

Figure 3.34 Truck wheel modelled as a two degree of freedom system: m', k' and c' are the mass, stiffness and damping of wheel system; k and c are the stiffness and damping of the suspension system; m is the portion of the truck mass supported by a specific wheel.

3.7.6 Road roughness

Road roughness can significantly affect the response of the bridge to vehicle loading; therefore, an estimation of road roughness is required as an input to calculate the vehicle dynamic loading on the bridge. To account for the random nature of the road roughness, the road profile can be modelled as a random Gaussian (normal) process and generated using certain power spectral density functions. One method for calculating road roughness profile was proposed by ISO Standard (Cebon 2000), as follows:

$$S_u(\kappa) = \begin{cases} S_u(\kappa_0)\left(\dfrac{\kappa}{\kappa_0}\right)^{-n_1} & \dfrac{\kappa}{\kappa_0} \le 1 \\ S_u(\kappa_0)\left(\dfrac{\kappa}{\kappa_0}\right)^{-n_2} & \dfrac{\kappa}{\kappa_0} > 1 \end{cases} \qquad [3.1]$$

where

κ = the wave number, in cycles/m, which expresses the rate of change with distance

κ_0 = the datum wave number, in cycles/m

$S_u(\kappa)$ = the displacement spectral density, in m^3/cycle

$S_u(\kappa_0)$ = the spectral density at κ_0, in m^3/cycle

The wave number, κ, expresses the rate of change with respect to distance in the same way as frequency expresses the rate of change with respect to time.

As recommended by Cebon (2000), the values of constants characterizing the random process were taken to be: $n_1 = 3$, $n_2 = 2.25$, $\kappa_0 = 1/(2\pi)$ cycles/m, and $S_u(\kappa_0)$ is defined in Table 3.1.

Table 3.1 Values for $S_u(\kappa_0)$ (Cebon 2000)

Road Class	$S_u(\kappa_0)$, 10^{-6} m^3/cycle
Very good	2 - 8
Good	8 - 32
Average	32 - 128
Poor	128 - 512
Very poor	512 - 2048

Figure 3.35 shows the road surface displacement spectral density (S_u) for different road classes (conditions).

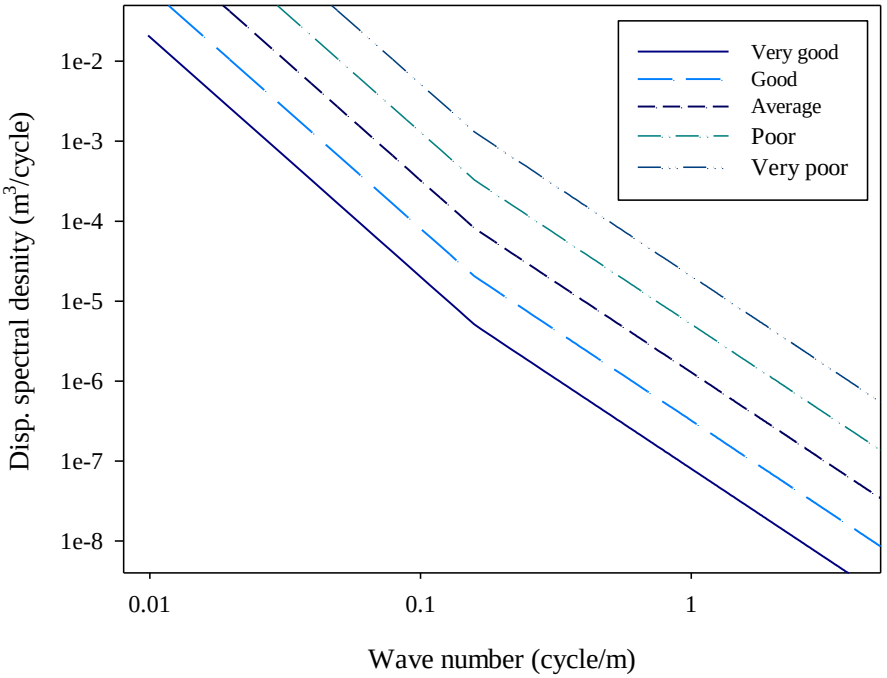

Figure 3.35 Spectral density plots of simulated road roughness profiles.

Pseudo-random road profiles can be generated from the spectral density given by Eq. 3.1 by applying a set of random phase angles uniformly distributed between 0 and 2π . The corresponding series of road heights z_r at regular intervals along the vehicle path is obtained by taking the inverse Fourier transform of the spectral density (Cebon 2000):

$$z_r = \sum_{k=0}^{N-1} \sqrt{S_k}\, e^{i(\theta_k + \frac{2\pi kr}{N})} \quad , r = 0,1,2,...(N-1) \qquad [3.2]$$

where

S_k = $(2\pi/N\Delta)\ S_u(\gamma\kappa)$

$S_u(\gamma\kappa)$ = the spectral density

$\gamma\kappa$ = $2\pi k/N\Delta$ = the wave number in *rad/m*

Δ = the distance interval between successive ordinates of the surface profile

$\{\theta_k\}$ = a set of random phase angles uniformly distributed between 0 and 2π.

The effect of road roughness on the dynamic response of the truck wheels was simulated as a support movement under each wheel, and the support reaction due to this excitation was evaluated. This reaction, in turn, was applied as a dynamic force on the bridge along the vehicle track, using the DNL method. Two roughness profiles were used, one for each of the left and the right wheels of the vehicle. Figure 3.36 shows a roughness profile for an "average" road class according to Table 3.1, with $S_u(\kappa_0)$ defined for a truck speed of 54 km/hr and sampling rate of 200 Hz.

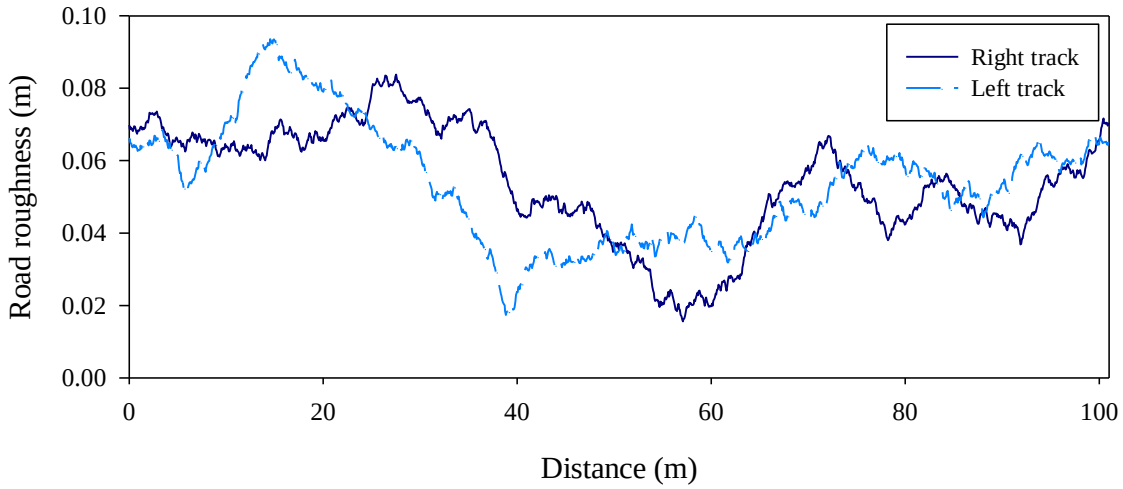

Figure 3.36 Simulated road roughness profiles.

3.8 MODAL ANALYSIS TECHNIQUES

Two modal analysis methods were used in this study: a frequency domain method and a time domain method. The selected frequency domain method was the SVD of the CPS method (Section 2.2.2), while the time domain method used was the SSI method, as detailed in Section 2.2.3. The SVD of CPS method was used mainly in conjunction with site measurements because it is fast and easy to implement and, along with expert judgment with more uncertain measured data, gives a quick idea of the bridge dynamic properties by visual inspection of the spectrum curves; on the other hand, the drawbacks of this method include its inability to distinguish closely spaced modes and/or separate the influence of forced excitation from the bridge modal response. The SSI method was used for the analysis of simulated data obtained from FE analyses. The SSI method is better able to distinguish between closely spaced modes and, in general, is superior to the peak picking method; however, it is computationally more intensive and requires more effort to process and interpret the data, thus making it more suitable for processing the simulated data (Peeters et al. 1998).

Pre-processing was performed on the measured signals before undertaking the modal analysis. First, zero shifts (the so-called DC component) in the sensor signals were removed. In the case of truck excitation, the measured acceleration-time records were trimmed so that only excitation from one truck was included in each record; furthermore, the truncated signal was windowed using a Tukey window (Section 3.5). The bridge free vibration response due to truck excitation was evaluated by trimming the record to include only the decaying free vibration response after the truck left the bridge; this free vibration signal was windowed using an exponential window to reduce the effects of leakage (Section 3.53.5).

3.9 PREPROCESSING FOR NUMERICAL SIMULATION

Before VBDD methods could be applied, a cubic spline curve was fitted to the mode shape data to interpolate the modal amplitude between the points of measurement on the bridge. The interpolated points were spaced at a uniform interval of 0.5 m, thus making the mode shape vector 201 nodes long. A cubic spline S_i, which is composed of

piecewise third-order polynomials that pass through a set of points (the points of the curve that needs to be interpolated), is defined as:

$$S_i(x) = a_i + b_i(x - x_i) + c_i(x - x_i)^2 + d_i(x - x_i)^3 \quad [3.3]$$

for $i = 0, 1, \ldots, n-1$, where n is the number of points and a_i, b_i, c_i and d_i are the polynomial coefficients. A natural cubic spline was used in this study. This type of cubic spline assumes zero curvature end conditions (Mathworks 2002), as shown:

$$S_0''(x_0) = S_n''(x_n) = 0 \quad [3.4]$$

Mode shapes need to be scaled before changes caused by damage can be identified. Therefore, a suitable normalization procedure was used in this study. The mode shapes were mass ortho-normalised assuming a unity mass matrix. A unity mass matrix assumes a uniform mass distribution along the bridge span. Mass ortho-normalization requires mode shapes to satisfy the following relationship:

$$\phi_n^T M \phi_n = 1 \quad [3.5]$$

where ϕ_n denotes the normalized eigenvector and M is the mass matrix (Humar 2002).

3.10 DAMAGE SCENARIOS

A number of different simulated damage scenarios were examined using the FE model. The first damage scenario consisted of cutting the external reinforcing bars from the middle region of all the girders within the centre span, which was approximately equivalent to an 18% reduction in the stiffness of the un-cracked girder cross section. The second damage scenario featured the cutting of external reinforcing bars near midspan on one of the exterior girders within the centre span. This damage scenario was chosen to examine the ability of VBDD methods to detect damage on one girder only (spatial resolution); also, since the severity of the 2nd damage case was less than that of the first, the sensitivity of VBDD methods to the extent of damage could be studied. The third damage scenario consisted of cutting the external rebar from the midspan region of all the girders within one of the end spans, thus examining the ability of VBDD methods to detect damage at different locations on the bridge. Finally, the fourth damage scenario was designed to compare the bridge in two condition states representative of the actual

bridge history: the original state when the bridge was reinforced with the external reinforcing bar and the second state when the external reinforcing bars were replaced by steel plates, which have 1.5 times the cross sectional area of the steel rebar. This scenario was intended to examine the effect of the new steel plates on the bridge modal properties, and to ascertain if such widely distributed changes to structural properties could be reliably identified.

3.11 VBDD METHODS

Six non-model based VBDD methods were selected for use in this study: change in mode shape, change in mode shape curvature, the damage index, change in modal flexibility, change in uniform load surface curvature, and change in unit load surface curvature (see Section 2.3). These VBDD methods were applied using simulated responses for each type of excitation described in Section 3.7, taking into account the different levels of noise that were added either to the input (excitation force) or output (simulated sensor readings). This was done to examine the effect of excitation force and data variability on the potential for the successful detection of damage using the specified VBDD methods. The MATLAB routines that were used in implementing these VBDD methods along with samples of input files are listed in Appendix H.

3.12 VARIABILITY IN MEASUREMENT

Different measurement sets taken at the same location and under the same form of excitation, but at different times, would vary to some extent due to random noise, errors in measurements, external interference, etc. As a result, it is usual practice to take several measurements for the same location or sensor setup, and then to average the measured or calculated quantities in order to increase the statistical reliability and attenuate the influence of random noise.

The influence of variability in measurements on estimated modal properties and damage indicators must be taken into consideration for practical applications; therefore, a statistical assessment of the damage indicators calculated using VBDD methods is essential to provide an indication of the level of confidence that may be placed in these damage indicators. A statistical t-test was used in this research to evaluate the

significance in difference between VBDD indicators calculated using different types of excitation forces and varying noise levels (DeCoursey 2003). In the case where the damaged bridge was compared to the FE model in pristine condition, the t-test was used to determine the confidence interval for individual VBDD damage indicators.

This statistical treatment of VBDD damage indicators is introduced to provide the investigator with a tool to reliably evaluate the bridge condition, as well as the indicated probability of the occurrence of damage.

Site tests are usually associated with many difficulties and subjected to many restrictions, such as the requirement of traffic control, limited time, difficulty in accessing some parts of the bridge, and a limited number of available sensors which requires several setups to be performed during the test. All of this would limit the number of potential tests that may feasibly be taken on the bridge; as a result, test personnel must make the best use of the limited data obtained during the test.

Based on experience gained in the course of this investigation, it appears to be reasonable to assume that an average of ten readings per set up can be achieved during a day of site testing on a bridge of this size, complexity and traffic loading characteristics. This limited sample size requires special statistical tools that take into account the sample size when evaluating the statistical confidence of the measured parameters. One commonly used method is the Student's t-distribution (DeCoursey 2003), which provides a procedure for estimating the reliability of the mean of a normally distributed population when the sample size is small by defining confidence intervals for a sample mean, as well as the statistical significance of the difference between two sample means.

The variable (t) of the t-distribution may be defined as:

$$t = \frac{\bar{x} - \mu}{s/\sqrt{n}} \qquad [3.\ 6]$$

where $\bar{x}$ is the sample mean, μ is the mean of the population from which the sample is taken, n is the sample size, and s is the standard deviation of the sample. Here, the variance, s^2, is defined as:

$$s^2 = \frac{\sum_{i=1}^{n}(x_i - \bar{x})^2}{(n-1)} \qquad [3.7]$$

in which x_i represents the i^{th} measured value within a data set. Confidence intervals for the population of the mean values can be calculated using the t-distribution as follows:

$$P(\bar{x} - t\frac{s}{\sqrt{n}} < \mu < \bar{x} + t\frac{s}{\sqrt{n}}) = 1 - \alpha \qquad [3.8]$$

where P is the probability that $\bar{x}$ is within "t" standard deviations from the population mean, and 100x(1-α) is the confidence level, such as a 95% confidence level for α =5.

3.13 ADDITIONAL TESTS

3.13.1 Strain Gauge Environmental Test

An environmental test was conducted on the selected strain gauges to evaluate their performance under the extremely cold conditions that are experienced on site. A strain gauge was attached to a concrete prism, which was placed in an environmental chamber within which the temperature was varied between -45° C and +20° C for one week at a rate of two cycles per day; also, higher than normal levels of humidity were induced. The physical condition of the strain gauge and its adhesion to the concrete were visually examined before and after the test. It was found that no deterioration or physical change could be noticed. Figure 3.37 shows the strain gauge attached to the concrete prism.

The concrete prism was placed in a universal testing machine and loaded by a 50 kN compression force (causing an average uniaxial stress of 5 MPa) before and after the environmental test to check if the strain gauge or its adhesive had been weakened or suffered deterioration. The gauge's readings were found to remain linearly related to the applied load before and after the environmental test, as shown in Figure 3.38. Therefore, it was concluded that this type of strain gauge is suitable for outdoor use on the Hudson Bay bridge which was the focus of this study.

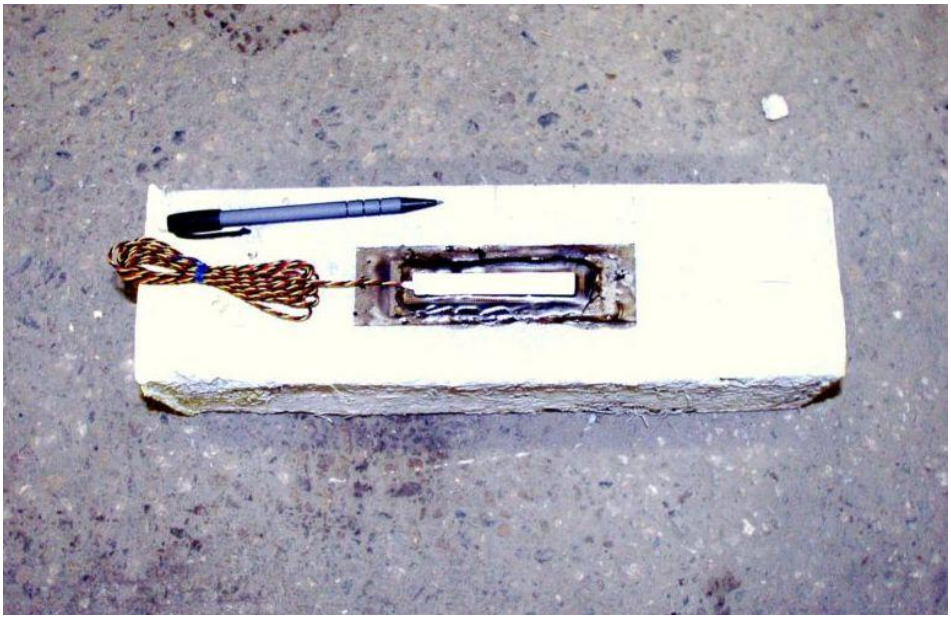

Figure 3.37 Strain gauge attached to concrete prism.

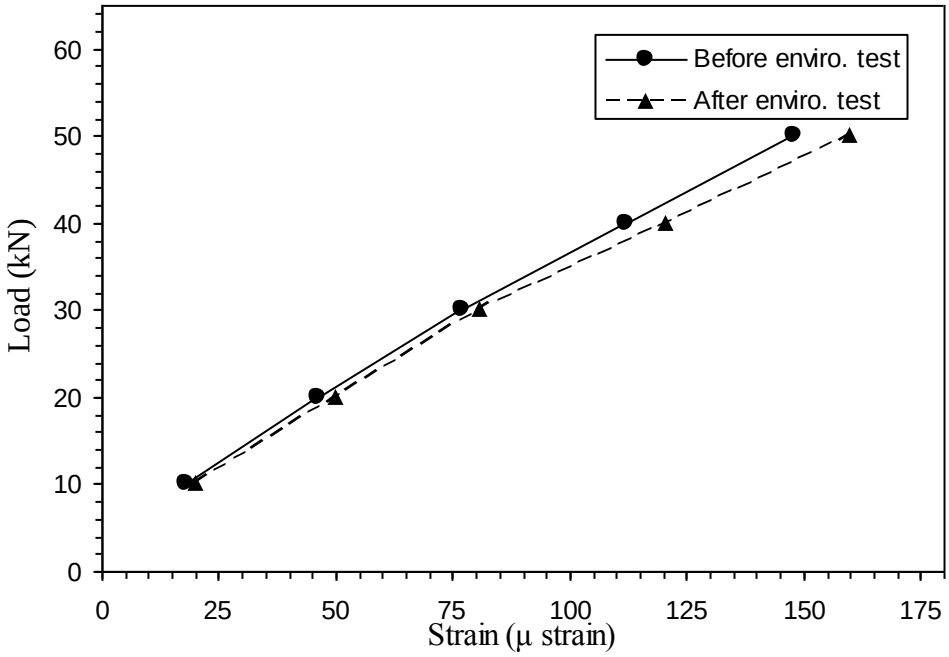

Figure 3.38 Load-strain relationship for environmental test of strain gauge.

3.13.2 Rebound Hammer Test

Rebound hammer tests were conducted on the bridge deck to obtain an improved estimate of the actual concrete compressive strength. Rebound hammer readings were taken at five locations on the bridge deck, including at the four corners of the deck and at the bridge's midspan. This was done to reduce the uncertainty in FE model parameters and increase the accuracy of the model updating procedure.

The rebound readings had previously been correlated to the concrete compressive strength in the lab by testing concrete cylinders of varying strength. Twenty one samples, 100 mm in diameter by 200 mm high, were tested, each of which was held firmly in place under a compression pressure of 7 MPa prior to obtaining twelve rebound hammer readings; the cylinders were then tested to failure in compression to determine the actual compressive strength. The relationship correlating hammer readings and concrete compressive strength was then established (Lee 1978, BS 1986, ASTM 2002).

An estimate of the concrete modulus of elasticity (E_c) that was used in calibrating the FE bridge model was calculated from the field estimated concrete compressive strength measurements (f'_c) using Eq. [3.9] (CSA 2004):

$$E_c = (3300\sqrt{f'_c} + 6900)\left(\frac{\gamma_c}{2300}\right)^{1.5} \qquad [3.9]$$

where γ_c is the concrete density in kg/m^3, and f'_c and E_c are in MPa.

Results from the laboratory calibrated tests are shown in Figure 3.39. The regression equation describing the relationship between rebound hammer readings and concrete compression strength for the lab results was calculated to be:

$$f'_c = 1.0406 * \mathrm{N} - 2.68 \qquad [3.10]$$

where N is the rebound number and f'_c is the concrete compressive strength in MPa.

A total of 45 rebound hammer readings were recorded at the bridge site. These readings were found to have an average reading of N=45.8 and a standard deviation of 4.04; the rebound hammer readings are listed in full in Table D.1 (Appendix D). From Eq. [3.10],

an average estimate for f_c' was found to be 45 MPa. By applying Eq. [3.9] and assuming that γ_c=2400 kg/m^3, the elastic modulus of the concrete would then be E_c=30,95 GPa.

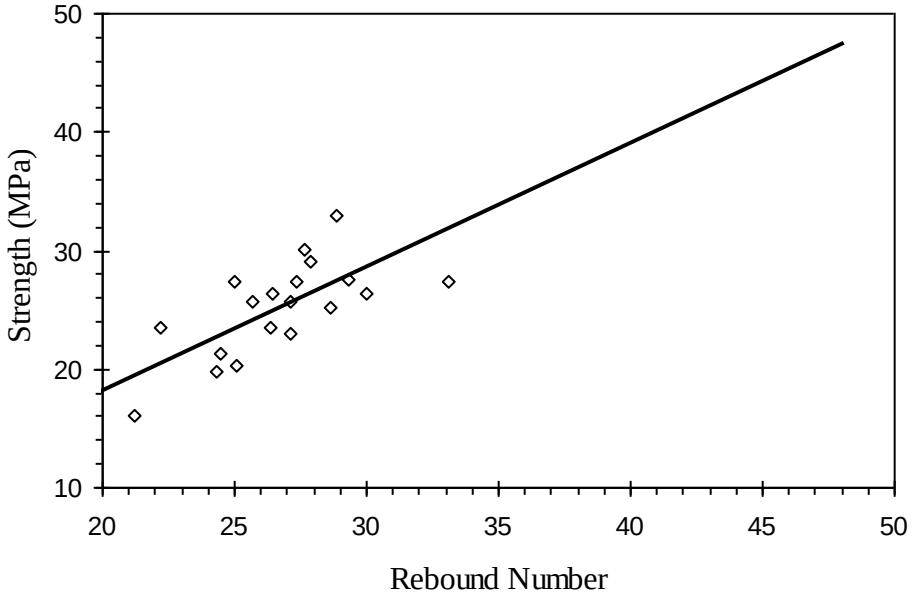

Figure 3.39 Relationship between rebound hammer number and concrete compressive strength.

Care should be taken in using this value of f'_c for two reasons: first, the surface hardness test provides information on the quality of the surface layer (about 30 mm deep) of the concrete only and, secondly, that the concrete surface gets harder with time due to carbonation. Therefore, the hardness of the surface layer may not be an accurate representative of the concrete within the bridge (BSI 1986). Based on what was mentioned earlier, the estimated value of f'_c was used as a guide only in calculating the concrete modulus of elasticity and updating the FE model.

4 EXPERIMENTAL RESULTS

4.1 OVERVIEW

In this chapter, comparisons are presented between the dynamic response characteristics derived from different excitation events and sources measured in the field. In addition to being used to compare excitation methods, the modal properties estimated from bridge excitation were used to update the FE model for later numerical simulations.

A static load test using a test truck was also performed on the Hudson Bay bridge. The purpose of this test was to evaluate the bridge response under static loading, and to evaluate the bridge strains at different locations. The response of the calibrated FE bridge model to the test truck was also compared to site test readings.

It is useful to mention again that the bridges in question were located in remote areas with limited traffic volumes. For this reason, it was possible to measure the bridge response to a single truck at a time, or to ambient (wind) excitation sources acting alone on the bridge.

4.2 MODAL TESTING AT THE HUDSON BAY BRIDGE

4.2.1 Truck Excitation

Figure 4.1a shows a typical acceleration time history induced by the crossing of a large truck (approximately 20 tonnes); the corresponding acceleration frequency spectrum is provided in Figure 4.1b. The results shown in Figure 4.1 are for the reference accelerometer on the west side of the bridge. The many peaks observed in Figure 4.1b demonstrate the difficulty in distinguishing between peaks representing the structure's natural frequencies from those associated with the truck loading.

In Figure 4.2a, only the decaying portion of the same acceleration time history is considered, representing free vibration of the bridge at its natural frequencies once the

truck had departed. Comparing the corresponding frequency spectrum in Figure 4.2b with that in Figure 4.1b, it is evident that the free vibration spectrum is smoother and better defined, making it relatively simple to identify modal peaks. It should be noted here that the various figures have been scaled differently so that each plot fits the size of the frame in that figure, in order to enhance the clarity of individual plots. This fact should be kept in mind when making comparisons between different figures. In these figures, the cross power spectra have been normalised by the mean-square response value σ^2.

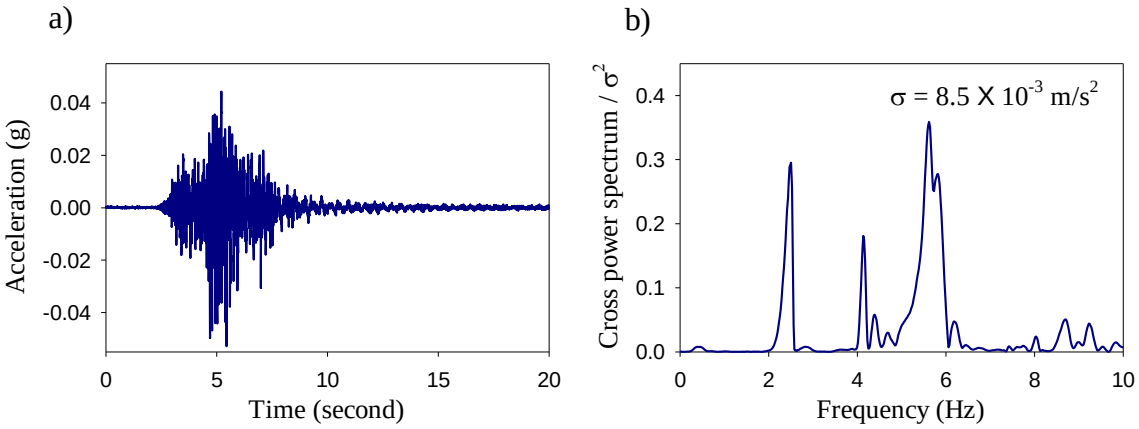

Figure 4.1 Example of Hudson Bay bridge response to a large truck: (a) acceleration time history; and (b) acceleration spectrum.

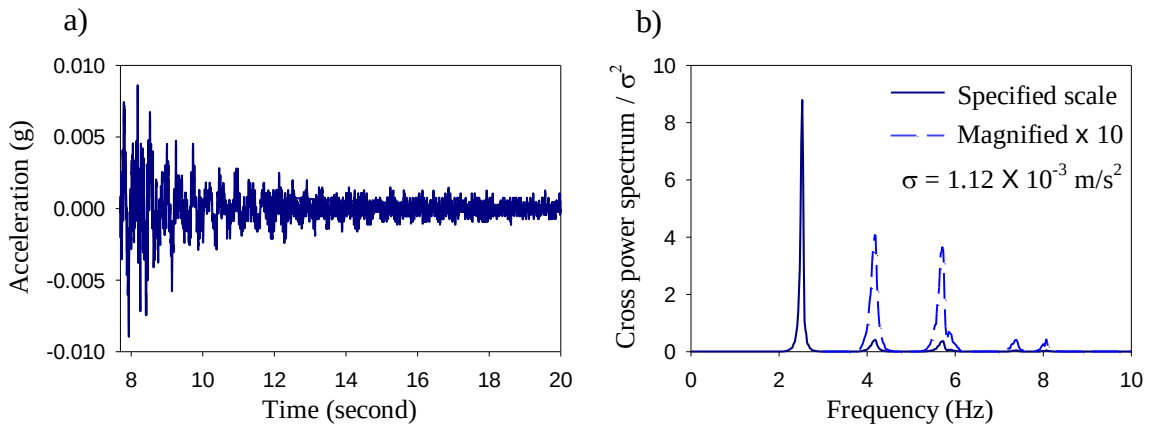

Figure 4.2 Decaying (free vibration) portion of Hudson Bay bridge response to a large truck: (a) acceleration time history; and (b) acceleration spectrum.

Figure 4.3 shows the acceleration time history and corresponding frequency spectrum produced by the passing of a small passenger truck (approximately 2 tonnes). The

decaying free vibration portion of this acceleration time history is shown in Figure 4.4a, with its corresponding frequency spectrum provided in Figure 4.4b. As with the large truck event, the bridge dynamic response with the truck still on the bridge (Figure 4.3) is seen to have a large number of spectral peaks, including many that are attributable solely to truck-induced forced vibrations. Once again, fewer and more well defined peaks are produced during free vibration (Figure 4.4).

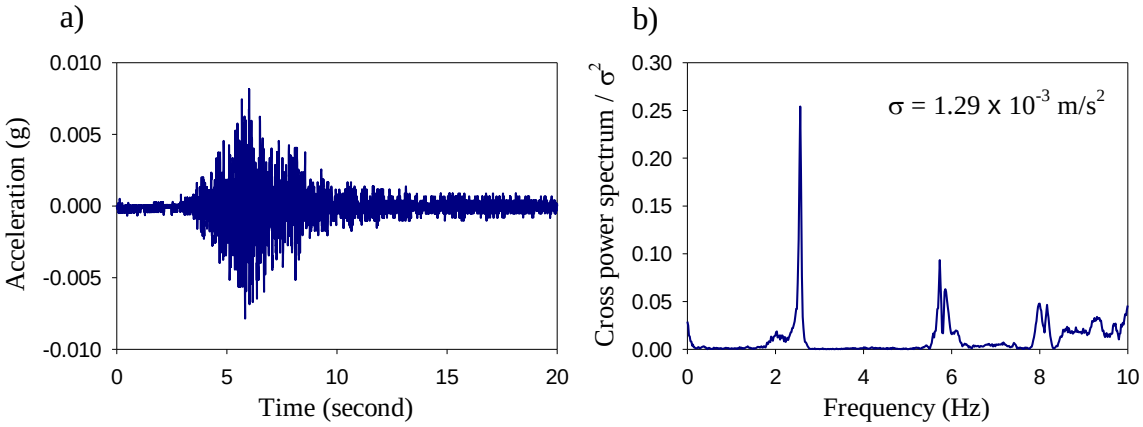

Figure 4.3 Hudson Bay bridge response to a small truck: (a) acceleration time history; and (b) acceleration spectrum.

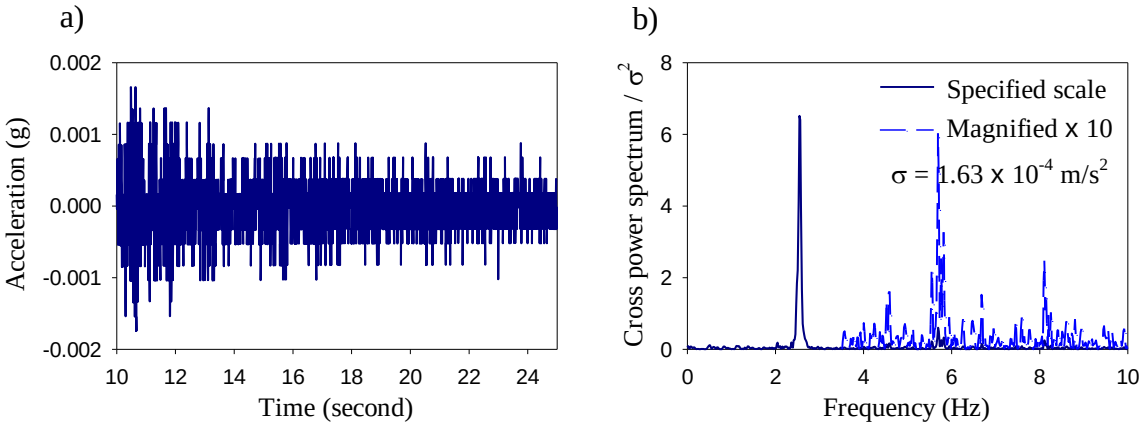

Figure 4.4 Decaying (free vibration) portion of Hudson Bay bridge response to a small truck: (a) acceleration time history; and (b) acceleration spectrum.

By examining Figure 4.2b and Figure 4.4b, however, it can be seen that the frequency spectrum of a small passenger truck is not as distinctive or clear as that due to a larger truck. Although the peak corresponding to the bridge's first natural frequency in Figure 4.4b is clear, the peaks of higher modes are difficult to distinguish in the same figure.

The degradation in the spectrum quality can be attributed, in part, to the lower measurement signal-to-noise ratio that was characteristic of the small truck excitation.

From the previous argument, one might conclude that the estimation of modal properties should improve with the intensity of the excitation event; interestingly, though, this proved not to be true in all cases. For example, Figure 4.5 describes the dynamic response caused by a large timber trailer truck, with a total mass of approximately 65 tonnes. It can be seen from Figure 4.5a that the maximum acceleration induced by the passing of this truck was 0.14g, a value significantly higher than the maximum acceleration of 0.05g in Figure 4.1a due to a somewhat smaller vehicle. The frequency spectrum of the decaying (free vibration) motion due to the larger vehicle is shown in Figure 4.5b. It can be seen from Figure 4.5 that, although the excitation level was high compared to previous records shown, this larger truck nevertheless managed to excite only the fundamental natural frequency in a strong manner, and two others weakly. This shows that both the excitation level and frequency content of the excitation source are important factors in the estimation of modal properties of the structure from measured responses.

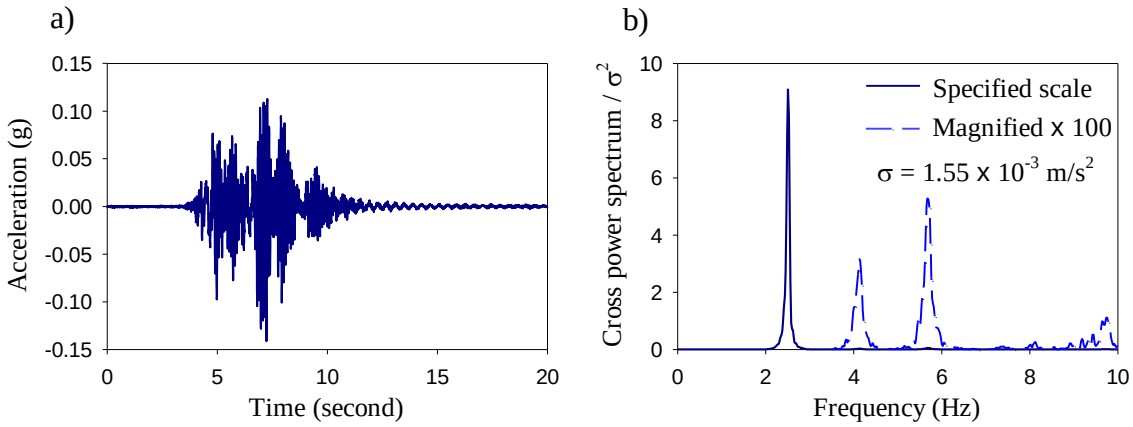

Figure 4.5 Hudson Bay bridge response to a large timber haul truck: (a) acceleration time history; and (b) acceleration spectrum of free decay.

It is instructive to show the excitation caused by different trucks crossing the bridge in succession so that the response to these trucks can be compared side by side. Figure 4.6 shows the different levels of excitation caused by a timber truck followed by a passenger car. Due to its larger weight, the timber truck excited the bridge much more strongly

than the passenger car. Figure 4.7 shows the bridge response to two timber trucks crossing the bridge successively. It is clear from Figure 4.7 that, although the two trucks were similar (although not identical) in loading and axle configuration, they nonetheless excited the bridge in different ways. This may be attributed to a different loading pattern, axle configuration, suspension system, or driving speed. It can therefore be concluded that using truck excitation for modal analysis is not straightforward and requires special attention, such as using only the decaying part of the accelerometer readings and grouping trucks of similar characteristics together when averaging the results, for example grouping accelerometer records due to large trucks, that induce large excitation on the bridge, in one group, and those due to pickup trucks and cars, with lower excitation level, in another. On the other hand, truck excitation is easy to implement from an operational perspective.

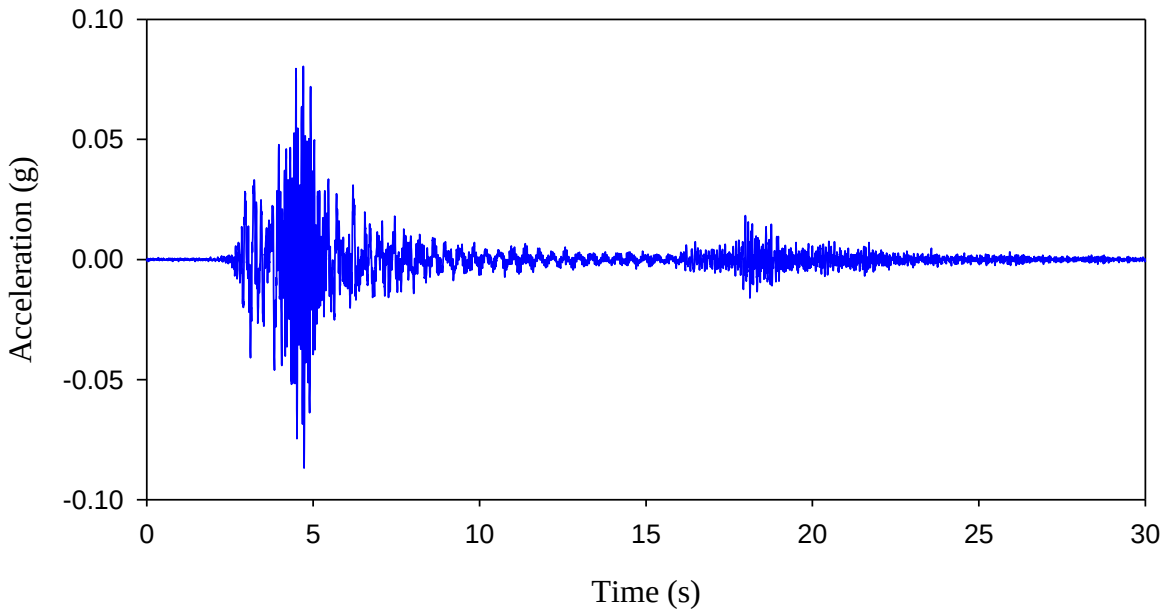

Figure 4.6 Hudson Bay bridge response to a large truck followed by a passenger car.

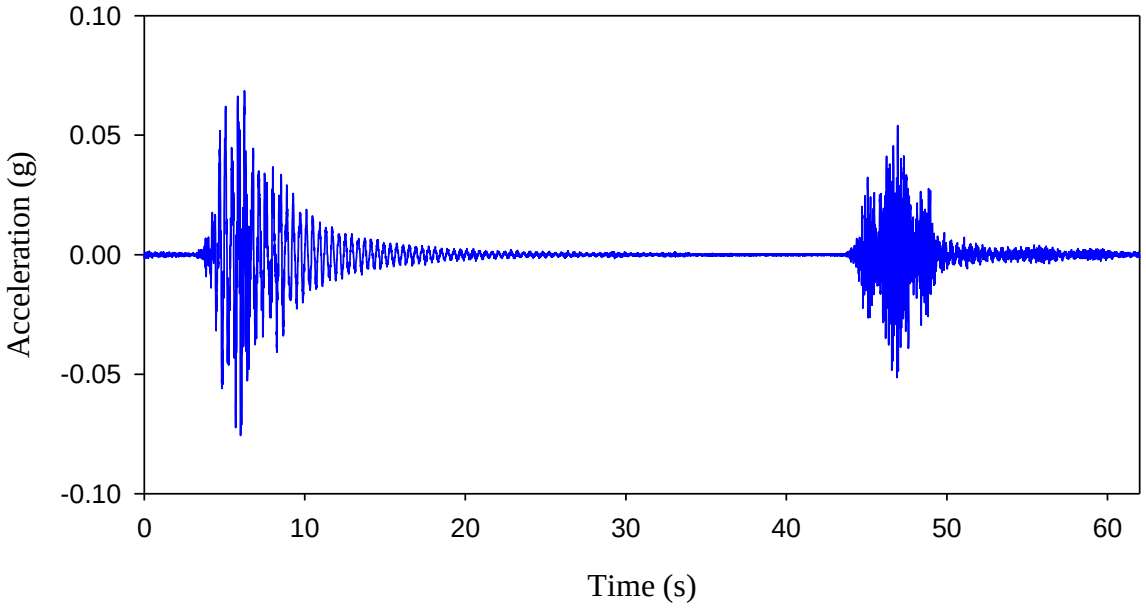

Figure 4.7 Hudson Bay bridge response to two large trucks crossing the bridge in succession.

4.2.2 Ambient Environmental Excitation

Figure 4.8 shows the frequency spectrum of the bridge acceleration, recorded by the reference accelerometer, due to ambient environmental forces such as wind. At the time of the test, the temperature was around 30^{o} C, with moderate winds and water flow in the river. For this figure, the sensor readings were logged for 30 seconds, or approximately 70 times the fundamental natural period (reciprocal of frequency) of the bridge. By comparing Figure 4.8 and Figure 4.2b, it can be observed that only the first mode can be confidently detected using the ambient vibration record, while the other modes are hard to distinguish from the random background response in the spectrum. This, again, can be attributed to the low signal-to-noise ratio for the response to ambient excitation forces, as well as to the significant natural variability in the ambient forcing spectrum.

The results produced by ambient excitation measurement can be improved through averaging by breaking the recorded time data into segments of equal length, applying a time window to each segment, calculating the FFT for each segment, and finally averaging the frequency spectra together (Stearns and David 1996). Figure 4.9a shows

the cross power spectrum of one of the accelerometers and the reference accelerometer calculated from a single 30 s acceleration time history segment, while Figure 4.9b shows a similar power spectrum calculated using a 140 s time record divided into 30 s segments with 60% overlapping between segments. In both cases, the 30 s segments have been modified using Hanning window function to reduce spectral leakage. It is clear from Figure 4.9b that averaging does improve the quality of the power spectrum; however, it still looks noisier than that derived from a free decay of a large truck. It should be noted that this bridge is lightly trafficked, with timber trucks being the main vehicles crossing the bridge, in addition to other types of vehicles. In this regard, the average time between two trucks crossing the bridge successively was close to the 140 s time record discussed above, which was the main reason why the 140 s period was selected for this study. It is expected that longer records would yield better results, as long as vehicle traffic did not interrupt the recording of the bridge response to ambient excitation.

The results presented in this section and the previous section are rather qualitative since the different excitation types are compared mainly in a visual manner; however, more quantitative comparisons are provided in subsequent sections.

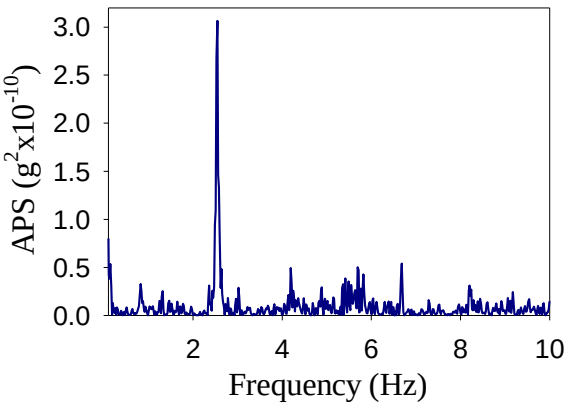

Figure 4.8 Auto power spectrum of the reference accelerometer due to ambient excitation.

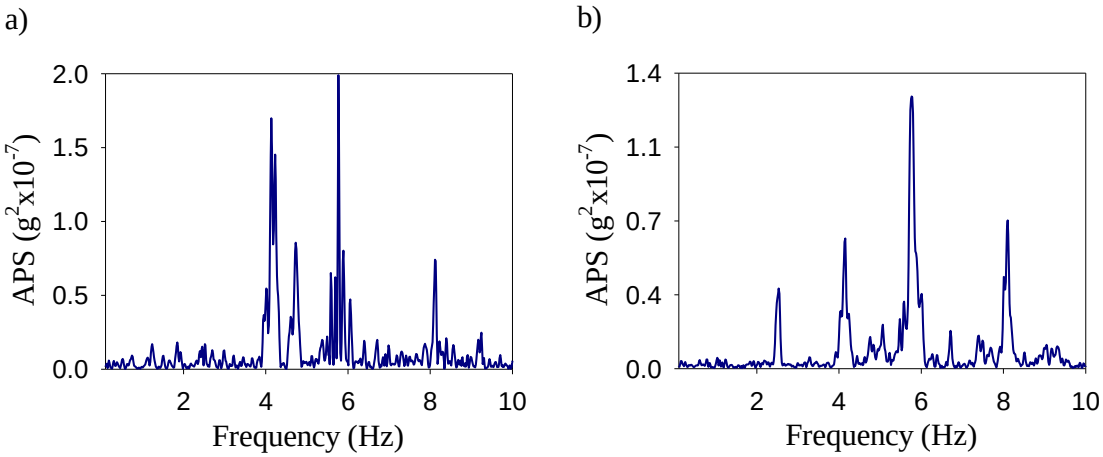

Figure 4.9 Auto power spectrum of the reference accelerometer produced by ambient excitation for: a) a single 30 s event, and b) a 140s time record divided into 30 s segments overlapping by 60%.

4.2.3 Variability of Modal Properties Measured Using Truck Excitation and Ambient Excitation

The variability of the modal properties calculated from site measurement was estimated by calculating the standard deviation of natural frequencies and mode shapes that were estimated from multiple site readings. The results of free decaying truck excitation and ambient excitation tests are discussed in this section.

The first set of site readings was taken during a one-day session. Eight large truck (timber truck) excitation events were recorded with instrumentation installed on the east side, as well as six events with instrumentation installed on the west side of the bridge; these events were averaged and their statistical properties were evaluated. For this purpose, only the free vibration portion of the response record was considered.

Table 4.1 lists the standard deviations (σ) for the first three natural frequencies of the bridge, based on these 14 large truck events. The highest coefficient of variation (CV) was 0.65%, which is a small value, indicating a low level of variability with respect to the lower natural frequencies over the course of this day.

Figure 4.10 shows the standard deviation of the normalised amplitudes of the first mode of the bridge for the middle span only, expressed in the form of error bars. For illustration purposes, the west side values have been artificially offset vertically to

enhance clarity. For this figure, the modal amplitudes were scaled according to the reference accelerometer which was assigned an amplitude of unity (1.0). The standard deviation of the first mode amplitudes ranged from 0.017 to 0.0488 (1.4% - 5.6% coefficients of variation) at the various accelerometer locations, which again may be considered to be small. Table D.2 in Appendix D lists the values used to create Figure 4.10. This low level of variation in the modal properties calculated from site measurements suggests the feasibility of using site readings for VBDD.

Table 4.1 Statistical characteristics of measured natural frequencies for Hudson Bay bridge, calculated from truck excitation.

Mode No.	Frequencies (Hz)	σ (Hz)	CV %
1	2.485	0.0162	0.65
2	4.160	0.0219	0.53
3	5.706	0.0372	0.65

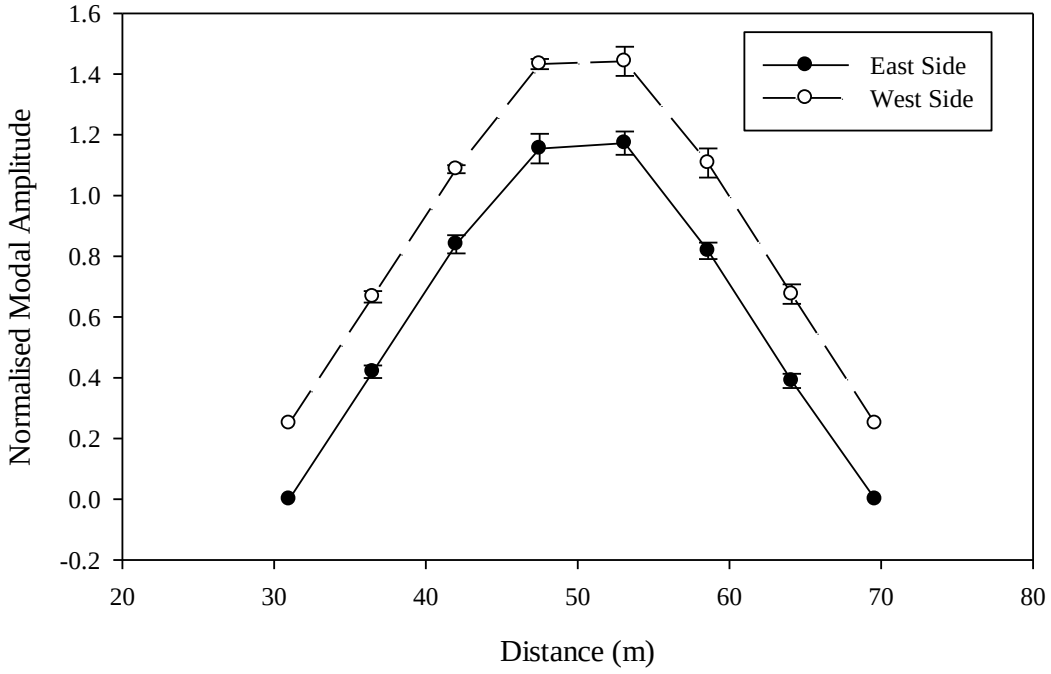

Figure 4.10 Standard deviations (shown as error bars) of the normalised amplitudes of the first mode in the middle span due to free decaying truck excitation, for the Hudson Bay bridge.

Another set of site readings was recorded using ambient excitation, measured during the same day in which truck excitation events were recorded. Six ambient excitation events

were recorded with instrumentation installed on the east side, as well as 14 ambient excitation events were recorded with instrumentation installed on the west side of the bridge. These events were 48 s long on average. The bridge readings due to ambient excitation were averaged and their statistical properties were evaluated. It was found that only the first mode could be reliably identified. For these conditions, the first natural frequency was 2.432 Hz with a computed standard deviation equal to 0.0245, corresponding to a coefficient of variation of 1.02%, which was almost twice the value of that due to the decaying part of truck excitation.

Figure 4.11 shows the standard deviation of the normalised amplitudes of the first mode of the bridge for the middle span only due to ambient excitation, expressed in the form of error bars. The standard deviation of the first mode amplitudes ranged from 0.015 to 0.051 (40.7% - 61.3% coefficients of variation) at the various accelerometer locations, which are much higher than those due to truck excitation. Table D.3 in Appendix D lists the values used to create Figure 4.11.

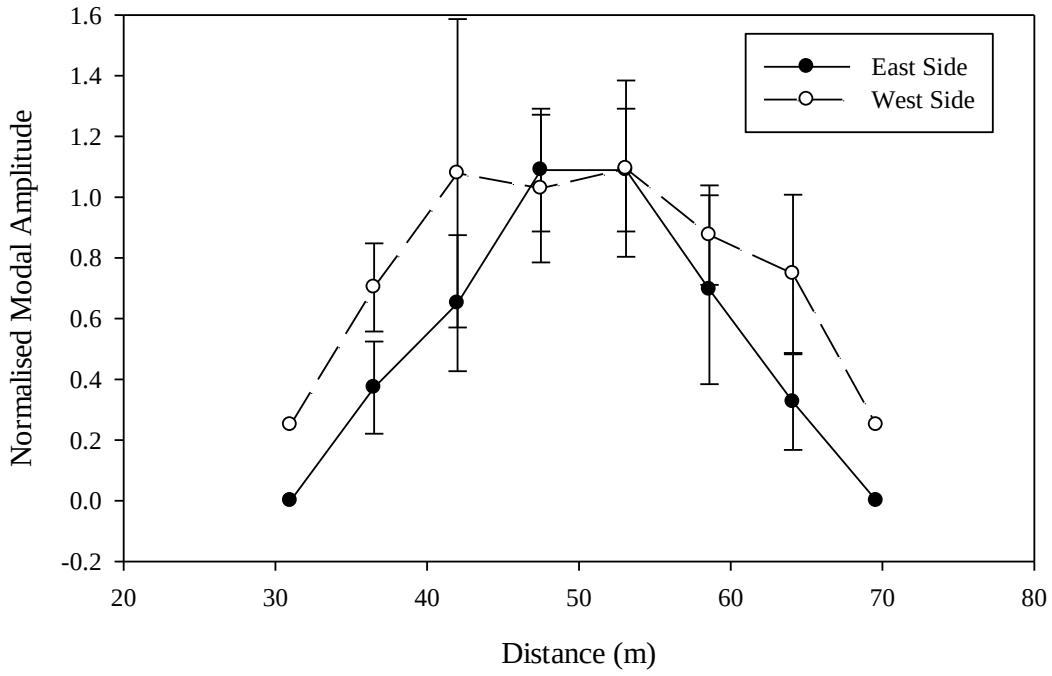

Figure 4.11 Standard deviations (shown as error bars) of the normalised amplitudes of the first mode in the middle span due to ambient excitation, for the Hudson Bay bridge.

It can be concluded that the modal properties calculated from ambient excitation were less accurate, with more variability, than those due to truck excitation. This may be attributed primarily to the higher level of excitation induced by trucks and the natural variability in the random ambient excitation. These results suggest that ambient excitation, at least for the recorded durations used in this study, would not be a reliable source of excitation for VBDD.

4.2.4 Impact Excitation Test at the Hudson Bay Bridge

An impact excitation test was conducted in May 2009 on the Hudson Bay bridge using the spring-hammer, as detailed in Section 3.6.2.3. The temperature was around 12° C during the test. The test was done using four instrumentation setups due to the limited number of accelerometers available for the test. Seven accelerometers were used to capture the bridge response due to the impact induced by the spring hammer. Six accelerometers were moved around the bridge to capture the full bridge response in four setups as shown in Figure 3.19. One accelerometer, the reference accelerometer, was kept in one place at all times so that the response of the other accelerometers could be referenced (scaled) in a consistent manner and the readings from the four setups could be glued together to capture the full bridge response. During this test, the response of the whole bridge was captured by the four setups (Figure 3.19), as opposed to capturing the response on the middle span only with two setups as was done when measuring the bridge response to traffic excitation. This was possible because the spring hammer testing was fast and easy to implement, making it suitable and efficient for bridge testing. Each test took approximately 10 seconds to complete, making it possible to instrument the whole bridge in approximately one-half a day.

Ambient excitation readings were also recorded in addition to the impact excitation, for each test setup. The purpose of conducting the ambient excitation test was to compare the quality of modal properties calculated from impact excitation to those calculated from ambient excitation. Each ambient record was five minutes long sampled at 300 Hz.

The impact excitation test using the spring-hammer was conducted on the Hudson Bay bridge after it underwent a rehabilitation process during the winter of 2006 that consisted of replacing the external reinforcing bars at the middle span with steel plates,

as detailed in Section 3.6.2.3. It is expected that the bridge dynamic properties would have changed due to this rehabilitation work in a similar way as if it had incurred some (in this case, beneficial) damage, because this rehabilitation would change the bridge stiffness and thus alter its natural frequencies and mode shapes. A typical acceleration time history and response spectrum at the reference accelerometer location due to spring-hammer excitation is shown in Figure 4.12.

The maximum acceleration response shown in Figure 4.12a due to impact excitation was 0.053 g, while the maximum acceleration response due to large trucks such as the ones shown Figure 4.1a or Figure 4.5a was 0.052 g and 0.14 g respectively. This comparison shows that the level of excitation induced on the bridge by the spring-hammer was of same order of magnitude of the excitation induced by large trucks. This leads to the conclusion that both types of excitation have comparable excitation levels, which means that the effect of noise on the modal properties calculated using either type of excitation would be similar.

The response spectrum shown in Figure 4.12b due to impact excitation showed clear peaks that would correspond to the natural frequencies of the bridge. It can also be noticed from Figure 4.12b that the spring-hammer excited higher modes to similar amplitude as those of the fundamental mode. This may be attributed to the nature of impact excitation in which the force has a flat spectrum over a wide range of frequencies, which means that the hammer imparts equal levels of energy to all frequencies within that range, thus exciting the different modes of the bridge to the similar levels. This means that several mode shapes, and not the fundamental mode only, can be calculated using impact excitation. On the other hand, the response peaks due to truck excitation shown in Figure 4.1b to Figure 4.5b are not as clear as those shown in Figure 4.12b; in addition, truck excitation has mainly excited the fundamental mode only.

Figure 4.13 shows the first four modes of Hudson Bay Bridge calculated from the bridge response to impact excitation using a rubber pad. It should be mentioned that the second mode of the bridge could not be easily excited using this test set up as this mode was observed only in 39 records for the whole bridge (20 records with using a rubber pad and 19 records without a rubber pad), as opposed to ten records per setup, with and

without the rubber pad, for a total of 80 records for the other modes. This difficulty in exciting the second mode may be attributed to the location of the spring hammer. By comparing the second mode shape in Figure 4.13b to the location of the spring hammer in Figure 3.19, it can be seen that the spring hammer was located near a nodal point (a point in the mode shape where there is zero response) in the second mode shape, thus making it difficult for the spring-hammer to excite this mode. The choice of this location for the spring hammer was made initially to accommodate having both the spring-hammer and the hydraulic shaker on the bridge at the same time, in order to perform excitation tests using both types of equipment. It is suggested, for future tests, to locate the spring hammer at a more favourable location, away from any modal nodal points if possible. Another suggestion is to conduct two sets of tests with two locations for the spring hammer, installing the spring hammer at locations of the maximum amplitude of one or more modes.

The quality of mode shapes based on the phase angle of the modal amplitude was also assessed. It was found that all the nodes had a phase angle relative to the response of the reference accelerometer of either 0° (in phase) or 180° (out of phase), with a maximum variation of 1.61°. This indicates that all calculated modes were real modes, and that the measured data were of high quality, with little random noise or phase shifting.

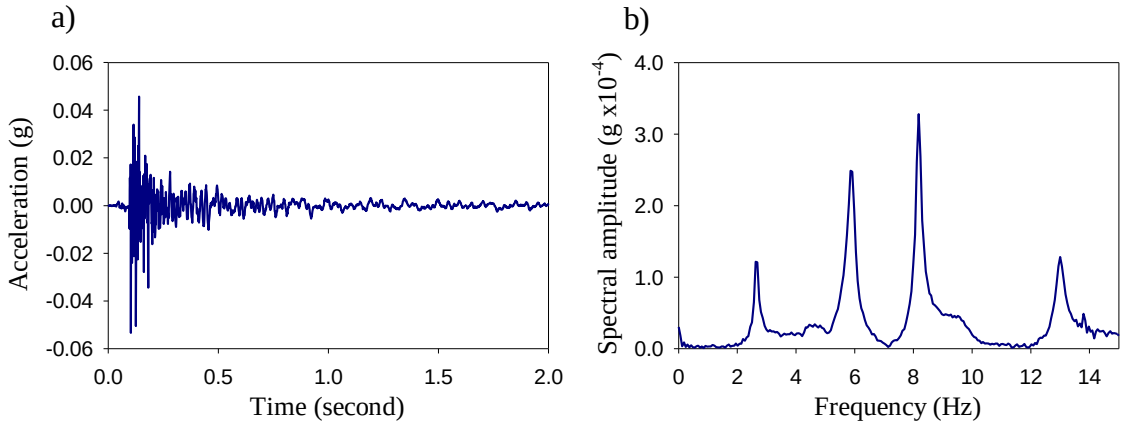

Figure 4.12 Hudson Bay bridge response to impact excitation: (a) acceleration time history; and (b) acceleration spectrum, for the reference accelerometer.

In contrast, for the ambient excitation, the quality of modes calculated was not as good as those calculated from impact excitation. For ambient excitation, the peak picking

method was used to calculate the natural frequencies and mode shapes, as opposed to the SSI method used for impact excitation, because the quality of readings was too low for SSI to give any useful values. The modal phase values obtained from the solution by the peak picking method were rounded to either 0 or 180 during the solution; therefore, no phase values were available to be compared to the impact excitation results.

The modal amplitude properties for the two types of impact excitation and ambient excitation are listed in Appendix E. In this appendix, the modal amplitudes were scaled according to the reference accelerometer, which was assigned an amplitude of unity (1.0).

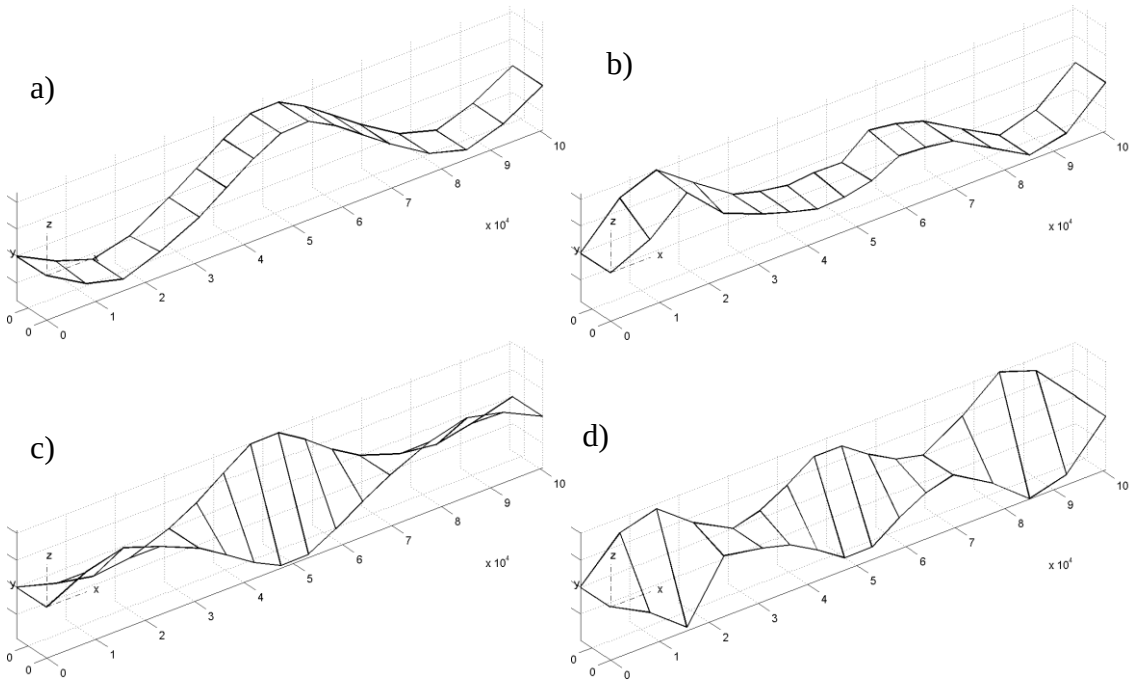

Figure 4.13 Lowest four vibration mode shapes calculated from the spring hammer excitation at the Hudson Bay bridge: a) mode 1 (2.640 Hz), b) mode 2 (4.253 Hz), c) mode 4 (5.812 Hz), and d) mode 6 (8.156 Hz).

4.2.5 Variability of Modal Properties Measured Using Impact Excitation and Ambient Excitation

The results of impact excitation and ambient excitation tests, that were conducted during the same day, are discussed in this section.

The repeatability of the measurements is illustrated graphically in Figure 4.14, which shows ten auto power spectra (APS) for the reference accelerometer due to bridge

excitation by the spring-hammer. It is clear from Figure 4.14 that the readings have very little variation in frequency content, as well as fairly consistent response amplitudes. This consistency between successive measurements is an important factor in VBDD applications. Repeatable excitation signals mean that there would be less variation in the calculated modal properties and thus more accurate VBDD evaluations. This argument will be discussed in more detail in Chapter 5.

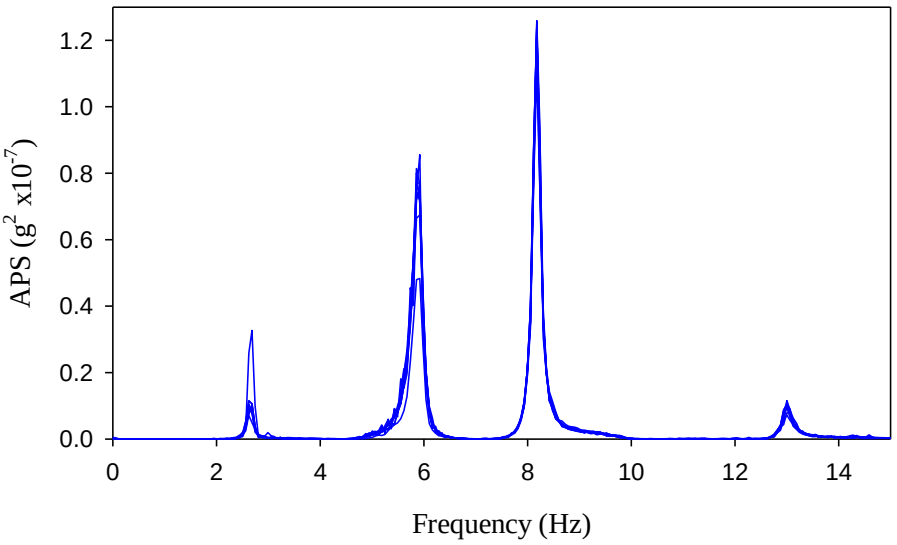

Figure 4.14 Auto Power Spectra of readings from 10 impact events measured by the reference accelerometer, for the Hudson Bay bridge.

The bridge natural frequencies calculated from the two types of impact excitation (with and without a rubber pad placed under the tip of the spring-hammer) and ambient excitation are listed in Table 4.2. It can be seen from Table 4.2 that the values of the bridge natural frequencies from the three types of excitation were very close (within 0.6% for the fundamental frequency). Table 4.2 also shows that the coefficients of variation for the fundamental frequency for the two types of impact excitation were very low and very close to each other, 0.542% and 0.578%, for impact excitation with the rubber pad and without the rubber pad, respectively. These results confirm the repeatability and low variation that was shown in Figure 4.14.

Table 4.2 Statistical characteristics of measured natural frequencies for Hudson Bay bridge, calculated from impact and ambient excitations.

Mode no.	Impact excitation with rubber pad			Impact excitation w/o rubber pad			Ambient excitation	
	Freq. (Hz)	σ^{*} (Hz)	CV† %	Freq. (Hz)	σ (Hz)	CV %	Freq. (Hz)	σ (Hz)
1	2.640	0.014	0.542	2.641	0.015	0.578	2.625	N.A
2^{+}	4.253	0.04492	1.056	4.276	0.075	1.763	4.217	N.A
4	5.812	0.041	0.707	5.813	0.030	0.512	5.900	N.A.
6	8.156	0.004	0.050	8.157	0.004	0.054	- -	N.A

* σ = Standard deviation;

† CV = Coefficient of variation;

\+ Second mode was calculated from 20 and 19 records only, with pad and without pad respectively.

By comparing the coefficients of variation for the bridge's natural frequencies listed in Table 4.1, which were calculated from truck excitation, to those in Table 4.2, that were calculated from spring hammer excitation, it can be observed that values of coefficients of variation for the two types of excitation were close to each other. For example, the coefficients of variation of the first natural frequency were 0.65% and 0.542% for truck excitation and spring-hammer excitation, respectively. This low coefficient of variation for both types of excitation may be attributed to the fact that both sets of modal properties were calculated from the bridge's free vibration, whether it was the free vibration following truck excitation, or the bridge free vibration due to hammer impact excitation.

The average coefficients of variation of the 1st mode amplitudes due to impact excitation, with and without a rubber pad placed below the tip of the spring-hammer, were 4.77% and 5.56%, respectively. This indicates that modal amplitudes determined without using a rubber pad had a higher level of variation. It should be mentioned here that the average coefficient of variation calculated from the test results excluded a value of 20.9% for one of the measurement locations, as it was much higher that the other values. External interference or temporary instrument error might have caused this high value of coefficient of variation.

Figure 4.15 shows the standard deviation of the normalised amplitudes of the first mode of the bridge, calculated using impact excitation with a rubber pad, expressed in the

form of error bars. For illustration purposes, the west side values have been artificially offset vertically to enhance clarity. For this figure, the modal amplitudes were scaled according to the reference accelerometer which was assigned an amplitude of unity (1.0). The standard deviation of the first mode amplitudes ranged from 0.018 to 0.045 (corresponds to 4.43% and 4.1% coefficients of variation) at the various accelerometer locations, which again may be considered to be small. These values are similar to standard deviation values of the modal amplitudes calculated from truck excitation in Section 4.2.3. Table E.1 in Appendix E lists the values used to create Figure 4.16.

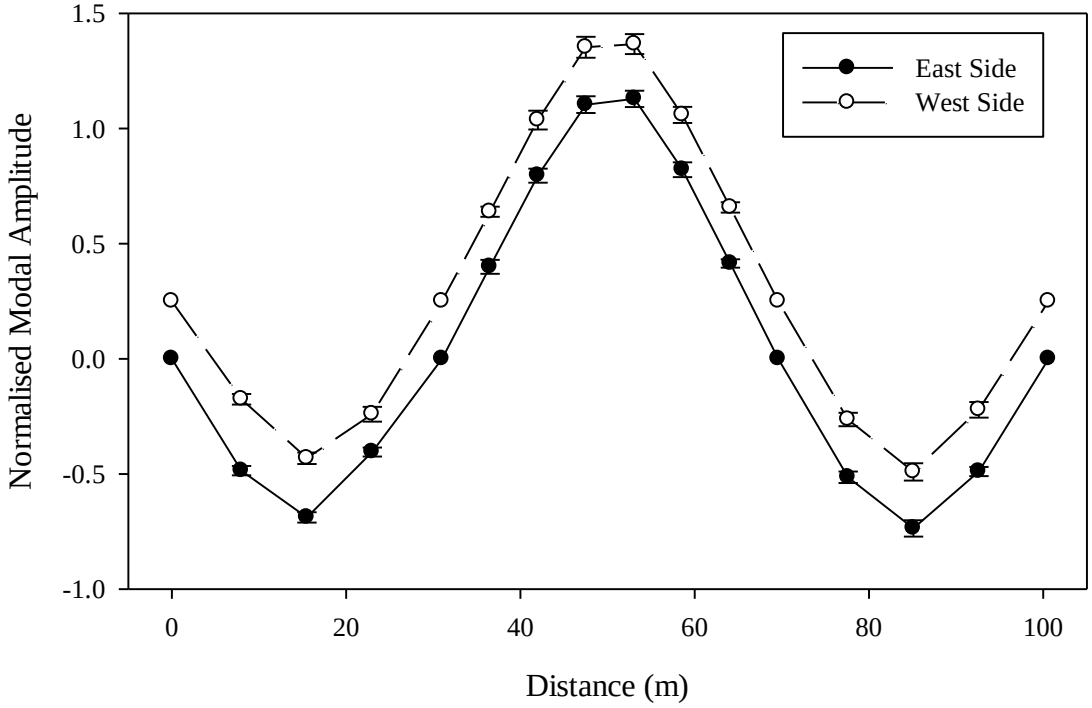

Figure 4.15 Standard deviation (shown as error bars) of the normalised amplitudes of the first mode due to impact excitation with rubber pad for the Hudson Bay bridge.

The first natural frequency of the bridge after it had been strengthened was 2.64 Hz, as shown in Table 4.2. This frequency was 5.9% higher than the first natural frequency before strengthening (2.485 Hz), as shown in Table 4.1. This suggested that the first natural frequency of the bridge has increased due to the stiffening of the bridge by replacing the external reinforcing bars by steel plates at the middle span of the bridge. To verify that this difference is statistically significant, the standard deviation of the frequency was considered. It can be seen that first natural frequency of the bridge after

the rehabilitation (2.64 Hz -/+ 0.014 Hz) is more than one standard deviation higher than the original first natural frequency of 2.485 Hz. The same argument can be made for the other modes.

By applying Equation 3.1 for the t test, comparing the fundamental natural frequency before and after rehabilitation, and considering a sample size of 40 averages, the value of the variable t can be found to be equal to 72.3, which is much higher than the t value of 1.684 corresponding to a two-sided 95% confidence level. It may therefore be concluded that the rehabilitation work caused a statically significant shift in the fundamental natural frequency.

4.2.6 Evaluating Noise Levels in Field Readings

As was shown above, ambient excitation can be used to determine the natural frequencies of a structure, as this type of excitation can be considered to be a random signal with an approximately smooth variation in the level of energy over a wide range of frequencies; however, when another form of excitation is used for modal analysis, then the existence of ambient excitation would have the effect of random noise that is superimposed over the primary excitation signal, such as that from truck or harmonic excitation (Pavic et al. 1997). It is useful to evaluate the energy ratio, defined as the ratio of the total areas under the power spectra of the ambient and the forced excitation responses in order to approximately determine the actual noise levels on site. However, it is important to acknowledge that this is only one source of noise in the recorded signal; in addition, the excitation force has some uncertainty in its definition too, but that is difficult, if not impossible, to quantify on site. Results from this evaluation are used later to select a reasonable level of noise for the numerical simulations.

The power (variance) for truck, ambient and impact excitation was evaluated by calculating the power for each sensor's acceleration reading, then averaging the readings of all the sensors in that setup.

For one site test that was conducted on the Hudson Bay bridge, 43 truck excitation records were compared to 21 ambient excitation records. The maximum noise level, defined as the ratio between the total variances of an ambient vibration event and a truck-induced event, was found to be 3.73%. This level of noise occurred when the

ambient vibration was high due to a moderate breeze or fast river flow and was paired with the excitation of a small truck (or passenger car). On the other hand, the minimum level of noise measured was 0.015% when a large truck excitation (timber truck) event was paired with low level of ambient excitation (quiet wind or low level of river flow). The average noise level was 0.2%.

For evaluating noise level in impact excitation, twenty records for impact excitation, each ten seconds long, were used, in addition to six ambient excitation records with a total duration of 330 s. It was found that the average noise level was 2.3%, while the maximum and minimum levels were 5.2% and 0.3%, respectively. These values are higher than the noise levels calculated for truck excitation. This could be attributed to that fact that the energy content of impact excitation was lower than the energy provided by the much heavier trucks. Nonetheless, the noise level calculated from impact excitation was low, and the quality of mode shapes calculated from impact excitation (standard deviation of modal amplitude ranged from 0.018 to 0.045) was comparable to those calculated from truck excitation (standard deviation of modal amplitude ranged from 0.017 to 0.0488), which may be attributed to the excellent repeatability of impact excitation compared to the variable nature of truck excitation. This leads to the conclusion that the type of excitation has a major role in determining the quality of modal properties calculated from dynamic testing.

4.3 STATIC LOAD TEST

A static load test was conducted on the bridge, as discussed in Section 3.6.2.4, by having a truck cross at crawl speed (approximately 10 km/hr), while strain gauge readings were logged at 300 Hz. The strain gauge signals were oversampled and then down-sampled afterwards as a means of improving the quality of the readings and reducing noise. As part of this process, the data were smoothed by applying a moving average, which involves the calculation of a series of averages of different subsets of sequential data points from the full data set, followed by down-sampling or decimating, which is the process of reducing the sampling rate of a signal by keeping every n^{th} sample and discarding the others. It was determined that good results were achieved using a span of 100 points for the moving average, and down-sampling by a factor of 25, thus making

the effective sampling rate equal to 12 Hz. This is considered adequate for the slowly varying signal caused by the load of the crawling truck. The bridge was closed to traffic while this test was conducted.

Figure 4.16 shows a strain gauge reading before and after smoothing was applied. The improvement in data quality after smoothing is clearly visible, as indicated by the substantial reduction in the apparent noise-to-signal ratio. This procedure effectively filtered out the high frequency noise in the measured signal, making it easier to identify the actual strain values caused by the truck loading.

Figure 4.17 shows strain readings at one location due to multiple passes of the test truck. It can be seen that the test repeatability was good, within the resolution range of the strain gauges (+/- 2 μ strain). It also shows that the bridge behaviour is predominantly elastic as the strain readings returned to zero after the truck left the bridge.

Figure 4.18 shows the strain readings for three strain gauges attached to the west girder near the north support of the middle span of the bridge (Figure 3.5). As noted in Chapter 3, these gauges were aligned vertically to facilitate the study of girder curvatures. For this particular test, strain gauge readings were logged while the test truck travelled southbound over the bridge in the west lane. It can be seen from Figure 4.18 that the recorded strain readings for all three gauges were compressive over the majority of the recording period; in addition, these strains are not consistently proportional, as would be the case for pure flexure. Both of these observations are indicative of the presence of an axial compressive force in the girder, which lends support to the contention that some degree of arching behaviour existed; such a condition could arise from partial support fixity such as that assumed in updating the FE model, as described in Section 3.3, or from the existence of a “tension tie” mechanism within the girder due to internal or external reinforcement.

Similarly, Figure 4.19 shows the strain readings of another group of strain gauges attached to the west girder near its midspan and subjected to the same truck load as that associated with the strain readings in Figure 4.18. It can be seen from Figure 4.19 that the lower gauge records compressive strains as the truck crosses the middle span of the bridge, rather than tension as would be expected from flexural behaviour, thus confirming the arching action within the bridge girders.

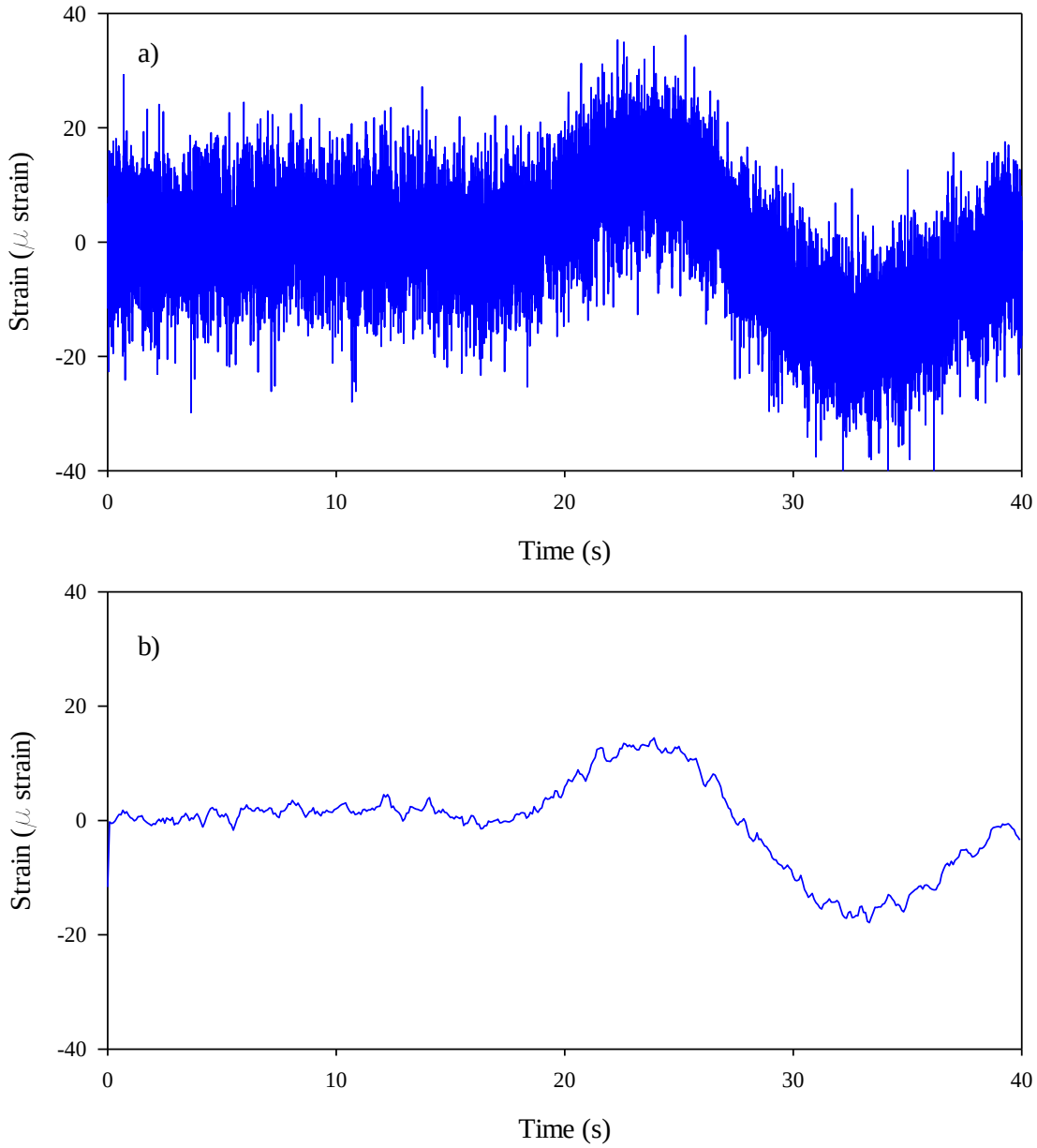

Figure 4.16 Typical strain gauge reading from truck static load test: a) before smoothing, and b) after smoothing.

Figure 4.20 shows the readings of three strain gauges attached near the soffit of the bridge girders and aligned transversely at one-quarter of the span from the north pier of the central span (Figure 3.5). These readings were logged while the test truck travelled over the bridge on the left lane in the northbound direction. Beam participation factors, which describe how load is shared between girders, can be deduced from Figure 4.20,

although this was not done as part of this study. The strain data show consistent trends in all three girders, suggesting that load is, in fact, being distributed amongst the girders.

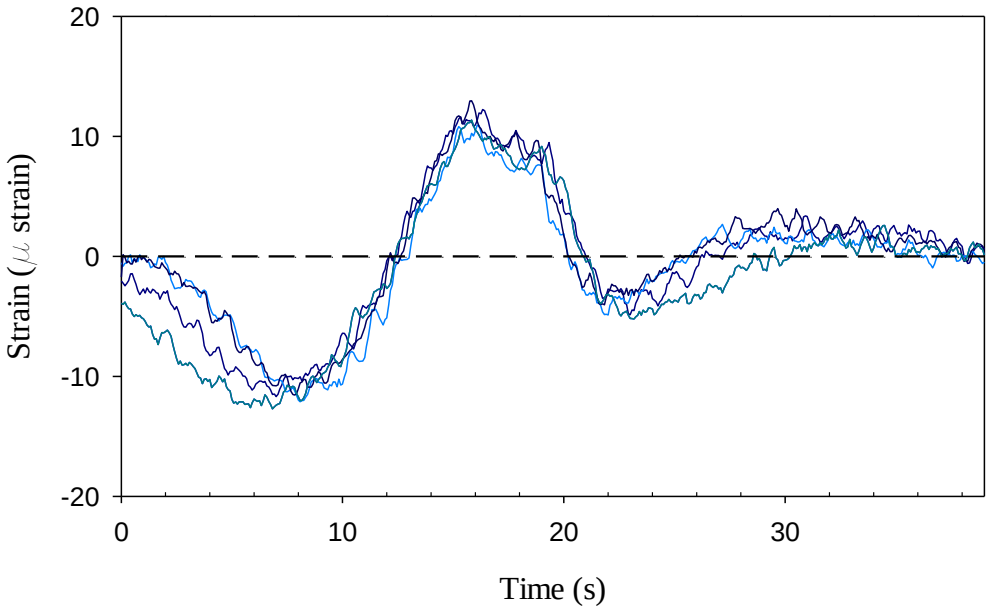

Figure 4.17 Strain signals from the bottom strain gauge of the second strain gauge cluster from the north on the east side of the bridge, obtained from four repeated tests.

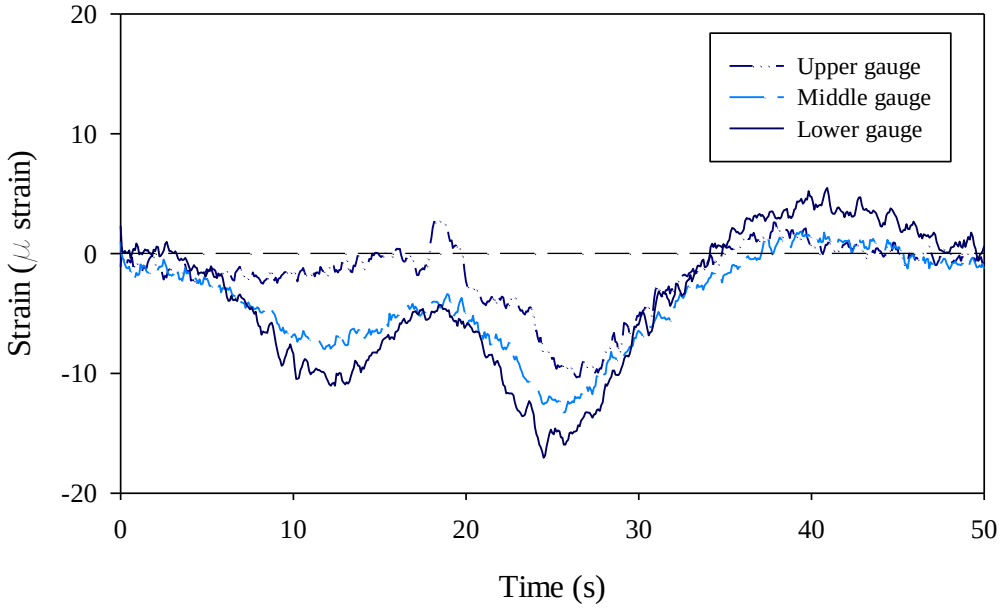

Figure 4.18 Readings of a cluster of strain gauges near the bridge north pier support.

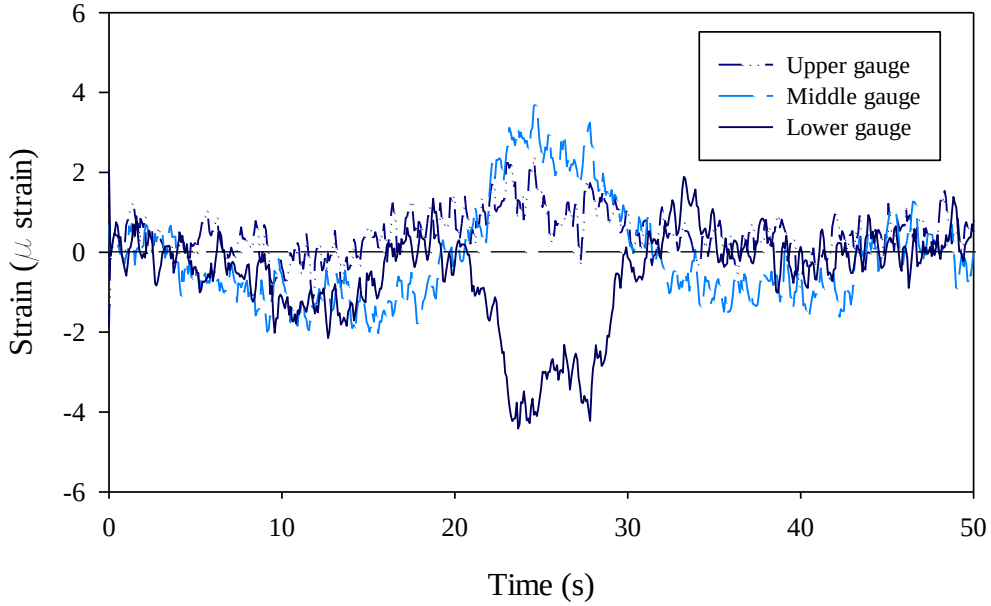

Figure 4.19 Readings of a cluster of strain gauges near the bridge midspan.

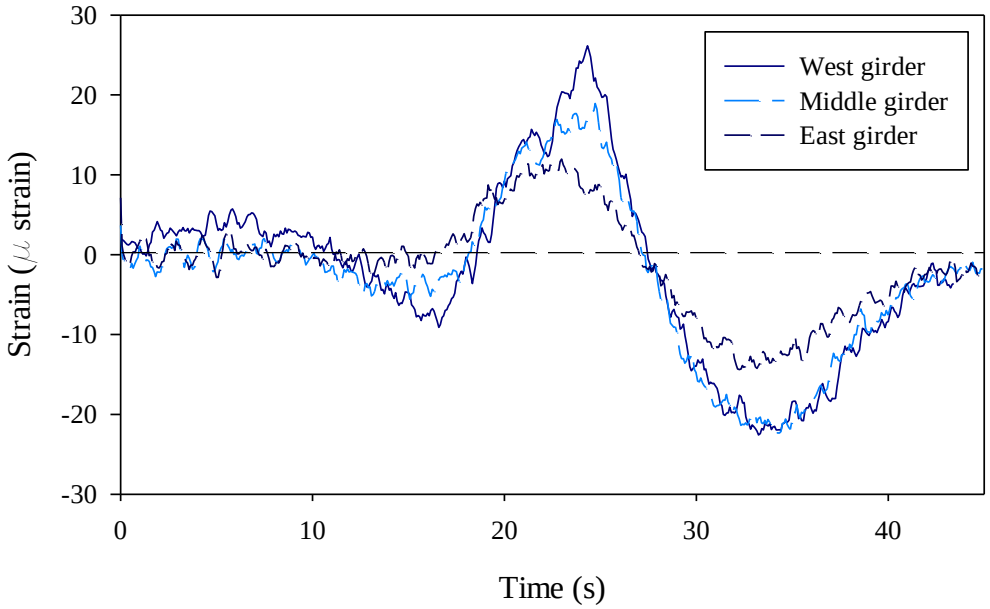

Figure 4.20 Strain gauge readings showing relative response of the bridge girders.

4.4 RESULTS OF THE IMPACT EXCITATION TEST AT THE BROADVIEW BRIDGE

The Broadview Bridge was tested using two levels of impact excitation applied by a Heavy Weight Deflectometer (HWD), and ambient excitation, as detailed in Section 3.6.3.2.

One advantage of the HWD tests was that the efficiency of the testing procedure made it possible to complete a large number of test setups and repetitions in the course of a single day, with the whole test completed in several hours. However, the quality of the results was impaired by the fact that multiple hits were noticed during the test as the drop weight rebounded, meaning that a simple impulse loading pattern was not achieved. Evidence suggesting the existence of these multiple hits can be seen in Figure 4.21. Figure 4.21a shows the acceleration time history of the reference accelerometer due to a 50 kN drop weight force, while Figure 4.21b shows the acceleration time history of the reference accelerometer due to a 25 kN drop weight. As seen here, the multiple hits were more prominent for the 50 kN drop weight.

On the other hand, the repeatability of the measurements was very good, with little variation apparent between successive readings for a specific set up. Figure 4.22 shows the Auto Power Spectra (APS) of the reference accelerometer for ten impact events due to the 25 kN drop weight. These APS were normalized by dividing their respective time signals by their root mean square values (RMS), so that they could be compared without considering event intensity.

It is clear from Figure 4.22 that the readings exhibited very little variation in frequency content or amplitudes, which is an important factor in the successful application VBDD. Figure 4.22 shows similar results to Figure 4.14 for the spring-hammer test on the Hudson Bay Bridge. It should be noted here that the APS contains information regarding the relative vibration amplitude over a range of frequencies, but it has no information regarding the phase relationship within the measured signal.

If more than a single impact occurs, as was observed in the Broadview testing, the Fourier transform of the pulse force will no longer produce a uniform spectrum over the desired range of frequencies; instead, the spectra of the repeated pulses will tend to attenuate or reinforce each other at certain frequencies, creating ripples or deep notches

in the force spectrum. This, in turn, would effectively degrade the quality of the measured signal by creating low signal-to-noise ratios in the force spectrum at the ripple locations (ISO 7626-5, 1994). This problem is more severe in output only modal testing, and has less effect on input-output tests where the input force is measured.

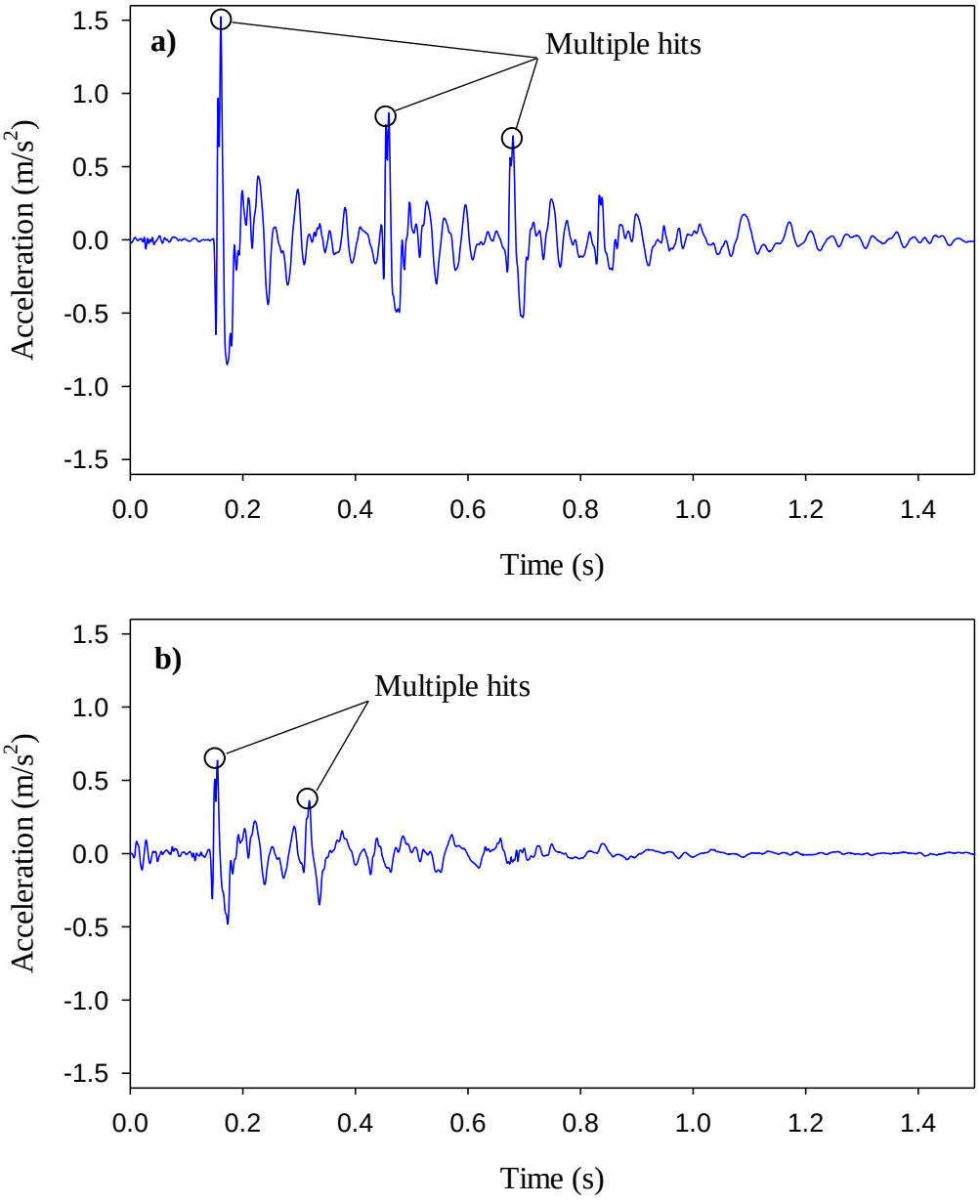

Figure 4.21 Acceleration-time history of reference accelerometer on the Broadview bridge due to HWD tests: a) 50 kN drop weight, and b) 25 kN drop weight.

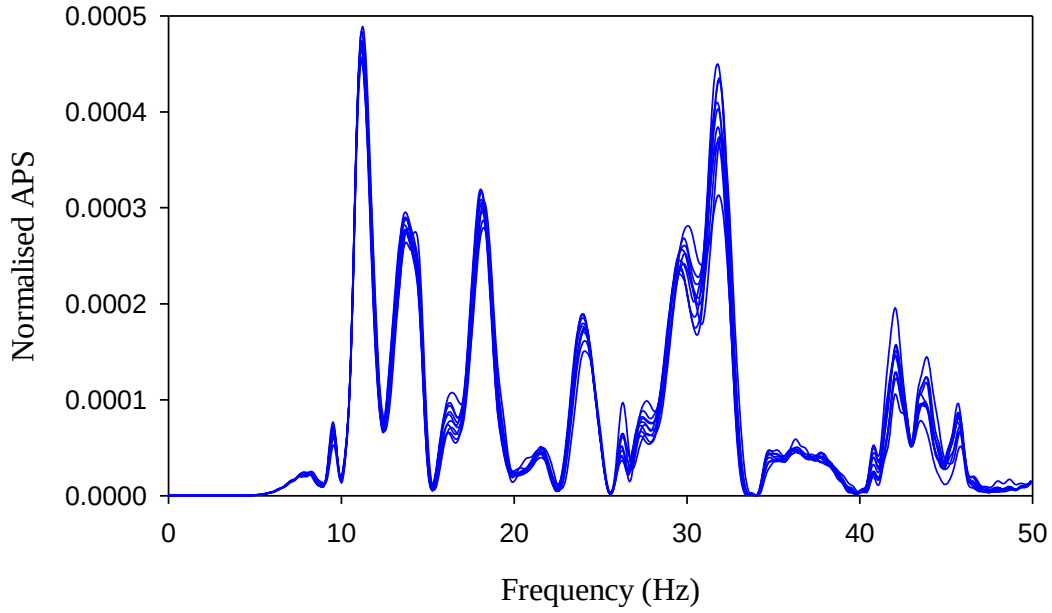

Figure 4.22 Superimposed normalised auto power spectra of readings from 10 impact events measured by the reference accelerometer on the Broadview bridge.

One way to reduce the effect of multiple hits is to reduce the magnitude of the impact force, so as to avoid the second and subsequent impacts altogether, or at least reduce their magnitude, so that their effect on the force spectrum is minimised (ISO 7626-5, 1994). This effect can be noticed when comparing the response to the 25 kN drop weight (Figure 4.21b) to that caused by the 50 kN drop weight (Figure 4.21a), as the response to the 25 kN drop weight exhibited fewer pronounced multiple hits.

The SSI method, although more involved, was used for extracting the modal properties of the Broadview Bridge, as it tends to be more robust than the peak picking method in filtering noise and interference from measured data. Results from the 50 kN drop weight tests suggested first and third natural frequencies of 9.697 Hz and 13.33 Hz, respectively; the second mode could not be reliably detected in these results. On the other hand, the 25 kN drop weight test could excite the second and third natural frequencies only, at measured frequencies of 11.17 Hz and 13.9 Hz, respectively. The difference in the modes detected between the 25 kN and the 50 kN drop weight tests may be attributed to the difference in the nature of multiple hits associated with each level of excitation (Figure 4.21), which may have had a different effect on the various modes for each

excitation level. Ambient excitation was found to excite the bridge's first and second natural frequencies at 9.526 Hz and 11.65 Hz, respectively (Table 4.3).

It is worth mentioning that the standard deviation of the natural frequencies calculated using this type of impact excitation was found to be higher than that shown in for the Hudson Bay bridge, which was determined using either truck excitation, or spring-hammer excitation. For example, the coefficient of variation for the first natural frequency of the Hudson Bay bridge was 0.65% for truck excitation (Table 4.1) and 0.542% for impact excitation (Table 4.2), in comparison with 2.66% for the same mode of the Broadview bridge (Table 4.3). It is understandable that, since the natural frequencies of two different bridges are being compared, the comparison may be considered as qualitative only.

Table 4.3 Statistical characteristics of measured natural frequencies for the Broadview bridge.

Mode no.	50 kN impact excitation			25 kN impact excitation			Ambient excitation		
	Freq. (Hz)	σ* (Hz)	CV† %	Freq. (Hz)	σ (Hz)	CV %	Freq. (Hz)	σ (Hz)	CV %
1	9.697	0.258	2.66	---	---	---	9.526	N.A	N.A
2	---	---	---	11.166	0.194	1.74	11.650	N.A	N.A
3	13.327	0.127	0.95	13.898	0.160	1.15	---	N.A	N.A

* σ = Standard deviation, † CV = Coefficient of variation.

It should be noted that the Broadview bridge is more rigid than the Hudson Bay bridge, which may have increased the bridge's susceptibility to multiple impact hits. The effect of multiple hits on the quality of the measured signal can be shown in terms of the coefficient of variation of the modal amplitudes at measurement points. For example, the coefficient of variation of the 1st mode amplitudes due to 50 kN impact excitation ranged from 8.0% to 148.7%, which was higher than the coefficient of variation calculated in Section 4.2.3 for the Hudson bay Bridge (1.4% - 5.6% due to truck excitation, or 3.1%-7.21% for spring-hammer excitation with a rubber pad), as listed in Appendix F. This increase in the coefficient of variation for the calculated modal amplitudes of the Broadview bridge in comparison to those of the Hudson Bay bridge may be attributed to the multiple hits of the HWD, which caused an uneven energy input in the bridge excitation at different frequencies, and phase shifting in the bridge

vibration. This, in turn, resulted in apparently complex extracted modes shapes, thus reducing their quality. Similar to what was done for the Hudson Bay bridge, modal amplitudes were scaled according to the reference accelerometer, which was assigned an amplitude of unity (1.0). A complete listing of modal amplitude properties for the different excitation types are listed in Appendix F.

By examining the results of the tests conducted on the Broadview bridge, it can be noticed that the quality of modes shape calculated from the impact excitation response, based on the phase angle of the modal amplitude (see explanation in Section 4.2.4) were comparatively better than those calculated using ambient excitation. Maximum mode phase angle differences were 46.0°, 61.0°, and 97.9° for 50 kN impact excitation, 25 kN impact excitation, and ambient excitation respectively. This may be attributed to the signal-to-noise ratio associated with each type of excitation. On the other hand, comparing those results to the corresponding findings from the spring-hammer excitation on the Hudson Bay bridge indicates that the mode phase angle relationship for various sensor locations on the Broadview bridge ranged from 0.36° to 56.5°, as opposed to 0.05°-1.61° for the Hudson Bay bridge. This suggests that the modal properties calculated for the Broadview bridge were of lesser quality than those calculated for the Hudson Bay bridge. Again, this may be attributed primarily to the multiple hits problem associated with the HWD machine. The test results are listed in Appendix F.

Figure 4.23 shows the first mode of the Broadview bridge, with a fundamental frequency of 9.967 Hz, generated using 50 kN impact excitation, while Figure 4.24 shows the second mode of the bridge at 11.17 Hz generated using 25 kN impact excitation. Finally, Figure 4.25 shows the first mode of the bridge at 9.526 Hz, generated using ambient excitation. Examining these figures confirms that these mode shapes are of inferior quality compared to those calculated for the Hudson Bay bridge using a spring-hammer, as shown in Figure 4.13. It difficult to assess the type of mode shape (flexural, torsional, etc.) from examining these figures.

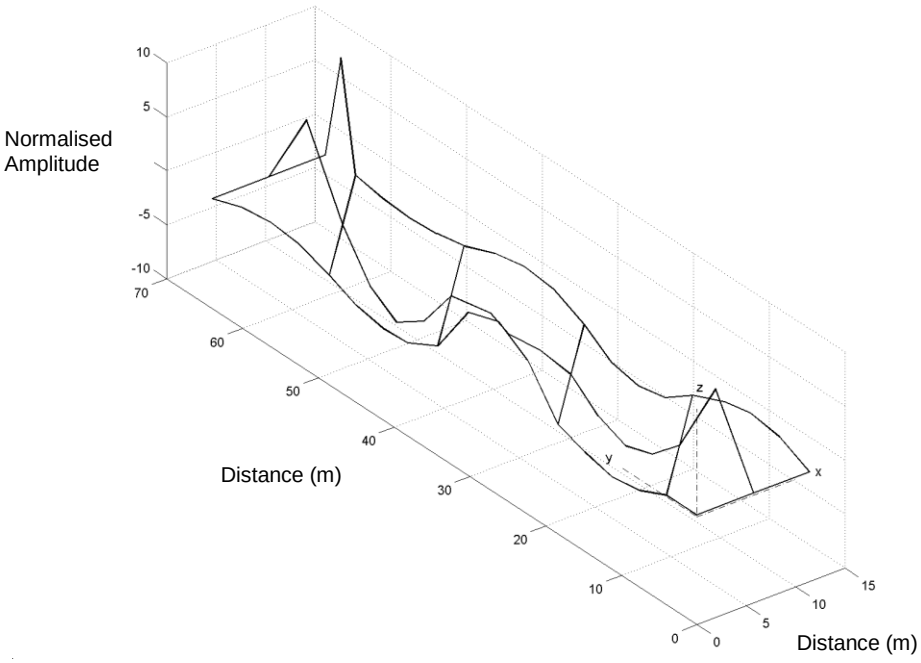

Figure 4.23 First mode of the Broadview Bridge (9.967 Hz) calculated from 50 kN impact excitation.

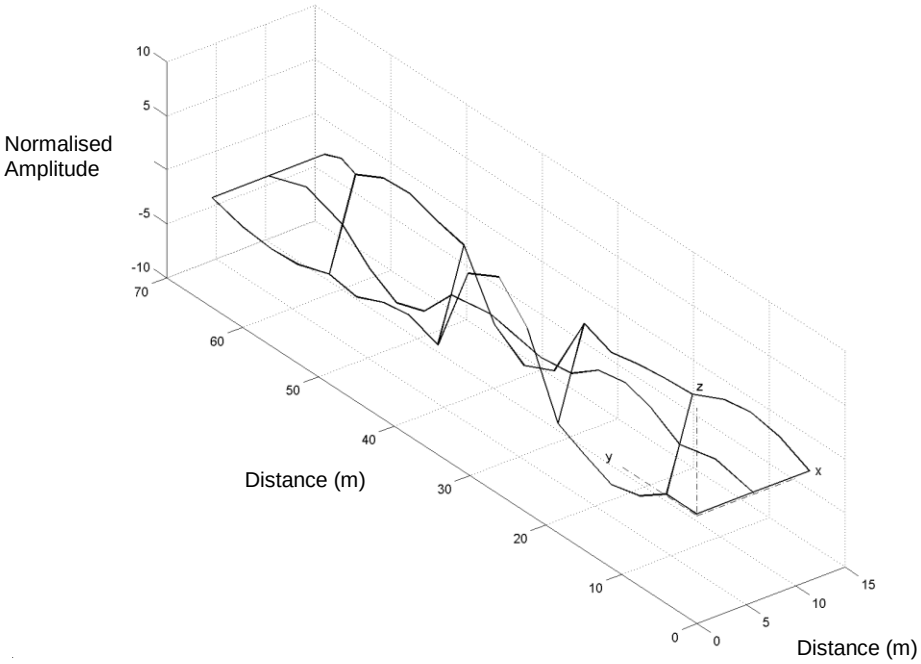

Figure 4.24 Second mode of the Broadview Bridge (11.17 Hz) calculated from 25 kN impact excitation.

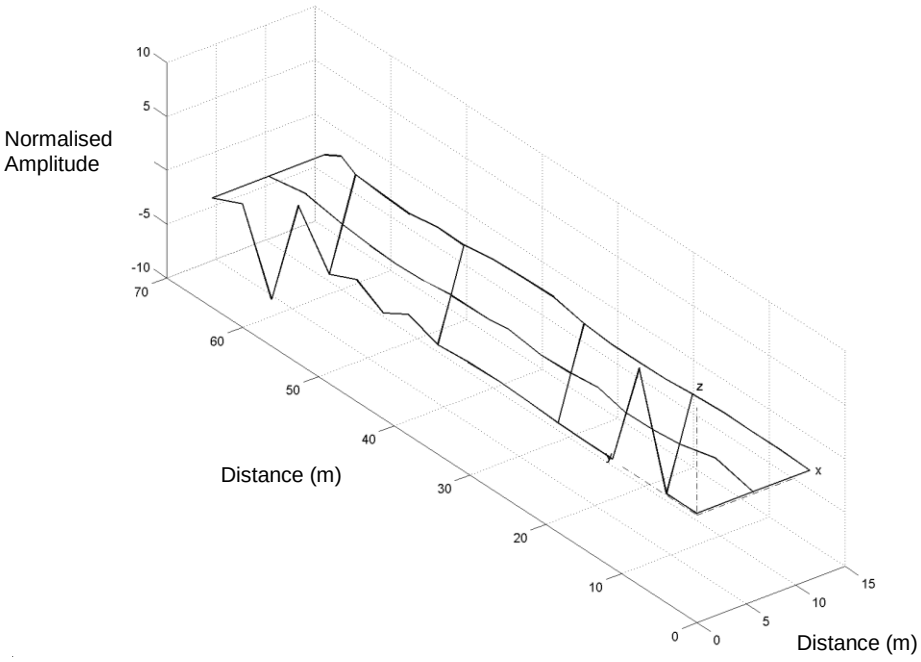

Figure 4.25 First mode of the Broadview Bridge (9.526 Hz) calculated from ambient excitation.

5 NUMERICAL SIMULATION OF DYNAMIC EXCITATIONS

5.1 OVERVIEW

In this chapter, the results of different numerical simulations are presented and discussed. These numerical simulations were carried out using a calibrated FE model of the Hudson Bay bridge as the basis for analyses using different dynamic excitation methods. The purpose of these simulations was to study the effect of the types of dynamic excitation on the extracted modal properties. The effect of uncertainty (or noise), whether it was contained in the input force or in the measured bridge response (output), was also evaluated. The SSI method was used for all modal analysis in the numerical study.

5.2 FE MODEL UPDATING OF HUDSON BAY BRIDGE

The FE model was manually calibrated to reproduce the modal properties (natural frequencies and mode shapes) extracted from site measurements as closely as possible. The parameters adjusted in the calibration process were primarily the effective modulus of elasticity of the concrete, adjusted to allow for the presence of cracking and reinforcing steel, and the support restraint provided at the bridge piers and abutments. The concrete modulus of elasticity was calibrated to 35,200 MPa for the concrete girders and 25,000 MPa for the other parts of the bridge. This difference in the values of the modulus of elasticity can be attributed to two factors. First, there is likely less cracking in the bridge girders due to apparent arching action in the girders that transfers a portion of the loads to the support by compression rather than bending; such arching was inferred from strain gauge readings. Secondly, the girders are more heavily reinforced than the deck, and thus experience less cracking and have higher transformed section properties. In addition, Poisson's ratio for concrete was set equal to 0.2, and concrete density was 2450 kg/m^3.

The support conditions were adjusted by introducing spring restraints to simulate the partial locking of the pinned and roller supports, as explained in Section 3.3. This adjustment was necessary to calibrate the FE model so that its natural frequencies and mode shapes matched the actual bridge dynamic properties that were measured on site as closely as possible. In addition, the support restraint from springs helped reproduce the observed arching behaviour mentioned previously. The introduced spring constants were 15,500 kN/m for longitudinal springs and 10,000 kN.m/rad for rotational springs. The mode shapes for the lowest six modes, as generated by the FE model, are shown in Figure 5.1, although only the first three modes were considered in the bridge calibration.

A comparison of representative natural frequencies extracted from the measured data and those calculated from the calibrated FE model is presented in Table 5.1 for the lowest three vibration modes of the bridge. It is evident that the observed agreement was excellent for all three natural frequencies (0.2%, 3.3% and 0.2% differences, respectively).

To quantify the level of agreement between measured and FE generated mode shapes, Modal Assurance Criteria (MAC) (Ewins 2000) values were calculated. The MAC value quantifies the least squares linear fit between two different mode shapes, with a MAC value of one indicating perfectly correlated modes and a value of zero indicating perfectly uncorrelated (orthogonal) shapes. As shown in Table 5.1, the computed MAC values indicate excellent agreement between calculated and measured responses for the fundamental mode shape, as well as good correlation for the two higher modes (MAC > 0.94). The high degree of agreement between the FE and the measured dynamic responses suggests that the model provided a reasonable representation of the dynamic response of the actual bridge.

Figure 5.2 compares the measured strain values at different locations on the middle span near the girders' soffits due to the loading induced by the test truck, along with corresponding strain at the same locations calculated from the FE analysis. In the FE analysis, the test truck was positioned near the centre of the middle span and on the east side facing south. The missing data points in Figure 5.2 correspond to locations where strains could not be measured. At these locations the recorded strain values were very

high, suggesting that these gauges crossed over a crack in the concrete; thus readings were no longer representative of the strain in the concrete but of the width of the crack opening.

It can be seen from Figure 5.2 that the agreement between analytical and measured strain values is reasonable. Most readings were seen to exhibit less than 10% difference from calculated values, which is considered an acceptable level of accuracy (Bridge Diagnostics 2003), while the strain values at few other locations were off by more than 10%. In general, though, it can be stated that there is good agreement between the response of the dynamically updated FE model and that of the bridge itself. The relative participation of the three girders can also be deduced from Figure 5.2, as the edge girder under the test truck (Figure 5.2a) is the most highly strained, while the edge girder on the other side of the bridge is strained at the lowest level (Figure 5.2c).

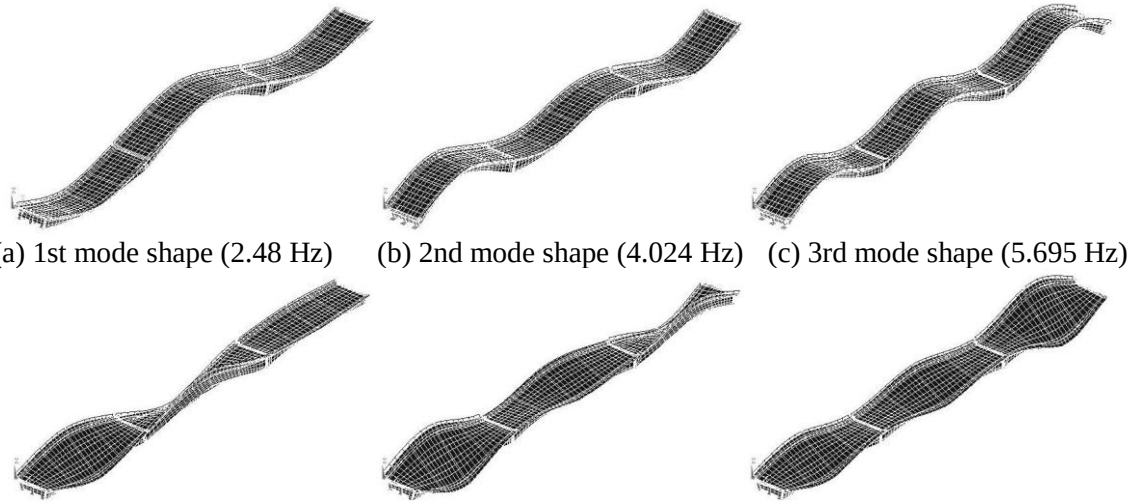

(a) 1st mode shape (2.48 Hz) (b) 2nd mode shape (4.024 Hz) (c) 3rd mode shape (5.695 Hz)

(d) 4th mode shape (5.875 Hz) (e) 5th mode shape (7.257 Hz) (f) 6th mode shape (7.710 HZ)

Figure 5.1 Lowest six vibration mode shapes generated from the FE model.

Table 5.1 Comparison of field measured natural frequencies to those calculated from a calibrated FE model, for Hudson Bay bridge.

Mode No.	Natural Frequencies (Hz)			MAC
	Measured on Site	Calculated using FE	Difference %	
1	2.485	2.480	0.2	0.9988
2	4.160	4.024	3.3	0.9594
3	5.706	5.695	0.2	0.9425

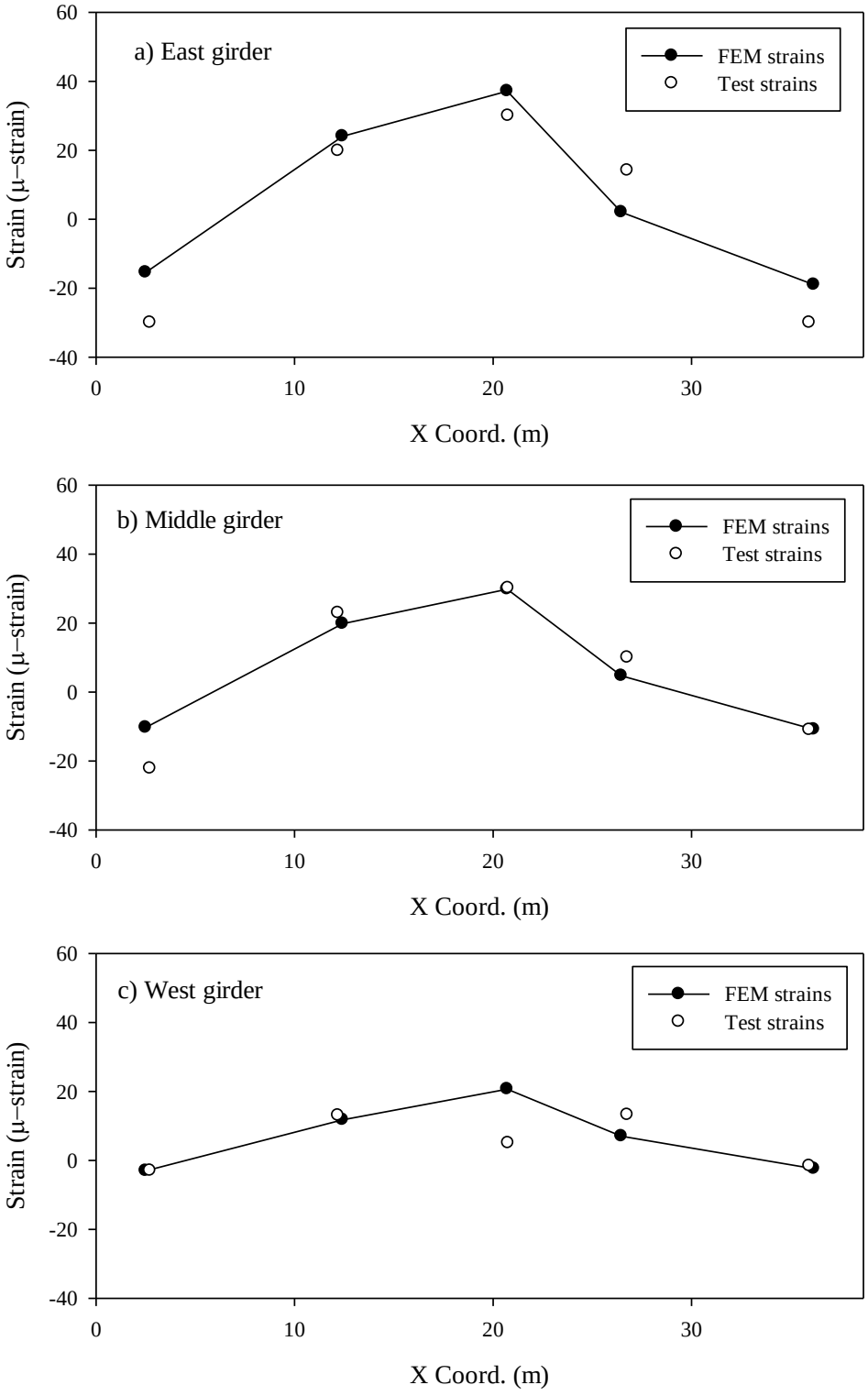

Figure 5.2 Comparison between strains calculated from FE analysis and a corresponding set of measured strains on the bridge using a test truck; strain gauge locations are near the soffit of the girders, on the (a) east girder, (b) middle girder, and (c) west girder.

5.3 COMPARISON OF DIFFERENT EXCITATION METHODS AND THE EFFECT OF UNCERTAINTY

5.3.1 Forced Harmonic Excitation

Harmonic excitation with an amplitude of 10 kN was simulated and applied to the bridge FE model at a stationary location. The harmonic force was applied at a location that corresponded to the location of the reference accelerometer in field tests, as detailed in Section 3.7.2. The bridge acceleration response spectrum under harmonic excitation with a forcing frequency equal to the bridge's first natural frequency is shown in Figure 5.3, plotted here at the location of the reference accelerometer. Figure 5.3a and Figure 5.3b show the bridge response spectrum to harmonic excitation that was defined without noise, i.e. perfectly harmonic, and with a white noise superimposed on the forcing function time history having a variance equal to 2% of that of the harmonic signal, respectively. It can be seen from Figure 5.3 that this level of noise had little or no effect on the bridge response.

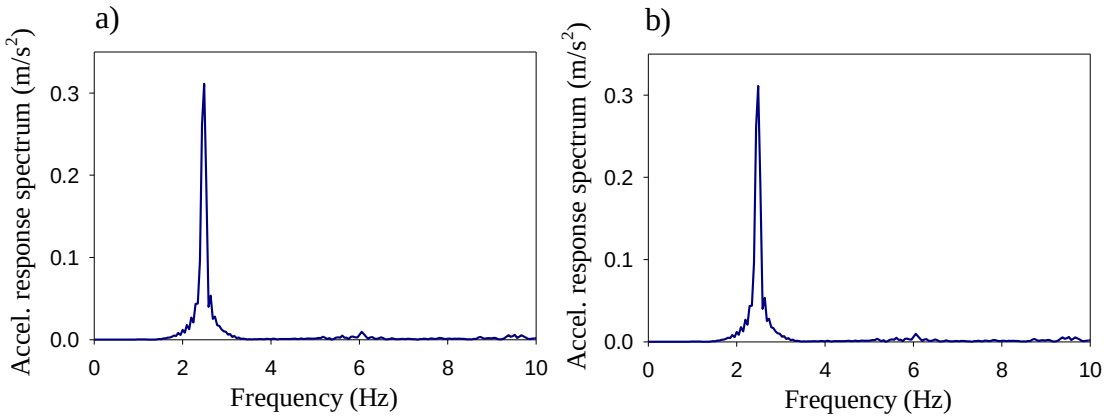

Figure 5.3 Bridge response acceleration spectrum due to harmonic excitation at the location of the reference accelerometer: a) excitation without noise, and b) excitation with 2% noise.

Table 5.2 summarises the MAC values for the first mode shape based on a comparison between mode shapes extracted from the time domain analyses with varying levels of uncertainty in the harmonic loading definition and two different reference mode shapes: one obtained directly from an eigenvalue analysis, and the second extracted from the calculated time domain response in which there was no uncertainty (noise) in the definition of the harmonic loading. The first row in Table 5.2 presents a comparison of

calculated mode shapes derived from the time domain analyses to the corresponding eigenvector, while the second row compares the same mode shapes to that derived using time domain analysis with no noise in the excitation definition.

Table 5.2 MAC values for 1st mode shape derived from harmonic loading (noise in input).

Reference mode shape	MAC values				
	No noise	1% noise	2% noise	5% noise	10% noise
Eigenvalue analysis	0.9923741	0.9924726	0.9924514	0.992405	0.9923694
Time domain (no noise)	1.0	0.9999979	0.9999991	0.99999992	0.99999971

It is evident that the level of noise in the harmonic loading had little effect on the reliability of the resulting fundamental mode shapes. This result is not unexpected since the random fluctuations in the superimposed noise were spread uniformly over a wide band of frequencies, meaning that the contribution to the excitation specifically at the fundamental natural frequency was small, despite the relatively large total variance levels in the noise.

For this particular bridge, forced harmonic excitation did not yield satisfactory definitions of the second and third mode shapes since the corresponding natural frequencies were relatively close together (4.0 Hz and 5.7 Hz) and the corresponding modal response contributions were of comparable magnitudes. MAC values for the 2nd and third mode shapes extracted from harmonic loading results were found to be 0.558295 and 0.236198, respectively, when compared to corresponding mode shapes derived from the eigenvalue analysis. The close proximity of these natural frequencies and the comparable magnitudes of modal response contributions made it difficult to differentiate the modal responses, and thus to identify the true mode shapes. Instead, modal parameter estimation routines yielded apparently complex mode shapes (actually operational deflected shapes) resulting from a combination of the two real-valued modes responding at the same frequency (i.e. the forcing frequency) but at different phase angles. This suggests that caution should be exercised when interpreting responses from forced harmonic excitation in the vicinity of closely spaced natural frequencies.

Table 5.3 shows the results when noise was added to the output displacement time history instead of to the excitation. The level of noise in Table 5.3 is expressed as a

percentage of the variance in the initial response signal variance prior to the addition of noise. Here also, the level of noise had little effect on the reliability of the resulting fundamental mode shapes. This indicates that, when successful in identifying a mode shape, harmonic excitation produces robust results, even in the presence of significant measurement uncertainty.

Table 5.3 MAC values for 1st mode shape derived from harmonic loading (noise in output).

Reference mode shape	MAC values				
	No noise	1% noise	2% noise	5% noise	10% noise
Eigenvalue analysis	0.994978	0.995400	0.994900	0.995500	0.994900
Time domain (no noise)	1.000000	1.000000	1.000000	1.000000	1.000000

5.3.2 Random Excitation

Random forced excitation was applied as a stationary concentrated load with a random time history defined such that the peak magnitude was 10 kN, as described in Section 3.7.3. The random force was applied at a location that corresponded to the location of the reference accelerometer in field tests (see Figure 3.25). Figure 5.4a shows the bridge's acceleration response spectrum, at the location of the reference accelerometer, during the period when the random force was being applied to the bridge. On the other hand, Figure 5.4b shows the response spectrum during free vibration following the random excitation. By examining Figure 5.4b it can be seen that, unlike the forced response in Figure 5.4a, peaks at the natural frequencies are clearly evident and smooth, and that no spurious non-resonant peaks are present, as the interference from the exciting force was no longer apparent in the response spectrum. This interference existed during the period of excitation because, although the random excitation should exhibit a nominally uniform forcing spectrum, natural variability in the single, short duration event will inevitably introduce non-uniform fluctuations in the force spectrum at frequencies other than the resonant frequencies.

Table 5.4 presents a comparison between the lowest three natural frequencies extracted from the forced and free vibration phases, averaged over the ten random loading events lasting 10 seconds each, along with those determined from an eigenvalue analysis; also shown are the corresponding standard deviations (σ) of the extracted natural frequencies,

as well as the error in the natural frequencies relative to the eigenvalue results. From Table 5.4, it can be seen that the natural frequencies extracted from the free vibration phase were consistently closer to the eigenvalue results. Perhaps more significant from a VBDD perspective, though, is that the standard deviations of the free vibration results were several orders of magnitude lower, indicating that a much more reliable measure of the true natural frequencies was achieved.

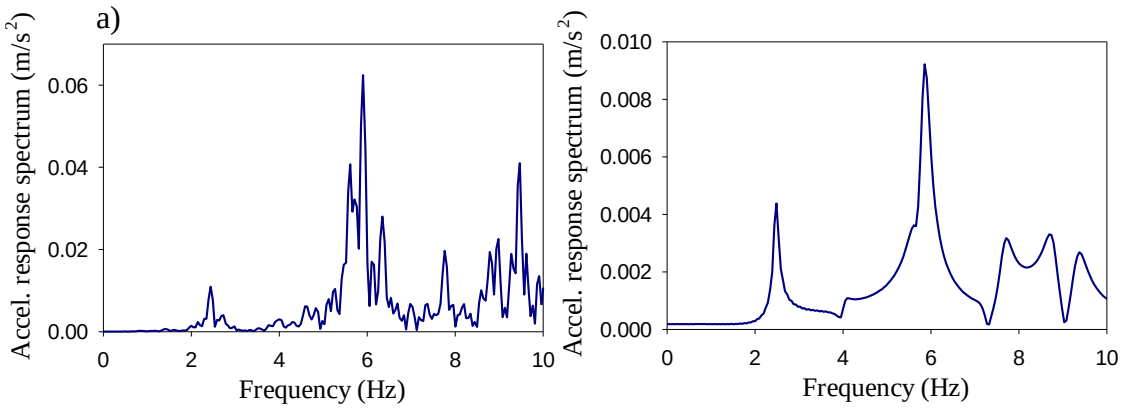

Figure 5.4 Bridge response acceleration spectrum due to random excitation: a) during forced excitation phase, and b) free vibration phase.

Table 5.5 summarises the MAC values comparing mode shapes derived from an eigenvalue analysis of the bridge model with averaged results extracted from the forced and free vibration phases of the ten random loading events. It is evident that better correlation was achieved using the free vibration data rather than those from the forced vibration, particularly for the higher modes. The MAC value for the fifth mode shape was found to be very low (0.0161) during the forced vibration, perhaps indicating that the location and/or frequency content of the random applied load was not effective in exciting this mode.

Table 5.4 Natural frequencies using random dynamic excitation.

Mode	Natural Frequencies [Hz]						
	Eigenvalue analysis	Forced random phase			Free vibration phase		
		Avg.	σ	Error [%]	Avg.	σ	Error [%]
1	2.480	2.477	0.047	0.12	2.479	1.542E-07	0.04
2	4.024	4.050	0.072	-0.65	4.019	1.488E-06	0.12
3	5.695	5.600	0.117	1.67	5.680	1.696E-06	0.26

Table 5.5 MAC values of random excitation.

Excitation phase	Mode number						
	1	2	3	4	5	6	7
Forced vibration	0.9957	0.6142	0.3244	0.9338	0.0161	0.7632	0.9969
Free vibration	0.9957	1.0000	1.0000	1.0000	1.0000	1.0000	1.0000

From these results, it can be seen that the modal properties extracted from the bridge free vibration response are of higher quality than those extracted from the bridge's response during random excitation. This shows that, when the random loading is removed from the bridge, the spurious influence from the excitation forces are also removed and the bridge is left to vibrate at its natural frequencies only, leading to the high consistency of modal properties extracted from the bridge free vibration response.

5.3.3 Impact Excitation

Simulating the effect of a drop weight test in the field, excitation from a short duration impact can be used to induce a force that has a flat spectrum in the frequency range of interest. In the present numerical study, the impact load-time history was defined as a half sine wave with a duration of 10 milliseconds and an amplitude of 10 kN (ISO 1994, Pavic et al. 1997), as shown in Figure 3.29. The subsequent bridge response was calculated over a 10 second period. As with the harmonic forcing discussed previously, the effect of random fluctuations in the impact load time history was investigated, but found to have little influence on estimates of either the natural frequencies or mode shapes for the lower modes of interest in this study.

An example bridge acceleration spectrum, at the location of the reference accelerometer, in response to forced impact excitation is shown in Figure 5.5, where Figure 5.5a and Figure 5.5b show the bridge response spectrum to impact excitation defined without noise, and with 2% noise, respectively. It can be observed from Figure 5.5 that levels of noise up to 2% did not have much effect on the bridge response. It is also noted from Figure 5.5 that the amplitudes of the peaks of the bridge response spectrum to impact excitation with noise are higher than without noise. This may be explained by examining Figure 3.30, from which it can be seen that, in this case, the superimposed random noise increased the peak amplitude of the impact force, thus increasing the energy imparted by the impact excitation of the structure.

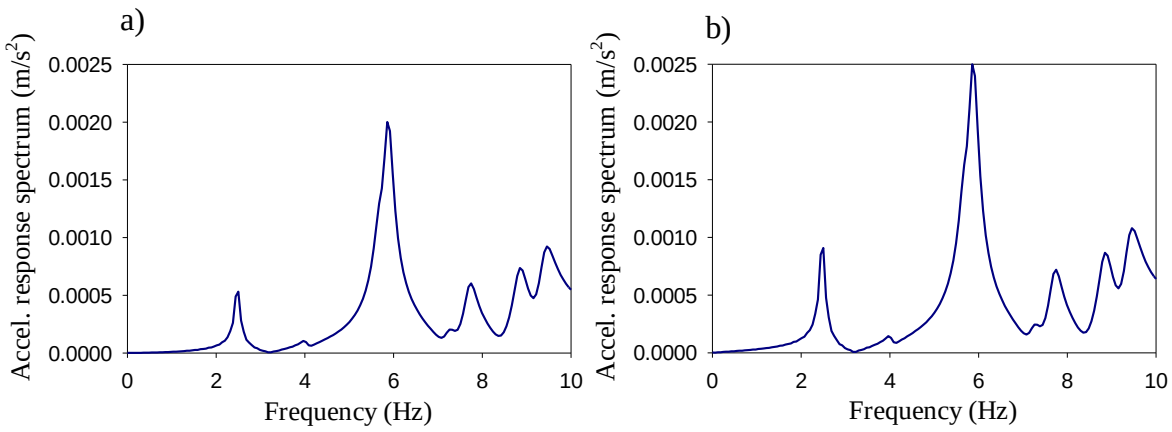

Figure 5.5 Bridge response acceleration spectrum due to impact excitation: a) excitation without noise, and b) with 2% noise.

Table 5.6 shows that the modal properties extracted from the impact loading response were found to be in good agreement with the eigenvalue results, with errors in the natural frequencies and mode shape MAC values for the lowest two modes being comparable to results derived from the free vibration phase following random loading (Table 5.4 and Table 5.5). Results for the third mode were less accurate, though, having a MAC value for the 3rd mode shape of 0.627, which would not be adequate for VBDD applications. This lower MAC value for the third mode may be attributed to the fact that the location of the forcing function was near a nodal point of the third mode shape (Figure 3.25 shows the location of the reference accelerometer, where the impact force was applied, and Figure 4.12c shows the third mode shape).

Table 5.6 Natural frequencies and MAC values from impact excitation.

Mode	Natural frequency			MAC values
	Eigenvalue [Hz]	Impact [Hz]	Error [%]	
1	2.480	2.472	0.32	0.9957
2	4.024	4.006	0.45	0.9902
3	5.695	5.609	1.51	0.6270

The effect of random fluctuations in the response, simulating noise in the measured signal, is shown in Table 5.7. It can be seen from Table 5.7 that the first mode of vibration was not affected to an appreciable extent by the introduced noise, with a maximum difference in the estimated natural frequency of less than 0.013 Hz (0.52 %) and a standard deviation equal to 0.0156 for the 5% noise level. On the other hand, the

standard deviations of second and third natural frequencies showed increased variation as the level of noise increased to 5 %; in fact, the second mode was not detectable at a noise level of 5%. The maximum difference in the third natural frequency was 0.463 Hz (8.33 %) with a standard deviation equal to 0.2797, which was experienced for the 5% noise level.

Similar observations can be made regarding the changes in MAC values with an increasing level of noise superimposed on the extracted responses (Table 5.8). The first mode shape did not seem to be affected by the introduced noise. The second and third mode shapes, on the other hand, were affected adversely by the increased level of noise, with the second mode not being detectable at the 5% noise level, and the third mode having a low MAC value (0.439) at the 2% noise level.

Table 5.7 Natural frequencies and standard deviations from impact excitation with random noise in measured output.

Pulse force	Natural frequency (Hz)					
	Mode 1		Mode 2		Mode 3	
	Avg.	σ	Avg.	σ	Avg.	σ
FEM model	2.480	-	4.024	-	5.695	-
no noise	2.478	-	4.019	-	5.677	-
1% noise	2.483	0.0123	4.153	0.1624	5.668	0.1089
2% noise	2.479	0.0194	4.130	0.1917	5.754	0.1182
5% noise	2.491	0.0156	-	-	6.140	0.2797

Table 5.8 MAC values from Impact excitation with random noise in measured output.

	Mode number		
Pulse force	1	2	3
no noise	0.9957	0.9986	0.9569
1% noise	0.9956	0.4890	0.5202
2% noise	0.9955	0.0319	0.4387
5% noise	0.9955	-	0.9787

From these results, it can be seen that noise induced in the input signal of impact excitation did not have much effect on the extracted modal properties. On the other hand, the output noise did reduce the quality of the extracted modal properties, although not for the first mode. With respect to VBDD application, it is apparent that the quality of

the first mode of the bridge was not significantly affected by the induced noise; therefore, it would be expected that impact excitation is a suitable source of excitation for the purpose of damage detection, particularly if only the fundamental mode is of interest.

5.3.4 Truck Excitation

5.3.4.1 Simplified truck model

In the simplified truck loading model, vertical wheel loads representing the truck under consideration were moved across the bridge at specified speeds along a straight path. The truck loading was applied on the bridge using the dynamic nodal loading method. Two truck loading configurations were used, PV1 and PV4, as detailed in Section 3.7.5. Figure 5.6 shows the acceleration-time history and the associated response spectrum at the location of the reference accelerometer due to truck PV4 crossing the bridge at 81 km/hr.

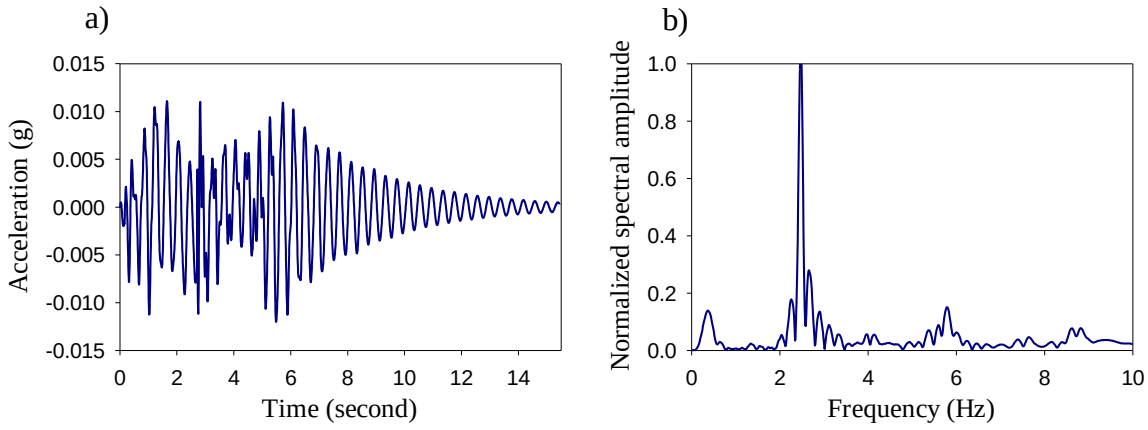

Figure 5.6 Bridge response to simulated truck PV4 crossing the bridge at 81km/h: (a) acceleration time history; and (b) normalized acceleration spectrum.

A summary of the lowest three natural frequencies derived from the truck-induced excitation using the simplified truck model, along with the MAC values for the corresponding mode shapes relative to the eigenvalue solution, are presented in Table 5.9. In general, the reliability of the modal properties extracted from the truck-induced response was comparable (or lower) to those based on the forced vibration phase of random loading, where the bridge response was taken while the random excitation force

was applied on the bridge, and significantly worse than those derived from the other excitation sources. Natural frequencies based on truck loading were found to differ from the eigenvalue results by 0.12-15.1%, 5.3-17.9%, and 0.16-4.9% for the 1st, 2nd and 3rd modes, respectively, depending on the truck loading case considered. Similarly, mode shape MAC values as low as 0.975 for the fundamental mode, and 0.546 and 0.738 for the 2nd and 3rd modes, respectively, were obtained.

Table 5.9 Natural frequencies and mode shape MAC values from simplified truck excitation model.

Analysis case	Natural frequency [Hz]			Mode shape MAC values		
	Mode 1	Mode 2	Mode 3	Mode 1	Mode 2	Mode 3
Eigenvalue	2.480	4.024	5.695	-	-	-
PV1 (54km/h)	2.483	3.719	5.704	0.9948	0.996	0.7375
PV1 (81km/h)	2.319	3.810	5.342	0.98	0.9446	0.745
PV4 (54km/h)	2.105	3.302	5.498	0.9754	0.5457	0.891
PV4 (81km/h)	2.511	3.672	5.417	0.994	0.9847	0.7782

The simplified truck loading cases were reanalysed using the same simplified truck loading model, but this time adding 10% of the axle loading as a sinusoidal variation acting at the first natural frequency of the bridge to simulate dynamic amplification due to vertical truck vibrations in a “body-bounce” (or uniform vertical oscillation mode), as detailed in Section 3.9.5. The acceleration-time history and the bridge response spectrum at the location of the reference accelerometer due to truck PV4, including the sinusoidal dynamic load, crossing the bridge at 81 km/hr, are shown in Figure 5.7. By comparing Figure 5.7 for truck excitation with the added sinusoidal component to Figure 5.6 for truck excitation without the added sinusoid, it can be observed that the contribution of higher modes were diminished for the case of truck excitation with added sinusoid. This can be attributed to the fact that motion due to the truck excitation with an added sinusoid was dominated by response at the fundamental frequency at which the sinusoidal forcing was acting.

The analysis results are summarised in Table 5.10, which shows the lowest three natural frequencies, along with the MAC values for the corresponding mode shapes relative to the eigenvalue solution. It can be seen from the results listed in Table 5.10 that the

reliability of the extracted modal properties was worse than for the simplified truck loading model without "body-bounce'. In fact, the second mode could not be detected. Similarly, the third mode was only detectable under one type of truck excitation (PV4 at 81 km/hr), for which the difference in the second natural frequency relative to the eigenvalue results was 9.7%, compared to a 4.9% difference under the same loading case, but without the superimposed sinusoidal force. However, the first mode results were comparable to the truck model without the sinusoidal force component.

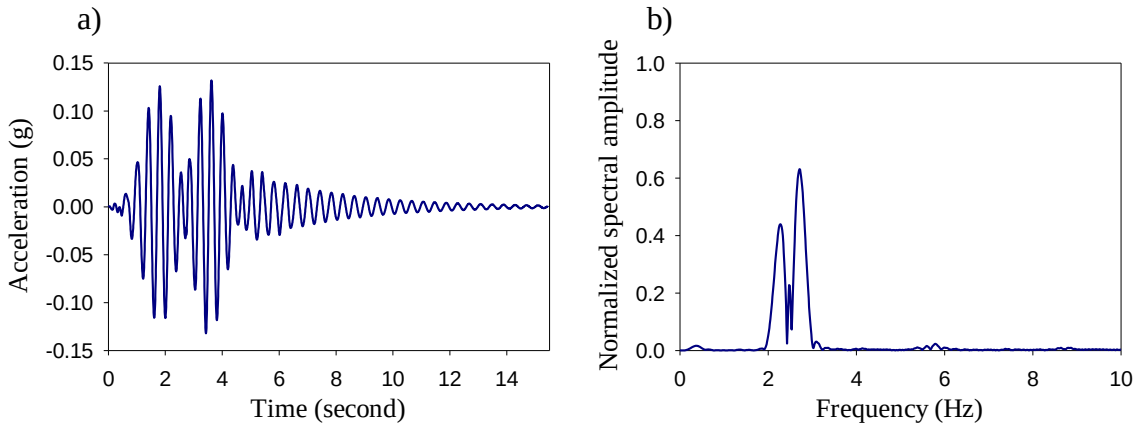

Figure 5.7 Bridge response to simulated truck PV4 plus sinusoid crossing the bridge at 81km/hr: (a) acceleration time history; and (b) normalized acceleration spectrum.

Table 5.10 Natural frequencies and mode shape MAC values from simplified truck excitation model plus sinusoid.

Analysis case	Natural frequency [Hz]			Mode shape MAC values		
	Mode 1	Mode 2	Mode 3	Mode 1	Mode 2	Mode 3
Eigenvalue	2.480	4.024	5.695	-	-	-
PV1 (54km/h)	2.307	-	-	0.9944	-	-
PV1 (81km/h)	2.529	-	-	0.9913	-	-
PV4 (54km/h)	2.311	-	-	0.9942	-	-
PV4 (81km/h)	2.389	-	6.248	0.9916	-	0.8739

The above results can be attributed to the strong interference of the truck loading characteristics with the resonant responses of the bridge, which made it difficult to separate forced and resonant responses during the modal analysis. In addition, superimposing a sinusoidal force acting at the bridge's first natural frequency on the truck loading time history encourages the bridge to vibrate predominantly at its first natural frequency, creating difficulty in detecting other modes. This is consistent with

the experimental bridge testing results described in Chapter 4, where Figure 4.1b shows the interference of the truck excitation with the bridge's free vibration, adding extra peaks to the bridge response spectrum that actually correspond to the truck dynamic loading characteristics and road roughness, and not to the bridge's properties.

5.3.4.2 Dynamic truck model

For the truck dynamic model, each tire was modelled as a two-degree of freedom damped spring-mass system (Figure 3.34), featuring two masses supported on a set of springs and dampers, representing the suspension system and body of the vehicle. Tire load was calculated as the vertical reaction of the system as the tire was displaced vertically due to the simulated roughness pattern. The tire loading from the dynamic truck model was applied on the bridge using the DNL method, as detailed in Section 3.9.5. The bridge response was simulated by exciting the bridge using the QS-660 truck model (Section 3.7.5).

Two road roughness profiles were used that were thought to be representative of the ranges in road surface conditions likely to be present at the Hudson Bay bridge site. The roughness profiles corresponded to two road classes, good and average, with $S_u(\kappa_0)$ values of $16*10^{-6}$ and $64*10^{-6}$ m^3/cycle, respectively, where $S_u(\kappa)$ is the displacement spectral density of the road roughness profile (Section 3.9.6). Two truck speeds were used, 54 km/hr and 81 km/hr, as in the previous simplified truck model studies.

Figure 5.8 shows the acceleration-time history and the bridge acceleration response spectrum at the location of the reference accelerometer due to truck QS-660 crossing the bridge at 81 km/hr, using a road roughness profile value $S_u(\kappa)$ equal to $64*10^{-6}$ m^3/cycle. By examining Figure 5.8, it can be seen that the simulated bridge response resembles the bridge response on site due to actual trucks, for example that shown in Figure 4.3. The bridge response spectrum in Figure 5.8b shows that the truck has excited the bridge over a wider frequency range compared to the response of the simplified truck models shown in Figure 5.6 and Figure 5.7. However, the dynamic model response range was mostly limited to 0-10Hz. Since this is the same range where most of the active bridge natural frequencies occur, the susceptibility of the bridge to excitation by a passing truck is evident.

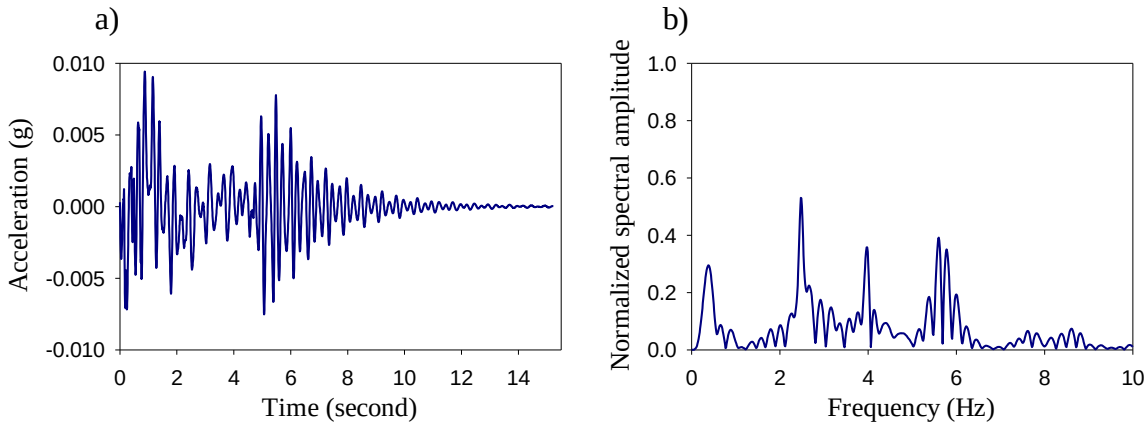

Figure 5.8 Bridge response to simulated truck QS-660 crossing the bridge at 81km/h, with road roughness, $S_u(\kappa_0)$, values of $64*10^{-6}$ m^3/cycle: (a) acceleration time history; and (b) normalized acceleration spectrum.

In general, the dynamic amplification factor (*DAF*) may be defined as:

$$DAF = \frac{\delta_{dyn} - \delta_{sta}}{\delta_{sta}} \qquad [5.1]$$

where δ_{dyn} and δ_{sta} are the peak dynamic and static deflections, respectively.

In calculating the *DAF*, the stiffness of the bridge was considered to be much larger than that of the vehicle; therefore, the bridge dynamic deflection was ignored, as detailed in Section 3.7.5. The values of the *DAF* for the axle spring-mass system, due to the dynamic interaction of this system with the road roughness profiles for different truck speeds and road roughness profiles are listed in Table 5.11. The *DAF* value was averaged over all the truck axles for each load case. It can be noticed from Table 5.11 that the largest *DAF* value was 0.04; this value was lower than the 10% of the axle load suggested by Chan and O'Conner (1990), or the values recommended by the Canadian Highway Bridge Design Code (CSA 2006), which range from 0.25 to 0.5. This implies that the *DAF* for roads with good surface conditions can be lower than the suggested design values; nonetheless, *DAF* code values take into account worse road conditions, potholes and bridge deck joints, which are expected to produce higher *DAF* values than those resulting from road roughness only.

Table 5.11 Dynamic load allowance resulting from dynamic truck loading model.

Truck speed, km/hr	Road Class	$S_u(\kappa_0)$, 10^{-6} m^3/cycle	DAF	DAF COV%
54	Good	16	0.015	40.15
54	Average	64	0.040	23.99
81	Good	16	0.004	30.13
81	Average	64	0.009	26.86

Another reason for the relatively low values is that the *DAF* had considered the dynamic effect of the interaction of the truck axles with the road roughness, and did not consider the interaction of the full dynamic system, including the truck, road roughness and bridge, which could increase the *DAF* values for flexible bridges and bring them closer to the values listed in the references mentioned above. Table 5.11 shows that the *DAF* increased with road roughness, but decreased with vehicle speed.

It is useful to examine the frequency content of the dynamic wheel force time history and compare it with the natural frequencies of the bridge. As an example, Figure 5.9 shows the dynamic force spectrum of the five wheels on one side of the QS-660 truck (Figure 3.33), all of which are subjected to the same roughness profile for a truck travelling speed of 54 km/hr, and an $S_u(\kappa_0)$ value of $64*10^{-6}$ m^3/cycle. It can be seen from Figure 5.9 that the frequency content of the dynamic wheel force ranged from 2 to 6 Hz, which encompasses the first three natural frequencies of the bridge (2.485, 4.16, 5.7 Hz). As a result, it was possible for the dynamic wheel loads to produce some degree of resonant response in those three modes.

A summary of the lowest three natural frequencies derived from the truck-induced excitation using the dynamic truck model under different truck speeds and road roughness is presented in Table 5.12, along with the MAC values for the corresponding mode shapes relative to the eigenvalue solution. Table 5.12 shows that the natural frequencies calculated from the dynamic truck excitation were close to the FE model natural frequencies, with average natural frequencies from the different truck speeds and road conditions being 2.539, 3.965 and 5.708 Hz for the first three vibration modes of the bridge, resulting in differences of 2.4, 1.5 and 0.2%, respectively, with the bridge eigenvalues.

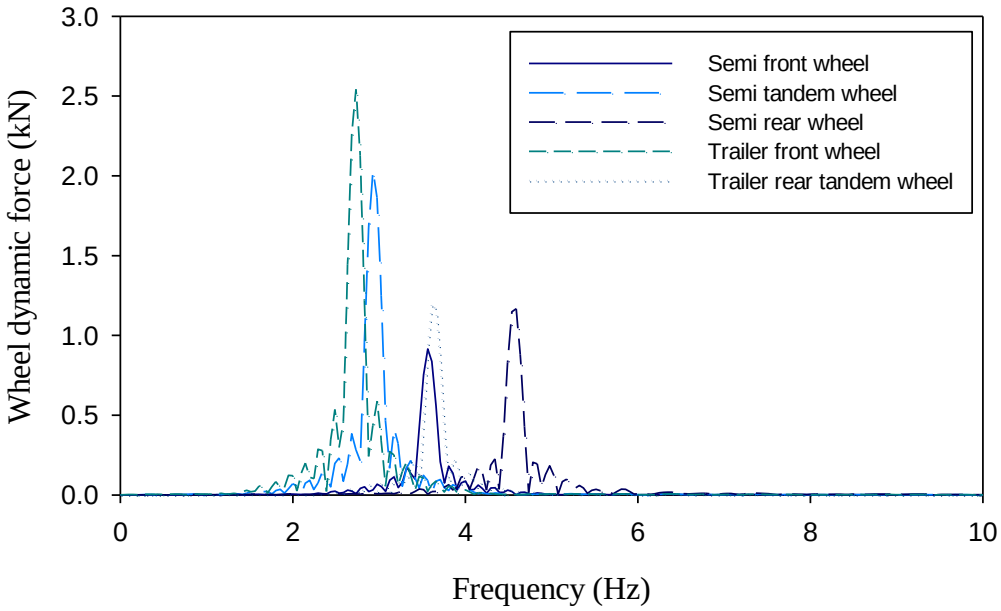

Figure 5.9 Frequency spectrum for QS-660 truck wheel forces.

In addition, the MAC values for the first three mode shapes were all found to be 0.9 or higher, which shows good correlation between the calculated mode shapes under different truck excitation events and those calculated from eigenvalue analyses.

Table 5.12 shows similar results to Table 5.9 (simplified truck model results), with high MAC values (close to 1.0) for the first mode in both cases, in addition to higher MAC values for the second and third modes. Also, both truck models, the dynamic and simplified truck models, produced better results for higher modes than those for the simplified truck models with a superimposed sinusoid, the MAC values of which are listed in Table 5.10. This suggests that when the road roughness is low (in other words, the road surface conditions are good) then the simplified (moving quasi-static) truck loading would yield similar results to the more complicated dynamic truck model.

The effect of noise on the output of the random excitation force and the truck excitation force was not investigated because the modal properties extracted from both types of excitations were of lower quality than those extracted from harmonic excitation or impact excitation.

Table 5.12 Natural frequencies and mode shape MAC values from dynamic truck model excitation.

Analysis case	Speed (km/hr)	$S_u(\kappa_0)$*10^{-6} m^3/cycle	Natural frequency [Hz]			Mode shape MAC values		
			1st	2nd	3rd	1st	2nd	3rd
Eigenvalue			2.480	4.024	5.695	-	-	-
QS-660	54	16	2.472	3.943	5.680	0.9952	0.9954	0.9465
QS-660	54	64	2.476	3.979	5.713	0.9949	0.9959	0.8992
QS-660	81	16	2.686	3.983	5.753	0.9676	0.9997	0.947
QS-660	81	64	2.523	3.955	5.687	0.995	0.9996	0.9438

As final note, the bridge response to the simulated truck excitation events shown in Figure 5.6 to Figure 5.8 may be compared to the measured bridge response to truck loading as detailed in Section 4.2.1. This comparison shows that there is a general agreement between the experimental measurements and the numerical model simulation. For example, the acceleration-time histories of both experimental and numerical studies look similar, with the frequency content of the bridge response mainly concentrated between 0 to10 Hz -the same range over which the first several natural frequencies of the bridge occur. This observation explains why such a bridge can be readily excited by traffic, and suggests that traffic can be considered a suitable source of excitation, taking into consideration the limitation of this type of excitation as explained in Section 4.2.1.

In addition, Figure 5.6 and Figure 5.8 show comparable time history responses and frequency content, suggesting that the simplified pseudo-static truck model can provide results similar to the more elaborate dynamic model for the scenarios constructed in this study. On the other hand, Figure 5.7b shows that most of the bridge response was concentrated around the first natural frequency of the bridge when a sinusoidal force acting at the first natural frequency of the bridge was superimposed on the truck excitation. However, this frequency content was different from that of the measured bridge response during field tests, leading to the conclusion that the simplified truck model and the dynamic truck model are more accurate representations of the actual truck excitation observed on the bridge.

The free vibration phase after truck excitation was not studied as it had similar characteristics to the free vibration after random excitation and impact excitation that were discussed in details in Section 5.3.2 and Section 5.3.3, respectively.

5.3.5 Modal Variability Due to Different Types of Excitation

As most VBDD methods use the mode shape amplitude, or its derivatives, in detecting damage, it becomes important to examine the effect that different types of dynamic excitation and noise have on the variability of mode shape amplitudes. The coefficient of variation (COV) of modal amplitudes was used to quantify this effect. In this section, using the results of ten simulations for each type of excitation, the COV was calculated for each FE node in a given mode shape. The node modal amplitude values for each mode were averaged in order to facilitate the comparison. Table 5.13 compares COV values for different types of excitation and noise levels. Truck excitation was not included in this table because each type of truck excitation was a single run event; therefore, there was no variability associated with it.

It is clear that free decay after random loading and harmonic excitation with different levels of induced noise produced lower averaged COV values compared to other types of excitations, while forced random excitation produced the highest COV values. Impact excitation produced intermediate COV values between the harmonic and random excitation. It can be seen from the table that higher modes exhibited higher levels of variability compared to the fundamental mode; in other words, the precision of the measured fundamental mode was higher than that for the higher modes. For this reason, only the fundamental mode was used in the comparison between different damage detection methods in the following chapter.

In Table 5.13, under harmonic excitation, the COV values for the first mode only were listed, due to the fact that higher modes were not reliably produced. This was caused by the fact that the forcing excitation was applied at the first natural frequency only, with no forcing excitation at higher modes; thus, no energy to excite the higher modes was present. As was discussed before, harmonic loading was not implemented for higher modes because, in field testing, only the first mode could be calculated with acceptable reliability.

Table 5.13 Averaged coefficient of variation of modal amplitudes due to different types of excitation.

Type of Excitation	Noise Type & Level		Average Coefficient of Variation (COV %) Mode 1	Mode 2	Mode 3
1st Mode Harmonic	Input noise	1%	0.0097	---	---
		2%	0.0079	---	---
		5%	0.0094	---	---
		10%	0.0182	---	---
	Output noise	1%	0.3400	---	---
		2%	0.4600	---	---
		5%	0.7000	---	---
		10%	0.9800	---	---
Impact	Input noise	1%	0.0964	4.9678	34.3575
		2%	0.0537	7.0584	120.5588
		5%	0.0982	12.3583	98.2902
	Output noise	1%	0.7406	555.3104	313.3711
		2%	1.0043	941.0427	52.1119
		5%	1.9520	151.8151	1085.3170
Random	Forced		0.8252	181.2134	239.8356
	Free decay		0.0001	0.0005	0.0078

Another observation from Table 5.13 is that the COV values increased with an increase in the noise level, and that these values were higher for output noise than for input noise. The second observation may be explained by that fact that input noise gets filtered to some degree by the bridge structure, thus making the bridge response less variable than when the noise was applied to the bridge response directly.

Also from Table 5.13, it can be noticed that the averaged COV values of modes calculated using the forced random excitation are much higher than those calculated using the free decay following the random excitation. This may be attributed to the fact that, during free decay vibration, the uncertainty associated with random forced vibration on the bridge is removed and no longer influences the bridge vibration; as a result, the bridge is vibrating at it own natural frequencies only.

As an illustrative example of the results listed in Table 5.12, Figure 5.10 shows the first mode shape along the middle girder of the bridge with error bars indicating the COV of

measurements plotted at each FE nodal point, obtained when the bridge was excited by a random varying force, as well as those when the bridge was vibrating freely after the random excitation was discontinued. It is clear that the variability values when the bridge was vibrating freely were much smaller than those when the bridge was actively being excited by a random force. The black arrows in Figure 5.10 represent the bridge supports.

Based on the variability of vibration modes, it can be concluded that harmonic excitation and freely decaying vibration produced the least variability in the bridge modal properties, thus making them good candidates for excitation strategies for VBDD application. One drawback, however, in the application of harmonic force excitation is that the bridge's natural frequencies need to be known beforehand in order to pick the vibration frequency for the harmonic force necessary for conducting the test. This means that an additional preliminary test is needed to identify the bridge natural frequencies before conducting the harmonic excitation test. Another limitation of harmonic excitation is that it can excite one natural frequency at a time, meaning that, if more than one mode is to be estimated, then an additional test is needed for each additional mode. Harmonic and random excitation would also require a shaker that needs to be transported to the bridge being tested, and installed to perform the test. This process requires planning, personnel and a truck for transportation of the shaker.

On the other hand, the response produced during active random excitation showed the highest variability in mode shape amplitude; thus, it may be considered less suitable than harmonic excitation for VBDD applications. Nonetheless, it can be used as a preliminary test to identify the structure's natural frequencies, since natural frequencies were estimated reliably using all excitation methods.

Impact excitation showed higher modal variability than harmonic excitation but lower variability than random excitation. In addition, impact excitation has the ability to excite several modes at once, as was shown in Section 5.3.3. These findings suggest that impact excitation is a suitable option for VBDD applications, especially when there is a time constraint that makes the application of harmonic excitation unsuitable.

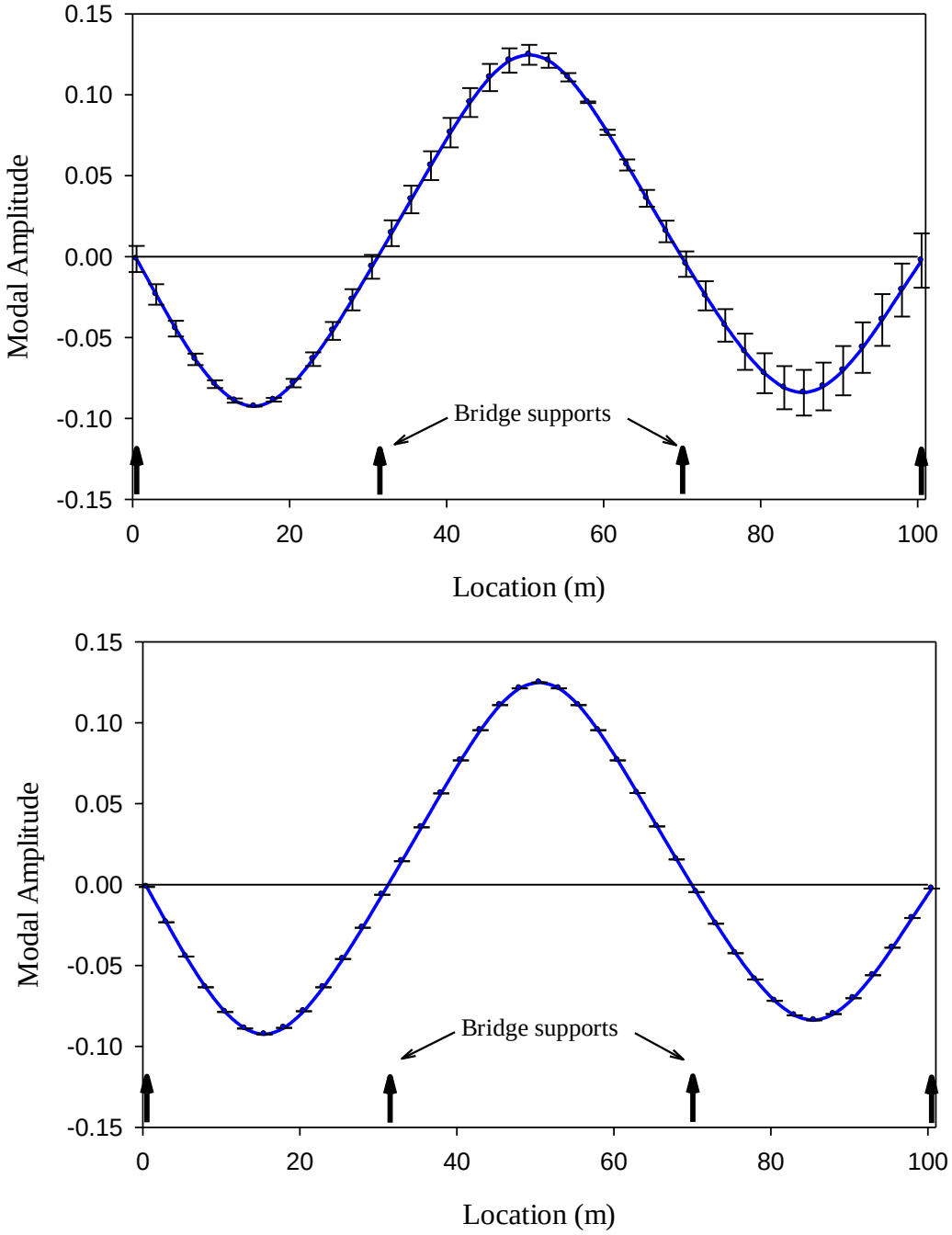

Figure 5.10 Variability of the first mode for the middle girder of the bridge calculated by a) random forced excitation, b) free vibration decay after random excitation.

6 NUMERICAL SIMULATION of VBDD

6.1 OVERVIEW

In this chapter, the results of selected numerical simulations related to damage detection are presented and discussed. These numerical simulations used the calibrated FE model of the Hudson Bay Bridge as the basis for analyses using various dynamic excitation methods.

The effects of the type of excitation and the source of uncertainty on the extracted modal properties, and thus the ability to detect damage, are studied in this chapter. Therefore, the purpose of the study presented in this chapter was to determine which damage detection methods were more robust and gave more accurate results under different types of dynamic excitation and uncertainty levels. In this regard, different damage scenarios were also considered. In addition, confidence levels for some damage detection methods, taking into consideration the limited number of tests that may be conducted on an actual bridge, are presented.

6.2 VBDD METHODS USING ERROR FREE MODE SHAPES

6.2.1 Overview

The results of applying the VBDD methods that were detailed in Sections 2.3 and 3.12 to the damage scenarios described in Section 3.11 are discussed here. For the results reported in this section, the VBDD methods were applied to two sets of modal properties calculated from the eigenvalue solutions (error free) of two FE models: the undamaged (original) and damaged models of the Hudson Bay bridge.

The VBDD methods used in these comparisons were the change in mode shape method, change in mode shape curvature method, damage index method, change in modal flexibility method, change in uniform load surface curvature method, and change in unit load surface curvature method.

Only the first mode shape was used in the analyses as it was the only mode that could be calculated from site measurements with a high level of confidence. Also, mode shapes calculated using output-only methods are not mass normalised; therefore, different modal contributions cannot easily be combined since their relative amplitudes are indeterminate. Before VBDD methods were applied, a cubic spline was implemented to interpolate the mode shape between the points of measurement on the bridge, and the mode shapes were mass ortho-normalised assuming a unity mass matrix; in effect, uniform mass distribution was assumed along the bridge span (Humar 2002). The mathematical background regarding the type of cubic spline used in this study, the interpolation interval, and the total length of the mode shape vector after interpolation are detailed in Section 3.9, along with a description of mass ortho-normalisation procedures.

The VBDD methods were applied to simulated readings taken from the east and west sides of the bridge, as well as to readings taken along the bridge girders; however, only readings taken from the bridge sides and the middle girder were used to produce the figures in this chapter to reduce clutter and improve clarity. The longitudinal distribution of the simulated measurement points was similar to that used for site measurements, as shown in Figure 3.25.

The MATLAB routines that were used in implementing the various VBDD methods, along with samples of input files, are listed in Appendix H.

6.2.2 First damage scenario - External reinforcing bars cut at the centre of all girders of the middle span

In this damage scenario, the external reinforcing bars were "cut" at the centre of all three girders of the middle span in the numerical model, reducing the flexural stiffness of the girder by 16%. This type of damage was chosen because the external bars were, in fact, removed from the actual bridge, providing an opportunity to measure the response in this condition. Figure 6.1 to Figure 6.6 show the distribution of the different VBDD parameters for this damage scenario. In these distributions, the highest peak in the graph corresponds to the likely location of damage. The vertical (red) line in the figures indicates the location of damage and the upward black arrows represent the locations of the bridge supports.

It can be seen from the above mentioned figures that, in general, all the methods could detect and localise the damage, with varying degrees of accuracy, since a pronounced peak is seen to occur in close proximity to the damage location. The exception to this finding was the change in uniform load surface curvature method, which showed several false positives (i.e., peaks indicating possible damage at locations where there was no damage) and failed to locate the actual damage itself.

The change in mode shape damage detection method (Figure 6.1) showed a peak in each of the bridge spans, but the highest peak was in the middle span, where the damage was located. The peak in the middle span had comparable amplitudes along all three measurement lines corresponding to the east and west sides of the bridge and the middle girder, indicating that this method could detect the damage with sensors placed along any of the three measurement lines.

In Figure 6.1, and other figures in this chapter that show different VBDD comparisons, the curves representing the damage indicators of the different girders may be closely spaced and only one or two lines could be distinguished instead of three.

The change in mode shape curvature (Figure 6.2), on the other hand, exhibited several peaks in the middle span and was almost flat in the end spans. This gave a better indication of the location of damage than the change in mode shape method, which showed peaks in all spans. Although the change in mode shape curvature method showed several peaks, nevertheless, the highest peak was the closest to the actual damage location.

The damage index method (Figure 6.3) showed similar results to the change in mode shape curvature method, with relatively flat curves being produced in the bridge end spans, where there was no damage. One difference as compared to Figure 6.2, though, was that only one peak was evident at the damage location, thus giving a clearer indication of the location of damage.

The distribution of the change in modal flexibility (Figure 6.4) was similar to the change in mode shape, with the highest peak in the middle span where the simulated damage was, along with smaller peaks in both exterior spans.

The change in uniform load surface curvature method (Figure 6.5), on the other hand, did not succeed in locating the damage, showing two peaks of nearly equal heights on either side of the damage location and higher peaks in the end spans, resulting in false positive readings, i.e. indicating damage at a location that is not truly damaged.

Finally, the change in unit load surface curvature method (Figure 6.6) showed results very similar to the change in mode shape curvature method (Figure 6.2), where the curve exhibited several peaks in the middle span and was almost flat in the end spans. Although the curve showed several peaks, nevertheless, the highest peak was the closest to the actual damage location.

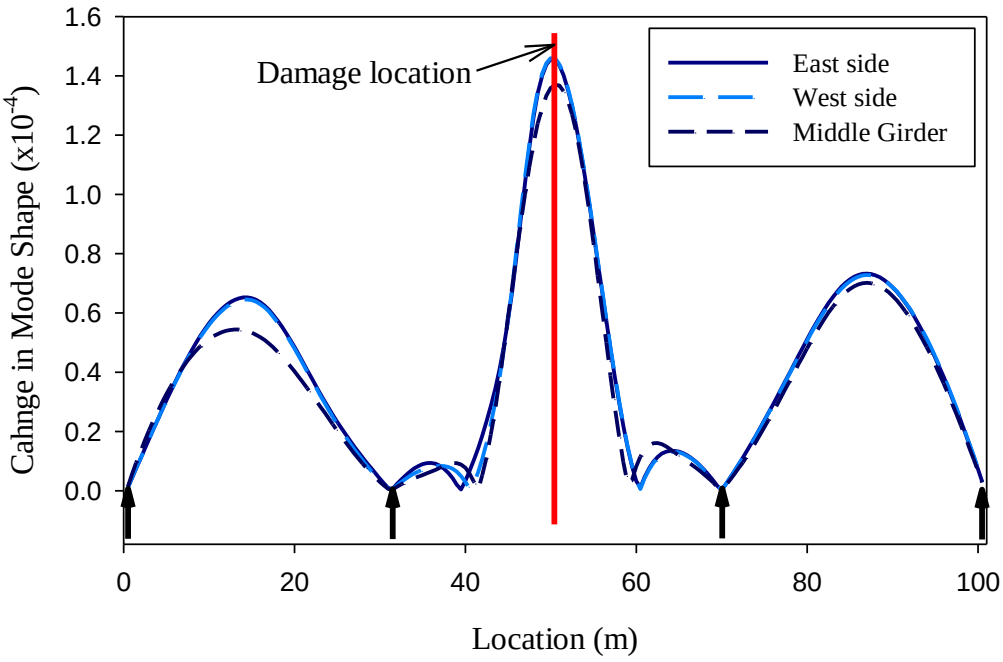

Figure 6.1 Distribution of the change in mode shape caused by cutting the external rebars from the middle of all the girders in the centre span.

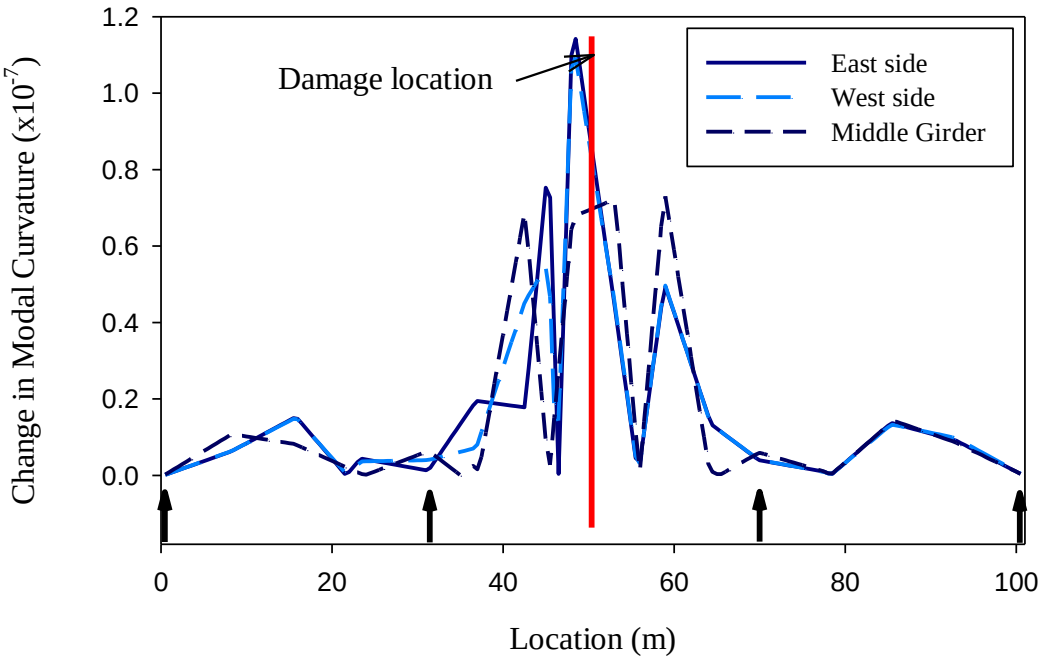

Figure 6.2 Distribution of the change in mode shape curvature caused by cutting the external rebars from the middle of all the girders in the centre span.

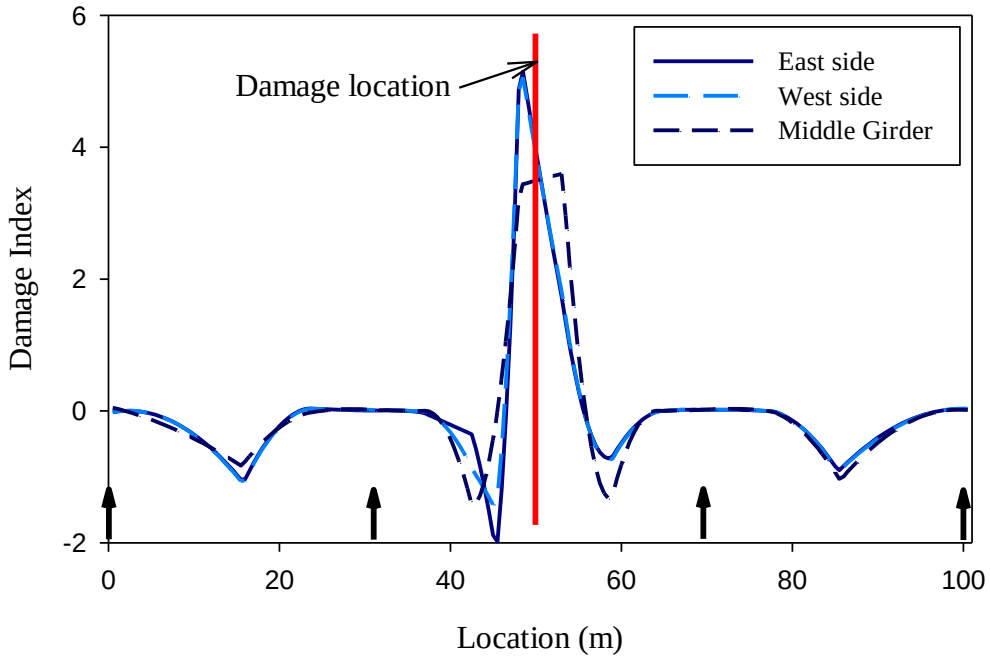

Figure 6.3.Distribution of the damage index caused by cutting the external rebars from the middle of all the girders in the centre span.

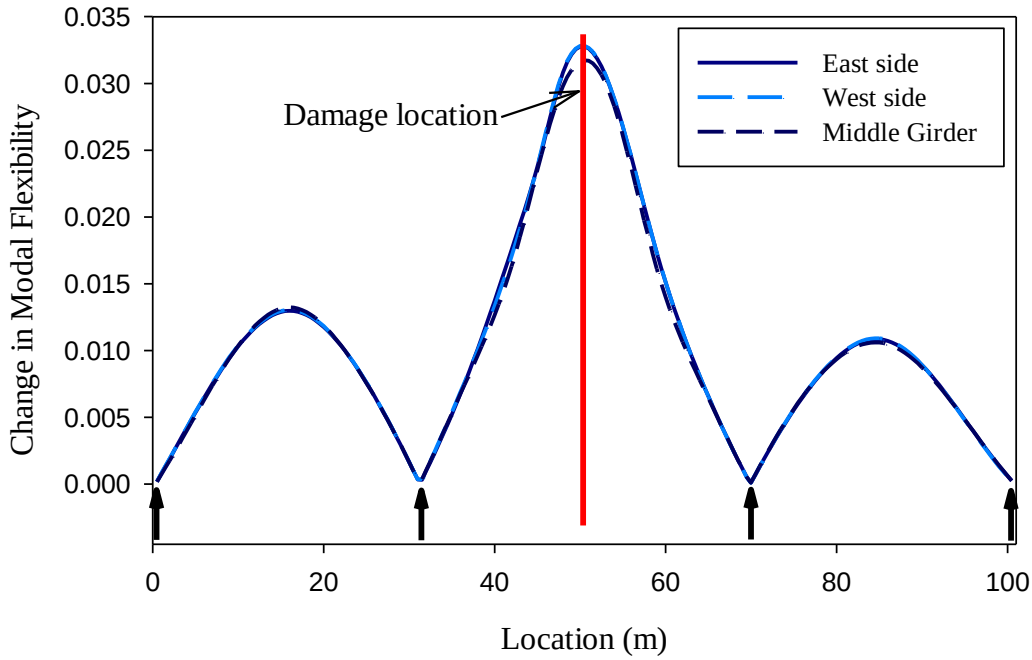

Figure 6.4 Distribution of the change in modal flexibility caused by cutting the external rebars from the middle of all the girders in the centre span.

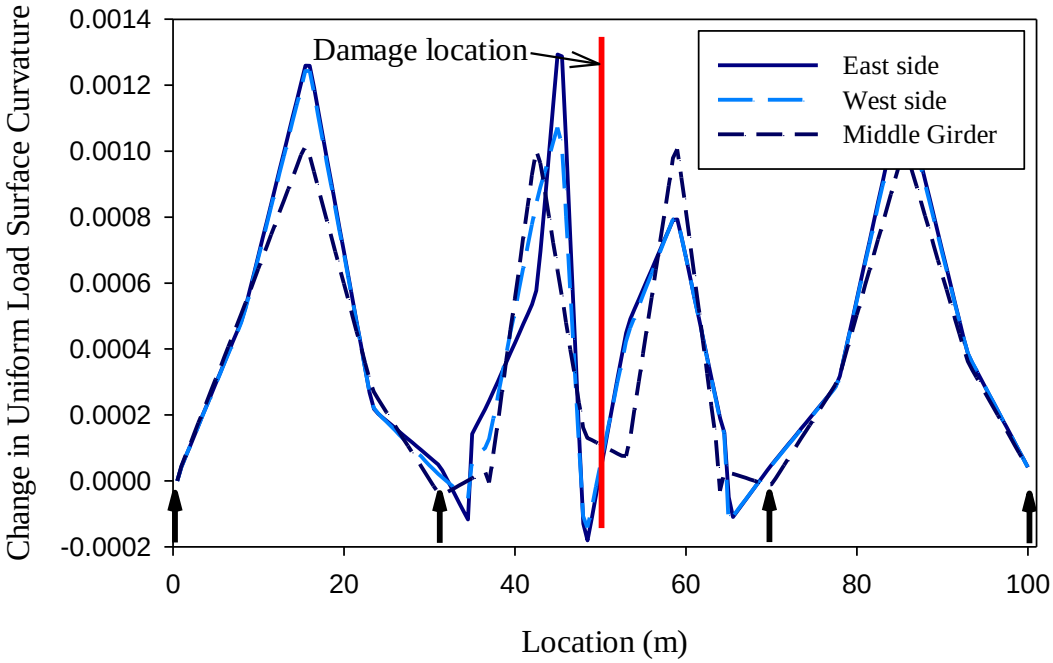

Figure 6.5 Distribution of the change in uniform load surface curvature caused by cutting the external rebars from the middle of all the girders at the centre span.

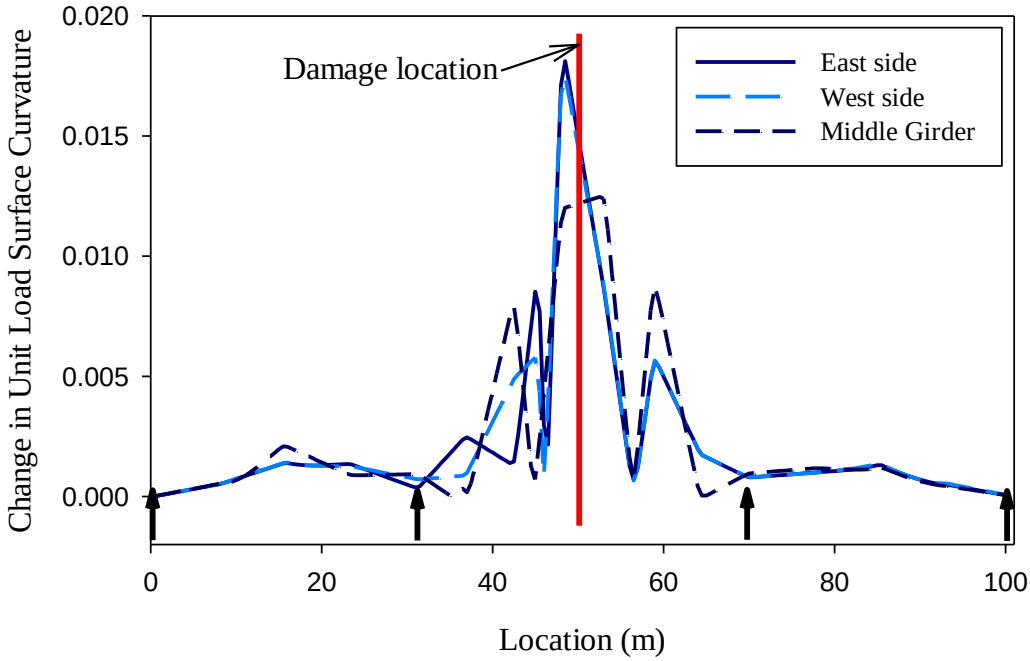

Figure 6.6 Distribution of the change in unit load surface curvature caused by cutting the external rebars from the middle of all the girders at the centre span.

6.2.3 Second damage scenario - External reinforcing bars cut on the middle of one girder within the centre span

In this scenario, damage was simulated by "cutting" the external rebar from the centre span of an exterior girder, reducing the flexural stiffness of the girders by 5.5% at this location. This damage scenario was used to check the ability of the different damage detection methods to detect damage in one girder only (localised damage that was not symmetric in the transverse direction). Girder 3, which is the edge girder on the west side of the bridge, was chosen to have its external reinforcing bars cut for this simulated damage case.

Figure 6.7 through Figure 6.12 show the distributions of the VBDD parameters for this damage scenario. It can be seen from the above mentioned figures that, in general, all the methods could detect and localise the damage, with varying degrees of accuracy, except for the change in uniform load surface curvature method (Figure 6.11). This method produced several false positives, and failed to locate the actual damage itself. The damage index method was able locate the damage along the bridge length but did

not provide an indication of which girder was damaged since the relative magnitudes of the peaks on all three girders were similar.

The change in mode shape method (Figure 6.7) showed peaks at two of the three girders in the middle span with the highest peak corresponding to the west girder, where the damage was located. This method therefore successfully located the damage. However, other lower peaks also appeared in the undamaged end spans.

The change in mode shape curvature method (Figure 6.8) showed the highest peak at the damage location on the west girder. In addition, this method provided a similar distribution to that in Figure 6.2, featuring multiple peaks near the damage location while remaining relatively flat in the end spans. On the other hand, the damage index method (Figure 6.9) was able locate the damage along the bridge length but could not provide an indication of which girder was damaged, as peaks of comparable amplitudes appeared along all girders at the centre of the middle span.

The change in modal flexibility method (Figure 6.10) showed similar results to the change in mode shape method (Figure 6.7) with the highest peak in the middle span of the bridge on the west girder where the simulated damage was located.

As mentioned above, the change in uniform load surface curvature method (Figure 6.11) did not provide a clear indication of the damage location, showing multiple peaks along the bridge; however, the curve corresponding to the west girder showed the highest peak amplitudes, suggesting that this girder could be damaged.

Finally, the change in unit load surface curvature method (Figure 6.12) showed results that were very similar to those of the change in mode shape curvature method, where the highest peak was at the damage location on the west girder. In addition, this method provided a similar distribution to that in Figure 6.8, featuring multiple peaks near the damage location while remaining relatively flat in the end spans.

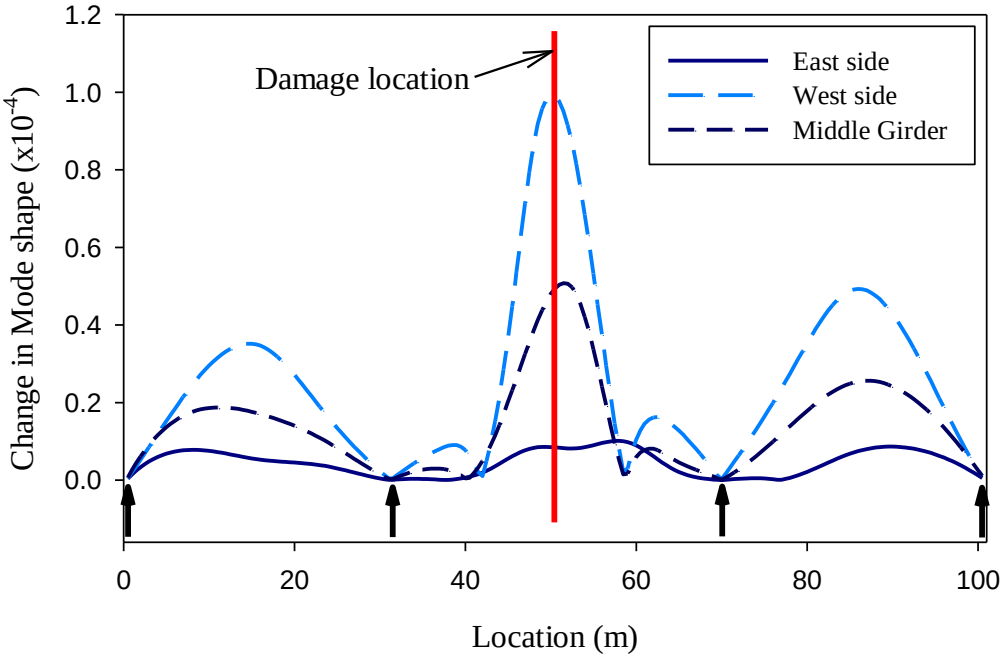

Figure 6.7 Distribution of the change in mode shape caused by cutting the external rebars from the west girder in the centre span.

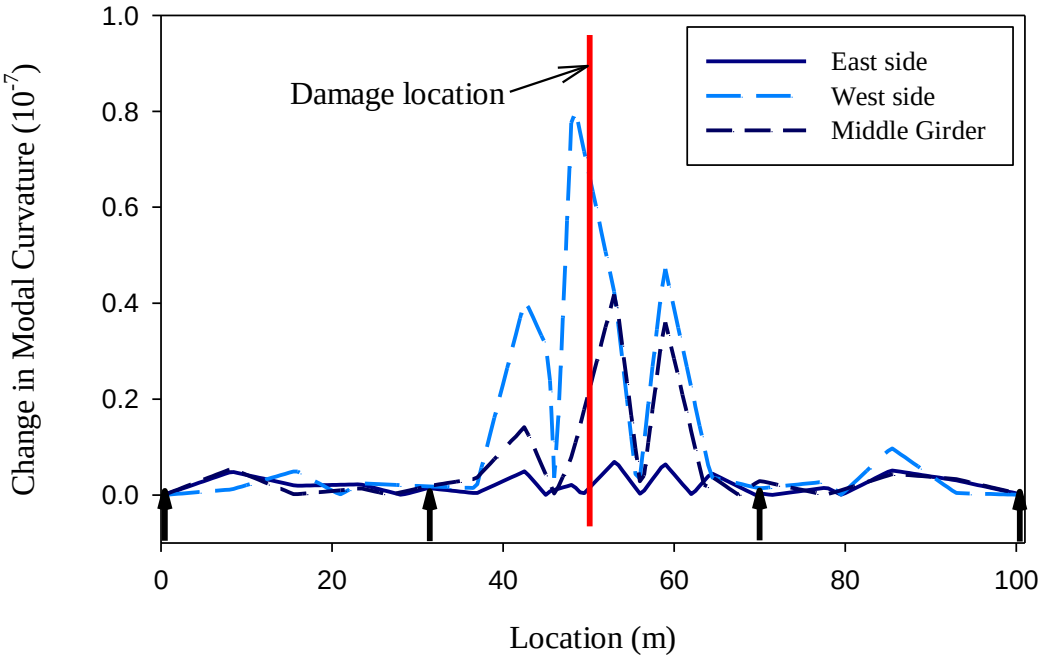

Figure 6.8 Distribution of the change in mode shape curvature caused by cutting the external rebars from the west girder in the centre span.

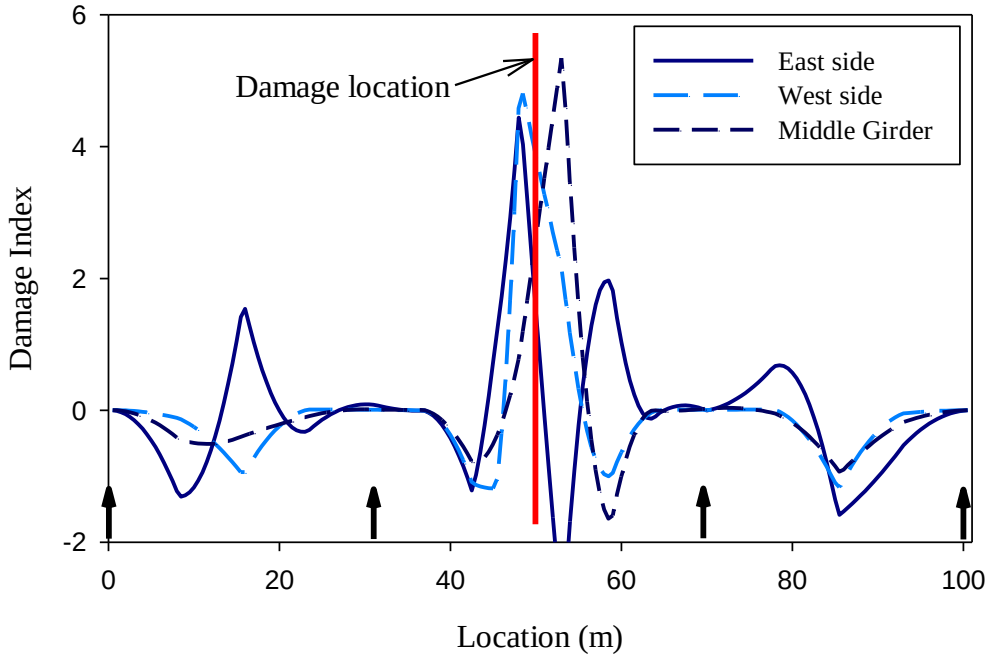

Figure 6.9 Distribution of the damage index caused by cutting the external rebars from the west girder in the centre span.

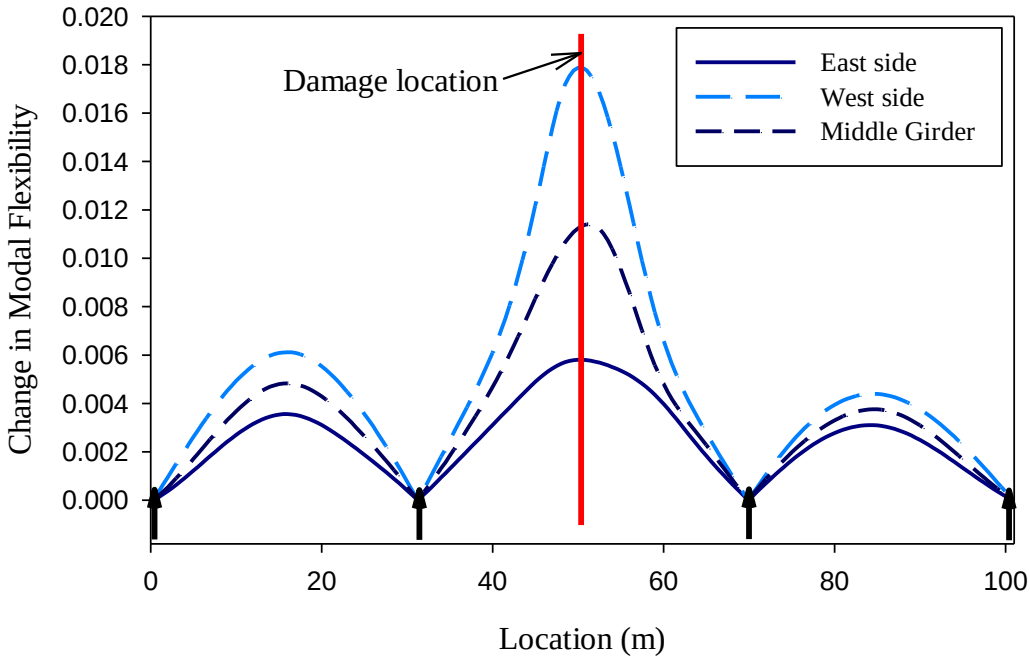

Figure 6.10 Distribution of the change in modal flexibility caused by cutting the external rebars from the west girder in the centre span.

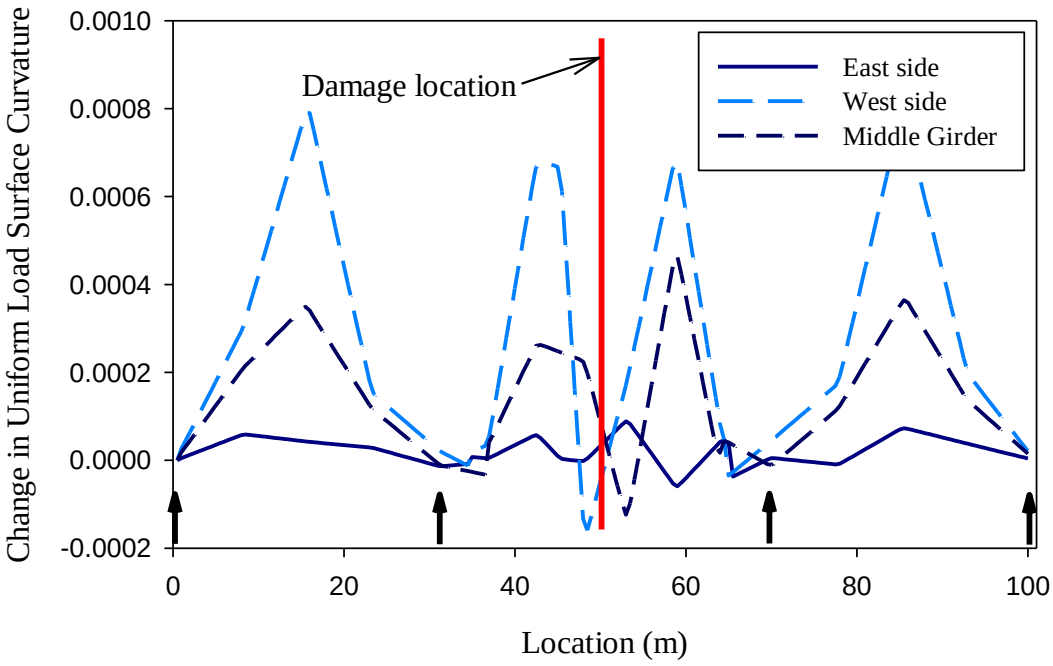

Figure 6.11 Distribution of the change in uniform load surface curvature caused by cutting the external rebars from the west girder in the centre span.

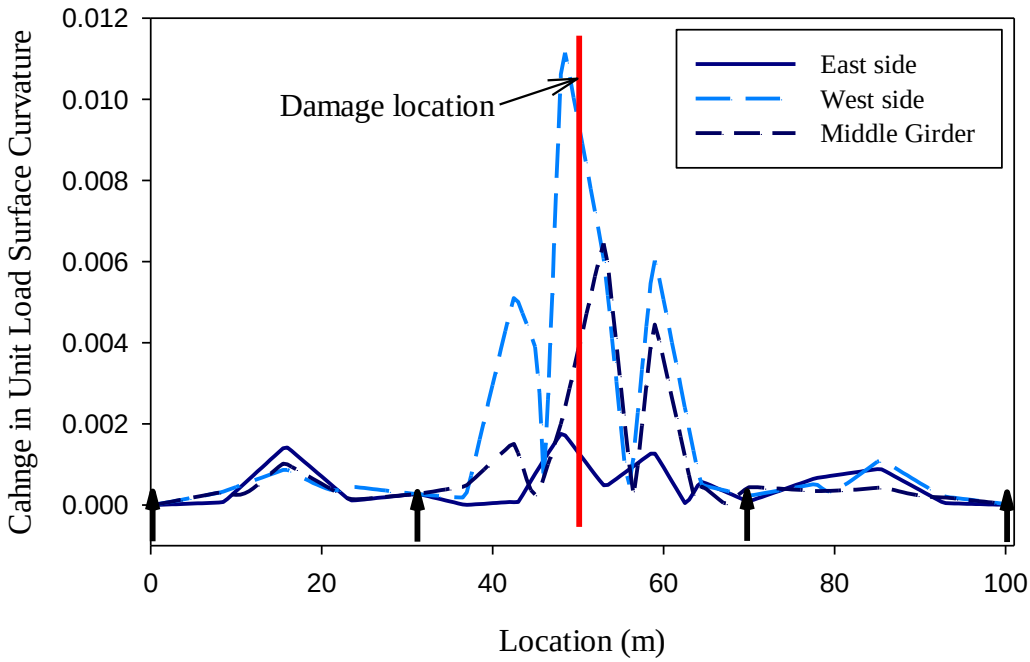

Figure 6.12 Distribution of the change in unit load surface curvature caused by cutting the external rebars from the west girder in the centre span.

6.2.4 Third damage scenario - External reinforcing bars cut from the middle of all girders in an end span

This damage scenario was used to check the ability of the damage detection methods to detect damage in one of the end spans. In this damage scenario, the external reinforcing bars in the north end span were cut at the middle of the three girders of the bridge. Figure 6.13 through Figure 6.18 show the distributions of the VBDD parameters for this damage scenario. In general, all the methods provided a clear indication of the actual damage location.

The change in mode shape method (Figure 6.13) showed several peaks along all measurement lines in each of the bridge spans, with the highest peak being at the damage location, as indicated by the red vertical line. The peaks at the damage location had comparable amplitudes for all three of the measurement lines, which indicates that measurements along any of the three lines would be sufficient to detect the damage.

The change in mode shape curvature method (Figure 6.14) showed a single high peak at the location of damage. Although Figure 6.14 shows several peaks along the bridge span, nonetheless, the peak at the damage location is clearly higher than other peaks in the graph. The indication of the damage location in Figure 6.14 is clearer than was observed for the previous damage scenarios (Figure 6.2 and Figure 6.8); this may be attributed to the fact that, for this damage scenario, a measurement point location coincided with the location of damage, thus giving a better estimate of the damage.

The damage index method (Figure 6.15) showed a distinct peak at the damage location and an almost flat curve elsewhere. The peak in Figure 6.15 appeared slightly clearer than the peaks in Figure 6.3 and Figure 6.9. This difference may be again attributed to the fact that, in the third damage scenario, a measurement point location coincided with the location of damage, thus giving a better estimate of the damage.

The change in modal flexibility method (Figure 6.16) showed similar results to the change in mode shape method, with the highest peak in the end span where the simulated damage was located.

Similarly, the change in uniform load surface curvature method (Figure 6.17) showed similar distributions to the change in mode curvature method (Figure 6.14). Also, the damage could be more easily located in Figure 6.17 than was the case for the two previous damage scenarios (Figure 6.5 and Figure 6.11). Again, this may attributed to the location of the measurement point in comparison to the damage location, as discussed earlier.

Finally the change in unit load surface curvature method (Figure 6.18) showed results that were very similar to the change in mode shape curvature method, with a single high peak at the location of damage. Although Figure 6.18 shows several peaks along the bridge span, nonetheless, the peak at the damage location is clearly higher than other peaks in the graph.

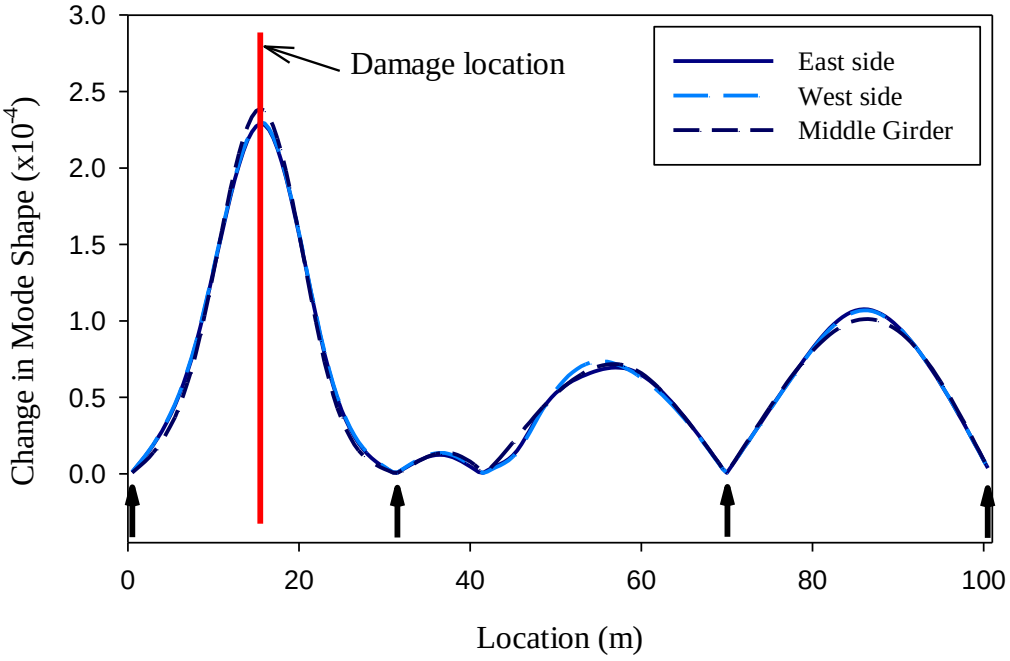

Figure 6.13 Distribution of the change in mode shape caused by cutting the external rebars from girders in the end span.

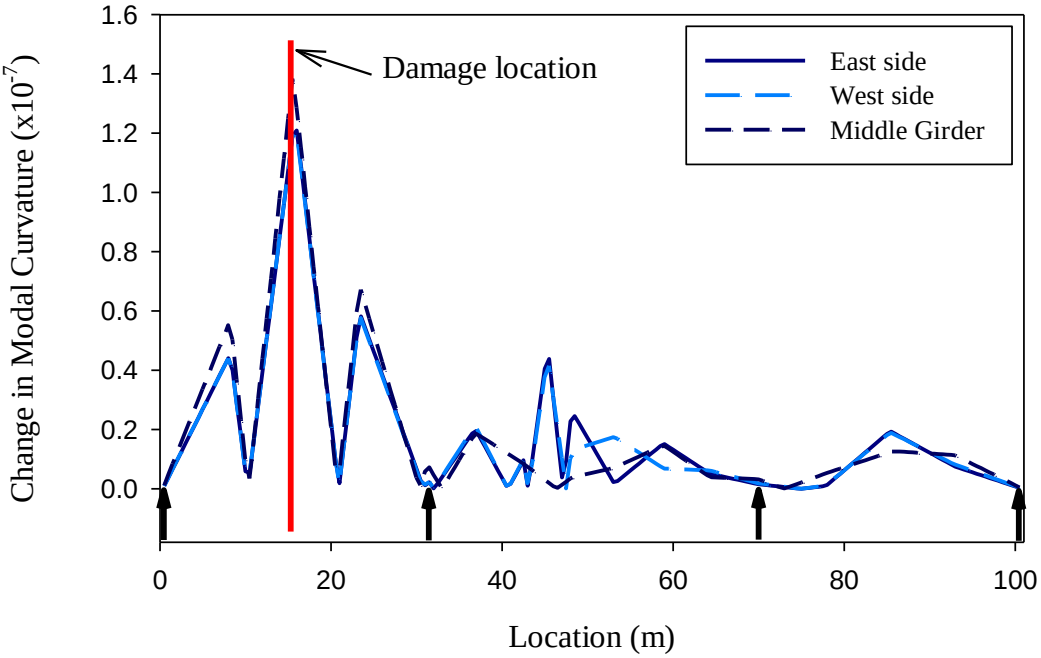

Figure 6.14 Distribution of the change in mode shape curvature caused by cutting the external rebars from girders in the end span.

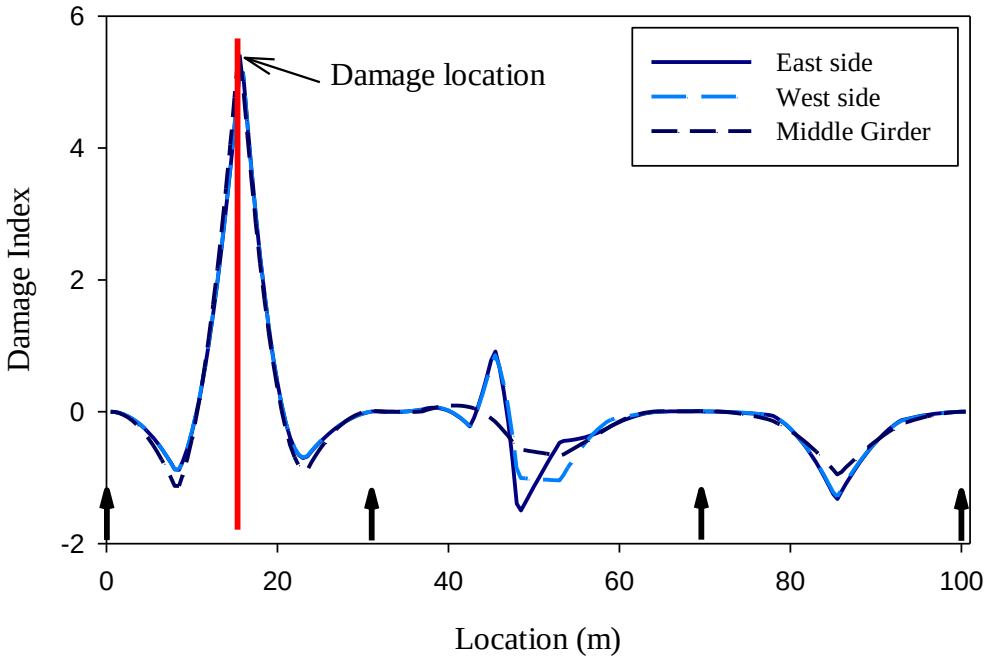

Figure 6.15 Distribution of damage index caused by cutting the external rebars from girders in the end span.

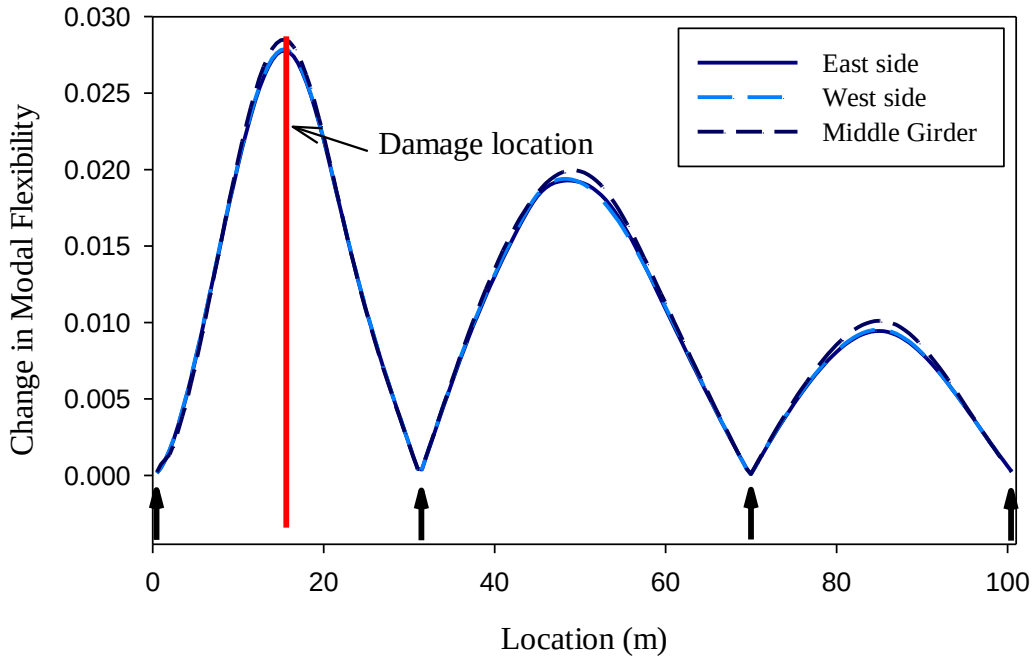

Figure 6.16 Distribution of change in modal flexibility caused by cutting the external rebars from girder in the end span.

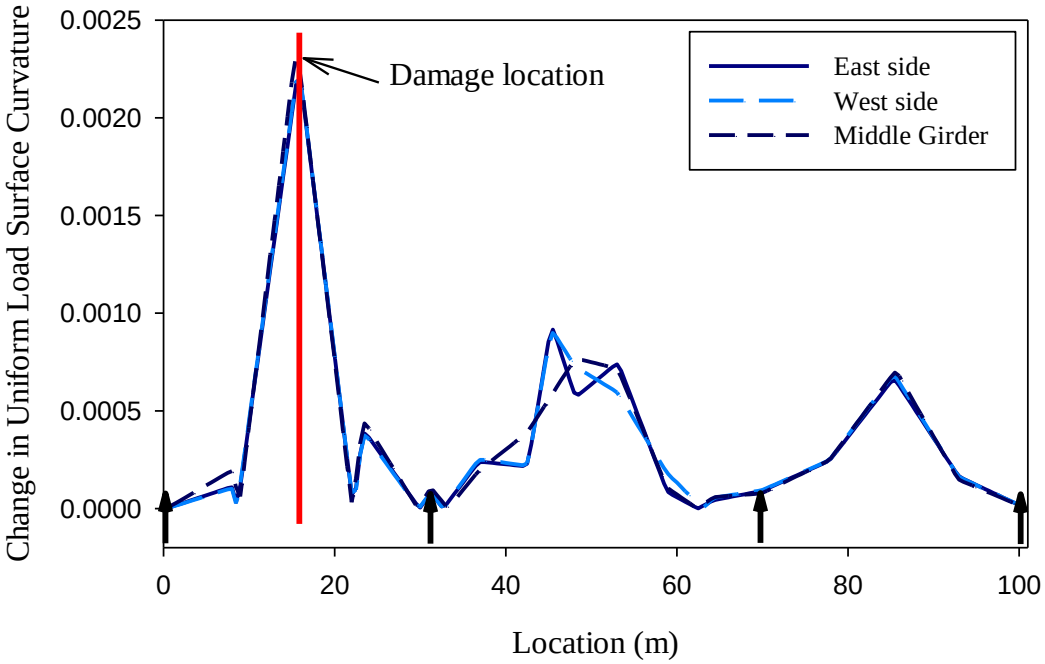

Figure 6.17 Distribution of the change in uniform load surface curvature caused by cutting the external rebars from girders in the end span.

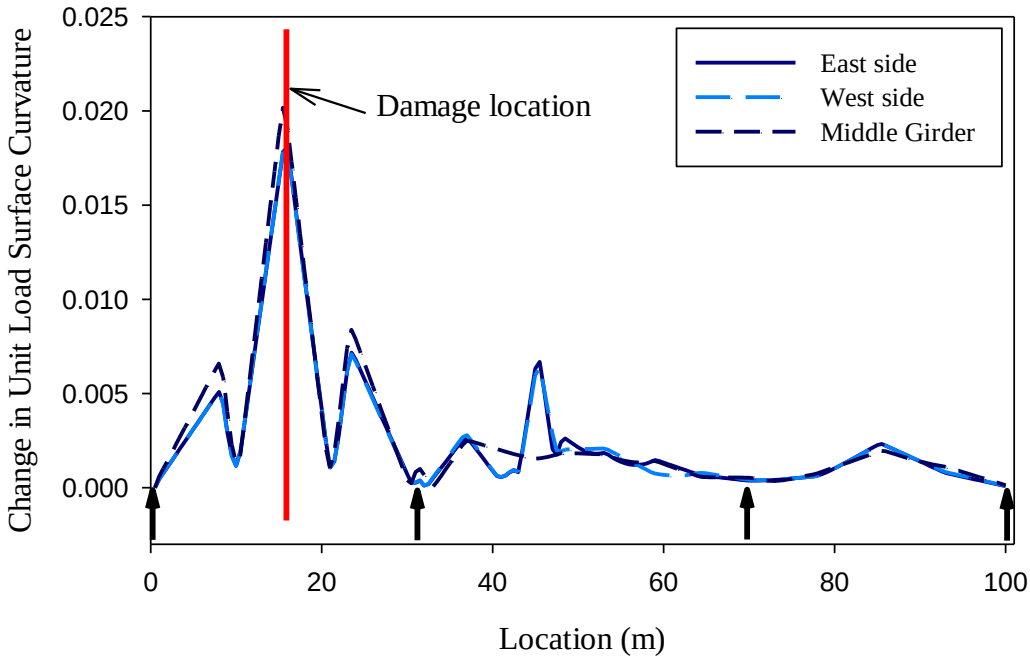

Figure 6.18 Distribution of the change in unit load surface curvature caused by cutting the external rebars from girders in the end span.

6.2.5 Fourth damage scenario - External reinforcing bars removed from the girders in the middle span and replaced by steel plates

In this scenario, the damage simulated the replacement of the external reinforcing bars of the girders in the centre span by steel plates, with the case of the bridge with external reinforcing bars representing the undamaged state of the bridge. Replacing the reinforcing bars by steel plates accounted for a 2% increase in flexural stiffness in the girders. This damage scenario simulated numerically the rehabilitation that was done on the bridge. The purpose of this damage simulation was to see if the rehabilitation that was done on the bridge could be detected using the VBDD methods. In addition, this damage scenario represented a "distributed damage" case, where the bridge properties were modified over a larger length of the bridge and not at a single point only, as was the case in the first three damage cases. It found to be informative to examine how the different VBDD methods perform under this damage scenario.

Figure 6.19 through Figure 6.24 show the distributions of the VBDD parameters for this damage scenario. It can be seen from the above mentioned figures that none of the

methods provided an adequate indication of the damage location, with all methods showing multiple peaks at different locations on the bridge.

The change in mode shape method (Figure 6.19) showed peaks of comparable heights in each of the bridge spans, making it difficult to locate the damage. The change in modal flexibility method (Figure 6.22) showed a similar behaviour to the change in mode shape method. The same can be said about the change in mode shape curvature method, in that Figure 6.20 features several peaks in each of the bridge spans.

The damage index method (Figure 6.21) showed higher peaks in the bridge end spans, possibly leading to the wrong conclusion that damage might have occurred in the end spans and not in the centre span. The change in uniform load surface curvature method (Figure 6.23) and the change in unit load surface curvature method (Figure 6.24) both showed multiple peaks with no useful indication regarding the damage location.

However, a closer look at this set of figures reveals that the amplitudes of the change, i.e. the difference between the damaged and undamaged state, are several orders of magnitude higher than those produced by the other damage scenarios. For example, the maximum amplitude in Figure 6.19 (change in mode shape due to installing the steel plate) was 0.243, while the maximum amplitude in Figure 6.1 (change in mode shape due to cutting the external reinforcing bars from the middle of all the girders in the centre span) was 0.00015. The same observation can be made by comparing the amplitudes of the different VBDD methods between the 1st and the 4th damage scenarios. The only exception is for the damage index method, because this parameter has been normalised by the standard deviation of the damage parameters (see Section 2.3.4).

This observation is shown graphically in Figure 6.25 by directly comparing the first mode shape before and after damage for the 1st and 4th damage scenarios, for the middle girder of the bridge. Damaged and undamaged mode shapes are virtually indistinguishable for the first damage scenario (Figure 6.25a), whereas they are clearly different for the fourth damage scenario (Figure 6.25b). Thus, while the fourth damage scenario could not be localised by the VBDD methods, a clear indication was provided of the presence of damage. One explanation for having an unsymmetrical damaged

mode shape (Figure 6.25b) could be due to the different support conditions at the bridge piers hinged support for the south pier and roller support for the north pier.

In conclusion, it appears that these VBDD methods cannot easily localise a "distributed damage" condition, as in the current case of bridge rehabilitation, or as would be experienced if the bridge deck was subjected to extensive delamination, for example. Instead, damage was successfully located by the VBDD methods only when it was localised, as might be experienced by a crack in the bridge girders or potholes on the bridge deck. However, the VBDD methods did actually indicate significant differences when comparing the bridge mode shapes before and after placing the steel plates, thus providing a clear indication of the presence of damage.

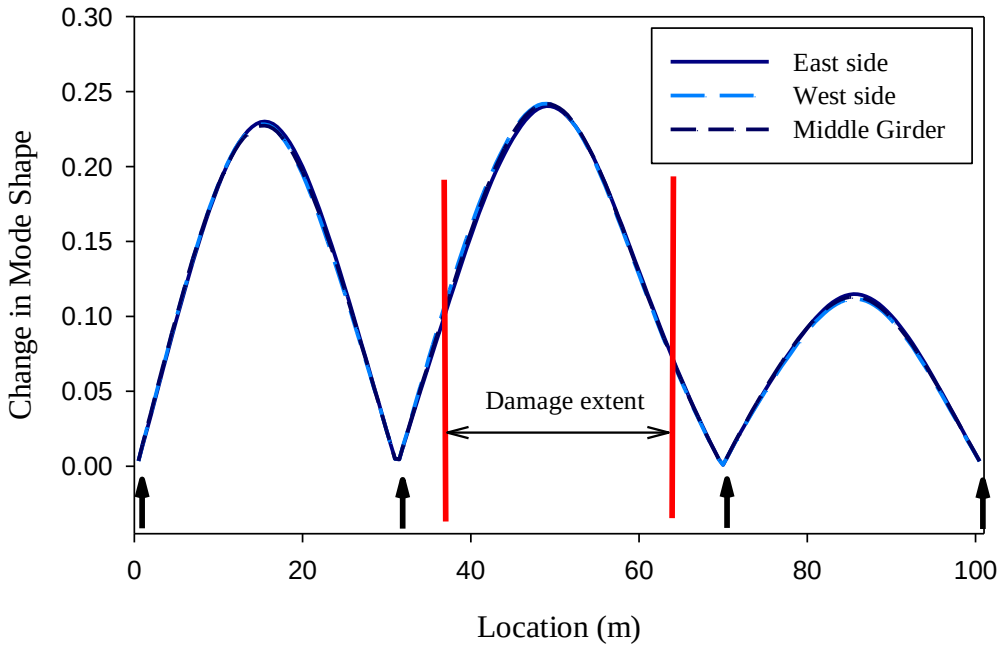

Figure 6.19 Distribution of the change in mode shape caused by replacing the external rebars from the girders in the centre span by steel plates.

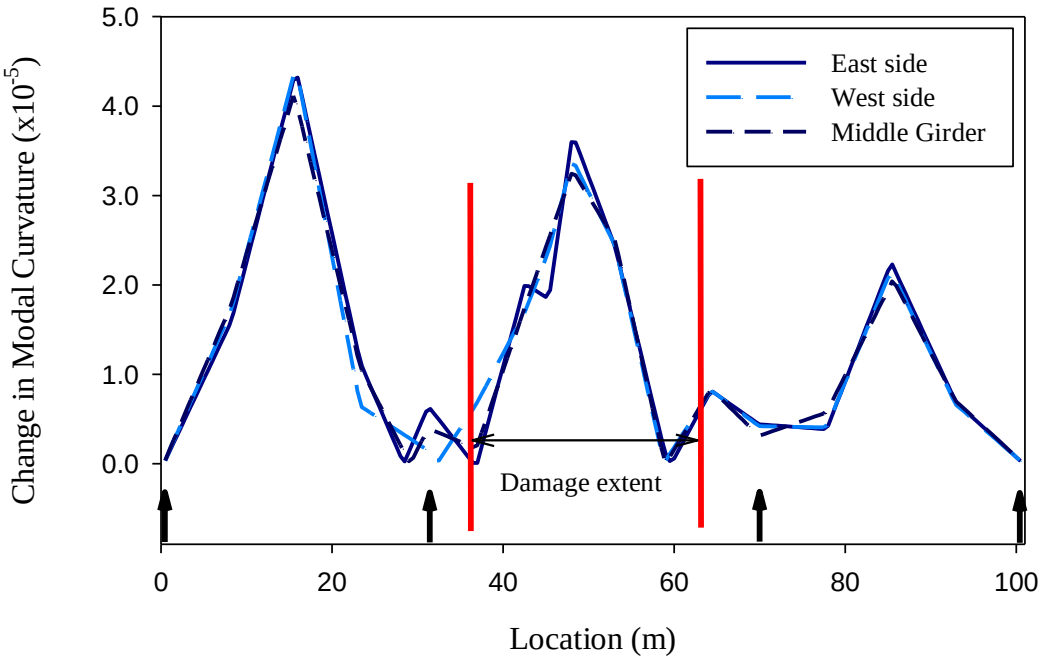

Figure 6.20 Distribution of the change in mode shape curvature caused by replacing the external rebars from the girders in the centre span by steel plates.

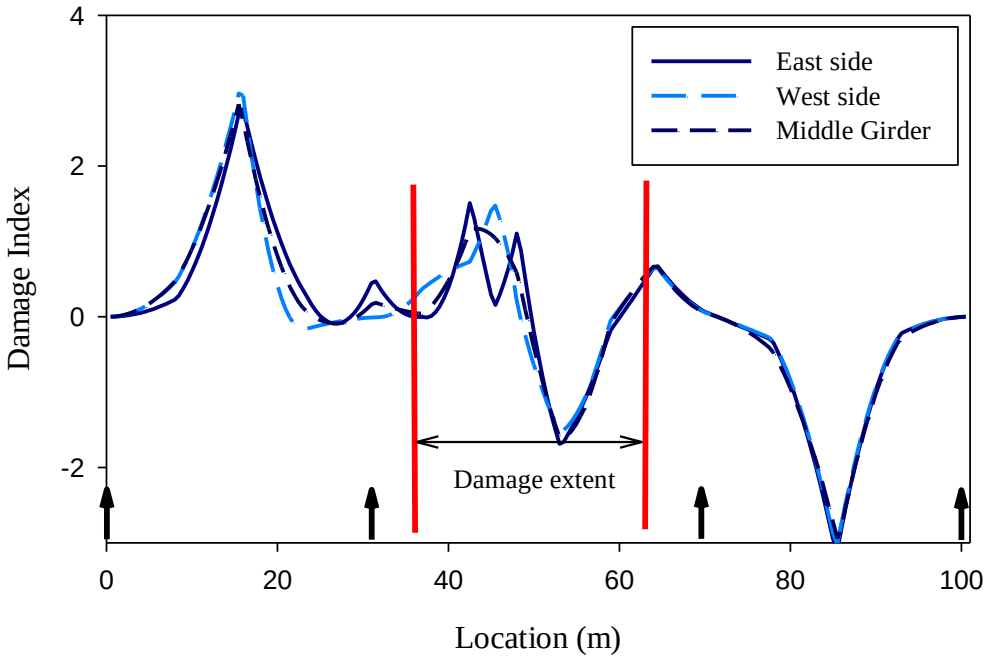

Figure 6.21 Distribution of the damage index caused by replacing the external rebars from the girders in the centre span by steel plates.

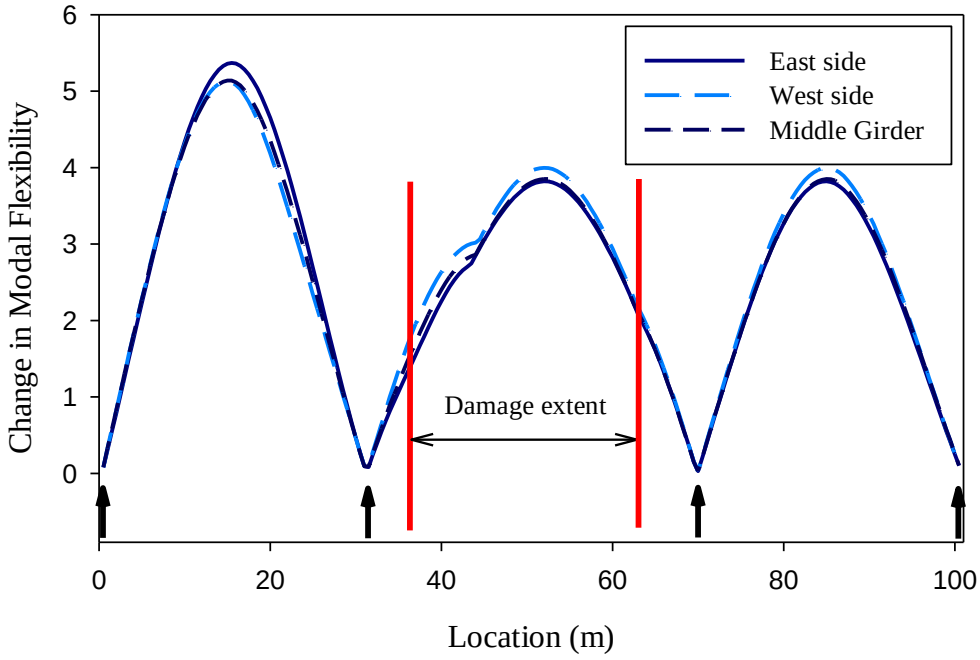

Figure 6.22 Distribution of the change in modal flexibility caused by replacing the external rebars from the girders in the centre span by steel plates.

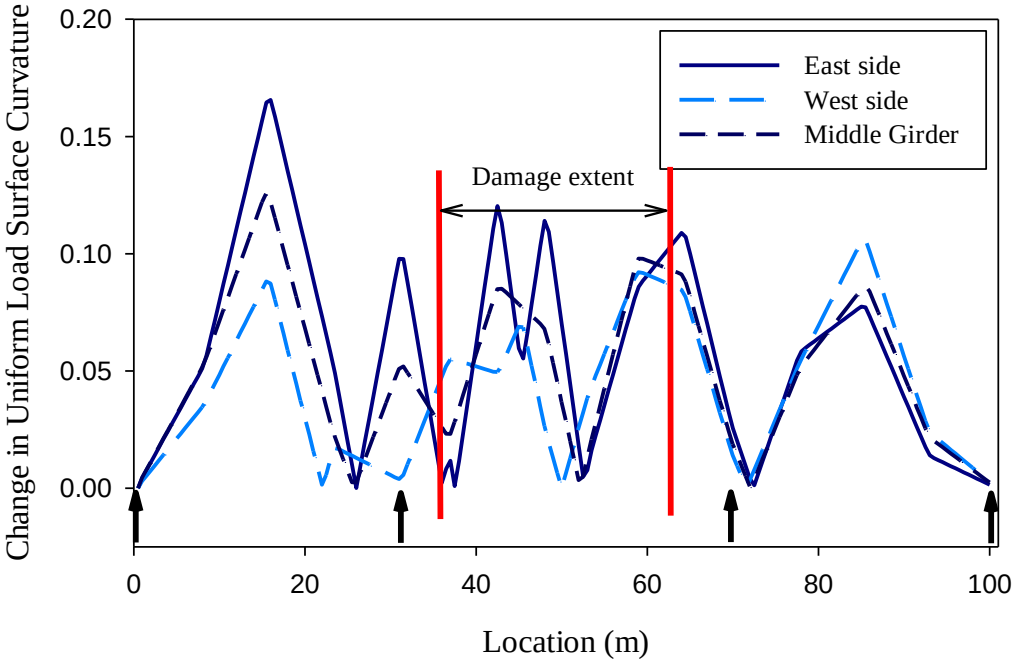

Figure 6.23 Distribution of the change in uniform load surface curvature caused by replacing the external rebars from the girders in the centre span by steel plates.

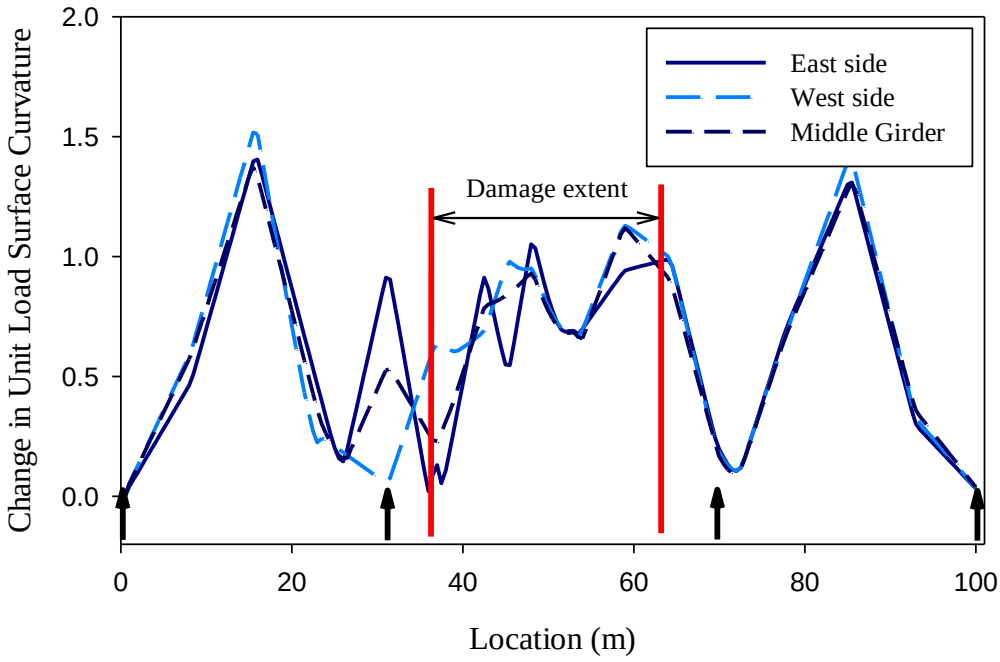

Figure 6.24 Distribution of the change in unit load surface curvature method caused by replacing the external rebars from the girders in the centre span by steel plates.

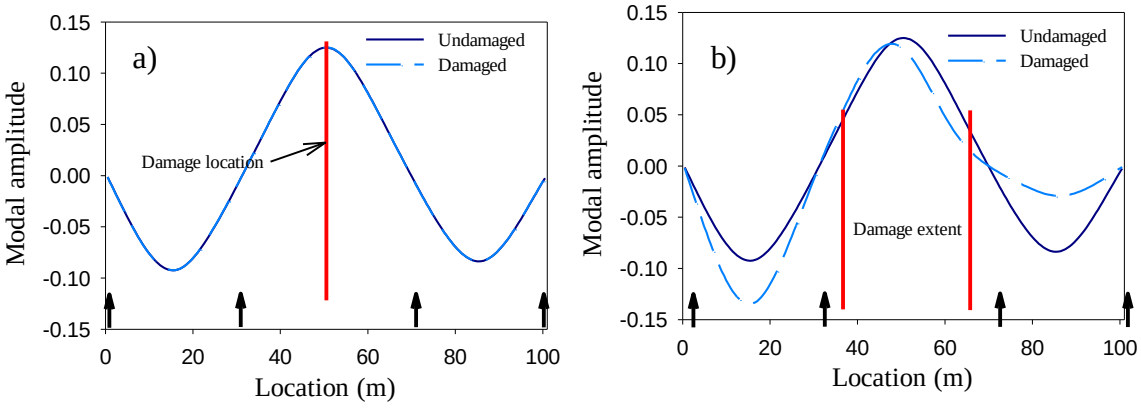

Figure 6.25 Comparison of the modal amplitudes for the 1st mode of the middle girder before and after damage: a) 1st damage scenario, and b) 4th damage scenario.

6.2.6 Discussion

Based on results reported in the literature, all the methods examined in Section 6.2 should perform well under "ideal" conditions. By ideal, it is meant that the contribution from all the vibration modes of the structure is accounted for, and that the measurement points are sufficiently closely spaced that one point should lie at the damage location,

wherever that damage might be. In addition, the damage should be severe enough to produce a numerically significant difference between the measured damage indicator before and after damage. It is also assumed that there is no uncertainty or variation in the measurement of the bridge vibration.

However, in actual test situations, the conditions are often far from ideal, with many restrictions limiting the amount and quality of data collected in the field. For example, the number of accelerometers available dictates how closely they may be spaced on the bridge. The available time window for the test, in addition to the limited number of accelerometers, limits the number of test setups planned for each bridge being tested. This fact forces the test team to optimise the number of test setups and number of accelerometers used to suit site conditions.

The severity of damage measured also has an effect on the successful application of the VBDD method, as these methods have no trouble in locating a severe damage case (for example, the loss of half of the member stiffness), but have varying degrees of success when the damage level is small (Farrar and Jauregui 1998a; 1998b).

Another factor is the quality of the measurements collected. From this study, it was found that only the first mode could be measured reliably in the field, thus limiting the number of modes that could be used in the various damage detection routines. In addition, mode shapes measured from field tests are not mass normalised because the input force is not usually measured; therefore, the various modal contributions cannot be readily added as their relative amplitudes are not known.

Strictly speaking, some of the damage detection methods require that the mode shapes be mass normalised. Included among these methods are the change in flexibility method, the change uniform load surface curvature method and the change in unit load curvature method. The modes measured on site, as was mentioned in the previous paragraph, were not mass normalised, but rather, ortho-normalised, as discussed Section 6.2.1. This limitation may affect the potential sensitivity of these methods to detect damage.

Considering the above discussion, the purpose of Section 6.2 was to examine the performance of the different VBDD methods under more realistic site limitations. In this study, the simulated limitations included the use of widely spaced accelerometers, the

consideration of the first mode only, and the application of results obtained from ortho-normalisation. These limitations reflect what was actually done in the field.

The results of applying VBDD methods to the bridge FE model simulating site limitations can be summarised as follows: most methods could detect localised damage of the type considered here, except for the uniform load surface curvature method. The poor performance of the uniform load surface curvature method may be attributed to the fact that this method is based on the dynamic flexibility matrix which requires mass normalised mode shapes, or it may be due to using the first mode only in building the flexibility matrix, thus introducing a truncation error due to the omission of the contribution of higher modes; although the change in modal flexibility method and the uniform load surface curvature method are based on measured modal flexibility also. Nonetheless, the uniform load surface curvature method could be used to successfully detect the damage in scenario 3 when the damage coincided with a measurement location. In addition, the damage index method seemed to generate consistent results for all the different localised damage scenarios and was more successful in detecting damage than other methods when all of the damage scenarios were considered; this may be attributed to the fact that the damage index method normalizes changes in the damage parameters relative to the undamaged case. Also, the damage index method uses mode shapes that are not required to be mass normalised.

6.3 COMPARING THE FOURTH DAMAGE SCENARIO TO SITE MEASUREMENTS DUE TO IMPACT EXCITATION ON HUDSON BAY BRIDGE

It would be expected that, since the FE model of the bridge was calibrated according to site measurements, any changes made on that model to reflect changes done on the actual bridge would result in an FE model that may still be considered to be calibrated and that represents the bridge in its new state. This is a common practice in the field of mechanical engineering. To save time and money on research and development, the engineers calibrate an FE model according to a prototype that has already been built, through the application of modal testing and vibration analysis. Then, instead of building several prototypes, changes are be made to the calibrated FE model only in

order to improve the design and performance of the piece of machinery that is being developed (Maia and Silva 1997, Ewins 2000).

In the case of the Hudson Bay Bridge, this proved not to be a valid assumption. Table 6.1 compares the natural frequencies of the calibrated FE model with steel plates (corresponding to the fourth damage scenario) to those calculated from site measurements described in Section 4.4 from impact testing of the rehabilitated bridge using a rubber pad for cushioning the hammer. It can be seen from Table 6.1 that the natural frequencies from the FE model do not match those measured on site. This sheds light on another difficulty in applying vibration testing of bridges and other civil structures. In contrast to mechanical engineering components and machinery, bridges are more complicated structures, making it difficult to predict their behaviour. Different parameters enter into this discussion. For example, support conditions, material properties and environmental factors add to the uncertainties in the evaluation of the bridge dynamic properties. The ambient temperature was around 30° C during the first test, whose results were used to calibrate the bridge FE model, while the temperature was around 12° C during the impact test, after the bridge rehabilitation. This temperature difference would cause some change in the bridge natural frequencies and mode shapes, as was observed by Pham et al. (2007).

Table 6.1 Comparison of the natural frequencies from FE model of the Hudson Bay bridge for the fourth damage scenario to measured ones after the rehabilitation work.

Mode No.	Bridge natural frequencies (Hz)	
	4^{th} damage scenario (FE model)	After rehabilitation (site measurements)
1	3.123	2.640
2	4.785	4.253
3	5.737	- - -
4	5.905	5.812
5	7.298	- - -
6	7.724	8.156

The difference in natural frequencies between the two cases listed in Table 6.1 may be also attributed to the fact that the behaviour of the actual bridge is nonlinear, while the FE model of the bridge was assumed to have a linear elastic behaviour. Also, the

difference could be caused by lack of complete shear connectivity between the steel plate and the bridge girders on the actual bridge.

6.4 EFFECT OF DYNAMIC EXCITATION ON THE PERFORMANCE OF VBDD METHODS

6.4.1 Overview

The purpose of this section is to examine the influence of the type of excitation used in extracting the modal properties on the possibility of detecting the damage using the different VBDD techniques that were introduced in Section 2.3. The dynamic properties (natural frequencies and mode shapes) of the FE bridge model were calculated from response time histories generated as a result of dynamic excitation of the bridge, before and after damage, using the excitation methods that were detailed in Section 3.7.

Only the first damage scenario was considered for the comparison, as the results for the other damage scenarios could be deduced from the results for the first scenario. It will be recalled that this damage scenario involved cutting the external reinforcing bars from the middle of all girders in the centre span.

6.4.2 Harmonic excitation

Simulated harmonic excitation was used to excite the bridge, both before and after damage was introduced into the FE model, as detailed in Section 3.7.2. The dynamic properties of the bridge were extracted for both conditions. Harmonic excitation with a frequency corresponding the bridge's first mode only was considered, as it was the only mode that could be estimated with acceptable accuracy from site measurements.

The results from the application of the VBDD methods are shown in Figure 6.26 to Figure 6.31. By examining these figures, it can be noticed that the results are not as clear as those presented in Section 6.2.2, where the results from eigenvalue analysis before and after damage were compared. This suggests that the introduction of harmonic excitation in the simulation has reduced the quality of the extracted modal properties, which is contrary to what was expected. One reason for that could be the contribution of other modes to the bridge vibration under the harmonic loading, even though resonant forcing frequency at the fundamental frequency was used. The resulting operational deflected shape that differed from a pure mode would likely make damage detection

more difficult, a fact that should be remembered when performing actual dynamic testing and damage detection in the field. In field testing, it is even more difficult to tune the harmonic excitation to the bridge's natural frequency as there would be some signal errors (in the signal's frequency or amplitude, or both) that would cause the excitation signal to be shifted slightly from the actual bridge frequency.

It can also be noticed from Figure 6.26 to Figure 6.31 that the change in mode shape and change in unit load surface curvature methods were somewhat ambiguous in their indication of the location of damage. Both methods (Figure 6.26 and Figure 6.31) showed many peaks along the three spans of the bridge, making it difficult to indentify the location of damage. On the other hand, the change in mode shape curvature method (Figure 6.27) showed multiple peaks near and at the damage location, similar to the distributions shown in Figure 6.2, where eigenvalue analyses were used to generate mode shapes.

It can be concluded, therefore, that the change in mode shape curvature method successfully localised the damage in these simulations when harmonic excitation was used to excite the bridge. A similar conclusion can be drawn by examining Figure 6.28, where the damage index method was used to detect damage. In this figure, the peaks coincided with the location of damage, thus successfully locating the damage.

The change in modal flexibility method (Figure 6.29) showed multiple peaks within each of the bridge spans. However, the highest peaks were at the centre of middle span where damage was located; this was not true though, along all measured lines, making the performance this method only slightly better than that of the change in mode shape method (Figure 6.26).

The change in uniform load surface curvature method (Figure 6.30) showed peaks of equal amplitudes in all spans, making it visually impossible to locate the damage.

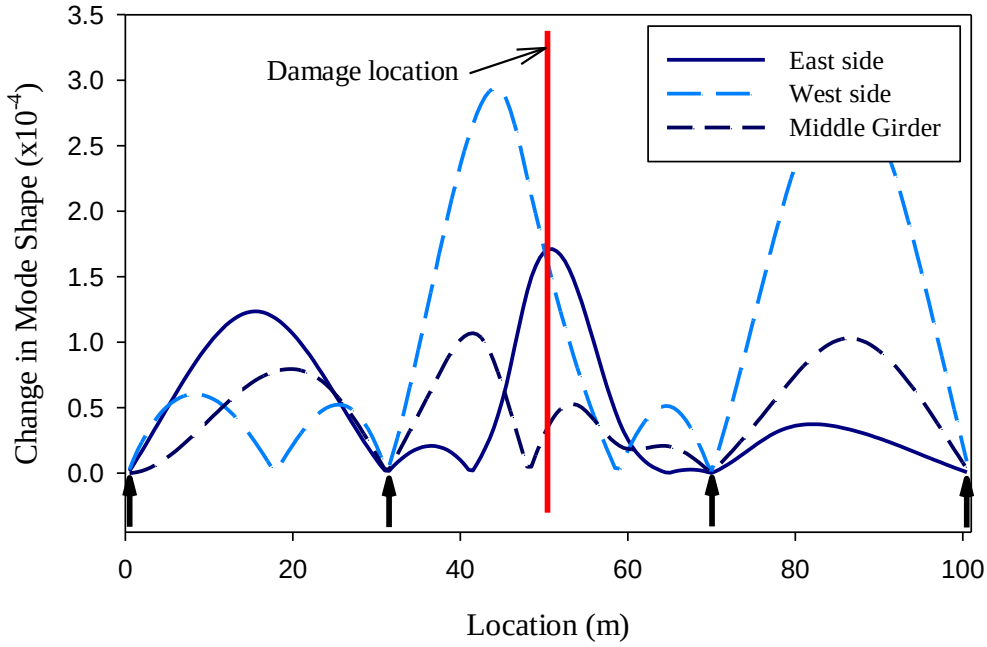

Figure 6.26 Distribution of the change in mode shape caused by first damage scenario using harmonic excitation.

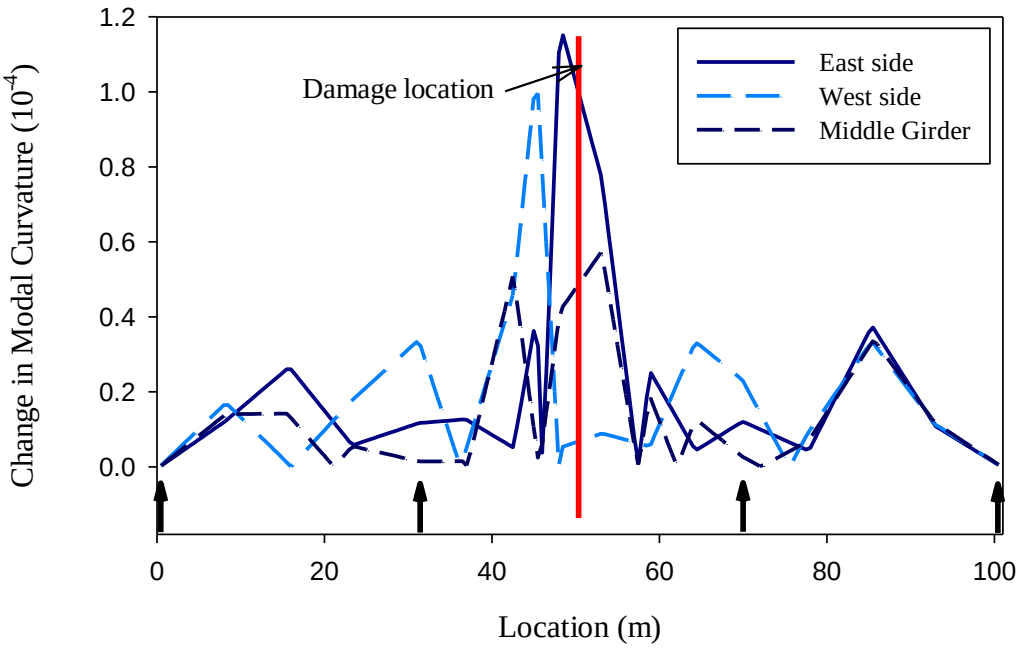

Figure 6.27 Distribution of the change in mode shape curvature caused by first damage scenario using harmonic excitation.

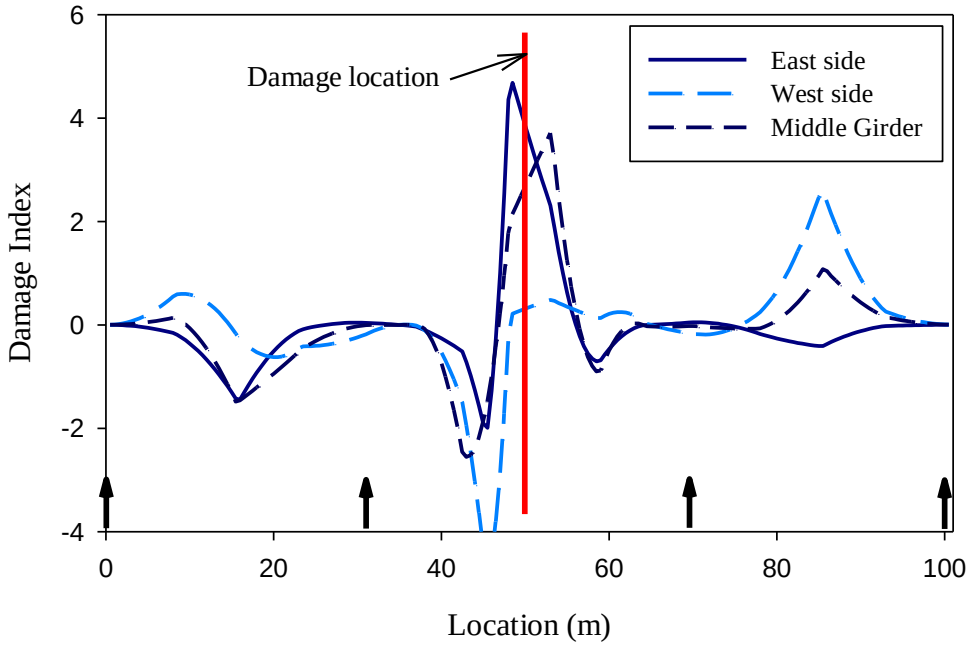

Figure 6.28 Distribution of the damage index caused by first damage scenario using harmonic excitation.

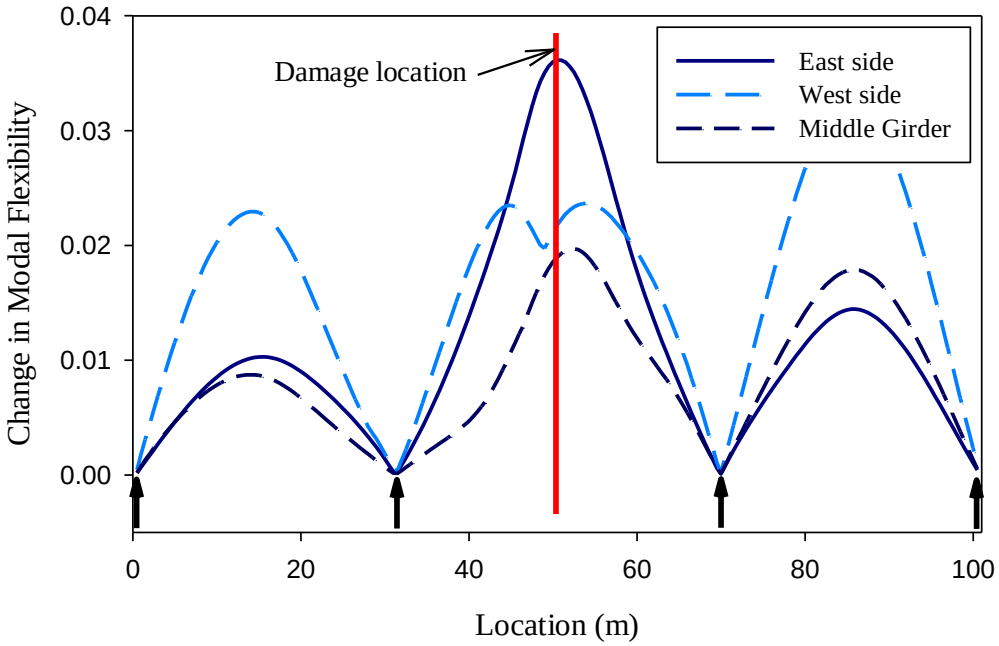

Figure 6.29 Distribution of the change in modal flexibility caused by first damage scenario using harmonic excitation.

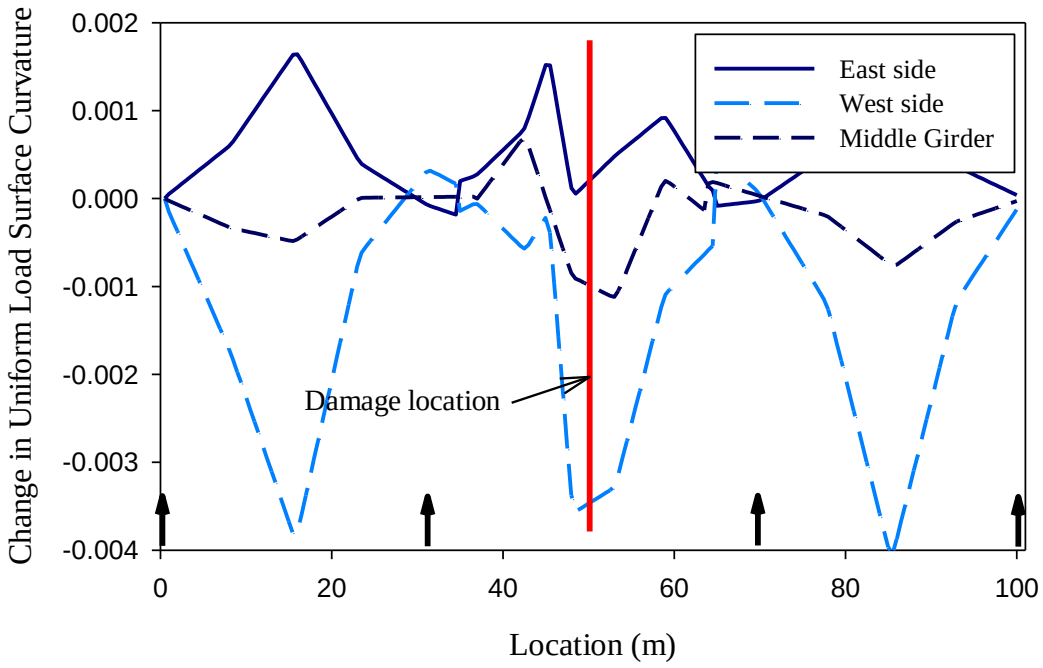

Figure 6.30 Distribution of the change in uniform load surface curvature caused by first damage scenario using harmonic excitation.

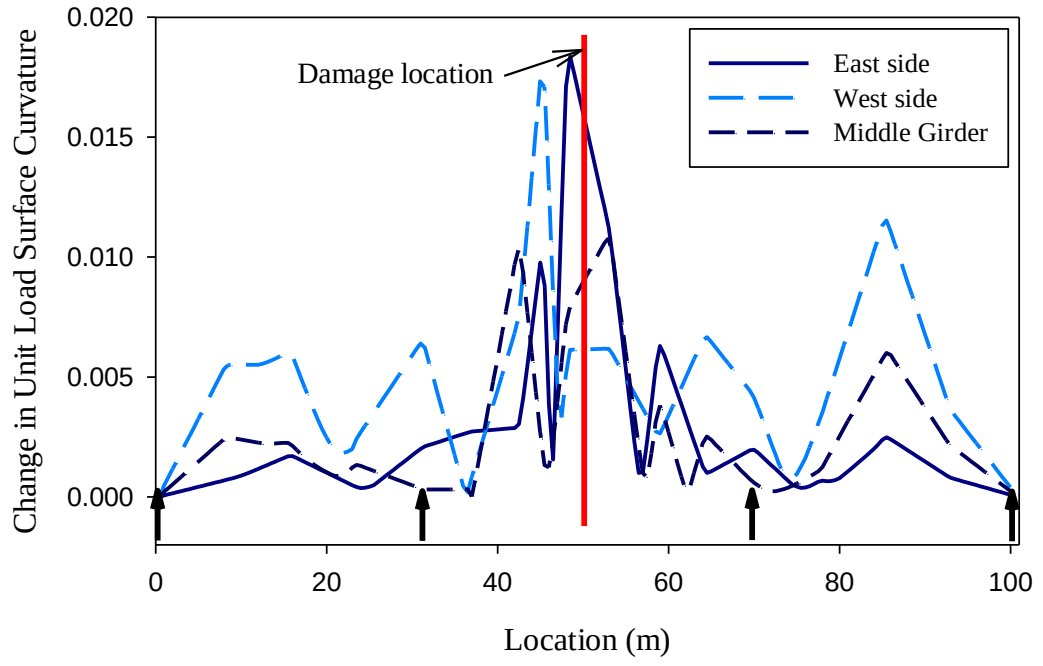

Figure 6.31 Distribution of the change in unit load surface curvature caused by first damage scenario using harmonic excitation.

6.4.3 Impact excitation

In this section, impact excitation was used to excite the bridge, as described in Section 3.7.4. The dynamic properties of the bridge were then calculated before and after damage. In general, all VBBD methods managed to locate the damage except the change in unit load surface curvature method, which also failed to locate the damage when mode shapes were found using an eigenvalue analysis (Section 6.2.2).

Damage parameter distributions associated with the application of the VBDD methods are shown in Figure 6.32 to Figure 6.37. By examining these figures, it can be noticed that they look very similar to Figure 6.1 to Figure 6.6, which were generated using eigenvalue analyses before and after damage. As in Figure 6.30, the change in uniform load surface curvature method (Figure 6.36) showed multiple peaks resulting in false positive readings, i.e. indicating damage at a location that was not damaged. It can be concluded, therefore, that impact excitation appeared to generate modal properties that were very close to those calculated from eigenvalue analysis, thus indicating that impact excitation is a suitable form of structural dynamic excitation for the purposes of VBDD.

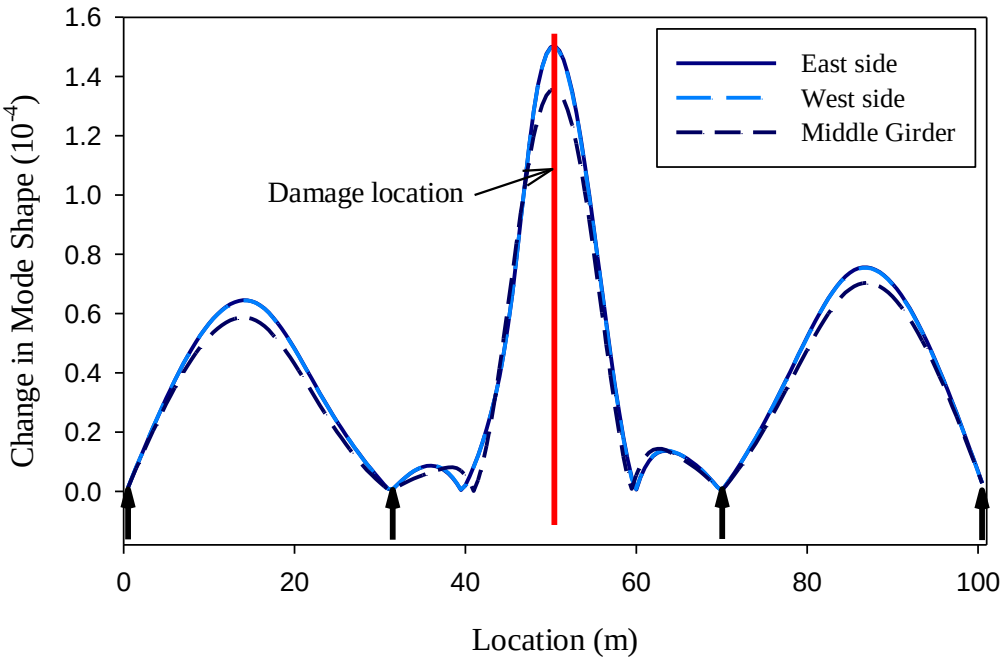

Figure 6.32 Distribution of the change in mode shape caused by first damage scenario using impact excitation.

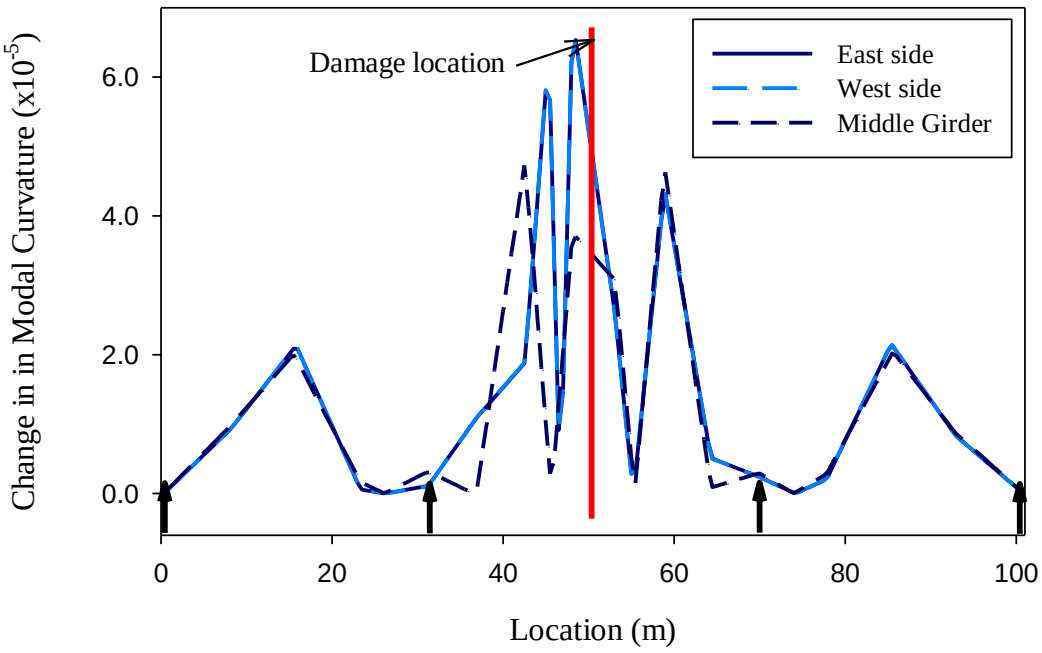

Figure 6.33 Distribution of the change in mode shape curvature caused by first damage scenario using impact excitation.

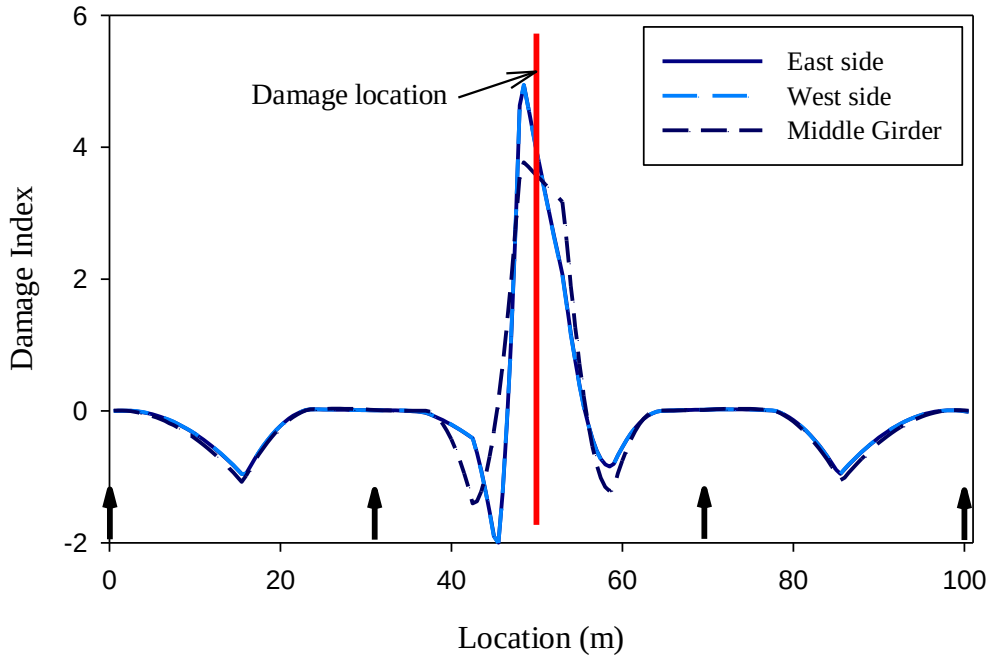

Figure 6.34 Distribution of the damage index method caused by first damage scenario using impact excitation.

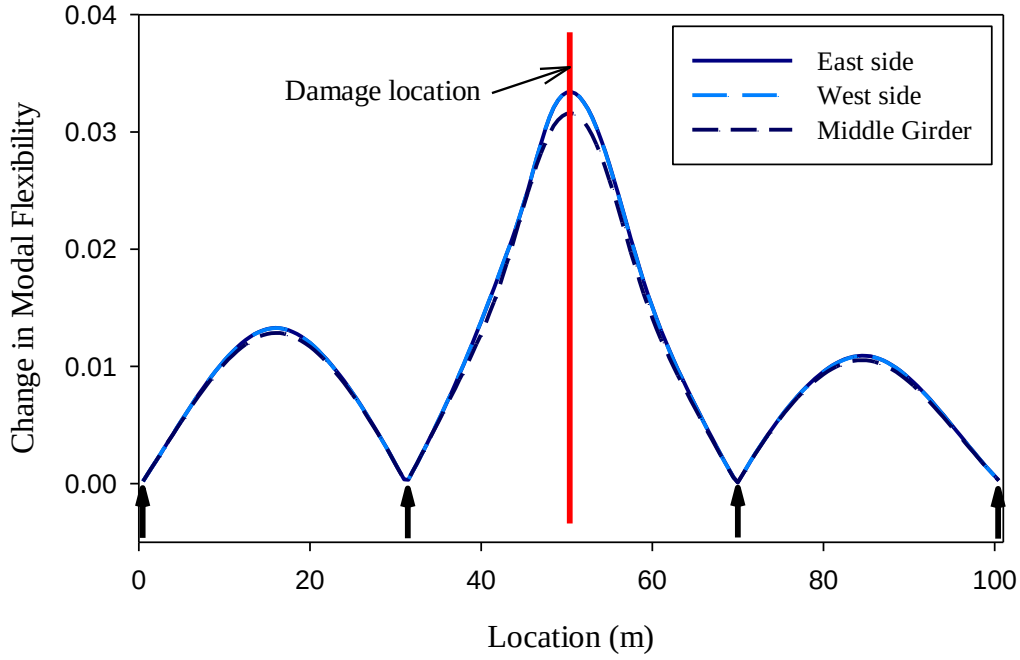

Figure 6.35 Distribution of the change in modal flexibility caused by first damage scenario using impact excitation.

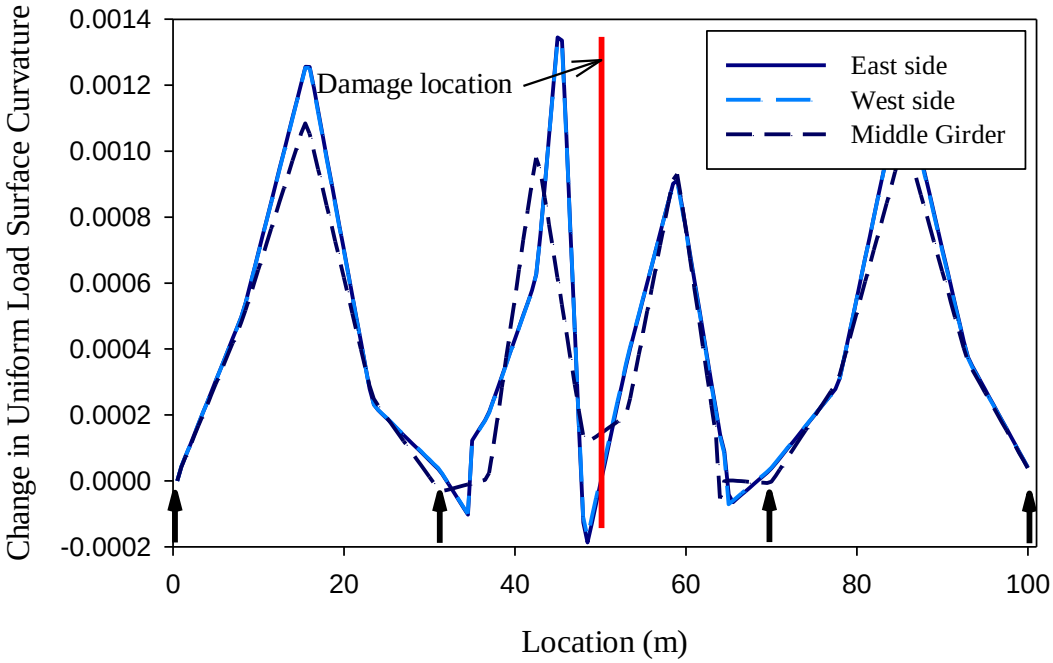

Figure 6.36 Distribution of the change in uniform load surface curvature caused by first damage scenario using impact excitation.

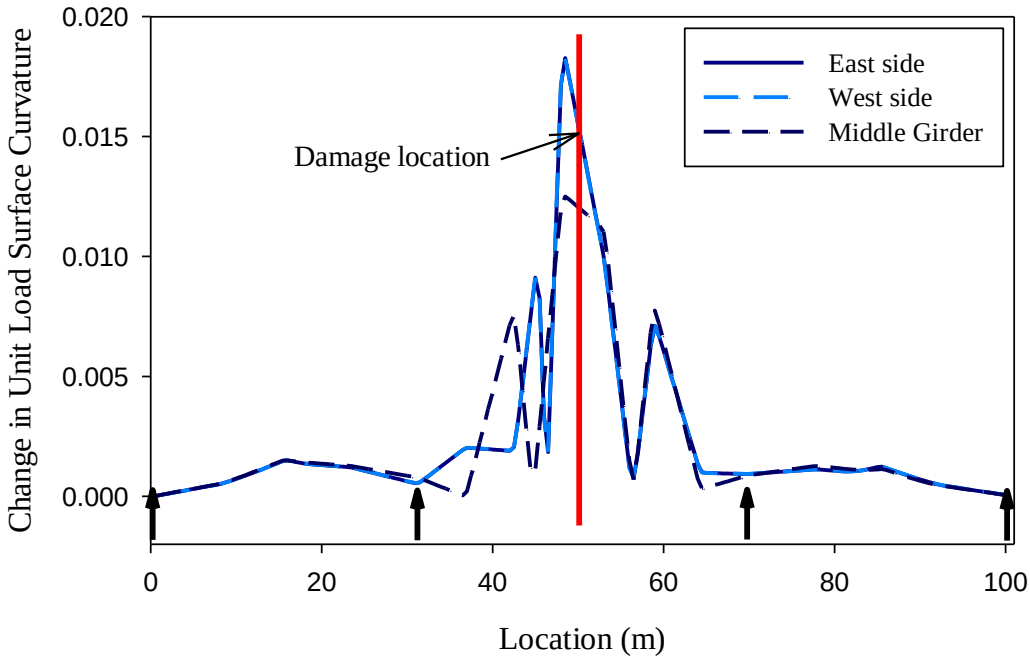

Figure 6.37 Distribution of the change in unit load surface curvature caused by first damage scenario using impact excitation.

One reason for the good quality of the results obtained from the impact excitation is that the excitation is applied on the structure as a short duration pulse, after which the structure would vibrate freely at it own natural frequencies without an external interfering force. In addition, this pulse force imparts an approximately equal level of energy at all the frequencies in the effective range, thus exciting all the bridge modes to the same level, as explained in Section 3.7.4.

6.4.4 Free decay of random excitation

In this section, the free vibration part (free decay) of the bridge response to the simulated random excitation was used to extract the dynamic properties of the bridge before and after damage defined by the first damage scenario (see Section 3.7.3 and Section 3.11). The results of applying VBDD methods are shown in Figure 6.38 to Figure 6.43. In general, the distributions shown in these figures are almost identical to those obtained when mode shapes were determined by eigenvalue analysis (Figure 6.1 through Figure 6.6).

Figure 6.38 to Figure 6.43, which show the results for the VBDD methods in this section, were very similar to the figures in Section 6.4.3 for impact excitation; thus, the same conclusions that were arrived at in Section 6.4.3 are applicable to this section also. In particular, it was noted that modal properties calculated from the free decay portion of random vibration events were close to the theoretically correct values that were calculated from an eigenvalue analysis, thus yielding good VBDD results.

Similar reasoning as that discussed in Section 6.4.3 can be made here also, regarding the quality of measurements calculated from free decay vibration, where the good quality of the results obtained from free decay vibration may be attributed to the fact that the structure was vibrating freely at it own natural frequencies without an external interfering force.

6.4.5 Conclusions

In this section, the effect of dynamic excitation on the performance of VBDD methods was examined. The types of dynamic excitation included: harmonic excitation, impact excitation, and free decay of random excitation.

The results of this section indicated that impact excitation and free decay following random excitation produced modal properties that were very close to those calculated from eigenvalue analysis. On the other hand, modal properties deteriorated when harmonic excitation was used. As a result, the VBDD methods were found to perform better under conditions of free vibration.

It was also demonstrated that the change in mode shape curvature method, the damage index method, and the unit load surface curvature method were more successful in localising damage than the change in mode shape method, the change in modal flexibility method, or the change in uniform load surface curvature method. The latter methods were somewhat ambiguous in their indication of the location of damage.

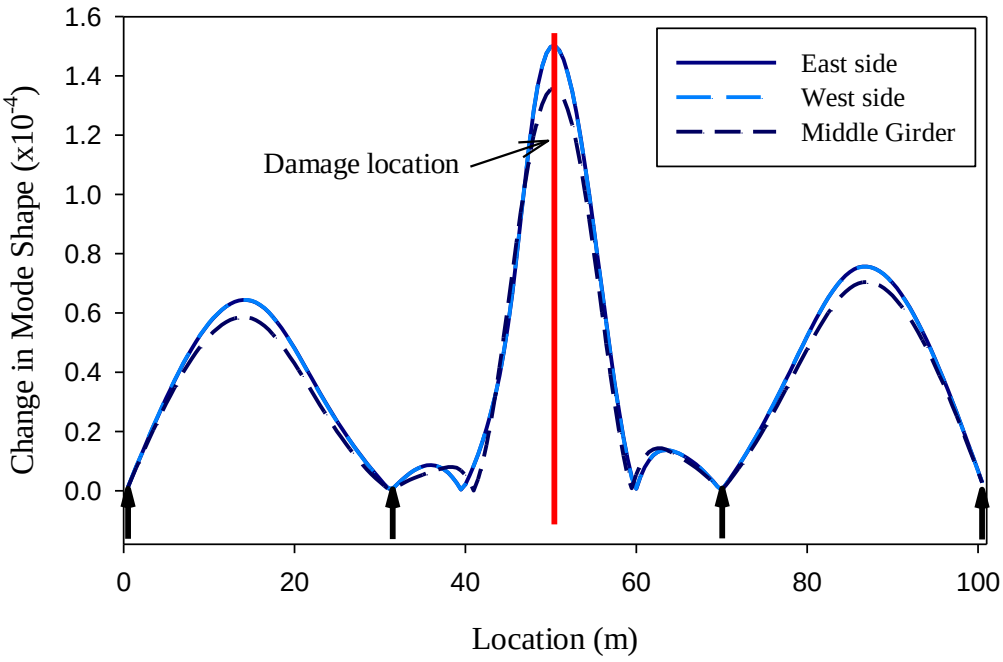

Figure 6.38 Distribution of the change in mode shape caused by first damage scenario using free decay vibration.

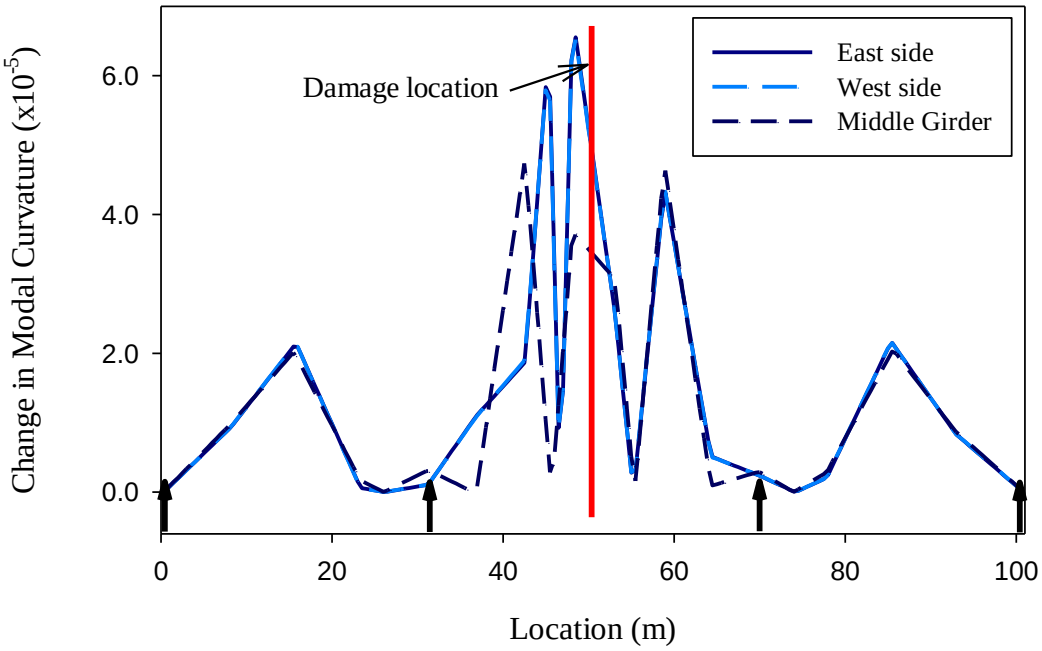

Figure 6.39 Distribution of the change in mode shape curvature caused by first damage scenario using free decay vibration.

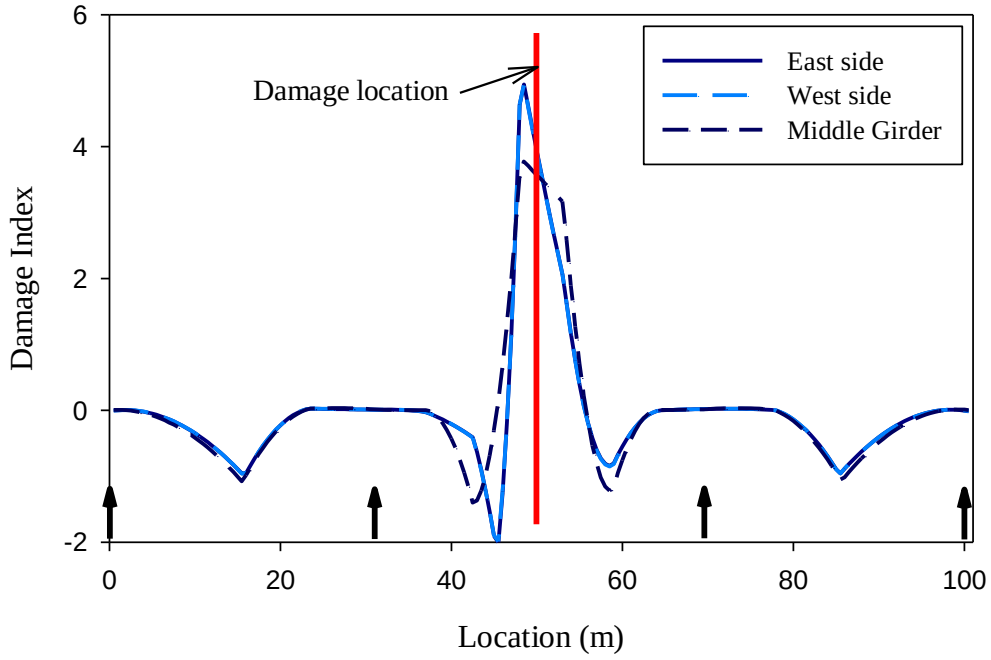

Figure 6.40 Distribution of the damage index caused by first damage scenario using free decay vibration.

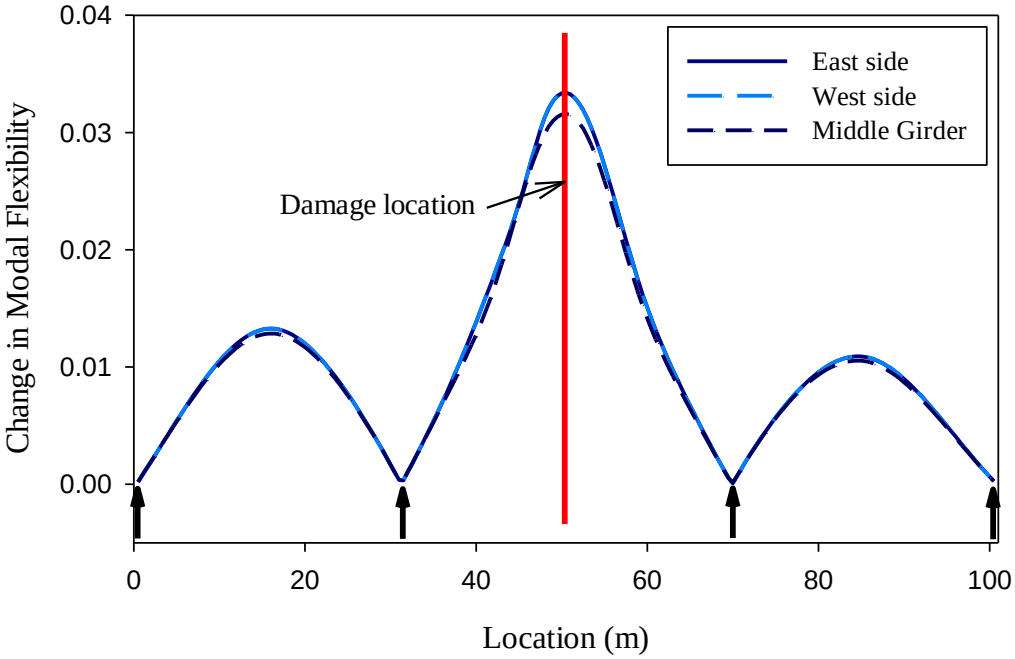

Figure 6.41 Distribution of the change in modal flexibility caused by first damage scenario using free decay vibration.

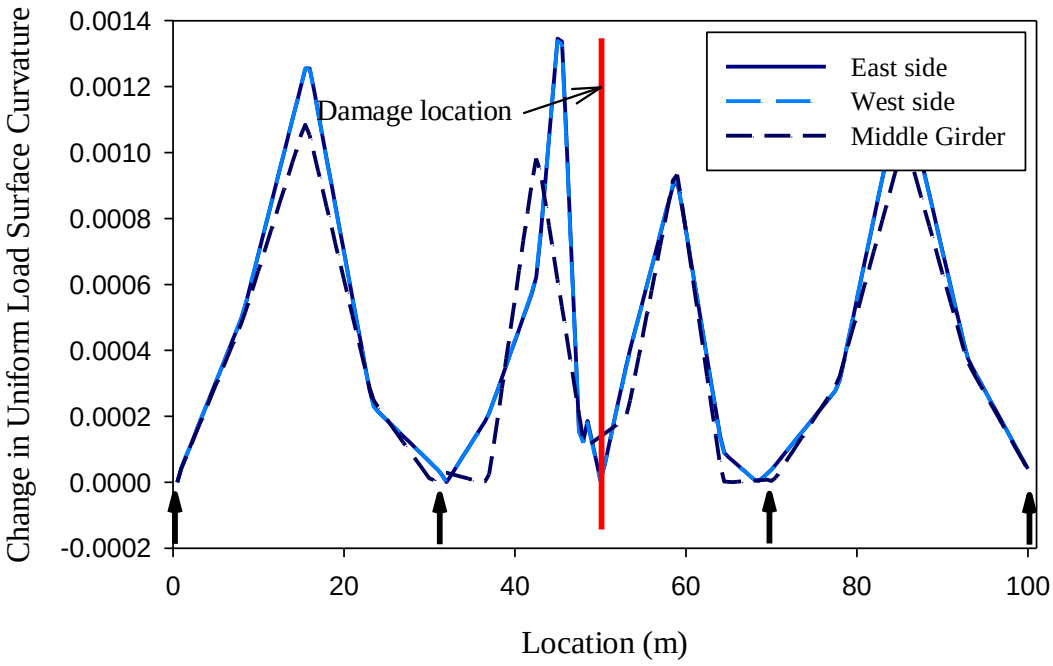

Figure 6.42 Distribution of the change in uniform load surface curvature caused by first damage scenario using free decay vibration.

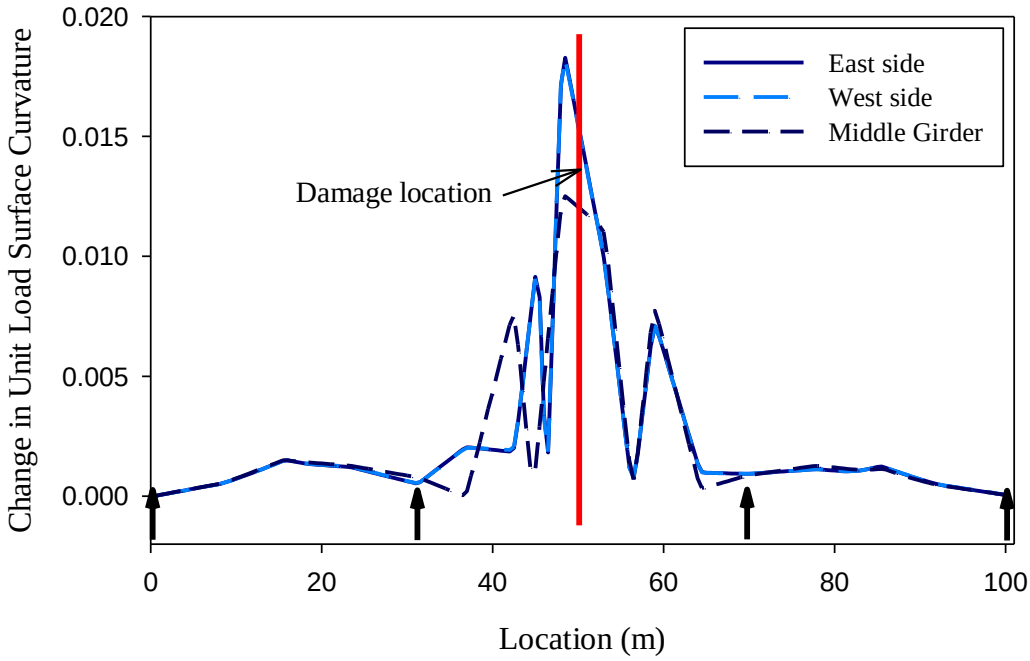

Figure 6.43 Distribution of the change in unit load surface curvature caused by first damage scenario using free decay vibration.

6.5 EFFECT OF NOISE ON THE APPLICABILITY OF VBDD

In this section, the influence of uncertainty and measurement error on the performance of VBDD methods is examined. Different levels of white noise were added either to the input excitation force to simulate uncertainty in the input force, or to the output bridge displacement time-history at measurement nodes (see Figure 3.25) to simulate uncertainty in the measured signal. The noise considered had variance levels of 1%, 2% and 5% of that of the original force or displacement signal upon which the noise was superimposed. These noise levels were selected on the basis of a maximum of 3.7% noise measured in the bridge response from truck excitation, and 5.2% for impact excitation, as defined in Section 4.2.6. In addition, a case with a noise level equal to 10% in conjunction with harmonic excitation was considered to examine the effects of a high level of noise on the performance of VBDD.

For each level of noise, ten measurements, 10 s long each (i.e. simulation runs) were performed and the modal properties for these runs were averaged for use in VBDD. This procedure was similar to that used for site measurements, where several tests were conducted and their results were averaged for further processing. Ten simulations were used because this is the approximate number of tests that can usually be conducted on site, taking into consideration time constraints, traffic control, set up times, etc.

Similar to the analyses described in Section 6.4, only the first damage scenario was considered for this part of the study, as the results of the other damage scenarios followed similar trends.

6.5.1 Effect of noise on VBDD when harmonic excitation is used

Figure 6.44 shows the effect of input noise level in the excitation force on the capability of the change in mode shape method to detect damage using harmonic excitation. It can be seen from Figure 6.44 that uncertainty in the definition of force time history had a minimal effect on the ability of the change in mode shape method to detect damage. On the other hand, it can be seen from Figure 6.45, that similar levels of uncertainty had an adverse effect on the performance of the change in mode shape method when the noise was introduced into the simulated sensor readings. It can be seen from Figure 6.45 that even for a 1% noise level, the distribution became ambiguous, and at higher noise levels

it became impossible to detect damage. This suggests that the change in mode shape method would have difficulty in field tests in detecting damage, and a more robust VBDD method is required for field testing.

The difference in performance between the two cases (noise in the excitation force and noise in the simulated sensors readings) may be attributed to the fact that, when the noise is added to the input force, the same noise signal is passed to all measurement points on the bridge. On the other hand, when noise is introduced to the output signal, a different noise signal is added to each output signal, even though all noise signals had the same statistical properties. In addition, the bridge itself can be considered as a filter or transfer function that reduces the effect of input force noise on the output response.

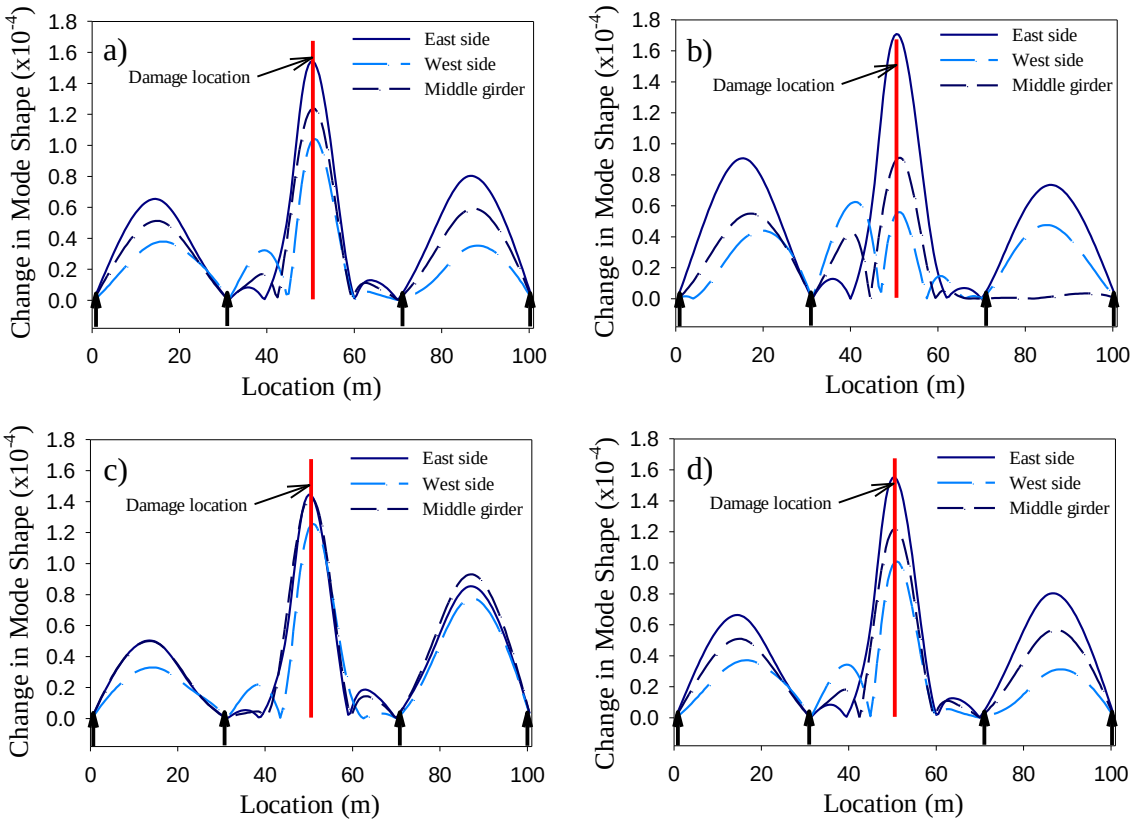

Figure 6.44 Distribution of the change in mode shape for the first damage scenario when harmonic excitation was used and noise was added to input force: a) 1% noise, b) 2% noise, c) 5% noise, d) 10% noise.

Figure 6.46 shows the effect of input noise on the damage index parameter using harmonic excitation. It can be seen from this figure that there was no observable effect

of the noise on the damage index method. By examining Figure 6.47, it can be seen that the noise did degrade the performance of the damage index method when it was introduced into the simulated sensor readings in that false peaks in the graph showed up at the end spans where there was no damage. Also, significant peaks were produced near the location of damage; nonetheless, all the peaks within the middle span were at, or very near, the damaged location on the bridge. This indicates that the damage index method is more robust than the change in mode shape method. This superior performance of the damage index method may be attributed to the fact that the damage index method normalizes changes in the damage parameters relative to the undamaged case, and that the damage index method uses mode shapes that are not required to be mass normalised. This is discussed in more details in Section 6.2.6.

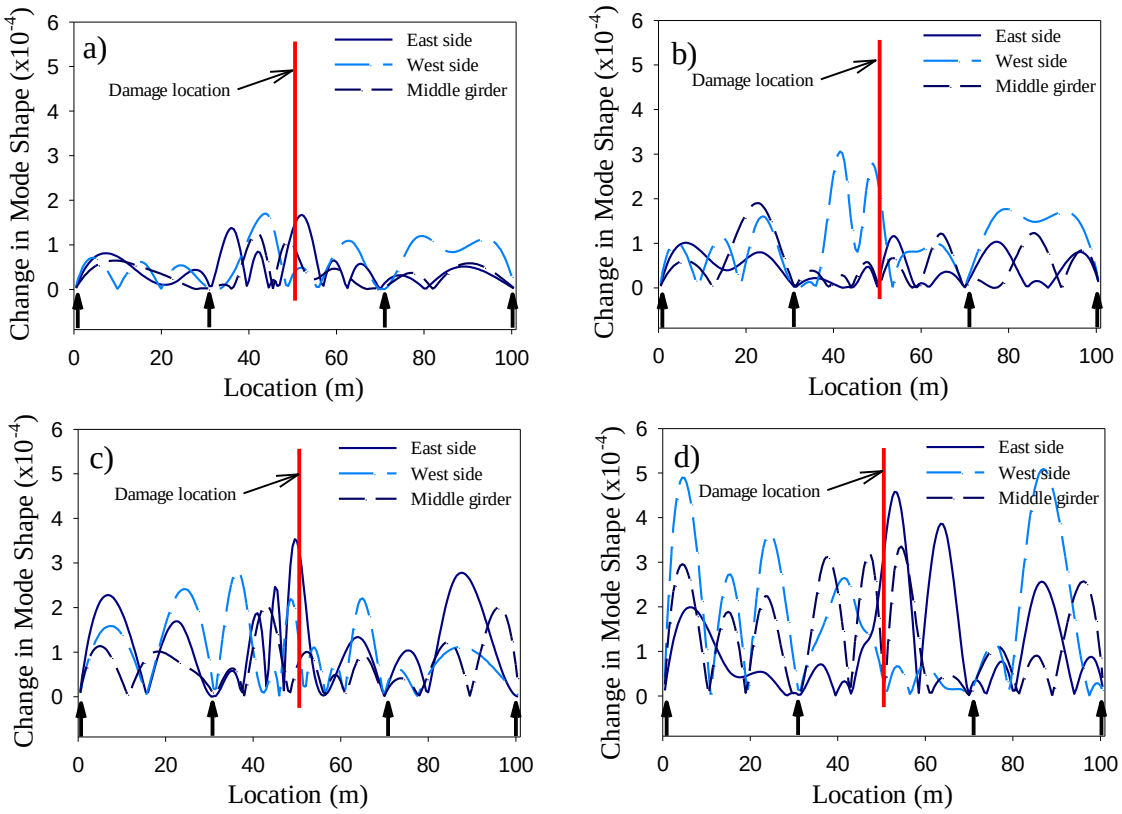

Figure 6.45 Distribution of the change in mode shape for the first damage scenario when harmonic excitation was used and noise was added to the output signal: a) 1% noise, b) 2% noise, c) 5% noise, d) 10% noise.

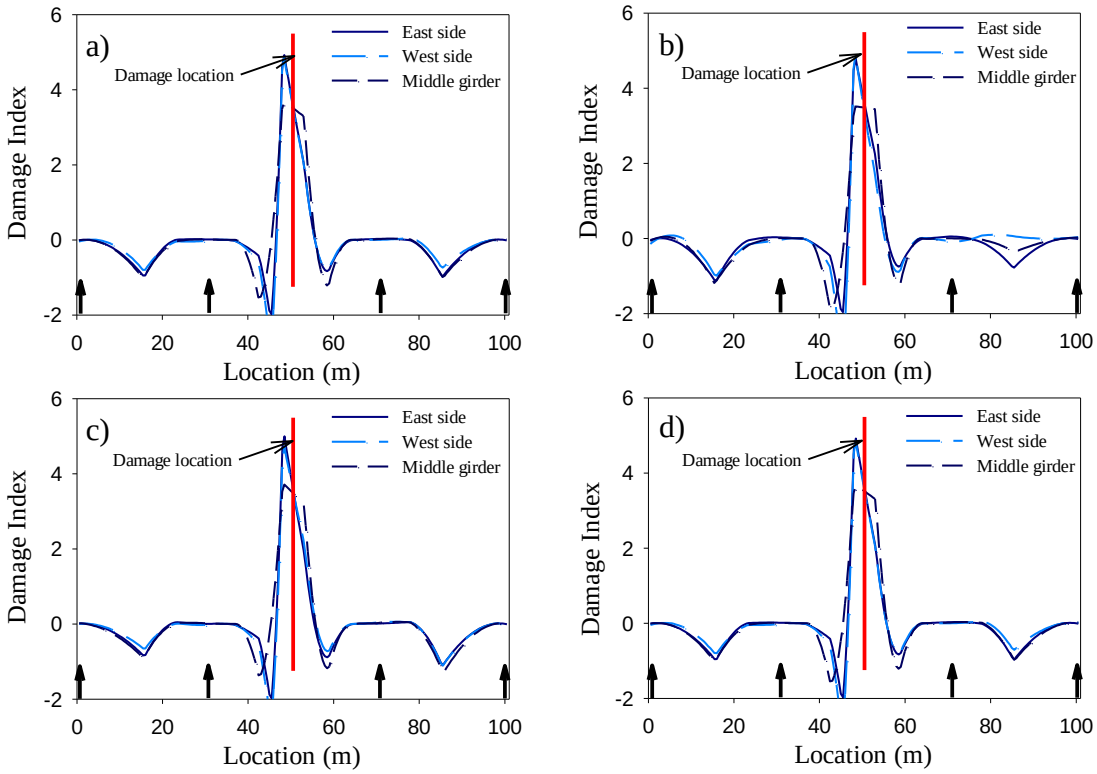

Figure 6.46 Distribution of the damage index for the first damage scenario when harmonic excitation was used and noise was added to input force: a) 1% noise, b) 2% noise, c) 5% noise, d) 10% noise.

6.5.2 Effect of noise on VBDD when impact excitation is used

Figure 6.48 shows the effect of input noise level in the excitation force on the capability of the change in mode shape method to detect damage using impact excitation. It can be seen from Figure 6.48 that uncertainty in the definition of force time history did have an effect on the ability of the change in mode shape method to detect damage, where high peaks could be noticed in other spans in addition to the middle span. In Figure 6.49, similar levels of uncertainty had an adverse effect on the performance of the change in mode shape method when the noise was introduced into the simulated sensor readings. It can be seen from Figure 6.49 that peaks in the curve in the end spans were of larger amplitude that the peaks in the middle span where damage was simulated. This suggests that the change in mode shape method would have difficulty in field tests in detecting damage, and a more robust VBDD method is required for field testing.

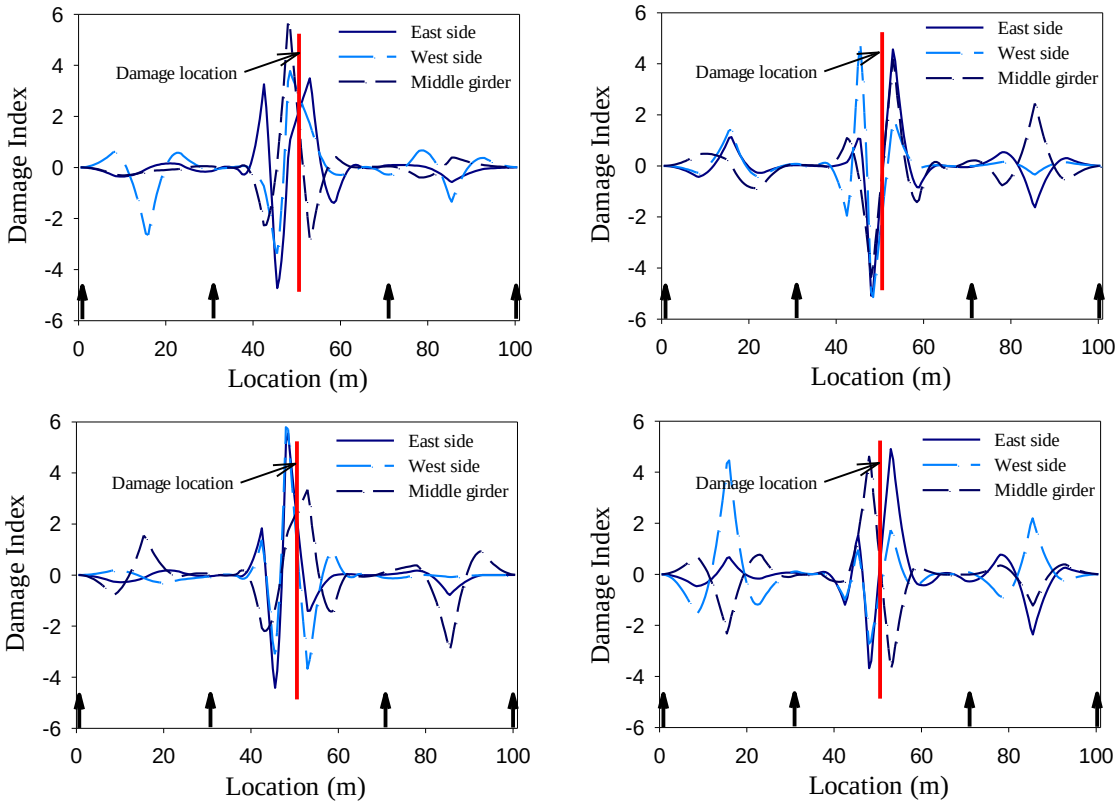

Figure 6.47 Distribution of the damage index for the first damage scenario when harmonic excitation was used and noise was added to output signal: a) 1% noise, b) 2% noise, c) 5% noise, d) 10% noise.

The same reasoning that was made in Section 6.5.1, regarding the difference in performance between the two cases (noise in the excitation force and noise in the simulated sensors readings), applies here too. For noise in the input force, the same noise signal is passed to all measurement points on the bridge, and for noise in the output signal, a different noise signal is added to each output signal.

By comparing the effect of noise on impact excitation (Figure 6.48 and Figure 6.49) to the effect of noise on harmonic excitation (Figure 6.44 and Figure 6.45), it can be observed that input noise had little effect when harmonic excitation was used. One reason for that could be that when harmonic excitation was used, the bridge was forced to vibrate at the applied forcing frequency. On the other hand, for impact excitation, the excitation energy was spread over a broad range of frequencies, and the bridge essentially vibrates freely under its own natural frequencies, thus allowing noise to have

more influence on the bridge vibration. Another observation was that harmonic excitation was more sensitive to output noise than impact excitation. That may be attributed to the contributions of other modes to the bridge vibration under the harmonic loading, as was argued in Section 6.4.2.

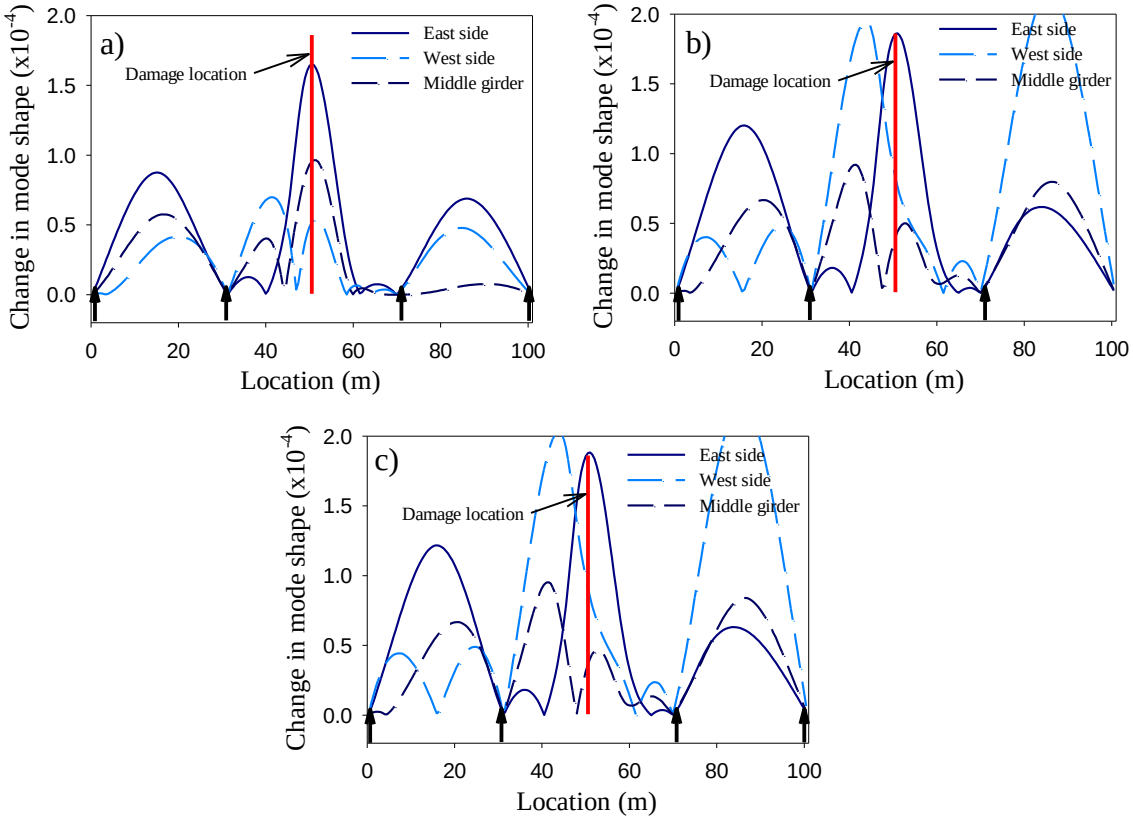

Figure 6.48 Distribution of the change in mode shape for the first damage scenario when impact excitation was used and noise was added to input force: a) 1% noise, b) 2% noise, c) 5% noise.

Figure 6.50 shows the effect of input noise on the damage index parameter using impact excitation. It can be seen from this figure that there was no observable effect of the noise on the damage index method. By examining Figure 6.51, it can be seen that the noise did degrade the performance of the damage index method when it was introduced into the simulated sensor readings in that false peaks in the graph showed up at the end spans where there was no damage. Also, significant peaks were produced near the location of damage; nonetheless, all the peaks within the middle span were at, or very near, the damaged location on the bridge. These results are similar to the results presented in

Section 6.5.1 when simulated harmonic excitation was used. The argument that was made in Section 6.5.1 regarding the performance of the damage index method would be applicable here also.

From the results presented in Section 6.5.2 and this section, it can be concluded that the damage index method was more successful in detecting and locating damage than the change in mode shape method, and that the performance of both methods was worse when noise was added to the output signal than when the noise was superimposed on the excitation force.

The effect of different levels of input and output noise on the performance of the VBDD methods considered is detailed in Appendix G.

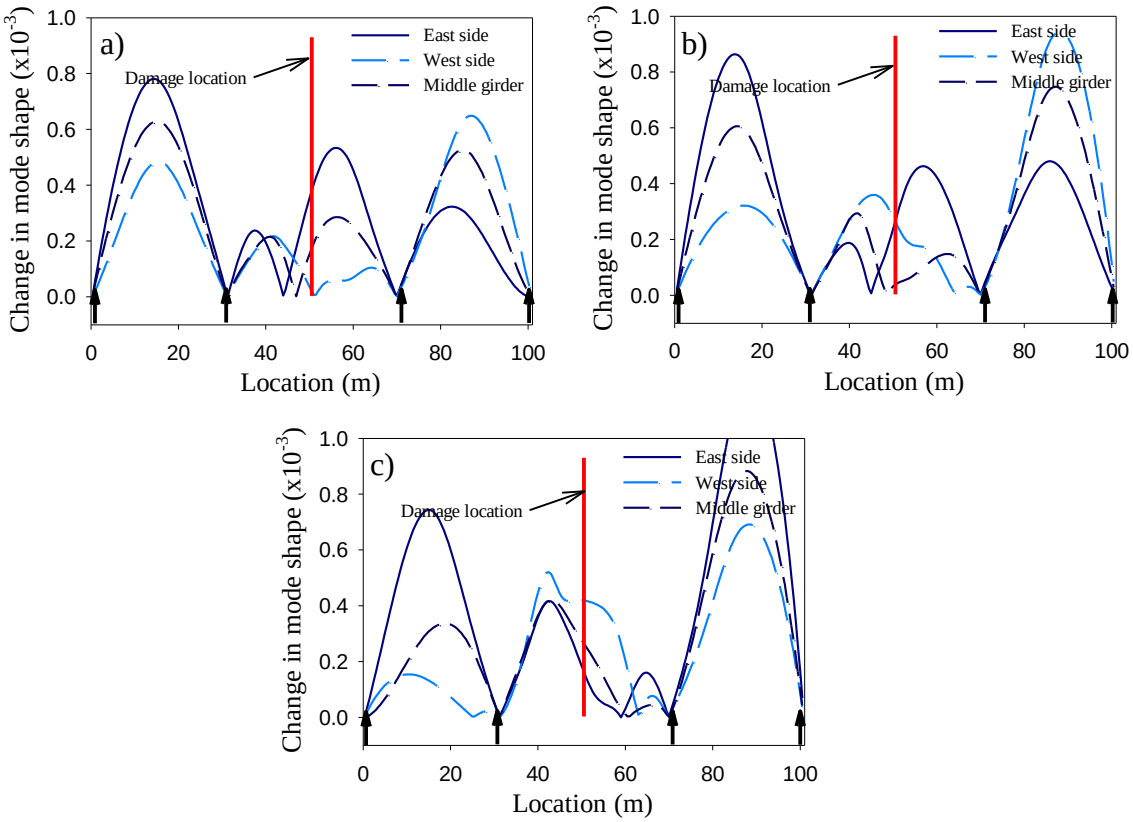

Figure 6.49 Distribution of the change in mode shape for the first damage scenario when impact excitation was used and noise was added to the output signal: a) 1% noise, b) 2% noise, c) 5% noise.

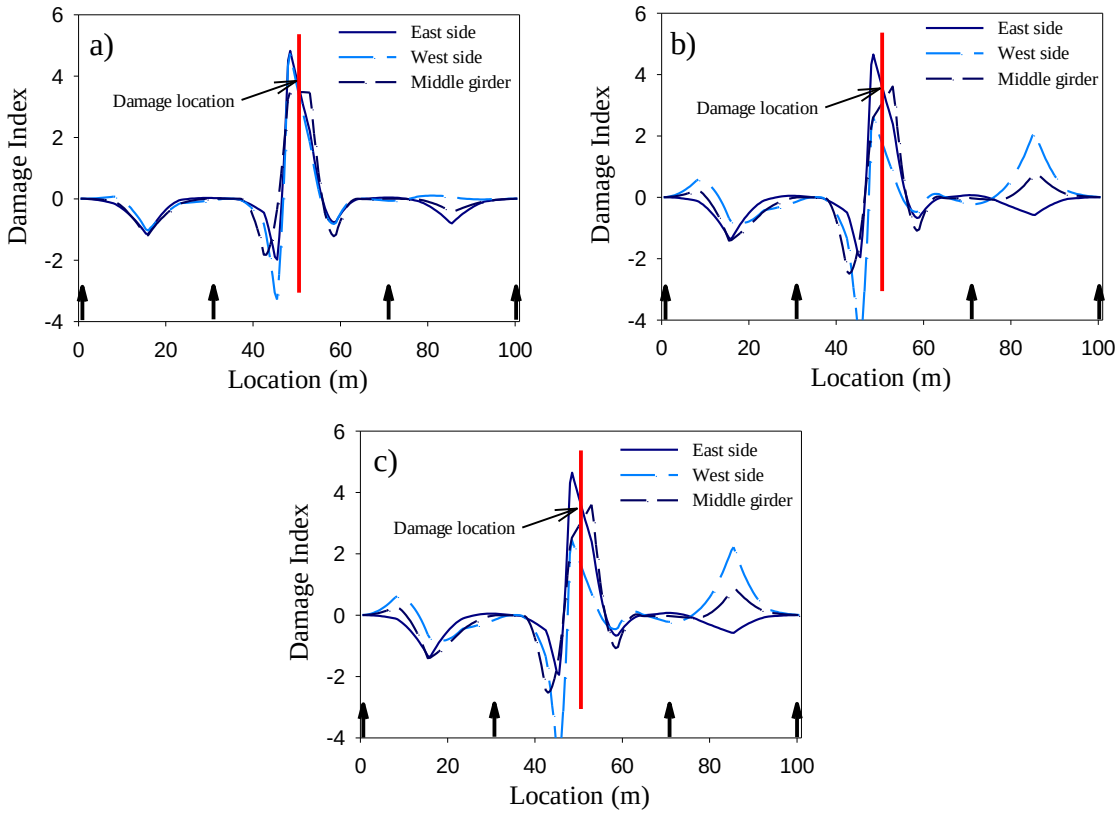

Figure 6.50 Distribution of the damage index for the first damage scenario when impact excitation was used and noise was added to input force: a) 1% noise, b) 2% noise, c) 5% noise.

6.5.3 Effect of averaging of readings on improving VBDD

Although it was not feasible to conduct a large number of runs on site due to time constraints and limited access, it would nevertheless be useful to examine whether increasing the number of trials included in the averaged results would improve the performance of VBDD methods. To investigate this question, simulations were performed with 5% noise for 10, 20, 50 and 100 runs. The mode shapes calculated from these runs were averaged and used in the VBDD methods. Figure 6.52 shows the application of the change in mode shape method for different numbers of averaged simulations using harmonic excitation. From this figure, it can be seen that, even if the number of runs was increased to 100, this number of repetitions did not improve the results in any meaningful way. This indicates that a larger number of simulations would be needed to reduce the effect of measurement noise on the performance of VBDD

methods. As a comparison, Figure 6.53 presents similar results to those shown in Figure 6.52, but this time using impact excitation along with the damage index method. From this figure, it can be seen again that the number of averaged repetitions used for this simulation was not sufficiently high to improve the performance of the damage index method, beyond that seen with 10 trials.

The above observation agrees with Zhou's (2006) conclusion that for random excitation, 400 trials were required for the change in mode shape method to achieve a 91.1% probability of successfully locating damage.

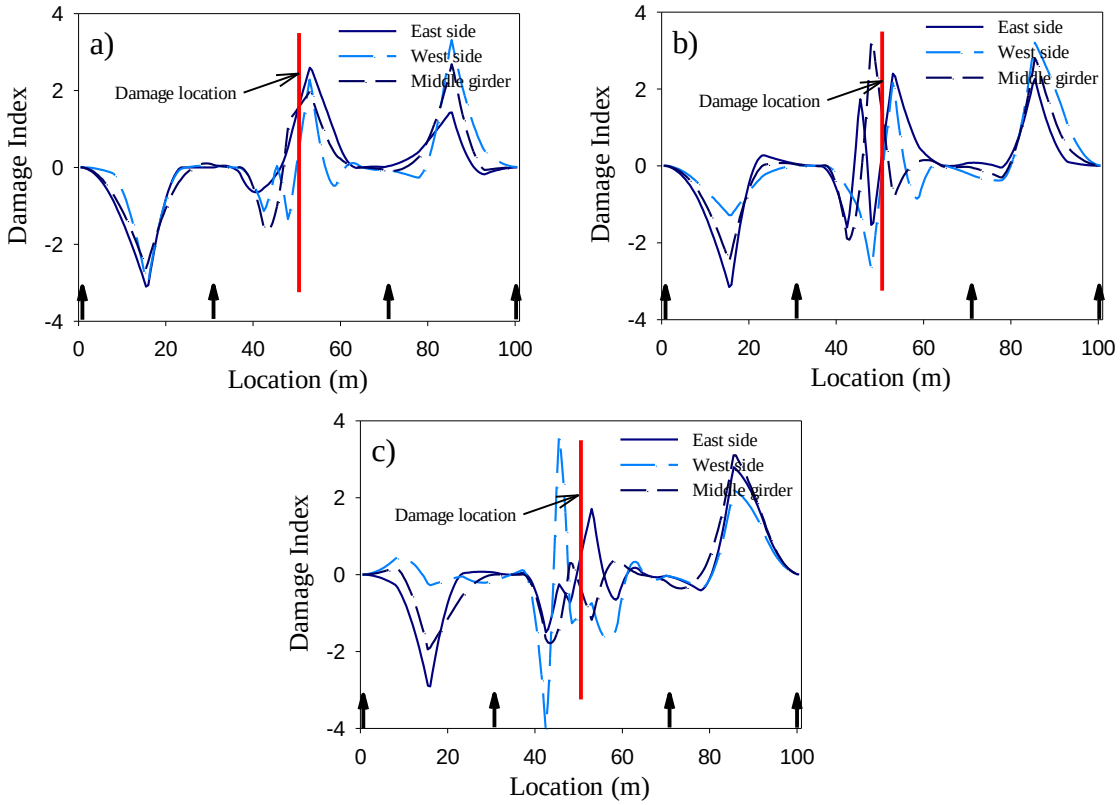

Figure 6.51 Distribution of the damage index for the first damage scenario when impact excitation was used and noise was added to output signal: a) 1% noise, b) 2% noise, c) 5% noise.

6.5.4 Conclusions

It can be seen from the results presented in this section (and Appendix G) that, in general, the VBDD methods were less sensitive to the noise when it was added to the input excitation signal than when that noise was applied to the output response of the

structure. Also, it can be noticed that the ability of VBDD methods to detect damage deteriorated as the noise level was increased. Of the different VBDD methods, the damage index method performed better that the other methods, successfully localizing the damage for 1st damage scenario even when noise was present. Also, it was found that more than 100 events were required to improve the ability of VBDD methods to successfully localize the damage with the presence of noise.

In conclusion, it can be suggested that using more that one method to detect damage would be beneficial, as different methods gave results of varying accuracy under different conditions (e.g. damage location and noise level), as can be seen from the results presented in this section and in Appendix G.

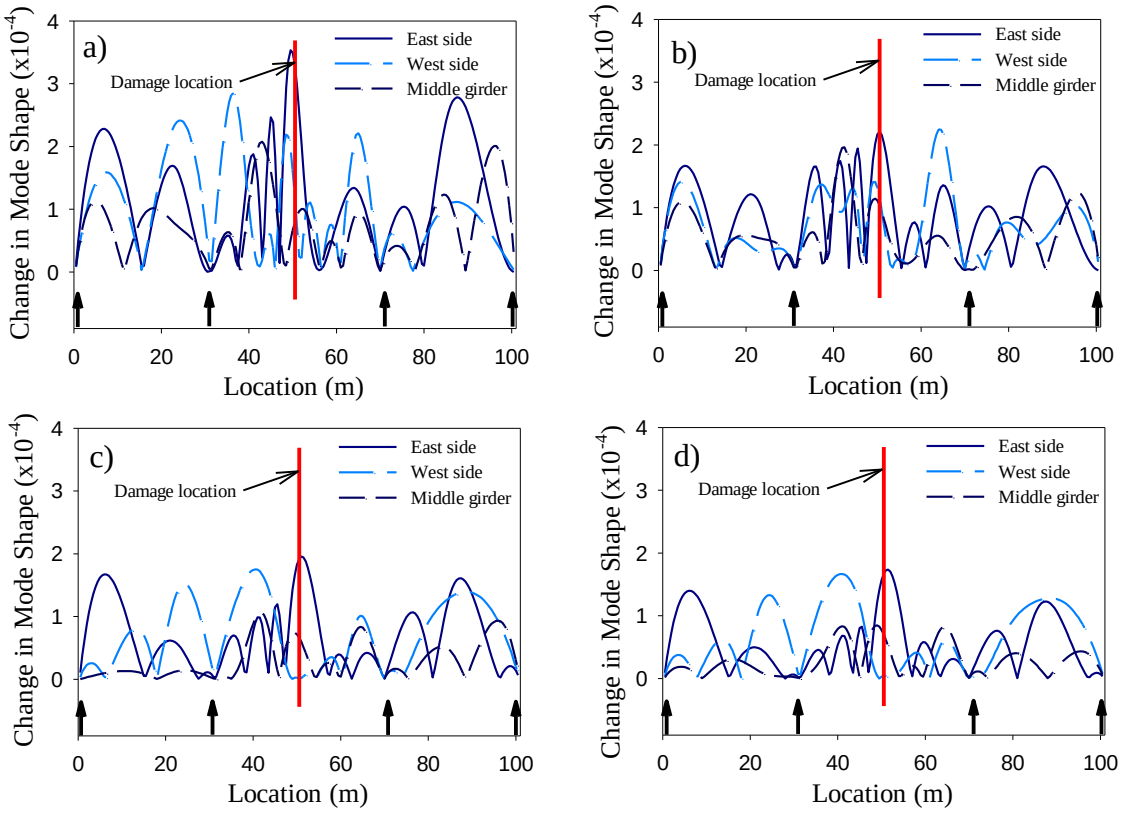

Figure 6.52 Distribution of the change in mode shape for the first damage scenario when harmonic excitation was used and 5% noise was added to output signal:
a) 10 simulations, b) 20 simulations, c) 50 simulations, and d) 100 simulations.

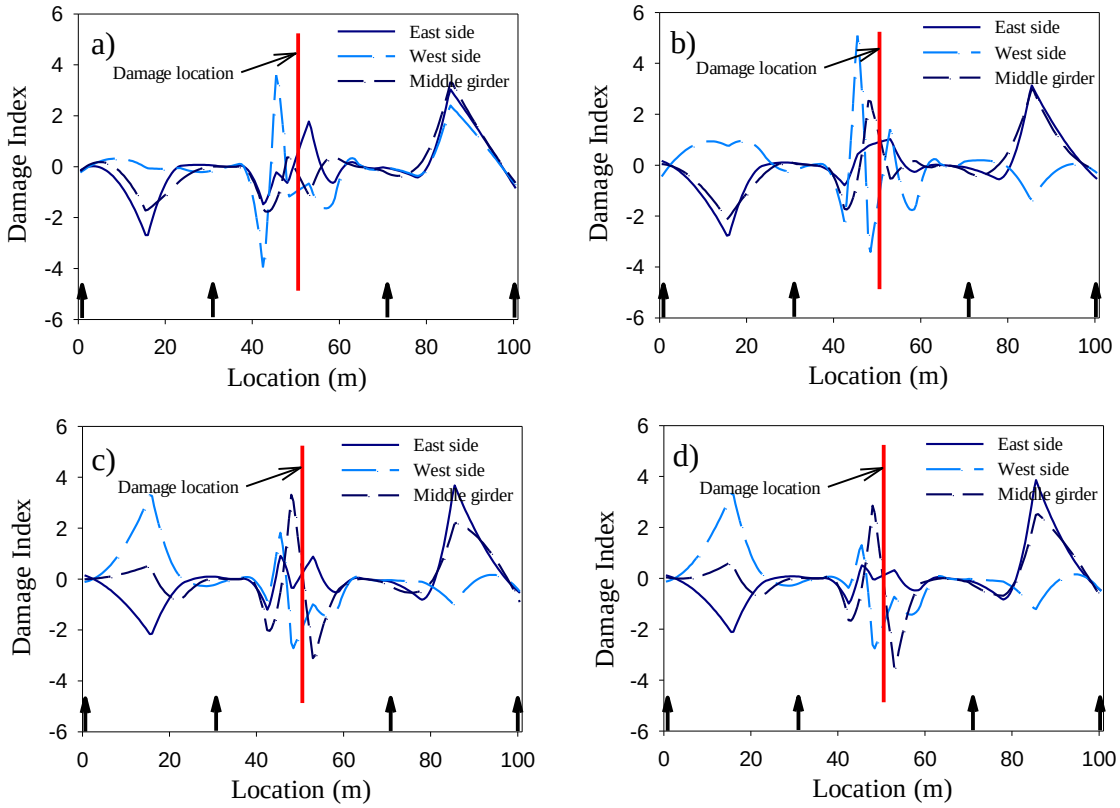

Figure 6.53 Distribution of the damage index for the first damage scenario when impact excitation was used and 5% noise was added to output signal: a) 10 simulations, b) 20 simulations, c) 50 simulations, and d) 100 simulations.

6.6 STOCHASTIC CONFIDENCE OF DETECTED DAMAGE

In this section, the level of confidence in the calculated VBDD parameter is evaluated to determine whether the differences in modal properties due to damage were statistically significant or not. The well known variable (t) of the t-distribution (DeCoursey 2003) was calculated to compare the mode shape amplitude values and modal curvatures at each measurement point before and after damage. At each measurement point, the modal amplitudes and mode shapes curvatures were assumed to follow a normal distribution according to the central limit theorem. The central limit theorem states that the mean of a sufficiently large number of independent random variables, taken from a population with finite mean and variance values, will be approximately normally distributed (DeCoursey 2003).

For the damaged state of the bridge, the mean value and standard deviation of the unit mass normalised modal amplitude and modal shape curvature at each measurement node were used to calculate the *t* value to establish the level of confidence that differences were statistically significant.

The modal properties before damage were calculated by using a dynamic excitation without superimposed noise, while the modal properties after damage were averaged from 10 simulations using either a noisy excitation force or a noisy output signal. No variability was added to the modal properties before damage because it can be assumed that the modal properties of the bridge before damage could be measured many times until the level of certainty in site readings is reduced so that the extracted modal properties can be considered to be known with a high level of certainty. On the other hand, measurements in the damage condition would usually be restricted by time limitations for bridge access.

The values of the *t* variable were compared to the value that corresponds to a one sided 95% confidence level. A one sided probability distribution was chosen because the VBDD methods that were used in this section, namely the change in mode shape and change in mode shape curvature methods, used absolute values, so that the changes were always equal to or greater than zero, as shown in Eq. 2.11 and Eq. 2.13.

The *t* value that corresponds to a one sided 95% level of confidence and nine degrees of freedom (10 samples less one) is 1.833 (DeCoursey 2003). Values falling below the threshold of 1.833 indicated than there was less than 95% confidence that the value of the modal amplitude or curvature of the damaged structure was different from the corresponding value of the undamaged structure; in other words, the damage could not be detected with a 95% level of confidence or certainty. The t-test was used because it takes into account the number of samples (tests performed) in calculating the confidence intervals, as explained in Section 3.12.

As an example, harmonic excitation with 1% noise added either to the input or output signals was used to demonstrate the application of the t-test. Figure 6.54a shows the change in mode shape distribution along the three measurement lines when damage was induced at the middle of the bridge (first damage scenario) and the bridge was excited

by harmonic excitation with 1% noise in the input signal, while Figure 6.54b shows the corresponding *t* variable for the change in mode shape. Figure 6.54c shows the distribution of change in mode shape when 1% noise was added to the output signal, while Figure 6.54d shows the *t* values obtained for that same condition. It can be seen by comparing Figure 6.54b and Figure 6.54d that the value of the *t* variable dropped significantly when the noise was introduced into the output signal (i.e. to sensor readings). However, *t* values still exceeded the critical value at the 95% level of significance at several locations, indicating that the mode shape changes were statistically significant. In addition, the highest levels of confidence appeared near the damage location.

The values of the *t* variable can be correlated to the change in mode shape as shown in Figure 6.54a and Figure 6.54c. From these figures it can be seen that high values of the *t* variable correlate with an improved estimate of the change in mode shape, as shown in Figure 6.54a; on the other hand, in Figure 6.54c the changes in mode shape are more ambiguous and result in lower values of the t variable. However, as mentioned above, *t* values still exceed the critical values at the 95% level of significance, particularly near the damage location. Thus, the statistical analysis shows that the rather ambiguous distribution of Figure 6.54c actually does indicate that damage is present, and even provides an indication as to the location of damage.

Results for the change in mode shape curvature method using harmonic excitation with 1% noise added either to the input or an output signal are shown in Figure 6.55. Figure 6.55a shows the change in mode shape curvature along the three measurement lines when damage was induced at the middle of the bridge (first damage scenario) and the bridge was excited by harmonic excitation with 1% noise in the input signal, while Figure 6.55b shows the corresponding *t* variable for the change in mode shape curvature. Figure 6.55c shows the distribution of change in mode shape curvature when 1% noise was added to the output signal, while Figure 6.55d shows the corresponding *t* values when 1% noise was added to the output signal. It can be seen by comparing Figure 6.55b and Figure 6.55d that the value of the *t* variable dropped significantly when the noise was introduced in the output signal (i.e. to sensor readings). However, even with the noisy output, *t* values still exceeded the critical value at the 95% level of significance

at many locations, indicating that the changes in the mode shape curvature were statistically significant. In addition, the highest levels of confidence appear near the damage location.

By comparing the *t* values calculated for the change in mode shapes with 1% noise in the output signal (Figure 6.54d) to the *t* values calculated for the change in mode shape curvature with 1% noise in the output signal (Figure 6.55d), it can be seen that there were many more points in Figure 6.55d where the *t* value exceeded the 95% confidence level compared to Figure 6.54d. This observation reinforces what can be visually deduced by comparing Figure 6.54c and Figure 6.55c, namely that Figure 6.55c shows a less ambiguous indication of damage as compared to Figure 6.54c, in which it is harder to determine the damage location, although the corresponding *t* values for the change in mode shape did provide an indication of the damage location.

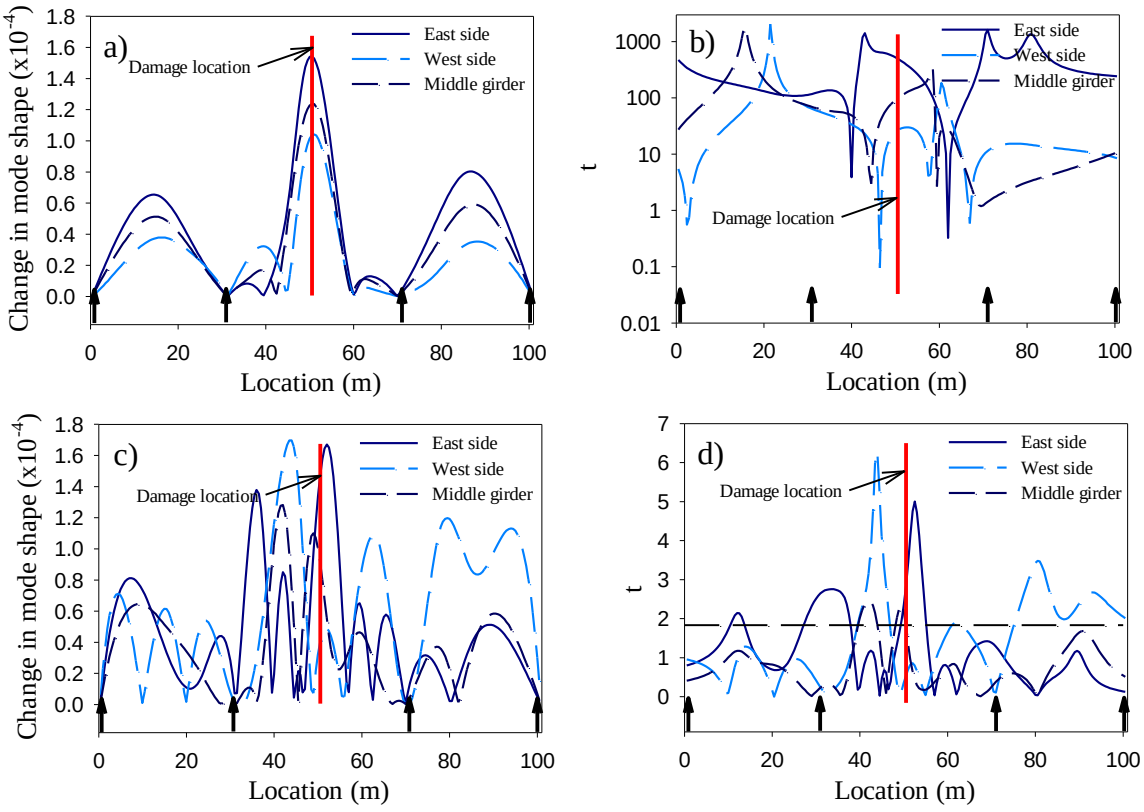

Figure 6.54 Effect of noise on the t-test value using impact excitation and the change in mode shape: a) change in mode shape with 1% noise in the input signal, b) *t* values for 1% input noise, c) change in mode shape with 1% noise in the output signal, and d) *t* values for 1% output noise.

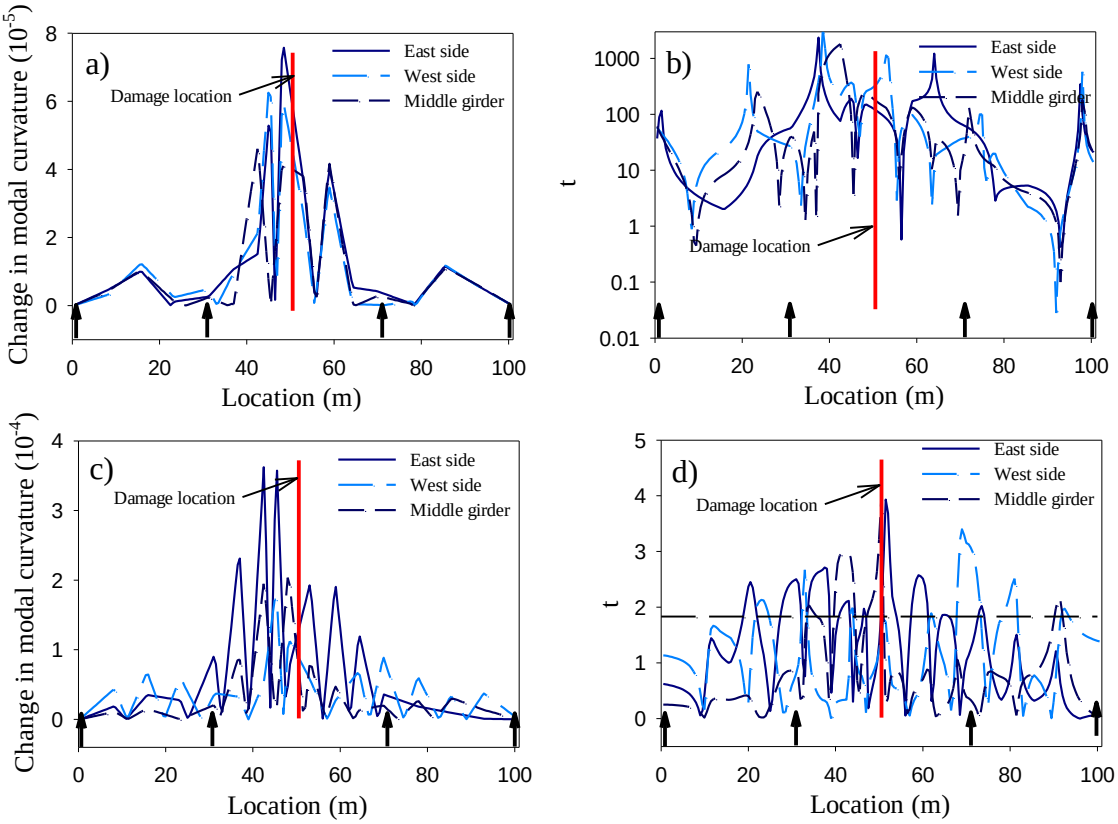

Figure 6.55 Effect of noise on the t-test value using harmonic excitation and change in mode shape curvature: a) change in mode shape with 1% noise in the input signal, b) *t* values for 1% input noise, c) change in mode shape with 1% noise in the output signal, and d) *t* values for 1% output noise.

To expand the discussion related to Figure 6.54 and Figure 6.55, Table 6.2 examines the effect of different types of excitation, noise levels and number of averaged trials on the level of confidence in detecting damage (using *t* values) for the first damage scenario. In this table, only harmonic and impact excitation were considered as they were the only types of excitation from which modal properties with good qualities suitable for VBDD could be calculated. Free vibration results were very similar to impact excitation; for this reason, it was not necessary to include them in Table 6.2. In addition, output signal noise only was considered, as the input noise did not have a significant effect on the calculated modal properties.

In preparing Table 6.2, the peak *t* values for all the measurement lines (east and west sides of the bridge and the three girders) at or as near as possible to the location of

damage were averaged together (one peak *t* value per line). These peak *t* values were compared to the averaged *t* values along the bridge span.

It can be seen from Table 6.2 that, with one exception, the *t* values near the damage location were higher than the *t* value at the 95% confidence level. This means that both the change in mode shape and the change in mode shape curvature were statically significant at this location. In addition, the *t* values increased with an increase in the number of trials that were averaged. For example, for 5% output noise, the *t* value for change in mode shape for 50 trials was 3.124, compared to a value of 2.213 for 10 trials. Also, the level of confidence dropped with an increase in the level of noise, as demonstrated by the fact the *t* value for 1% noise in the mode shape change was 4.184, compared to 2.213 for 5% noise, when both values were determined using 10 trials.

For harmonic excitation, the *t* values for the change in mode shape were higher than the corresponding values for the change in mode shape curvature. This contrasts with a visual impression from the graphical presentation of the same results shown in Figure 6.54c and Figure 6.55c for the change in mode shape and change in mode shape curvature, respectively, for 1% noise level in the output. It can be deduced from this that, although the results may look inconclusive graphically, useful information can be still extracted from these data if they are processed statistically. The effect of other levels of noise in the output on the change in mode shape method and change in mode shape curvature method are shown in Appendix G.

It is important to mention that, although the *t* values near the damage location were higher than the averaged *t* values along the bridge span, nonetheless the *t* values at other locations along the bridge span did exceed the 95% confidence level, as can be seen in Figure 6.54d and Figure 6.55d. This may lead to the incorrect assumption that there could be damage at locations that are not damaged (a false positive result). Therefore, the t-test by itself was able to assess the occurrence of damage, but in some cases it may not able to locate the damage by itself only. It can be concluded that using statistical methods such as the t-test along with the VBDD methods can enhance the ability of these methods to detect damage.

The damage index method (Section 2.3.4) assumes a normal distribution for the damage index β along the beam span, and uses the criterion that values falling two or more standard deviations from the mean are assumed to be indicative of damage. The implementation of the damage index method, and the effect of noise on the performance of this method, has already been discussed the previous sections of this chapter and will not be repeated here.

The implementation of the confidence intervals on the change in the modal flexibility method is not as straightforward as their implementation for the change in mode shape or change in mode shape curvature methods. For the latter two methods, there is a direct comparison of the damage indicators before and after damage; therefore, the t-test can be used. On the other hand, for the change in modal flexibility method, the damage indicator $\overline{\delta_j}$ is taken as the absolute maximum value of the elements of each column in the change in flexibility matrix, [ΔF]. This means that the variability of the other elements of [ΔF] is not taken into account, and that the location of the maximum element in the flexibility matrix for one case may not be the same element location for another case, thus precluding the ability to average different parameters. Therefore, it can be seen that the change in the modal flexibility method in its current form is not amendable to statistical treatment as described in this section and would have to be to be modified to take the variability of the damage indicator into account. The change in uniform load surface curvature method was not considered because this method, in the context of this study, did not produce good results regarding the indication and location of damage.

It can be concluded from the discussion presented in this section that a statistical evaluation of the modal properties of a structure before and after damage can be used to detect the presence of damage, or even enhance the ability to localise damage, by combining this statistical evaluation with one or more VBDD methods. In addition, it is suggested that the development of any new VBDD method should incorporate statistical methods so as to provide a level of confidence for the damage indicators.

Table 6.2 Comparison of the t value calculated from different types of excitation, output noise levels, and number of trials.

Excitation type	VBDD method	Output noise level	Number of trials	Avg. *t*-value at or near the damage	Avg. *t*-value along the bridge	*t*-value for 95% confidence level
Harmonic	Change in mode shape	1%	10	4.184	1.211	1.833
		2%	10	2.259	1.097	1.833
		5%	10	2.213	1.014	1.833
		5%	20	2.292	0.961	1.729
		5%	50	3.124	1.329	1.677
	Change in mode shape curvature	1%	10	3.700	0.962	1.833
		2%	10	2.098	1.030	1.833
		5%	10	2.201	0.929	1.833
		5%	20	2.183	0.869	1.729
		5%	50	2.540	1.073	1.677
Impact	Change in mode shape	1%	10	0.010	1.621	1.833
		2%	10	2.730	1.974	1.833
		5%	10	2.154	1.314	1.833
	Change in mode shape curvature	1%	10	3.276	1.609	1.833
		2%	10	2.566	1.695	1.833
		5%	10	2.556	1.269	1.833

7 SUMMARY AND CONCLUSIONS

7.1 SUMMARY

This thesis has presented the results of experimental and numerical studies investigating a number of issues related to the potential use of vibration-based damage detection (VBDD) techniques in the structural health monitoring of bridges, the primary issue being the influence of the excitation source.

VBDD is implemented by performing vibration tests on the structure under consideration to extract the modal parameters of the structure (natural frequencies, mode shapes and damping ratios) from measurements of its responses due to dynamic excitation. The dynamic properties of the structure before and after damage are then compared in order to detect damage.

Different sources of dynamic excitation are available for dynamic testing, including harmonic or random excitation induced by a shaker, impact excitation, traffic, or ambient excitation due to wind and river flow. The quality of information that can be extracted from the dynamic response of the bridge is dependent, to a large extent, on the characteristics of the force time history responsible for causing the vibration, in addition to the added noise due to measurement uncertainty. The above-mentioned factors affect the reliability of the extracted modal properties and, ultimately, the ability to successfully detect damage using VBDD methods.

The primary objective of this research was to investigate the influence of various dynamic excitation sources and sources of uncertainty on the reliability of measured natural frequencies and mode shapes and, therefore, on the likelihood of successfully applying VBDD techniques.

In the present study, two bridges were investigated. One is located on Provincial Highway No. 9 over the Red Deer River south of Hudson Bay, Saskatchewan. The

second bridge is located near the Town of Broadview, Saskatchewan, on an abandoned section of the Trans-Canada Highway No. 1, approximately 150 km east of the City of Regina.

Field tests were conducted using different sources of dynamic excitation: ambient, traffic excitation, impact excitation. The bridge response under the different types of dynamic excitation was recorded using accelerometers that were attached to the bridge deck. The purpose of field tests was to assess the different types of dynamic excitation and determine which types of excitation are more suited towards VBDD application. In addition, the field results were also used to calibrate an FE model of the bridge that was used in further simulations.

In addition, 45 strain gauges were installed on the girders of the Hudson Bay bridge to record the bridge strains under static loading conditions (crawl speed truck loading).

A calibrated FE model of the Red Deer River bridge was also subjected to different types of dynamic excitation: harmonic, random (white noise), impact and different models of truck excitation. In addition, different levels of noise were superimposed on this excitation or on the calculated bridge response to simulate random noise and interference that is normally present in field tests. The modal properties calculated from these tests were evaluated statistically and compared to evaluate which excitation method gave more accurate and reliable results.

The calibrated FE model was subjected to different damage scenarios by removing the external steel reinforcement from different locations on the bridge. Different types of dynamic excitation were then applied to the FE model and the bridge modal properties were calculated accordingly. Six VBDD methods were used to evaluate the feasibility of detecting different types of damage using the above mentioned types of dynamic excitation with different levels of superimposed noise.

The results of the different VBDD methods were examined and evaluated. Statistical evaluations were also performed to see whether the damage indicators suggested by the VBDD methods were statistically significant.

7.2 CONCLUSIONS

It was demonstrated in this study that the quality of information that could be extracted from the dynamic response of a bridge was dependent, to a large extent, on the characteristics of the force time history responsible for causing the vibration. The main conclusions for this research may be summarised in the following points:

- The quality of extracted modal properties was dependent on the characteristics of dynamic excitation, and the quality of measured response signal;
- Impact excitation was easier to implement and produced better results than other types of excitation;
- Using statistical methods such as the t-test along the VBDD methods can enhance the ability of these methods to detect damage.

Field tests showed that more intense disturbances, such as those due to the passing of large trucks, generally produced more reliable data due to higher signal-to-noise ratios in the measured response to these events, although this was not equally true for all large truck events, depending on the frequency content of the individual loading events. Furthermore, it was found that considering only the free vibration phase of the response after the vehicle left the bridge was more reliable than including data from the entire excitation event. Short duration records of wind-induced vibrations were less effective for defining modal properties than large vehicle loading, particularly with respect to defining the higher vibration mode characteristics; on the other hand, this study showed that ambient vibration results could be improved by taking measurements for longer periods of time and using a moving average in calculating the modal properties.

For the Hudson Bay bridge, the level of noise observed in field measurement, defined as the ratio of the energy of the ambient and the forced excitation responses, ranged from 0.07% to 3.7%. The lower levels of noise corresponded to events with large excitation forces (large trucks). In addition, the standard deviation of the measured first mode amplitudes ranged from 0.017 to 0.0488; here, standard deviation values were based on mode shapes that were normalised according to the reference accelerometer value, which was assigned an amplitude of unity (1.0). This range of field measurement noise

was found to make it feasible to implement VBDD methods on actual structures, as was confirmed from the results of the numerical simulation.

The use of spring hammer excitation on the Hudson Bay bridge showed that impact was an effective source of dynamic excitation. The modal properties calculated from impact excitation were of higher quality that those obtained from ambient or truck induced excitation. Adding to this, impact excitation was found to be faster and easier to implement than other types of excitation.

Static load tests (crawl speed truck tests) conducted on the Red Deer River Bridge showed that strain measurements were repeatable and could give reliable results regarding the strain levels in different parts of the bridge. The results also showed that a dynamically calibrated FE model of the bridge did yield roughly equivalent strain values when subjected the same truck loading that was applied on the actual bridge. However, more research on different types of bridges with different geometric configurations and construction materials is required to generalise this conclusion.

The implementation of impact testing on the Broadview bridge using a Heavy Weight Deflectometer (HWD) showed that results of impact testing were repeatable, with little variation. In addition, the findings indicated that the impact testing would yield better results if the side effects of multiple hits could be eliminated.

The numerical simulations showed that the free vibration response following random loading, as well as, the response to impact excitation, consistently yielded the most accurate modal properties (frequencies and modes shapes) compared to theoretical values derived from an eigenvalue analysis of the bridge FE model. Neither the response obtained during random loading, nor the response due to truck excitation, produced consistently accurate modal properties, although estimates of the fundamental mode shape using these excitation sources were significantly more reliable than those for higher modes.

The simplified pseudo-static truck model provided results similar to the more elaborate dynamic model for the scenarios constructed in this study. Both models were more accurate representation of the actual truck excitation observed on the bridge, than the simplified pseudo-static truck model with super-imposed sinusoid. This may be

attributed to the fact that that motion due to the truck excitation with an added sinusoid was dominated by response at the fundamental frequency at which the sinusoidal forcing was acting.

A comparison of the bridge response to the simulated truck excitation events and the measured bridge response to truck loading showed that there is a general agreement between the experimental measurements and the numerical model simulation.

Examining the variability of mode shape amplitudes for different types of excitation and superimposed noise levels showed that free decay after random loading and harmonic excitation produced lowest COV values compared to other types of excitation, while forced random excitation produced the highest COV values. Impact excitation produced COV values that fell between those for harmonic and random excitation. In addition, higher modes exhibited higher levels of variability compared to the fundamental mode. Another observation was that the COV values increased with an increase in the noise level, and these values were higher for output noise than for input noise.

The field measured modal properties for a damage scenario on the actual bridge (replacing external steel reinforcing bars by steel plates) did not match those properties calculated from simulating the same damage on the dynamically calibrated FE model. The reason for this difference could be attributed to the fact that bridges are rather complicated structures making it difficult to predict their behaviour. This difficulty may arise from non ideal support conditions, nonlinear material properties and environmental factors (temperature variation).

The simulated "distributed damage" condition, as in the current case of bridge rehabilitation could not be easily localised using the VBDD methods examined in this study. However, the VBDD methods did indicate significant differences when comparing the amplitude of the VBDD distribution before and after placing the steel plates, thus providing a clear indication of the presence of damage.

Numerical simulation results showed that, in general, all of the six VBDD methods examined in this study could detect damage if comparisons were made between two FE models of the bridge, before and after damage. However, the results were not the same once the dynamic properties of the bridge were calculated from response time histories

into which noise was introduced. These time histories were generated from the dynamic excitation of the bridge, before and after damage. The simulation results showed that only harmonic excitation and impact excitation yielded results that were consistent enough to indicate damage; also, the reliability of VBDD methods in detecting damage was seen to drop once noise was introduced. In general, the damage index method performed better than other damage detection methods.

Studying the statistical confidence intervals of the change in mode shape method and change in mode shape curvature method showed that there was correlation between the peaks in the curves of VBDD methods that localize damage and the high confidence level indicated by the t-test values. The values of the variable *t* were lower when the noise was introduced in the output signal (i.e. to sensors readings), compared to when the noise was superimposed on the input excitation; however, the values still exceeded the critical values at the 95% level of significance, particularly near the damage location. In addition, the *t* values increased with an increase in the number of trials that were averaged. It can be concluded that using statistical methods such as the t-test along the VBDD methods can enhance the ability of these methods to detect damage.

For a successful dynamic testing programme, based on the conclusions above, it is recommended that impact excitation be used for bridge dynamic testing using a spring-hammer, as it was demonstrated that this type of dynamic excitation was efficient, fast and yielded reliable and repeatable dynamic measurements. Moreover, the testing apparatus (the spring-hammer and the hydraulic driving system) was quite portable as it can be loaded in a regular truck and operated by two persons only. In addition, it is recommended that at least ten measurement sets for each test setup be acquired to reduce the noise in the measured bridge response. It is also recommended to have as many measurement locations as is practically possible within the test constraints (available accelerometers, and test time limits), in order to increase the spatial resolution of the measured bridge response, and provide better dynamic representation of the bridge.

Finally, it is recommended that more than one VBDD method be applied simultaneously, as different methods had different rates of success in detecting and locating damage. It is

suggested to use the change in mode shape curvature method along with the dynamic index method, as these two methods provided better indications of damage, in general, than the other methods. It is also recommended that statistical confidence limits be implemented on the results of the applied VBDD methods

7.3 RECOMMENDATIONS FOR FUTURE WORK

The results and conclusions presented in his study should be considered to be applicable to the bridges under consideration; therefore, it is suggested that this research be extended to cover different types of bridges so that the conclusions for this study can be generalised and be more useful for future implementation of structural health monitoring for a wide range of bridges.

More research is required to confirm the conclusion that a dynamically calibrated FE model of a bridge would yield the same results as a model that is calibrated by static load testing. If this conclusion can be proven valid in general, and not to be specific for the bridge in this study only, then this would have beneficial results in the field of bridge SHM because dynamic testing is easier, faster and less expensive to perform than static load testing.

It is suggested to develop new VBDD methods that incorporate statistical evaluations of the VBDD indicators in order to provide level of confidence for these indicators.

More research is needed to study the effect of temperature variation combined with the effect of the type of dynamic excitation and superimposed variation on the extracted modal properties, and thus on the accuracy of the VBDD indicators.

REFERENCES

ADINA. 2002. ADINA System Manuals. ADINA R&D Inc. Watertown, MA, USA.

Aktan, A. E., Lee, K. L., Chuntavan, C. and Aksel, T. 1994. Modal testing for ttructural identification and condition assessment of constructed facilities. Proceedings of the 12th International Modal Analysis Conference, Honolulu, Hawaii, USA, pp. 462-468.

Alampalli, S., Fu, G. and Dillon, W. 1997. Signal versus noise in damage detection by experimental modal analysis. ASCE Journal of Structural Engineering, **123**(2): 237-245.

Andersen, P. and Brincker, R. 1999. Estimation of modal parameters and their uncertainties. Proceedings of the 17th International Modal Analysis Conference (IMAC) Kissimmee, Florida, pp.323-329.

Pham, A.T., Sparling, B.F. and Wegner, L.D. 2007. Temperature effects on structural health monitoring of an integral abutment bridge. 2nd International Operational Modal Analysis Conference. Copenhagen, Denmark, Paper No. 63.

ANSYS Inc. 2005. ANSYS Release 9.0. Canonsburg, PA, USA.

Anvar, S.A. and Rahimian, M. 1996. Dynamic characteristics of reinforced concrete curved-bridge by ambient vibrations survey. Proceedings of the 3rd Asia-Pacific conference on structural engineering and construction, Hussein, M.W. (Ed.) Johor, Malaysia, pp. 123-130.

American Society for Testing and Materials (ASTM) 2002. C805-02 Standard test method for rebound number of hardened concrete. Philadelphia, USA.

Bendat, J.S. and Piersol, A.G. 1993. Engineering application of correlation and spectral analysis. 2nd Ed. John Wiley and Sons, New York.

Beck, J.L. and Katafygiotics, L.S. 1992. Probabilistic system identification and health monitoring of structures. Proceedings of the 10th World Conference on Earthquake Engineering, Balkema, Rotterdam, pp. 3721-3726.

Bridge Diagnostics Inc. 2003. Live load testing and load rating – University Bridge (North approach spans). Project no. 080301-105. Colorado, USA.

Brownjohn, J.M., Moyo, P., Omenzetter, P. and Lu, Y. 2003. Assessment of highway bridge upgrading by dynamic testing and finite-element model updating. ASCE Journal of Bridge Engineering, **8**(3): 162-172.

British Standards Institution (BSI) 1986. BS 1881 - Part 202: Testing concrete: Recommendations for surface hardness testing by rebound hammer. UK.

Canadian Standards Association. 2004. A23.3-04: Design of Concrete Structures. CSA, Etobicoke, ON, Canada.

Canadian Standards Association. 2000. S6-00: Canadian Highway Bridge Design Code. CSA, Etobicoke, ON, Canada.

Cafeo, J.A., Feldmaier, D.A. and Doggett, S.J. 1998. Considerations to reduce modal analysis test variability. Proceedings of the 16th International Modal Analysis Conference (IMAC), Santa Barbara, Calif., pp. 470-476.

Cebon, D. 2000. Handbook of vehicle-road interaction. Swets & Zeitlinger B.V., Lisse, the Netherlands.

Chan, T.H.T. and O'Conner, C. 1990. Vehicle model for highway bridge impact, Journal of Structural Engineering, ASCE, **116**: 1772-1791.

Chopra, A. K. 1995. Dynamics of structures: Theory and applications to earthquake engineering. Prentice Hall, New Jersey.

Clough, R.W., and Penzien, J. 2003. Dynamics of Structures, 3rd Edition. Computers and Structures Inc., Berkeley, CA, USA.

DeCoursey, W.J. 2003. Statistics and probability for engineering applications. Newnes, USA.

Deger, Y., Cantieni, R. and Pietrzko, S. 1994. Modal analysis of an arch bridge: experiment, finite element analysis and link Proceedings of the 12th International Modal Analysis Conference (IMAC), Honolulu, USA, pp. 425-432.

DeWolf, J.T., Culmo, M.P. and Lauzon, R.G. 1998. Connecticut's Bridge infrastructure monitoring program for assessment. ASCE Journal of Infrastructure Systems, **4**(2): 86-90.

De Roeck, G, Peeters, B. and Ren, W.X. 2000. Benchmark study on system identification through ambient vibration measurements. Proceedings of the 18th International Modal Analysis Conference (IMAC), San Antonio, TX, USA, pp. 1106-1112.

Doebling, S.W., Farrar, C.R., Prime, M.B. and Shevitz, D.W. 1996. Damage identification and health monitoring of structural and mechanical systems from changes in their vibration characteristics: a literature review. Los Alamos National Laboratory Report LA-13070-MS, New Mexico, U.S.A.

Doebling, S.W., Farrar, C.R. and Goodman, R.S. 1997. Effects of measurement statistics on the detection of damage in the Alamosa Canyon Bridge. Proceedings of the 15th International Modal Analysis Conference (IMAC), Orlando, FL. pp. 919-929.

Doebling, S.W. and Farrar, C.R. 1998. Statistical damage identification techniques applied to the I-40 Bridge over the Rio Grande River. Proceedings of the 16th International Modal Analysis Conference (IMAC), Santa Barbara, Calif. pp. 1717-1724.

Earth Tech (Canada) Inc. 2001. Strengthening project of Red Deer River Bridge on provincial highway no. 9. Saskatchewan, Canada.

Ewins, D.J. 2000. Modal testing: theory, practice and application. 2nd Ed. Research Studies Press Ltd., Baldock, Hertfordshire, England.

Fafard, M., Laflamme, M., Savard, M., and Bennur M. 1998. Dynamic analysis of existing continuous bridge. ASCE Journal of bridge engineering. **3**(1): 28-37.

Fanning, P., Healy, P., Pavic, A., Reynolds, P. and Brownjohn, J. 2007. Sean O'Casey Bridge: comparison of operational and traditional modal analysis test results. Proceedings of the 2nd International Operational Modal Analysis Conference. Copenhagen, Denmark, pp. 293-298.

Farrar, C.R., Baker, W.E., Bell, T.M., Cone, K.M., Darling, T.W. and Duffey, T.A. 1994. Dynamic characterization and damage detection in the I-40 Bridge over the

Rio Grande. Los Alamos National Laboratory report LA-12767-MS, New Mexico, U.S.A

Farrar, C.R. and Cone, K.M. 1995. Vibration testing of the I-40 bridge before and after the introduction of damage. Proceedings of the 13th International Modal Analysis Conference, Nashville, TN, pp. 203–209.

Farrar, C.R. and Jauregui, D.A. 1996. Damage detection algorithms applied to experimental and numerical modal data from the I-40 Bridge. Report LA-13074-MS. Los Alamos National Laboratory, New Mexico, U.S.A.

Farrar, C.R. and Doebling, S.W. 1997. An overview of modal-based damage identification methods. EUROMECH 365 International Workshop: DAMAS 97, Structural Damage Assessment Using Advanced Signal Processing Procedures, Sheffield, UK,

Farrar, C.R. and James, G.H. 1997. System identification from ambient vibration measurements on a bridge. Journal of Sound and Vibration, **205**(1): 1-18.

Farrar, C.R. and Jauregui, D.A. 1998a. Comparative study of damage identification algorithms applied to a bridge: I. Experiment. Smart Materials and Structures, **7**: 704-719.

Farrar, C.R. and Jauregui, D.A. 1998b. Comparative study of damage identification algorithms applied to a bridge: II. Numerical study. Smart Materials and Structures, **7**: 720-731.

Farrar C.R., Duffey, T.A., Cornwell, P.J. and Doebling, S.W. 1999. Excitation methods for bridge structures. Proceedings of the 17th International Modal Analysis Conference (IMAC) Kissimmee, Florida, pp. 1063-1068.

Farrar, C. R., Cornwell, P. J., Doebling, S.W. and Prime, M. B. 2000. Structural health monitoring studies of the Alamosa Canyon and I-40 Bridge. Los Alamos National Laboratory Report LA-13635-MS, New Mexico, U.S.A.

Friswell, M.I. & Mottershead, J.E. 1995. Finite element model updating in structural dynamics. Kluwer Academic Publishers, Dordrecht, the Netherlands.

Fox, C.H.J. 1992. The location of defects in structures: a comparison of the use of natural frequency and mode shape data. Proceedings of the 10th International Modal Analysis Conference (IMAC), San Diego, Calif., pp. 522–528.

Hermans, L. and Van Der Auweraer, H. 1999. Modal testing and analysis of structures under operational conditions: industrial applications. Mechanical Systems and Signal Processing. **13**(2): 193-216.

Humar, J.L. 2002. Dynamics of structures, 2nd edition, Princeton-Hall, Inc. Englewood Cliffs, New Jersey. U.S.A.

International Organization for Standardization 1994. ISO 7626-5: Vibration and shock – experimental determination of mechanical mobility - Part 5: Measurements using impact excitation with an exciter which is not attached to the structure. Switzerland.

Jackson, K. 2007. Reliability-based load management of the Red Deer River Bridge. M.Sc. thesis, Department of Civil and Geological Engineering, University of Saskatchewan, Saskatoon, SK, Canada.

James, G.H., Crane, T.G., Lauffer, J.P., and Nord, A.R. 1992. Modal testing using natural excitation. Proceedings of the 10th International Modal Analysis Conference (IMAC), San Diego, USA, pp. 1209-1216.

James, G.H., Carne, T.G., and Lauffer, J.P. 1995. The natural excitation technique (NExT) for modal parameter extraction from operating structures. The International Journal of Analytical and Experimental Modal Analysis **10**(4): 260-277.

Juang, J.–N., Papa, R.S. 1985. An eigensystem realization algorithm for modal parameter identification and model reduction. Journal of Guidance, Control and Dynamics, **8**(5): 620-627.

Kaouk, M. and Zimmerman, D.C. 1993. Evaluation of the minimum rank update in damage detection: an experimental study. Proceedings of the 11th International Modal Analysis Conference (IMAC), Kissimmee, FL, pp. 1061-1068.

Kim J.T. and Stubbs, N. 1995. Model-uncertainty impact and damage-detection accuracy in plate girder. ASCE, Journals of Structural Engineering, **121**(10): 1409-1417.

Kirkegaard, P.H. and Andersen, P. 1998. Use of statistical information for damage assessment of civil engineering structures. Proceedings of the 16th International Modal Analysis Conference (IMAC) Santa Barbara, CA. pp. 363-368.

Lee, E.S.L. 1978. Non-destructive testing of concrete compressive strength. M.Sc. thesis, Department of Civil and Geological Engineering, University of Saskatchewan, Saskatoon, SK, Canada.

Levi, A. 1997. Instrumented monitoring and diagnostic load testing for condition assessment and evaluation of bridges. Ph.D. Dissertation, College of Engineering, University of Cincinnati, Cincinnati, Ohio, USA.

Livingston, R.A., Jin, S. and Marzougui, D. 2001. Stochastic modeling of ambient traffic loadings in LS-DYNA nonlinear FE analysis. Proceedings of SPIE, **4337**: 422-431, Health Monitoring and Management of Civil Infrastructure Systems, Steven B. Chase A. and Emin Aktan, Editors.

Maguire, J.R. 1990. Assessing the dynamic properties of existing bridge structures by hammer testing. Bridge Management: Inspection, Maintenance, Assessment and Repair. Elsevier Applied Science, London UK. Harding J.E., Parke, G. and Ryal, M. J. (eds.).

Maia, N. and Silva, J. Eds. 1997. Theoretical and experimental modal analysis. Research Studies Press Ltd., Somerset, England.

Marzougui, D., Jin, S. and Livingston, R.A. 2001. Development of an LS-DYNA nonlinear finite element model for use in damage detection and health monitoring of highway bridges. Proceedings of SPIE, **4337**: 432-440, Health Monitoring and Management of Civil Infrastructure Systems, Steven B. Chase; A. Emin Aktan; Editors.

Mathworks, Inc. 2002. MATLAB users manual. Massachusetts, USA.

Mathworks Inc. 2007. Data Acquisition Tool Box 2 User's Guide. Massachusetts, USA.

Mazurek, D.F. & DeWolf, J.T. 1990. Experimental study of bridge monitoring technique. ASCE Journal of Structural Engineering, **116**(9): 2532-2549.

Mazurek, D.F. 1997. Modal sensitivity to damage in multi-girder bridges. Proceedings, 15th International Modal Analysis Conference (IMAC), Florida, USA, pp. 1892-1898.

Mufti, A.A. 2001. Guidelines for structural health monitoring. ISIS Canada (The Canadian Network of Centres on Intelligent Sensing for Innovative Structures), Design Manual No.2, Winnipeg, Manitoba.

Mufti A.A., Bakht, B., Tadros, G., Horosko, A.T. and Sparks, G. 2005. Are civil structural engineers "risk averse"? Can civionics help? Sensing issues in civil structural health monitoring. F. Ansari, ed. Springer, Netherlands, pp. 3-12.

Nassif, H.H. and Liu, M. 2004. Analytical modelling of bridge-road-vehicle dynamic interaction system. Journal of Vibration and Control, **10**:215-241.

National Instruments Corporation 1998b. Application note 078: Strain gauge measurement - a tutorial. USA.

Ndambi, J.M., Peeters, B., Maeck, J., De Visscher, J., Whab, M.A., Vantomme, J., De Roeck, G. and De Wilde, W. P. 2000. Comparison of techniques for modal analysis of concrete structures. Engineering Structures, **22**: 1159-1166.

Newland, D. E. 1984. An introduction to random vibrations and spectral analysis. 2nd edition, Longman Group Limited, England.

Pan, T-C., Li, J. 2002. Dynamic vehicle element method for transient response of couples vehicle-structure systems. ASCE Journal of Structural engineering. **128**(2): 214-223.

Pandey, A.K., Biswas, M., Samman, M.M. 1991. Damage detection from changes in curvature mode shapes. Journal of Sound and Vibration, **145**(2): 321-332.

Pandey, A.K. and Biswas, M. 1994. Damage detection in structures using changes in flexibility. Journal of Sound Vibration, **169**(1): 3-17.

Park, S., Stubbs, N., Bolton, R., Choi, S. and Sikorsky, C. 2001. Field verification of the damage index method in a concrete box-girder bridge via visual inspection. Computer-aided civil and infrastructure engineering, **16**: 58–70.

Pan, T-C. and Li, J. 2002. Dynamic vehicle element method for transient response of coupled vehicle-structure systems. ASCE Journal of Structural Engineering, **128**(2): 214-223.

Paultre, P., Proulx, J. and Talbot, M. 1995. Dynamic testing procedures for highway bridges using traffic loads. ASCE, Journals of Structural Engineering, **121**(2): 362-376.

Pavic, A., Pimentel, R. and Waldron P. 1997. Instrumented sledge hammer impact excitation: worked examples. Proceedings of the 16th International Modal Analysis Conference (IMAC), Santa Barbara, CA, pp. 929-935.

Peeters, B., D Roeck, G., Hermans, L., Wauters, T., Kramer, C., De Smet, C. 1998. Comparison of system identification methods using operational data of a bridge test. Proceedings of ISMA 23, pp. 923-930, K. U. Leuven, Belgium.

Peeters, B. and De Roeck, G. 2001. Stochastic system identification for operational modal analysis: a review. ASME Journal of Dynamics Systems, Measurement and Control, **123**(4): 659-667.

Peeters, B., Maeck, J. and De Roeck, G. 2001. Vibration-based damage detection in civil engineering: excitation sources and temperature effects. Smart Materials and Structures, **10**: 518-527.

Ren, W. and De Roeck, G. 2002. Structural damage identification using modal data. I: simulation verification. ASCE Journal of Structural Enginering, **128**(1): 87-95.

Rotter, T., Kohoutek, R. and Marusiak, G. 1994. Modal Analysis of Railway Bridge in Malda Boleslav. Proceedings of the 12th International Modal Analysis Conference (IMAC), Honolulu, USA, pp. 1316-1320.

Ruotolo, R. and Surace, C. 1997. Statistical approach to damage detection through vibration monitoring. Proceedings of the 5th Pan American Congress of Applied Mechanics, Puerto Rico.

Salane, H.J., Baldwin, J.W. and Duffield, R.C. 1981. Dynamics approach for monitoring bridge deterioration. Transportation Research Record. **832**: 21-28.

Salawu, O.S. and Williams, C. 1994. Damage location using vibration mode shapes.

Proceedings of the 12th International Modal Analysis Conference (IMAC), Honolulu, HI, pp. 933-939.

Santamaria, J.C. and Fratta, D. 1998. Introduction to discrete signals and inverse problems in civil engineering. ASCE Press, Virginia, USA.

Samman, M.M. and Biswas, M. 1994a. Vibration testing for non-destructive evaluation of bridges. I: theory. ASCE Journal of Structural Engineering, **120**(1): 269-289.

Samman, M.M. and Biswas, M. 1994b. Vibration testing for non-destructive evaluation of bridges. II: results. ASCE Journal of Structural Engineering, **120**(1): 290-306.

Shah, S.J 1992. Application note 025: Field wiring and noise considerations for analogue signals. National Instruments Corporation, USA.

Shih, C.Y., Tsuei, Y.G., Allemang, R.J., and Brown, D.L. 1988. Complex mode indicator function and its application to spatial domain parameter estimation, Mechanical Systems and Signal Processing, **2**: 367-377.

Siddique, A B., Sparling, B.F. and Wegner, L.D. 2007. Assessment of vibration-based damage detection for an integral abutment bridge. Canadian Journal of Civil Engineering, **34**(3): 438-452.

Sohn, H., Farrar, C.R., Hemez, F.M., Shunk, D.D., Stinemates, S.W., Nadler, B.R. and Czarnecki, J.J. 2003. A review of structural health monitoring literature: 1996-2001. Los Alamos National Laboratory report LA-13976-MS, New Mexico USA.

Spyrakos, C., Chen, H.L., Stephens, J. and Govidaraj V. 1990. Evaluating structural deterioration using dynamic response characterization. Proceedings of the International Workshop on Intelligent Structures, Elsevier Applied Science, London, UK, pp. 137-154.

Srinivasan, M.G. and Kot, C.A. 1992. Effects of damage on the modal parameters of a cylindrical shell. Proceedings of the 10th International Modal Analysis Conference, San Diego, Calif., pp. 529-535.

Stearns, S.D. and David, R.A. 1996. Signal processing algorithms in MATLAB. Prentice Hall, New Jersey, USA.

Stubbs, N., Kim, J.T. and Farrar, C. 1995. Field verification of a nondestructive damage localization and severity estimation algorithm. Proceedings of the 13th International Modal Analysis Conference, Nashville, TN, pp. 210-218.

Trethewey, M.W, and Cafeo, J.A. 1992. Tutorial: Signal processing aspects of structural impact testing. The International Journal of Analytical and Experimental Modal Analysis, **7**(2):129-149.

Toksoy, T. & Aktan, A.E. 1994. Bridge-condition assessment by modal flexibility. Experimental Mechanics, **34**(3): 271-278.

Van den Branden, B., Peeters, B., De Roeck G. 1999. Introduction to MACEC 2, modal analysis of civil engineering constructions, Dept. Civil Engineering. K. U. Leuvwen.

Van Overschee P., De Moor B. 1996. Subspace identification for linear systems: theory, implementation, applications. Kluwer Academic Publishers. Dordrecht, the Netherlands.

Ventura, C.E., Felber, A. and Prion, H.G.L. 1994. Seismic evaluation of a long span bridge by modal testing. Proceedings, 12th International Modal Analysis Conference (IMAC), Hawaii,USA, pp. 1309-1315.

Ventura, C.E., Onur, T. and Tsai P.C. 2000. Dynamic characteristics of Crowchild Trail Bridge. Canadian Journal of Civil Engineering, **27**: 1046-1056.

Vishay Micro Measurements. 2007. Application note TT-612: The three-wire quarter-bridge circuit, USA,

Wang, M.L., Xu, F.L. and Lloyd, G.M. 2000. Results and implications of the damage index method applied to multi-span continuous segmental presstressed concrete bridge. Structural Engineering and Mechanics, **10**(1): 37-51.

Wang, Y., Sparling, B.F. and Wegner, L..D. 2008. Vibration-based damage detection on a multi-girder bridge deck. Proceedings of the 37th Annual Conference of the Canadian Society for Civil Engineering, Quebec City, Canada.

Ward H.S. 1984. Traffic generated vibrations and bridge integrity. ASCE Journal of Structural Engineering, **110**(10): 2487-2498.

Wegner, L.D., Zhou, Z., Alwash, M., Siddique, A.B. and Sparling, B.F. 2004. Vibration-based damage detection on bridge superstructures. Proceedings of the 2nd International Workshop on Structural Health Monitoring of Innovative Civil Engineering Structures, Winnipeg, MA, Canada, pp. 429-439.

Wolf, T. & Richardson, M. 1989. Fault detection in structures from changes in their modal parameters. Proceedings of the 7th International Modal Analysis Conference, Las Vegas, USA, pp. 87-94.

Wong, F.S. 2001. Health monitoring and structural reliability as a value chain. Computer-Aided Civil and Structural Engineering, **16**: 71-78.

Yang, Y.B., Yau, J.D. and Wu, Y.S. 2004. Vehicle-bridge interaction dynamics: With applications to high-speed Railways. World Scientific Publishing Co., Singapore.

Zhang, Z. 1994. Error study of bridge tests for the purpose of structure identification. Proceedings of the 12th International Modal Analysis Conference (IMAC), Honolulu, USA, pp. 433-441.

Zhang, Z. and Aktan, A.E. 1995. The damage indices for constructed facilities. Proceedings of the 13th International Modal Analysis Conference, Nashville, TN, pp. 1520-1529.

Zhou, Z., Wegner L.D., Sparling, B.F. 2004. Vibration-based damage detection on a prestressed concrete girder. Proceedings of the 5th Structural Specialty Conference of the Canadian Society for Civil Engineering, Saskatoon, Saskatchewan, Canada.

Zhou, Z. 2006. Vibration-based damage detection of simple bridge superstructures. Ph.D. thesis, Department of Civil and Geological Engineering, University of Saskatchewan, Saskatoon, SK, Canada.

Zhou, Z., Wegner L.D., Sparling, B.F. 2007. Vibration-based detection of small-scale damage on a bridge deck. ASCE Journal of Structural Engineering **133**(9): 1275-1267.

APPENDIX A

HUDSON BAY BRIDGE DETAILED ELEVATIONS AND SECTIONS

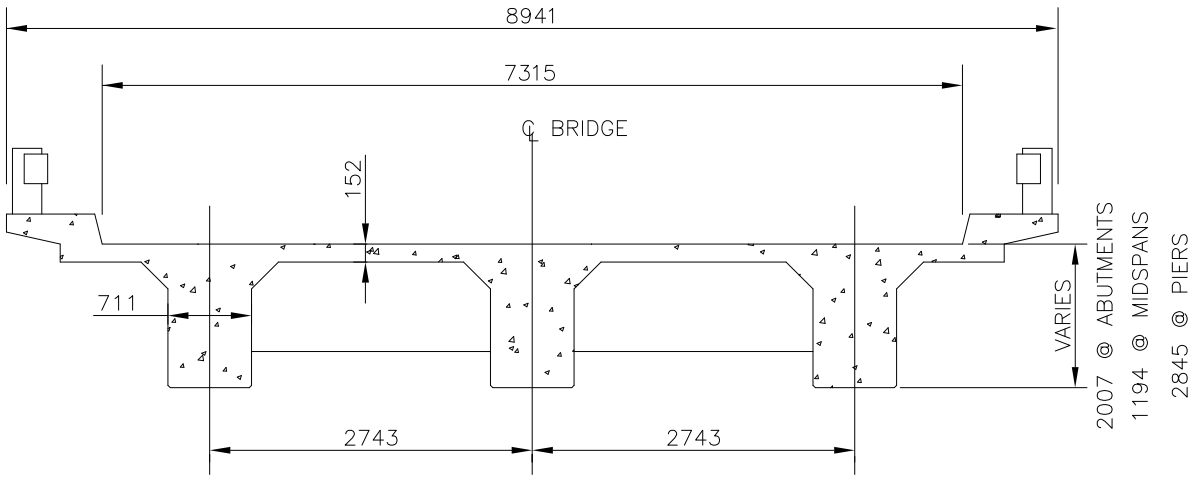

Figure A.1. Typical bridge cross section.

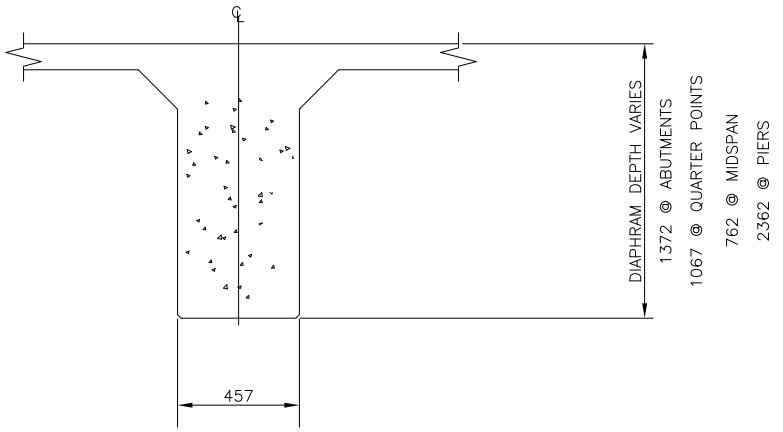

Figure A.2. Bridge diaphragm.

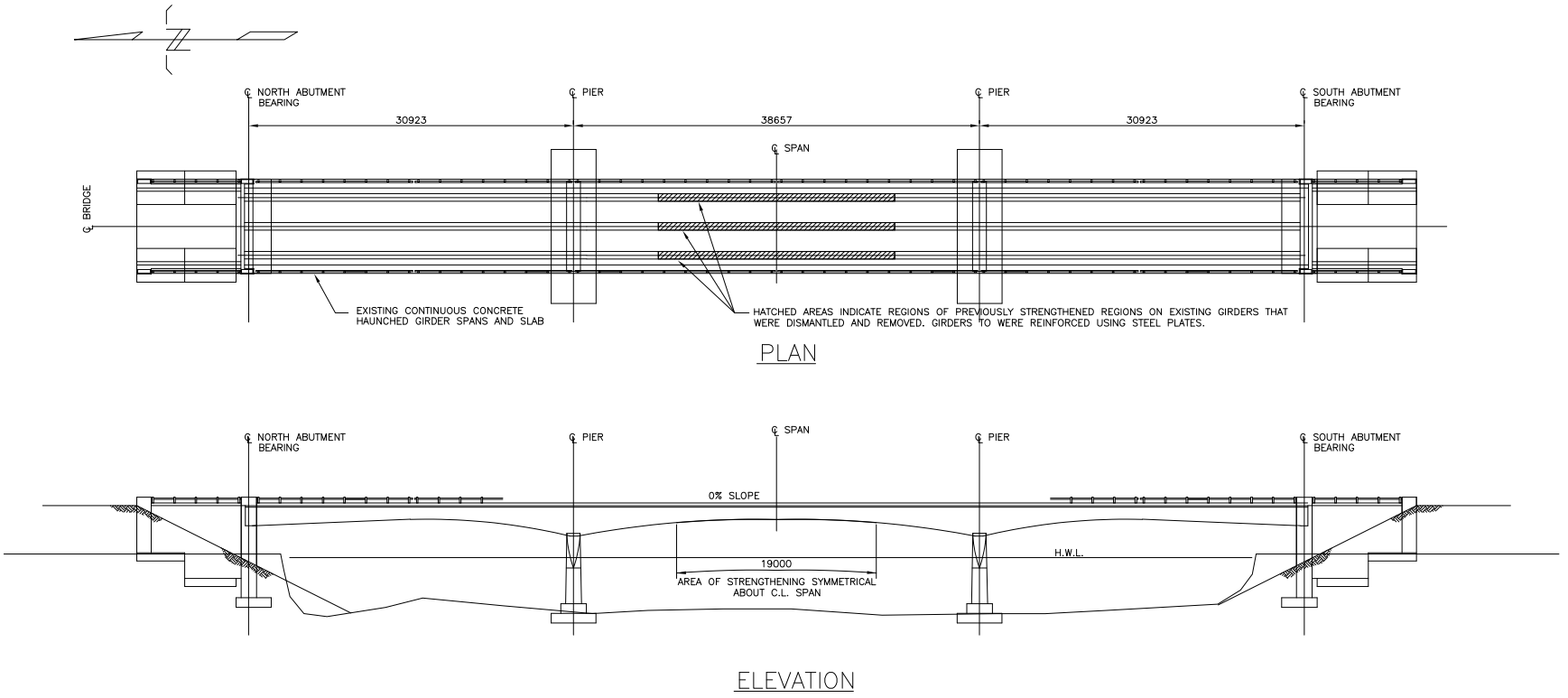

Figure A.3. Hudson Bay Bridge plan and elevation.

APPENDIX B

EXPERIMENTAL TRUCK TESTS ON HUDSON BAY BRIDGE

B.1 Introduction

This appendix lists the number of site visits performed to conduct bridge testing under truck excitation on the Hudson Bay Bridge. The type, weight and direction of travel for each truck are listed in this appendix for every site visit that was conducted as part of this research. However, not all of the previously mentioned parameters were available during each test. For example, some truck weights were not available, or the type and direction of travel of a truck were not noted.

B.2 Trucks listing during site test on August 26, 2003

During this test the accelerometers were placed on both side of the bridge; thus, the "E" and "W" prefixes in each file name refer to the accelerometers' setup location and specifies whether it was on the east side or west side. The ambient temperature during this test series ranged from 28° to 32° C.

Table B.1. Truck description for east side setup.

Record number	Truck description	Direction of travel	Record length (second)
E01a	Large truck		20.0
E02	Ambient		11.4
E03a	Log Truck		20.0
E03b	1/2T truck		22.7
E04	Large truck		14.0
E05a	Log truck		20.0
E05b	Large truck		15.4
E06	Large truck		27.7
E07	Large truck		35.7
E08a	Log Truck		16.0
E08b	1/2T truck		26.4
E09	Log Truck		24.4
E10	Log Truck		25.0
E11a	Log Truck		21.0
E11b	1/2T truck		15.4

Table B.1 cont.

E12	Log Truck	22.7
E14a	Large truck	13.0
E14b	Large truck	13.4
E15a	Log Truck	28.0
E15b	Ambient	31.0
E15c	Log Truck	27.0

Table B.2. Truck description for west side setup.

Record number	Truck description	Direction of travel	Record length (second)
W000a	1/2T truck		12.0
W000b	Ambient		23.0
W000c	Log Truck		20.0
W00	Ambient		38.4
W01	Two large trucks, 1/T truck		32.7
W02	Large truck		22.4
W03	Two trucks, 1/2T truck		15.7
W04	Log Truck, two 1/2T trucks		24.4
W05	Log truck		20.7
W06	Ambient		27.4
W07	Log truck		23.4
W08a	Log truck		9.7
W08b	Log truck		13.7
W09	Log truck		31.0
W10	Log truck		26.4
W11	Large truck		17.0
W12a	Log truck		24.4
W12b	Large truck		9.0
W13	Large truck, two Log trucks		31.4
W14	Large truck, 1/T truck		25.0
W15	Log truck		18.4
W16	1/2T truck		27.4
W17	Large truck		31.0
W18	Ambient		23.8

B.3 Trucks listing during site test on June 24, 2004

As in Section B.2, the "E" and "W" prefixes in each file name refer to the accelerometers' set up location and whether it was on the east side or west side.

Table B.3. Truck description for east side setup.

Record number	Truck description	Direction of travel	Record length (second)
E01	1/2T truck		17.9
E02	Car		16.7
E14	Ambient		22.0
E15a	Ambient		30.0
E15b	1/2T truck		18.0
E15c	Ambient		21.0
E15d	Large truck		35.0
E16a	Ambient		44.0
E16b	1/T truck		25.0
E17a	Ambient		48.0
E17b	Two large trucks		52.6
E18a	Ambient		18.0
E18b	Two large trucks		30.0
E18c	Car		20.0
E18d	Ambient		44.0
E18e	1/2 T truck		30.0

Table B.4. Truck description for west side setup.

Record number	Truck description	Direction of travel	Record length (second)
W01	1/2T truck		20.3
W02	Car		30.9
W03	Car N, large truck, car	N,S,N	58.7
W04	1/2T truck		41.9
W05	Car, car	N,S	47.5
W06	Large truck		43.3
W07a	Car		24.0
W07c	SUV		24.3
W08a	Ambient		33.0
W09a	Car		22.0
W09b	Car		24.0
W10a	1/2T Truck		16.0
W10b	3_axle Truck		24.0

Table B.4 continued.

W11a	Ambient		21.0
W11b	Car	N	24.0
W11d	1/T Truck, 1/T truck	N, S	22.5
W12a	Truck		30.0
W12c	5-axle semi trailer		21.7
W13	3-axle truck		32.7
W14a	Ambient		16.0
W14b	7-axle Log truck (empty)		45.9
W15a	6-axle truck		25.0
W15b	1/T truck		11.5
W16a	Car	N	12.0
W16b	Ambient		19.0
W16c	Semi trailer		24.0
W17a	Ambient		41.5
W17b	Van	N	26.0
W17c	Van		26.0
W18a	Van	N	18.0
W18b	Log Truck 8-axle (empty)		37.3
W19	Van		31.7
W20	Ambient		68.3
W21a	Ambient		30.0
W21b	Car	N	21.7
W22	Car	S	41.7
W22a	Ambient		16.0
W23	Car		33.5
W24	6-axle truck		46.1
W25	Two large trucks		43.3
W26	1/2T Truck		25.7
W27	1/2T Truck		33.5
W28	Ambient		76.5
W29	Ambient		90.3
W30	Ambient		23.3
W31	Ambient		47.1
W32	1/2T Truck, Car		37.3
W33	Ambient		145.7
W34	Van, 1/2T Truck, Trailer	N, S, N	34.3
W35a	Car	N	15.0
W35b	Large truck, 1/2T truck	N, N	18.7
W36	Ambient		139.3
W37	Large truck		16.9

B.4 Trucks listing during site test on August 26, 2004

During this site visit, only the west side of the bridge was instrumented, because the testing team was busy installing the strain gauges on the bridge and insufficient resources could be spared for installing the accelerometers and measuring the bridge vibration.

Table B.5. Truck description for west side setup.

Record number	Truck description	Direction of travel	Record length (second)
aug26a	Septic truck	S	28.0
aug26b	1/2T truck	S	28.4
aug26c	1/2T SUV	S	32.7
aug26d	Highway Oiler	N	23.0
aug26e	Crane truck	S	14.7
aug26f	Septic truck	N	20.0
aug26g	Crane truck	S	26.7
aug26h	Crane truck with trailer	S	31.4
aug26i	Pepsi semi trailer	S	30.0
aug26j	Ambient		41.7

B.5 Trucks listing during site test on September 17, 2004

During this site visit, the installation of strain gauges on the bridge girders was completed and acceleration and strain readings were recorded during the bridge excitation under normal traffic. During this test, the accelerometers were placed on both side of the bridge; thus, the "E" and "W" prefixes in each file name refer to the accelerometers' setup location and whether it was on the east side or west side. Due the limited number of channels available on the data acquisition system, the strain gauge logging was also split into two groups, east and west, and were logged with the accelerometers for the corresponding east or west setup.

Table B.6. Truck description for east side setup.

Record number	Truck description	Direction of travel	Record length (second)
E02a	Car, 12T truck		42.0
E10	Log truck		19.4
E11	Log truck		22.4
E12	Gravel Truck	N	25.4

Table B.6 continued.

E14	Four small vehicles	N, N, N,S	20.4
E15	Farm tractor (2-wheel drive)		25.4
E16	Log truck, loaded		14.4
E17	Ambient		19.7
E18a	Log truck		11.0
E18b	1/2T truck		8.7
E19	1/2T truck		9.7
E20	1/2T truck		15.7
E21	SUV		19.0

Table B.7. Truck description for west side setup.

Record number	Truck description	Direction of travel	Record length (second)
W01	1/2T truck		23.0
W02	Log truck	N	35.4
W03a	Large truck		20.0
W03b	Log Truck, loaded	N	23.0
W03c	Multiple 1/2T trucks		26.0
W04	Ambient		26.7
W05	Three 1/2T trucks	S, N, S	47.0
W06	1/2T truck		33.0
W07	SUV	N	24.7
W08	Log Truck, empty		37.4
W08a	Ambient		15.0
W08b	Log truck		27.3
W09	1/2T truck, 1/2T truck		34.4
W10	Log Truck (empty), 1/2T truck		48.7
W11	Ambient		56.0
W12	Car, 1/2T truck		45.7
W13	Large truck, Log truck, Van, 1/2T truck		40.0
W13a	Ambient		13.3
W14	1/2T truck		27.7
W15a	Ambient		17.0
W15b	Gravel Truck (loaded), 1/2T truck, 1/2T truck		47.0
W23a	Ambient		18.0
W23b	Log truck	N	37.0
W24	Log truck + multiple cars		54.7
W25	Ambient		35.7
W26	School bus		26.0

Table B.7 continued.

W27	1/2T truck, 1/2T truck, school bus	49.4
W28	Multiple cars	49.4
W29	Log truck	37.7
W30	Three Gravel Trucks	11.7
W31	Small vehicles	20.7
W32	Ambient	18.0
W33	Log Truck, empty	26.7

B.6 Trucks listing during site test on September 29-30, 2005

During this site visit, a controlled test was conducted on the bridge by having a truck of known axle weight and configuration cross over the bridge in different directions and at different speeds. In addition, the bridge response to normal traffic was also recorded. During this test the accelerometers were placed on both side of the bridge, in east and west setups. Due the limited number of channels available on the data acquisition system, the strain gauge logging was also split into two groups, east and west, and were logged with the accelerometers for the corresponding east or west setup. The ambient temperature during the test was around 12° C. Tables E8–E11 list the traffic description for Hudson Bay Bridge during this test.

Table B.8. Truck description for west side setup on September 29, 2005.

File #	Truck description	Direction of travel	Lane (wrt direction)	# of axles	Log truck #	Speed	Gross weight (kg)	Tare weight (kg)
1	test truck	SB	R	5		crawl	51660	
2	test truck	NB	L	5		crawl	51660	
3	test truck	SB	R	5		crawl	51660	
4	test truck	NB	L	5		crawl	51660	
5	test truck	SB	R	5		crawl	51660	
6	test truck	NB	R	5		crawl	51660	
7	test truck	SB	R	5		crawl	51660	
8	test truck	NB	R	5		crawl	51660	
9	test truck	SB	L	5		crawl	51660	
10	test truck	NB	R	5		crawl	51660	
11	test truck	SB	R	5		highway	51660	
12	test truck	NB	R	5		highway	51660	
13	test truck	SB	R	5		highway	51660	
14	log truck, gas truck	NB	R	7, 7		highway		
15	test truck	NB	R	5		highway	51660	

Table B.8 continued.

16	test truck	NB	L	5		highway	51660
17	trailer truck	SB	L	6		highway	
18	test truck	SB	L	5		highway	51660
19	test truck	NB	L	5		highway	51660
20	test truck	SB	L	5		highway	51660

Table B.9. Truck description for east side setup on September 29, 2005.

File #	Truck description	Direction of travel	Lane (wrt direction)	# of axles	Log truck #	Speed	Gross weight (kg)	Tare weight (kg)
21	test truck	SB	R	5		crawl	51660	
22	test truck	NB	L	5		crawl	51660	
23	test truck	SB	R	5		crawl	51660	
24	test truck	NB	L	5		crawl	51660	
25	test truck	SB	L	5		crawl	51660	
26	test truck	NB	R	5		crawl	51660	
27	test truck	SB	L	5		crawl	51660	
28	test truck	NB	R	5		crawl	51660	
29	test truck	SB	R	5		highway	51660	
30	log truck	NB	L	7		highway		
31	test truck	NB	L	5		highway	51660	
32	two trailer trucks	SB	Middle	6		highway		
33	test truck	SB	R	5		highway	51660	
34	test truck	NB	L	5		highway	51660	
35	test truck	SB	L	5		highway	51660	
36	test truck	NB	R	5		highway	51660	
37	test truck	SB	L	5		highway	51660	
38	log truck	NB	R	6	6814	highway	60340	18230
39	test truck	NB	R	5		highway	51660	
40	Coop gas truck	SB	R	9		highway		
41	log truck	SB	R	6	6602	highway	60080	18820
42	log truck	SB	R	6	6203	highway	60880	18240
43	ambient							
44	trailer truck	SB	R	6		highway		
45	truck	SB	R	5		highway		
46	ambient							
47	gravel truck, 1 ton truck	SB	R	5, 2		highway		
48	log truck, empty	SB	R			highway		
49	log truck	NB	R	7	6102	highway	69800	20970
50	log truck	NB	R	8	6800	highway	58690	21850

Table B.9 continued.

51	ambient							
52	log truck, empty	SB	R	8	6808	highway	67830	21080
53	ambient							
54	log truck	NB	R	8	6504	highway	72830	21270
55	log truck	NB	R	6	6201	highway	60910	17900
56	gravel truck	NB	R	3		highway		
57	log truck	NB	R	7	6604	highway	72930	20800
58	ambient							
59	gravel truck, empty	SB	R	5		highway		
60	log truck, empty	SB	R	7		highway		
61	ambient							
62	ambient							
63	log truck	NB	R	8	6106	highway	71590	21060
64	log truck	NB	R	6	6600	highway	60350	18330
65	ambient							
66	log truck, empty	SB	R	8	6604	highway	72150	21000
67	gravel truck	SB	R	5		highway		
68	log truck	NB	R	6	6506	highway	60960	17490
69	grain truck	NB	R	8		highway		
70	log truck	NB	R	8	6804	highway	70640	20040

Table B.10. Truck description for west side setup on September 30, 2005.

File #	Truck description	Direction of travel	Lane (wrt direction)	# of axles	Log truck #	Speed	Gross weight (kg)	Tare weight (kg)
1	ambient							
2	log truck, empty	SB	R	7	6604	highway		20720
3	log truck	NB	R	7	6806	highway	69030	19650
4	ambient + light truck + 3 ton	NB and SB	R	3, 3		highway		
5	ambient							
6	log truck, empty	SB	R			highway		
7	ambient							
8	gravel truck	NB	R	5	4013	highway		
9	log trucks	NB	R	8	6809	highway	68900	21920
				6	6201		58420	17980
10	log truck, empty and gravel truck	SB	R	6, 5		highway		
11	standard trailer and pickup	SB and NB	R	6, 2		highway		
12	ambient							
13	log truck, empty	SB	R	8	6807	highway	62440	20220
14	ambient							

Table B.10 continued.

15	ambient							
16	gravel truck	NB	R	5		highway		
17	log truck, empty	SB	R	6	6201	highway	60490	18090
18	gravel truck, empty	SB	R	5		highway		
19	gravel truck, empty	SB	R	5	4013	highway		
20	log truck	NB	R	6	4509	highway	60470	17770
21	ambient							
22	2 pickups and truck	SB, SB, and NB	R	2, 2, and 5		highway		
23	gravel truck, empty	SB	R	5		highway		
24	gravel truck	NB	R	5	4013	highway		
25	gravel truck	SB	R	5		highway		
26	ambient							
27	ambient							
28	gravel truck	NB	R	5		highway		
29	gravel truck, empty	SB	R	5		highway		
30	log truck	NB	R	8	6606	highway	72310	22260
31	log truck	SB	R	8	6809	highway	68140	20980
	gravel truck			5				
32	ice cream truck	SB	R	3		highway		
33	gravel truck	SB	R	5		highway		
34	log truck, empty	SB	R	6	6303	highway		17260
	log truck, empty	SB	R	8				
35	log truck	NB	R	6	6200	highway	56670	18210

Table B.11. Truck description for east side setup on September 30, 2005.

File #	Truck description	Direction of travel	Lane (wrt direction)	# of axles	Log truck #	Speed	Gross weight (kg)	Tare weight (kg)
36	gravel truck	NB	R	5	6501	highway		
37	ambient							
38	gravel truck, empty	SB	R	5		highway		
39	log truck	NB	R	8	7	highway		
40	ambient							
41	log truck, empty	SB	R	6	6600	highway		18200
	3 pickups	SB	R	2, 2, 2				
42	log truck, empty	SB	R	8	6206	highway		
43	empty gravel truck, full gravel truck	SB and NB	R	7, 7		highway		
44	ambient							
45	grain truck	SB	R	3		highway		
46	standard trailer	NB	R	6		highway		

Table B.11 continued.

47	gravel truck	NB	R	5		highway		
48	truck w/o trailer	NB	R	3	6810	highway		
49	gravel truck	NB	R	5		highway		
50	gravel truck	NB	R	5	4013	highway		
51	log truck, empty	SB	R	8	5066	highway	61430	22250
52	standard trailer	SB	R	6		highway		
53	ambient							
54	ambient							
55	log truck	SB	R	8	6604	highway	72120	21210
56	grain truck	SB	R	3		highway		
57	log truck	NB	R	6	6103	highway	60390	16910
58	log truck	NB	R	6	6500	highway	60310	17040
59	log truck	NB	R	6	6203	highway	60900	17970
60	gravel truck	SB	R	5		highway		
61	gravel truck	SB	R	5		highway		
62	standard trailer	SB	R	6		highway		
63	gravel truck	NB	R	5		highway		
64	gravel truck and pickup	SB and NB	R	5 and 2		highway		
65	log truck, and two 3-axle trucks	SB, NB, and NB	R	9, 3, and 3		highway		

APPENDIX C

DYNAMIC TRUCK SIMULATION

C.1 Properties of QS-600 truck

Table C.1. Properties of QS-600 trcuk (Fafard et al. 1998).

a) Semi-tractor	Properties	
	value	units
Total weight of truck	40775	kg
Mass of wheel assembly	340	kg
Spring stiffness of suspension of front wheels	4000	kN/m
Spring stiffness of suspension of 2nd wheel row (tandem), and rear wheels	8000	kN/m
Spring stiffness of front wheel assembly	2250	kN/m
Spring stiffness of 2nd wheel row (tandem), and rear wheels assembly	8000	kN/m
Damping of suspension	20	kN.s/m
Damping wheel assembly	20	kN.s/m

b) Trailer	Properties	
	value	units
Total weight of truck	26504	kg
Mass of wheel assembly	340	kg
Spring stiffness of suspension of front wheels	4000	kN/m
Spring stiffness of suspension of rear wheels (tandem)	8000	kN/m
Spring stifness of front wheel assembly	2250	kN/m
spring of tire of rear wheel (tandem)	8000	kN/m
Damping of suspension	20	kN.s/m
Damping of wheel assembly	20	kN.s/m

APPENDIX D

RESULTS OF FIELD TESTS ON HUDSON BAY BRIDGE

D.1 Results of rebound hammer test

Table D.1. Field test rebound hammer readings.

		Rebound hammer number (N)		
Region	Location	Reading 1	Reading 2	Reading 3
NE corner	1	47	47	49
of deck	2	52	48	50
	3	46	50	51
NW corner	1	48	47	51
of deck	2	50	45	38
	3	48	48	48
SE corner	1	46	46	52
of deck	2	40	46	42
	3	47	38	50
SW corner	1	38	36	45
of deck	2	45	46	48
	3	48	48	46
Midspan	1	43	44	43
of deck	2	44	44	50
	3	38	42	42

D.2 Variability of modal parameters calculated from site measurement on Hudson Bay Bridge

Table D.2. Standard deviation of the normalised amplitudes of the first mode in the middle span due to free decaying truck excitation.

X coord.	East Side			West Side		
(m)	Modal amplitude	σ	CV %	Modal amplitude	σ	CV %
31	0	- - -	- - -	0	- - -	- - -
36.5	0.42	0.02	4.93	0.42	0.02	4.51
42	0.84	0.03	3.55	0.84	0.01	1.58
47.5	1.15	0.05	4.23	1.18	0.02	1.44
53.1	1.17	0.04	3.26	1.19	0.05	4.02
58.6	0.82	0.03	3.30	0.86	0.05	5.60
64.1	0.39	0.02	5.96	0.43	0.03	7.52
69.6	0	- - -	- - -	0.00	- - -	- - -

Table D.3. Standard deviation of the normalised amplitudes of the first mode in the middle span due to ambient excitation.

X coord.	East Side			West Side		
(m)	Modal amplitude	σ	CV %	Modal amplitude	σ	CV %
31	0	- - -	- - -	0	- - -	- - -
36.5	0.37	0.15	40.68	0.45	0.15	32.11
42	0.65	0.22	34.43	0.83	0.51	61.33
47.5	1.09	0.20	18.58	0.78	0.24	31.24
53.1	1.09	0.20	18.58	0.84	0.29	34.39
58.6	0.70	0.31	44.77	0.62	0.16	26.22
64.1	0.33	0.16	48.40	0.50	0.26	52.37
69.6	0	- - -	- - -	0.00	- - -	- - -

APPENDIX E

HDUSON BAY BRIDGE IMPACT TEST RESULTS

E.1 Locations of Impact Hammer and Accelerometers

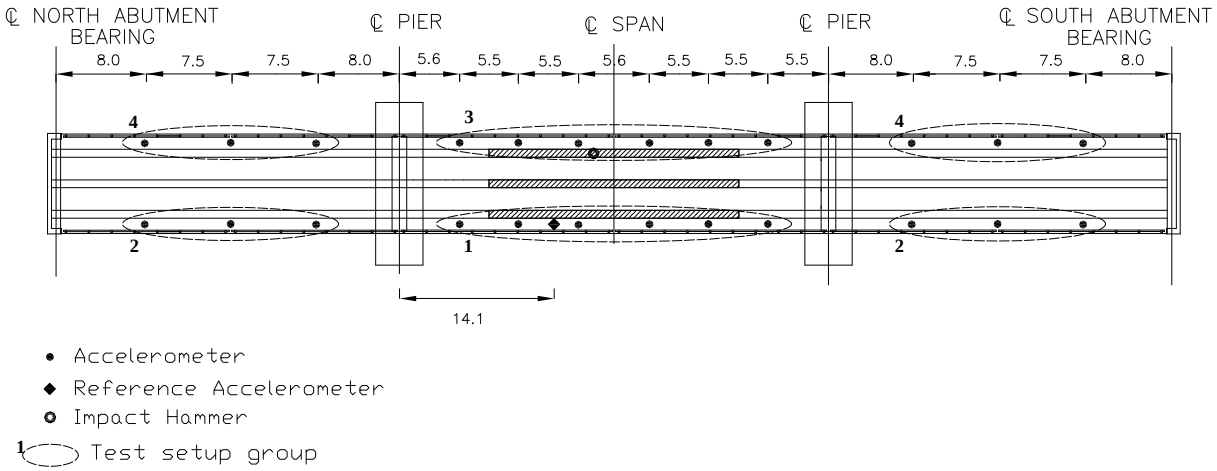

Figure E.1. A plan view showing test setup for impact testing at Hudson Bay Bridge.

E.2 Modal Amplitude and Statistical Characteristics of Mode 1 (2.640 Hz) Calculated From Spring Hammer Excitation, with rubber pad

Table E.1. Modal amplitudes and statistical characteristics of Mode 1 Spring Hammer Excitation, with rubber pad

Node number	Normalized modal amplitude	Phase angle (degrees)	σ	CV %
3	0.49	-179.70	0.02	4.14
4	0.43	179.24	0.02	5.42
5	0.69	179.62	0.02	3.25
6	0.68	179.05	0.03	3.69
7	0.40	-179.49	0.02	4.91
8	0.49	179.18	0.03	6.53
11	0.40	0.43	0.03	7.59
12	0.39	1.65	0.02	5.69
13	0.80	1.03	0.03	3.77
14	0.79	1.61	0.04	5.17
15	1.10	0.61	0.04	3.30
16	1.10	1.10	0.05	4.12
17	1.13	0.39	0.04	3.10

Table E1 contd.

18	1.12	1.20	0.04	3.88
19	0.82	0.05	0.03	3.91
20	0.81	1.11	0.04	4.34
21	0.41	0.71	0.02	4.43
22	0.41	1.05	0.02	5.58
25	0.51	179.51	0.02	4.82
26	0.51	178.37	0.03	5.61
27	0.74	-179.85	0.04	4.84
28	0.74	179.07	0.04	5.04
29	0.49	179.30	0.02	4.09
30	0.47	179.73	0.03	7.21
33	1.00	0.00	0.00	0.00

σ = Standard deviation, CV = Coefficient of variation.

E.3 Modal Amplitude and Statistical Characteristics of Mode 1 (2.641 Hz) Calculated From Spring Hammer Excitation, without rubber pad

Table E.2. Modal amplitudes and statistical characteristics of Mode 1 Spring Hammer Excitation, without rubber pad

Node number	Normalized modal amplitude	Phase angle (degrees)	σ	CV %
3	0.48	179.48	0.05	9.66
4	0.42	179.47	0.03	8.06
5	0.67	179.92	0.03	4.80
6	0.68	178.69	0.05	7.33
7	0.39	179.60	0.03	8.51
8	0.45	179.91	0.09	20.89
11	0.40	0.41	0.02	4.46
12	0.40	-0.20	0.02	5.77
13	0.81	0.04	0.03	3.09
14	0.82	-0.61	0.05	6.00
15	1.12	-0.01	0.03	2.71
16	1.11	0.30	0.01	1.28
17	1.12	-0.34	0.04	3.68
18	1.15	-0.25	0.04	3.58
19	0.82	-0.21	0.03	3.12
20	0.81	-0.26	0.03	3.51
21	0.42	1.12	0.02	4.72
22	0.41	-0.29	0.03	6.86

Table E2 contd.

25	0.51	179.77	0.03	6.65
26	0.51	179.21	0.04	8.58
27	0.70	179.47	0.05	6.57
28	0.75	178.56	0.04	5.47
29	0.48	-179.65	0.04	8.74
30	0.46	178.26	0.05	10.38
33	1.00	0.00	0.00	0.00

σ = Standard deviation, CV = Coefficient of variation.

E.4 Modal Amplitude of Mode 1 (2.625 Hz) Calculated From Ambient Excitation

Table E.3. Modal amplitudes and statistical characteristics of mode 1 induced by ambient excitation

Node number	Normalized modal amplitude	Phase angle (degrees)
3	1.52	180.00
4	1.29	180.00
5	0.88	180.00
6	1.88	180.00
7	0.54	0.00
8	1.22	180.00
11	0.54	0.00
12	0.29	0.00
13	0.92	0.00
14	0.26	180.00
15	1.11	0.00
16	0.71	0.00
17	1.54	0.00
18	0.91	0.00
19	1.44	0.00
20	0.35	180.00
21	0.95	0.00
22	0.33	0.00
25	0.59	0.00
26	0.38	180.00
27	0.89	0.00
28	0.61	180.00
29	0.76	0.00
30	0.44	180.00
33	1.00	0.00

APPENDIX F

BROADVIEW BRIDGE TEST RESULTS

F.1 Locations of Accelerometer Measured Response

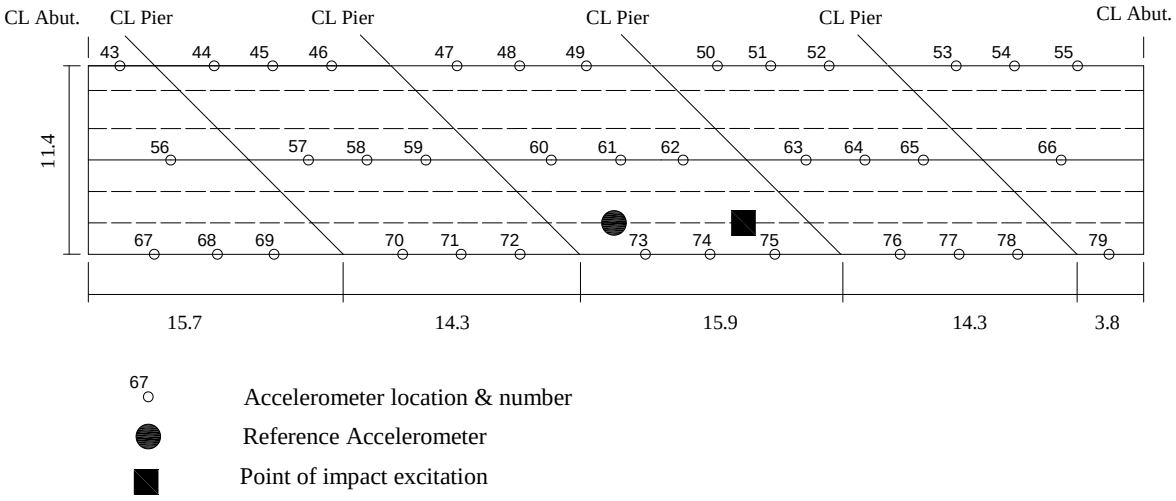

Figure F.1. Schematic plan showing nodes numbers of accelerometer response for Broadview Bridge.

F.2 Modal Amplitude and Statistical Characteristics of Mode 1 (9.967 Hz) Calculated From 50 kN Impact Excitation

Table F.1. Modal amplitudes and statistical characteristics of Mode 1 induced by 50 kN impact excitation

Node number	Normalized modal amplitude	Phase angle (degrees)	σ	CV %
44	0.36	164.87	0.22	119.23
45	0.48	167.04	0.28	104.70
46	0.28	169.10	0.15	91.76
47	1.23	-11.76	0.72	104.77
48	1.77	-11.31	1.04	106.57
49	1.47	-12.24	0.89	114.34
50	0.45	-176.34	0.17	33.46
51	0.50	169.64	0.43	66.92
52	0.35	157.86	0.48	101.82
53	0.32	18.59	0.27	101.25
54	0.41	11.88	0.23	59.48
55	0.31	9.21	0.14	48.69
56	2.21	-3.51	0.48	22.86
57	0.74	179.71	0.06	8.02
58	0.99	178.83	0.11	10.84
59	0.67	177.91	0.10	14.85
60	0.11	8.31	0.04	31.26
61	0.01	123.49	0.01	148.68
62	0.24	1.06	0.03	10.48
63	1.19	177.55	0.40	36.26
64	1.70	177.92	0.51	31.93
65	1.18	178.19	0.32	29.42
66	2.26	-2.40	0.66	31.34
67	0.42	40.86	0.57	66.09
68	0.55	40.65	0.79	68.82
69	0.40	45.97	0.60	73.31
70	0.56	-167.95	0.42	46.77
71	0.72	-164.41	0.62	50.93
72	0.55	-156.40	0.58	58.00
73	0.43	1.95	0.27	62.42
74	0.53	-0.27	0.32	61.60
75	0.35	-0.36	0.25	72.70
76	0.15	-161.13	0.07	45.07
77	0.20	-159.86	0.10	49.17
78	0.15	-153.16	0.09	64.86
79	2.98	-2.11	0.78	27.90
80	1.00	0.00	0.00	0.00

σ = Standard deviation, CV = Coefficient of variation.

F.3 Modal Amplitude and Statistical Characteristics of Mode 2 (11.17 Hz) Calculated From 25 kN Impact Excitation

Table F.2. Modal amplitudes and statistical characteristics of Mode 2 induced by 25 kN impact excitation

Node number	Normalized modal amplitude	Phase angle (degrees)	σ	CV %
44	0.43	5.51	0.27	63.18
45	0.58	9.49	0.40	72.23
46	0.31	15.52	0.27	94.62
47	1.65	-170.96	0.99	62.74
48	2.38	-170.61	1.42	63.00
49	2.02	-171.72	1.14	58.70
50	0.25	145.74	0.36	143.53
51	0.15	102.58	0.42	272.47
52	0.11	60.99	0.28	257.30
53	0.23	-37.41	0.33	139.68
54	0.28	-41.54	0.43	155.63
55	0.20	-43.86	0.33	165.40
56	0.19	-130.66	0.41	213.35
57	0.38	160.59	0.32	83.19
58	0.58	164.77	0.39	66.91
59	0.46	167.21	0.26	56.61
60	0.09	-27.71	0.09	111.14
61	0.06	159.34	0.06	86.48
62	0.15	165.67	0.08	50.57
63	0.75	-1.17	0.25	32.31
64	0.95	-1.56	0.37	37.59
65	0.59	-2.84	0.25	41.40
66	0.30	-158.30	0.62	193.81
67	0.32	-166.70	0.43	135.84
68	0.44	-167.19	0.57	131.37
69	0.34	-166.94	0.45	130.75
70	0.04	21.38	0.16	376.22
71	0.12	19.17	0.30	247.77
72	0.25	9.07	0.29	118.66
73	1.48	-4.10	0.22	15.40
74	1.79	-5.63	0.30	16.92
75	1.32	-5.62	0.23	18.07
76	0.15	-176.71	0.03	22.87
77	0.36	-176.75	0.07	20.08
78	0.31	-173.39	0.09	28.53
79	0.14	-130.74	0.71	409.30
80	1.00	0.00	0.00	0.00

σ = Standard deviation, CV = Coefficient of variation.

F.4 Modal Amplitude of Mode 1 (9.526 Hz) Calculated From Ambient Excitation

Table F.3. Modal amplitudes and statistical characteristics of mode 1 induced by ambient excitation

Node number	Normalized modal amplitude	Phase angle (degrees)
44	21.74	65.88
45	0.12	-135.89
46	0.09	-78.21
47	0.45	27.87
48	0.71	19.47
49	0.51	15.73
50	2.24	103.63
51	0.74	-142.42
52	2.51	112.15
53	9.86	5.01
54	12.70	-109.76
55	2.82	97.86
56	1.82	-15.88
57	0.65	169.54
58	0.75	165.26
59	0.69	146.45
60	0.22	-174.93
61	0.67	142.93
62	0.08	27.35
63	0.65	-168.40
64	0.90	-169.57
65	0.60	-167.60
66	1.37	6.62
67	0.30	-5.21
68	0.22	4.09
69	0.35	18.76
70	0.48	165.48
71	0.61	163.34
72	0.60	174.95
73	1.36	-8.10
74	1.26	25.07
75	0.96	21.42
76	0.19	80.14
77	0.85	-123.96
78	0.48	-131.02
79	1.87	8.06
80	1.00	0.00

APPENDIX G

EFFECT OF NOISE ON THE APPLICABILITY of VBDD

G.1 OVERVIEW

In this appendix, the effect of noise on the applicability of VBDD is demonstrated. Different damage detection methods under different noise levels are shown in the effort to come up with some recommendations regarding which one of the VBDD methods was more robust and capable of detecting small levels of damage using noisy site measurements. One damage scenario was considered in the comparison, namely the first damage scenario - cutting the external reinforcing bars from the middle of all girders at the centre span, as the results for the other damage scenarios can be deduced from this case of simulated damage. Two types of excitation were examined, namely harmonic excitation with a frequency corresponding the first natural frequency of the bridge and impact excitation, because these two types of excitation provided the best quality for extracted modal properties, thus making them good candidates for field application of VBDD. The VBDD methods examined in this appendix were: the change in mode shape method, the change in mode shape curvature method, the damage index method, the change in measured modal flexibility method, change in uniform load surface curvature method, and the change in unit load surface curvature method.

Two examples of the effect of noise on the ability of VBDD methods to detect damage were shown in Section 6.5. Appendix G, on the other hand, lists the results for all of the VBDD methods that were discussed in Section 2.3, with 1%, 2%, 5% and 10% noise levels introduced to either the input force or the output bridge response.

G.2 First damage scenario - cutting the external rebars from the middle of all girders at the centre span

G.2.1 Harmonic excitation (input noise)

G.2.1.1 Change in mode shape method

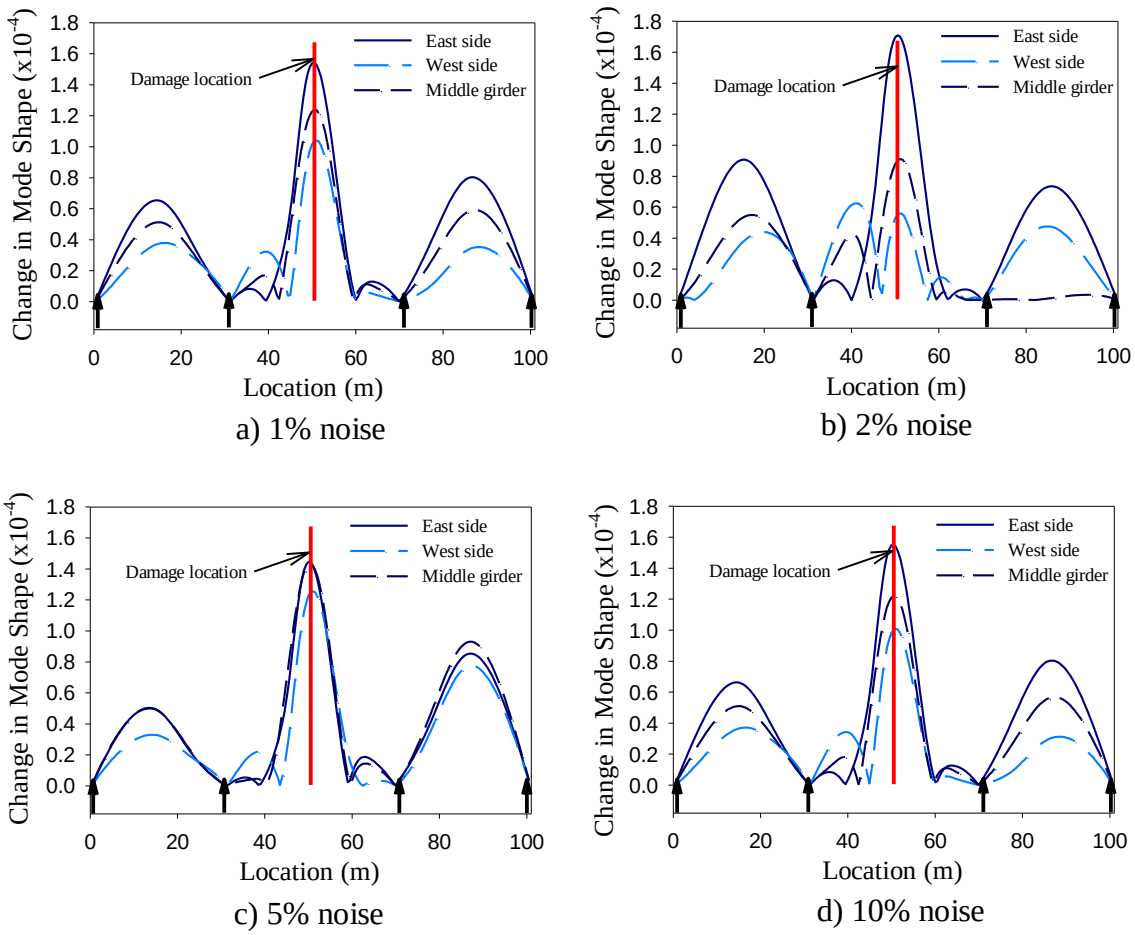

Figure G.1. Distribution of the change in mode shape for the first damage scenario when harmonic excitation was used and noise was added to input force: a) 1% noise, b) 2% noise, c) 5% noise, d) 10% noise.

G.2.1.2 Change in mode shape curvature method

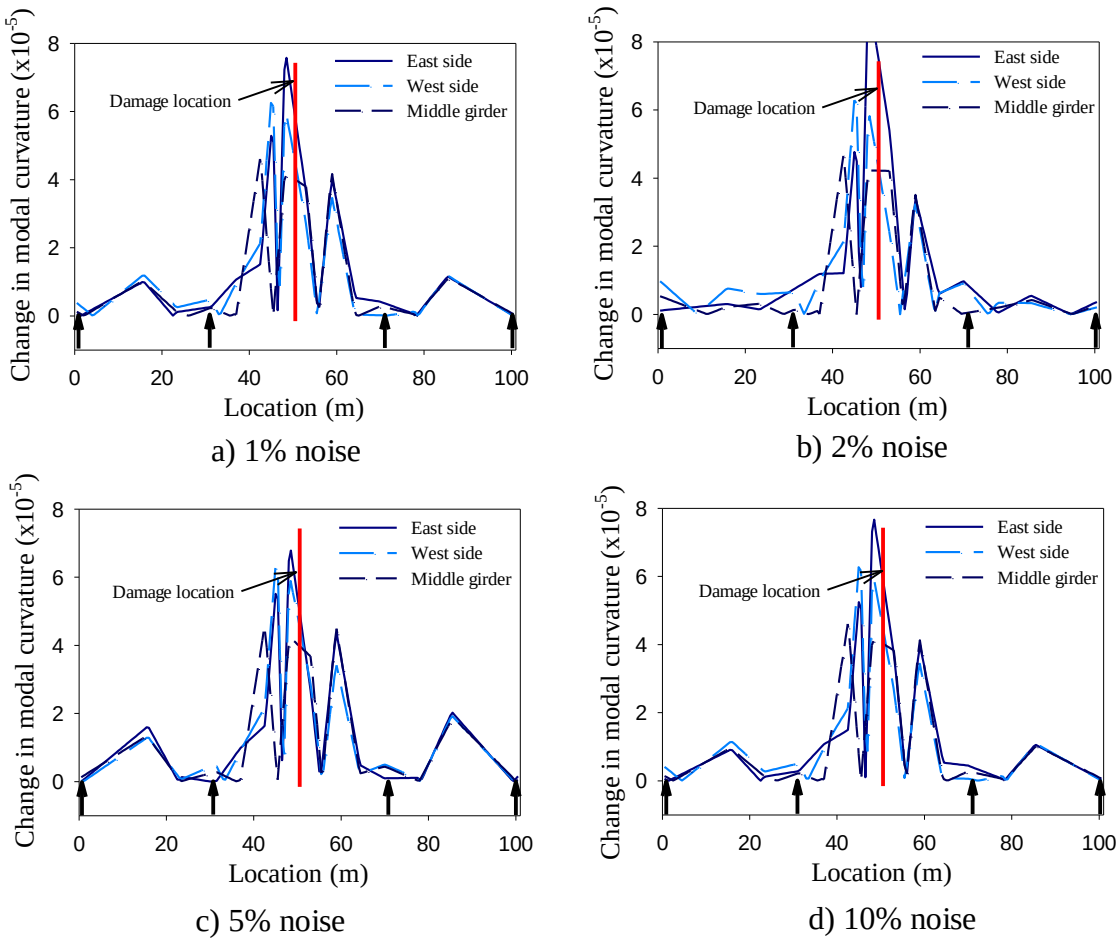

Figure G.2. Distribution of the change in mode shape curvature for the first damage scenario when harmonic excitation was used and noise was added to input force: a) 1% noise, b) 2% noise, c) 5% noise, d) 10% noise.

G.2.1.3 Damage index method

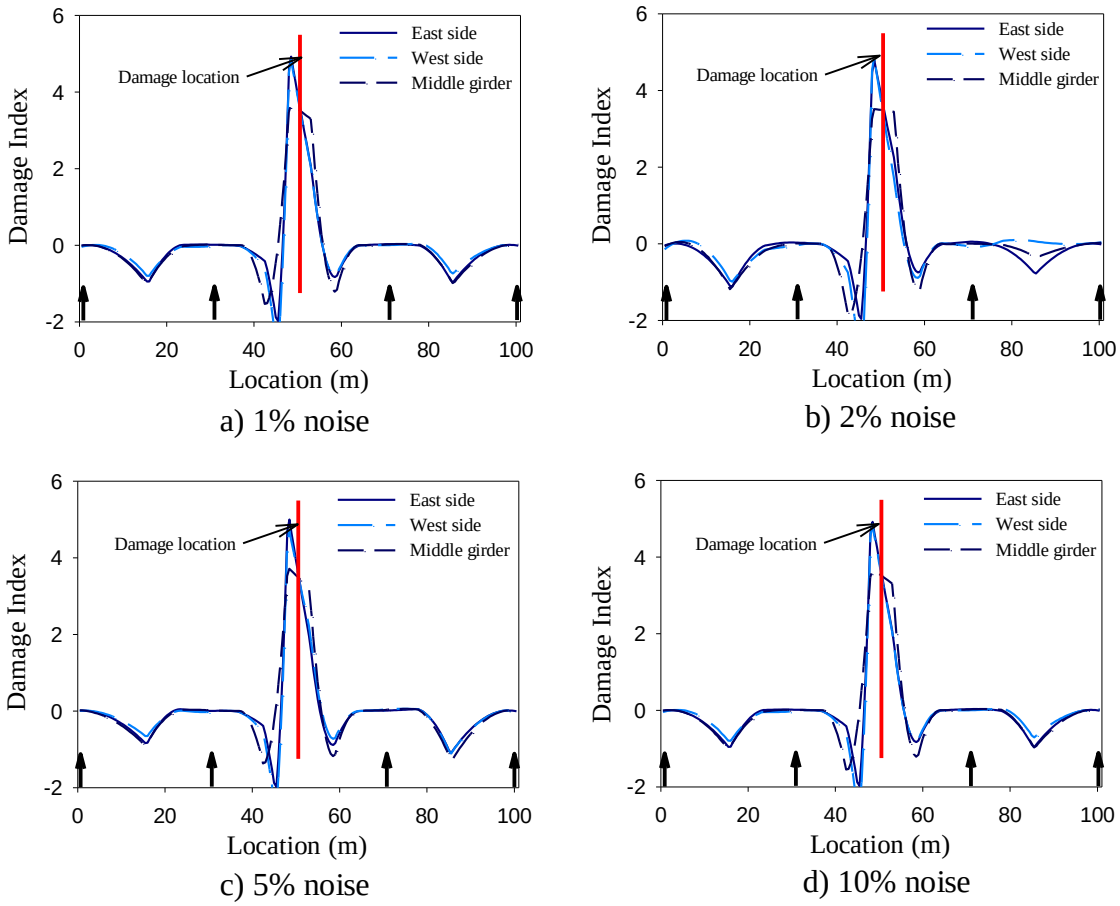

Figure G.3. Distribution of the damage index for the first damage scenario when harmonic excitation was used and noise was added to input force: a) 1% noise, b) 2% noise, c) 5% noise, d) 10% noise.

G.2.1.4 Change in modal flexibility method

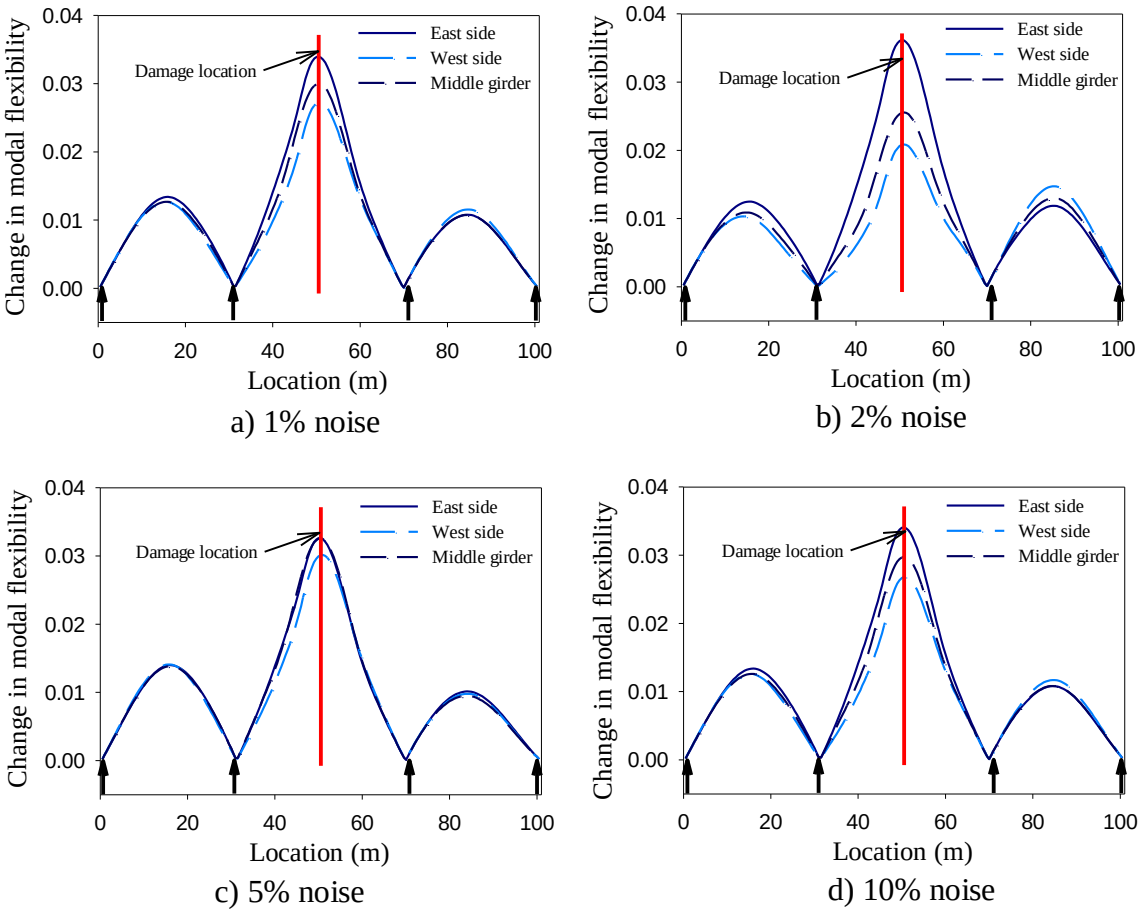

Figure G.4. Distribution of the change in modal flexibility for the first damage scenario when harmonic excitation was used and noise was added to input force: a) 1% noise, b) 2% noise, c) 5% noise, d) 10% noise.

G.2.1.5 Change in uniform load surface curvature method

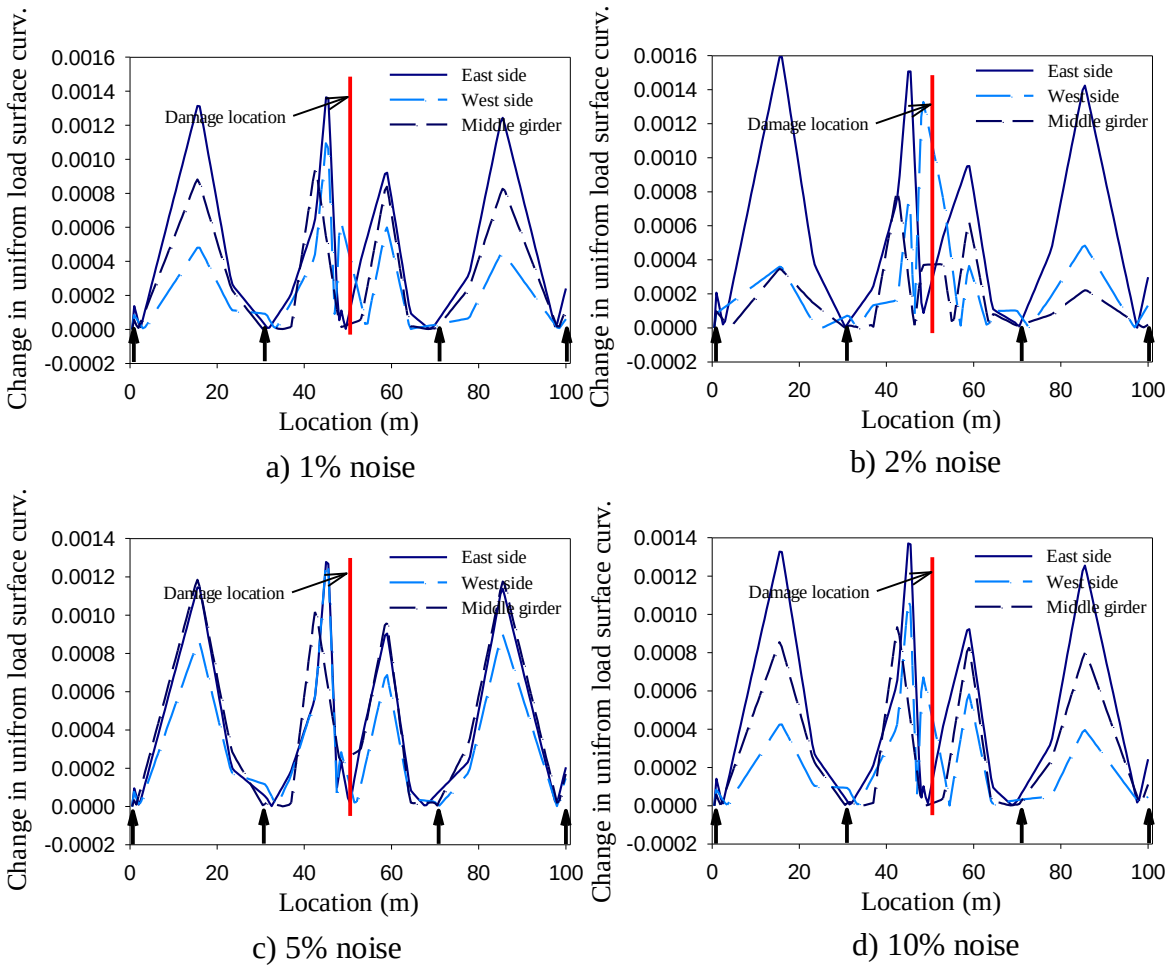

Figure G.5. Distribution of the change in uniform load surface curvature for the first damage scenario when harmonic excitation was used and noise was added to input force: a) 1% noise, b) 2% noise, c) 5% noise, d) 10% noise.

G.2.1.6 Change in unit load surface curvature method

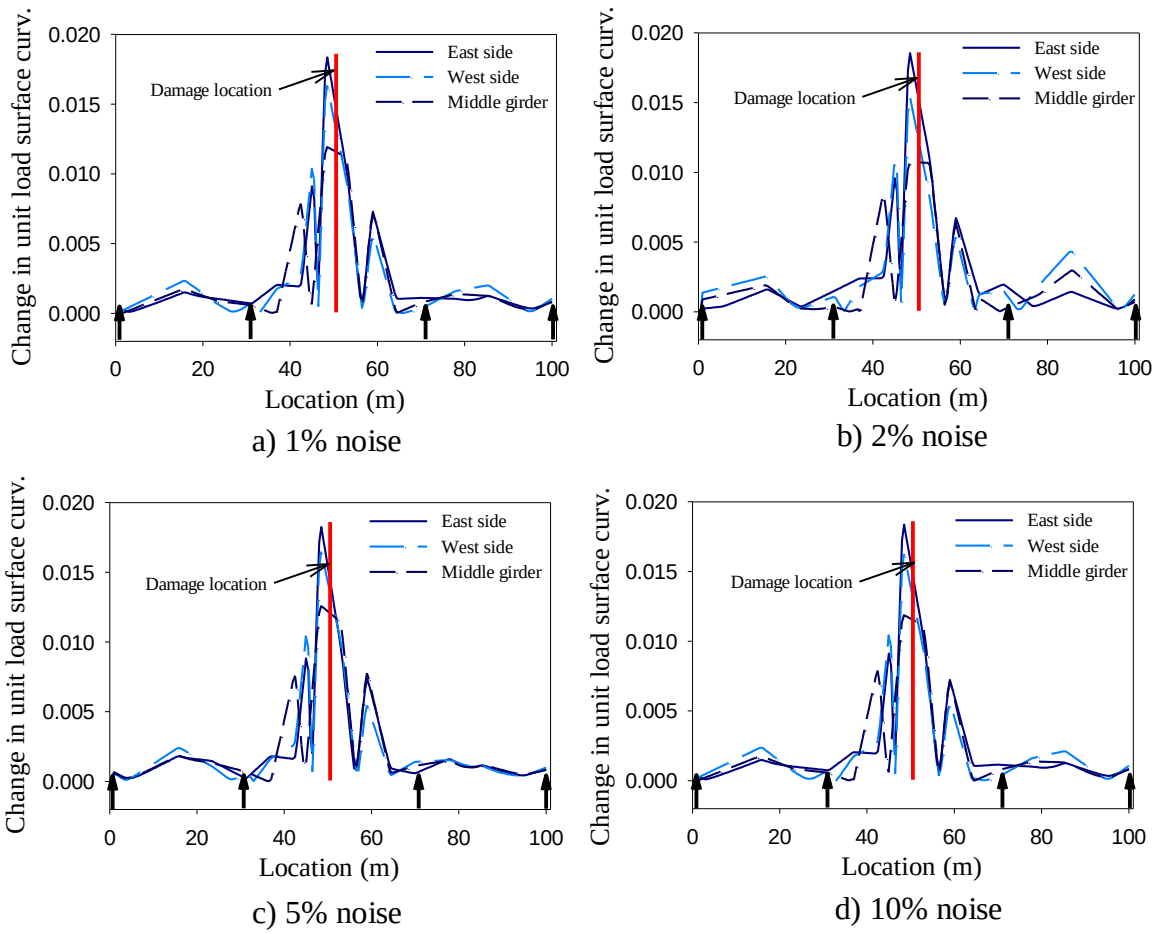

Figure G.6. Distribution of the change in unit load surface curvature for the first damage scenario when harmonic excitation was used and noise was added to input force: a) 1% noise, b) 2% noise, c) 5% noise, d) 10% noise.

G.2.2 Harmonic excitation (output noise)

G.2.2.1 Change in mode shape method

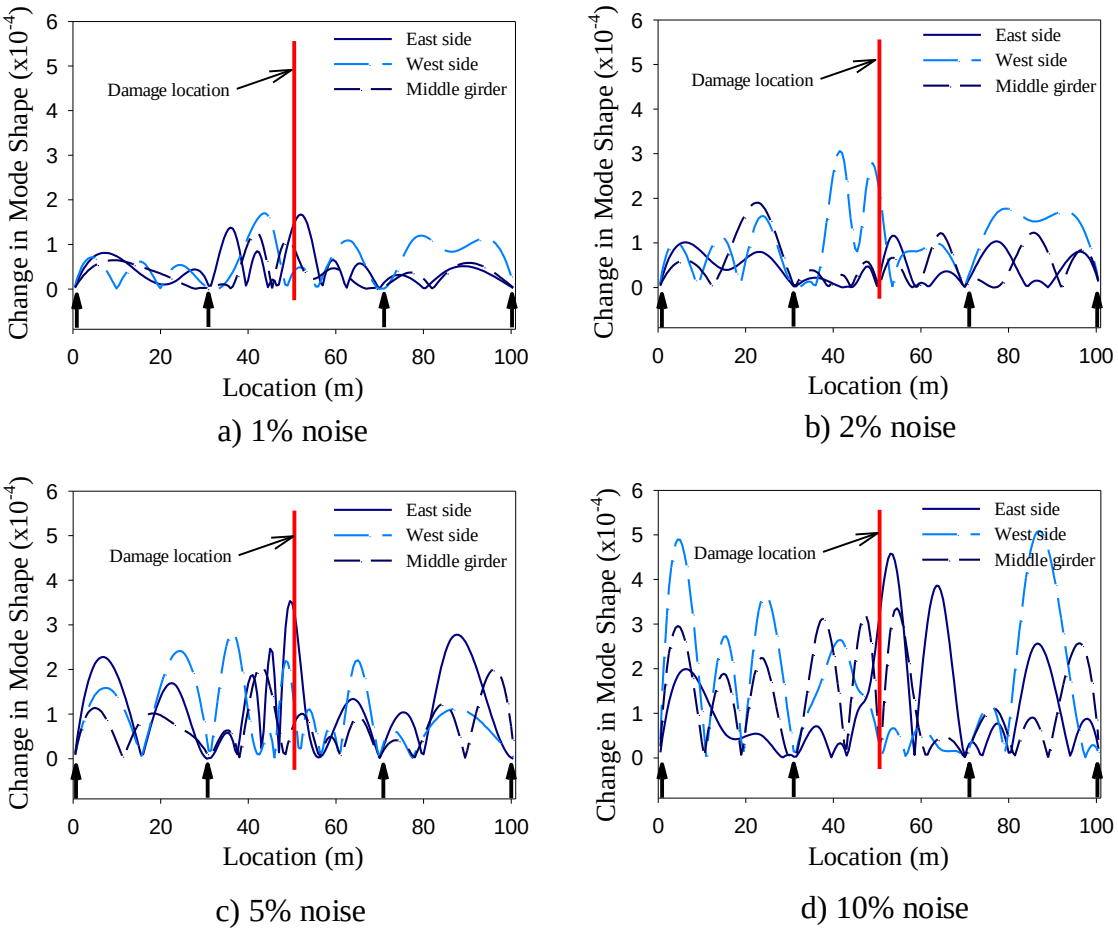

Figure G.7. Distribution of the change of mode shape for the first damage scenario when harmonic excitation was used and noise was added to the output signal: a) 1% noise, b) 2% noise, c) 5% noise, d) 10% noise.

G.2.2.2 Change in mode shape curvature method

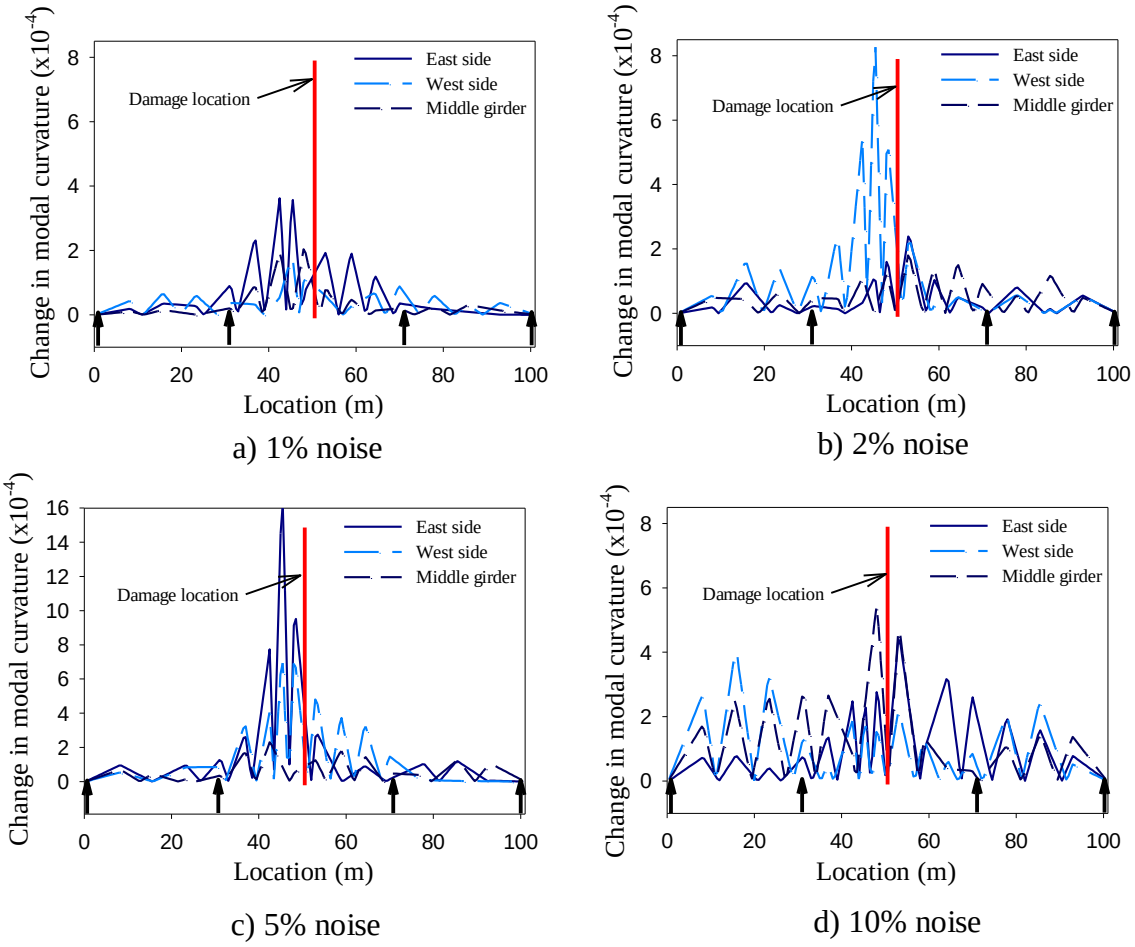

Figure G.8. Distribution of the change in mode shape curvature for the first damage scenario when harmonic excitation was used and noise was added to the output signal: a) 1% noise, b) 2% noise, c) 5% noise, d) 10% noise.

G.2.2.3 Damage index method

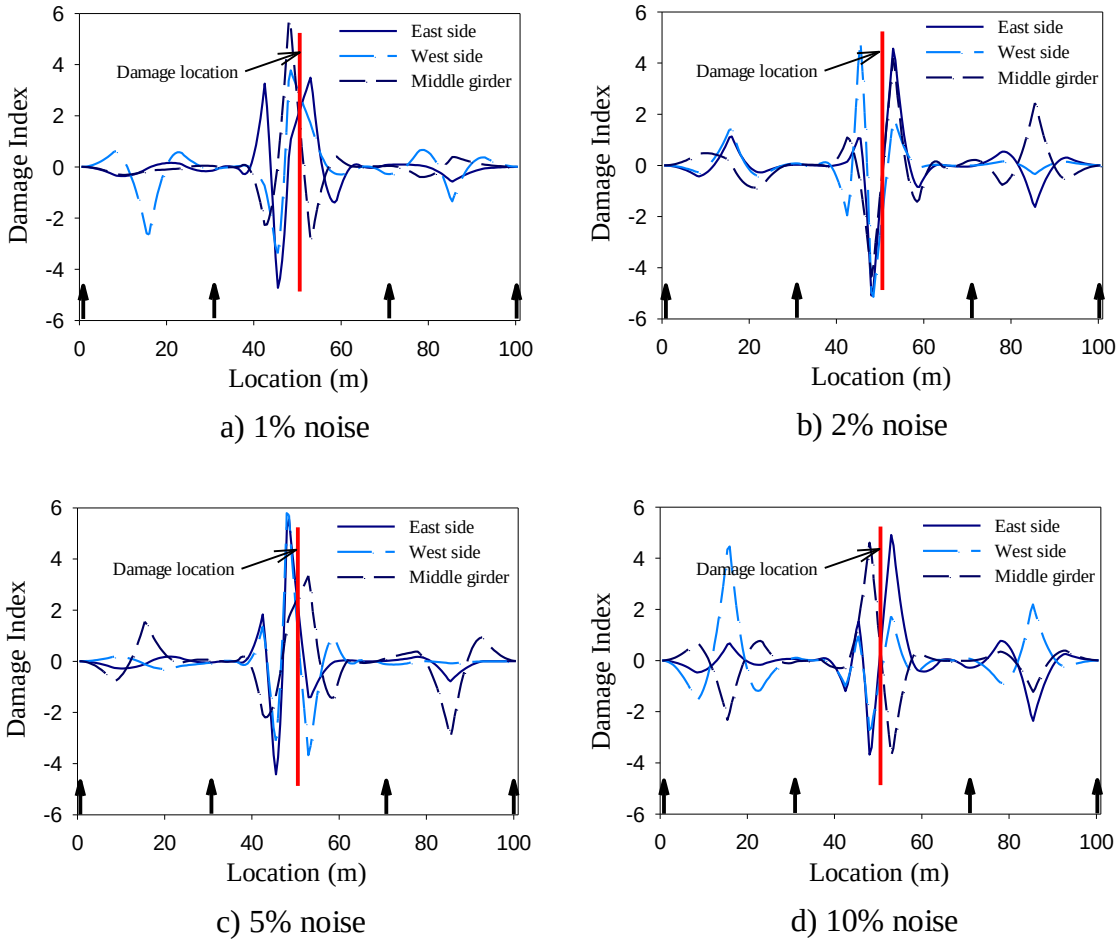

Figure G.9. Distribution of the damage index for the first damage scenario when harmonic excitation was used and noise was added to the output signal: a) 1% noise, b) 2% noise, c) 5% noise, d) 10% noise.

G.2.2.4 Change in modal flexibility method

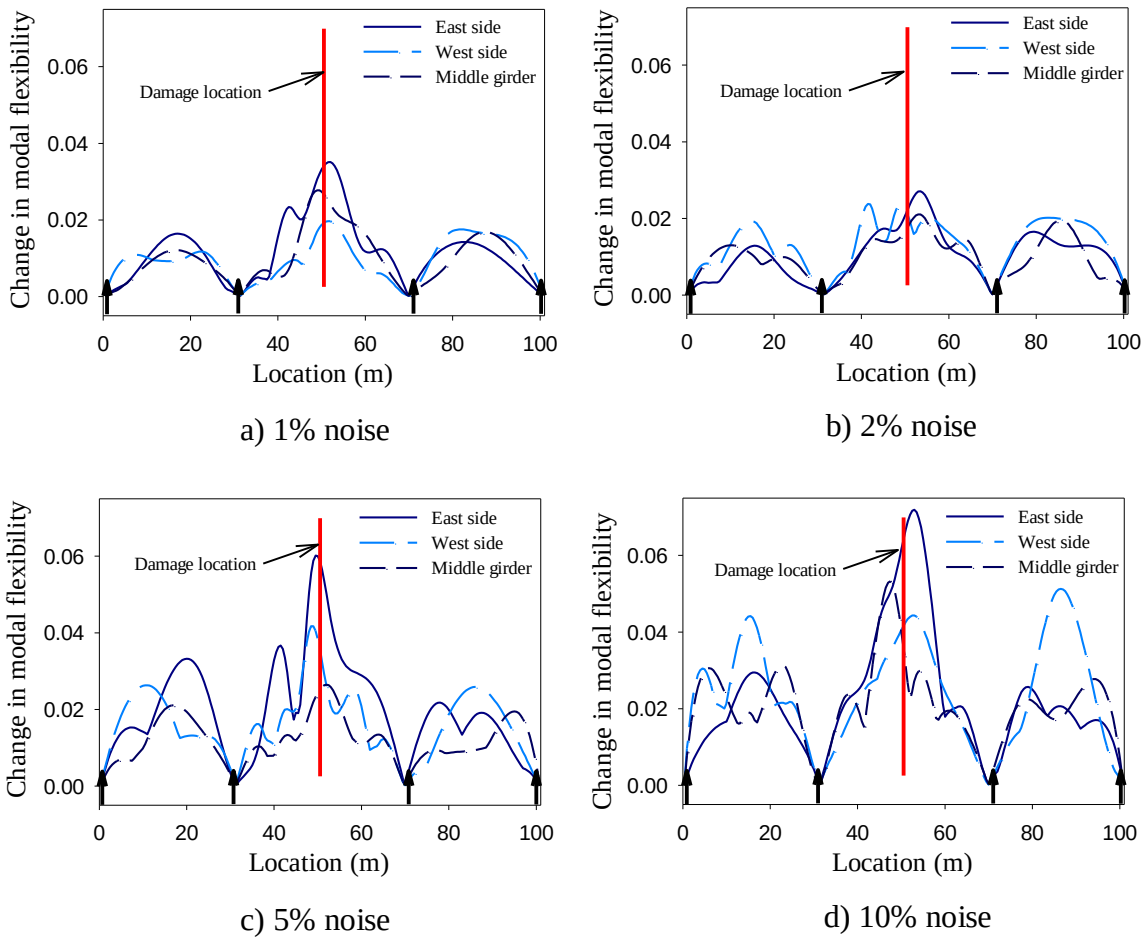

Figure G.10. Distribution of the change in modal flexibility for the first damage scenario when harmonic excitation was used and noise was added to the output signal: a) 1% noise, b) 2% noise, c) 5% noise, d) 10% noise.

G.2.2.5 Change in uniform load surface curvature method

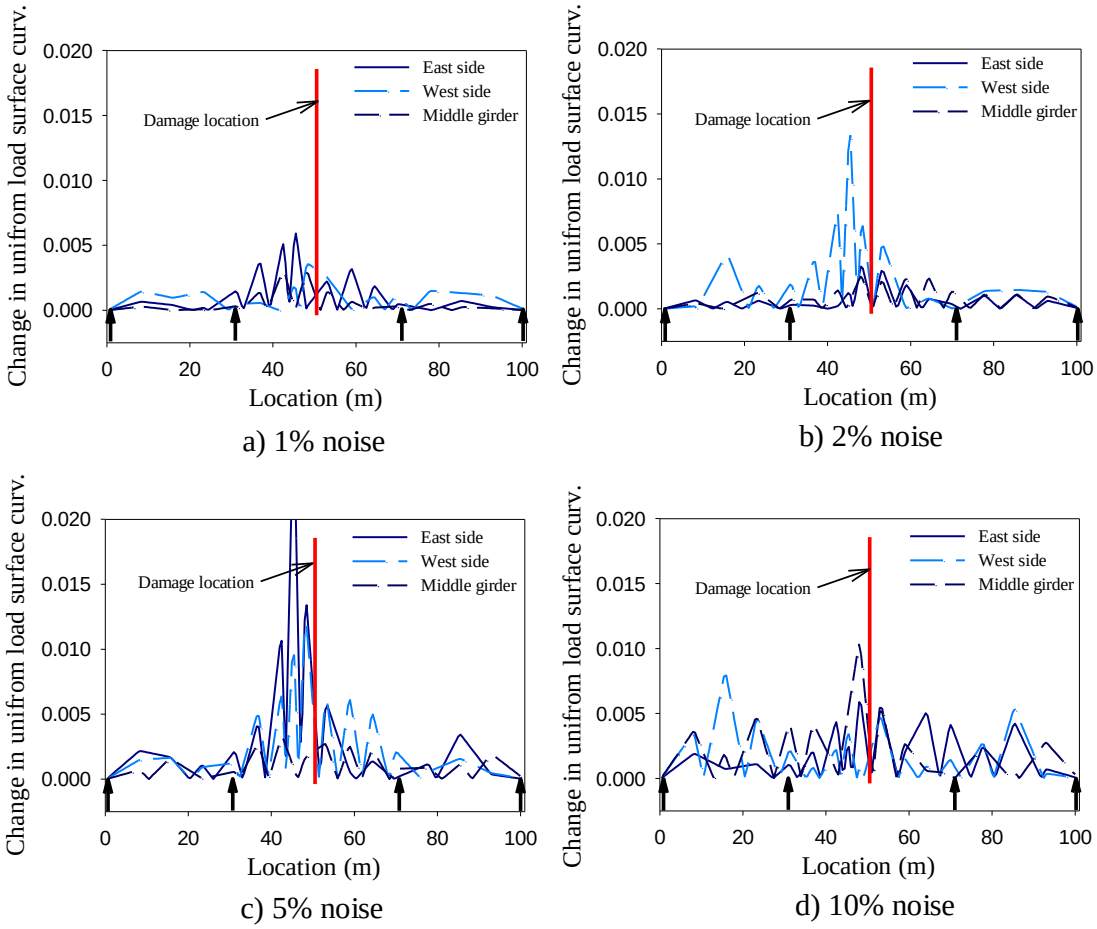

Figure G.11. Distribution of the change in uniform load surface curvature for the first damage scenario when harmonic excitation was used and noise was added to the output signal: a) 1% noise, b) 2% noise, c) 5% noise, d) 10% noise.

G.2.2.6 Unit load surface curvature method

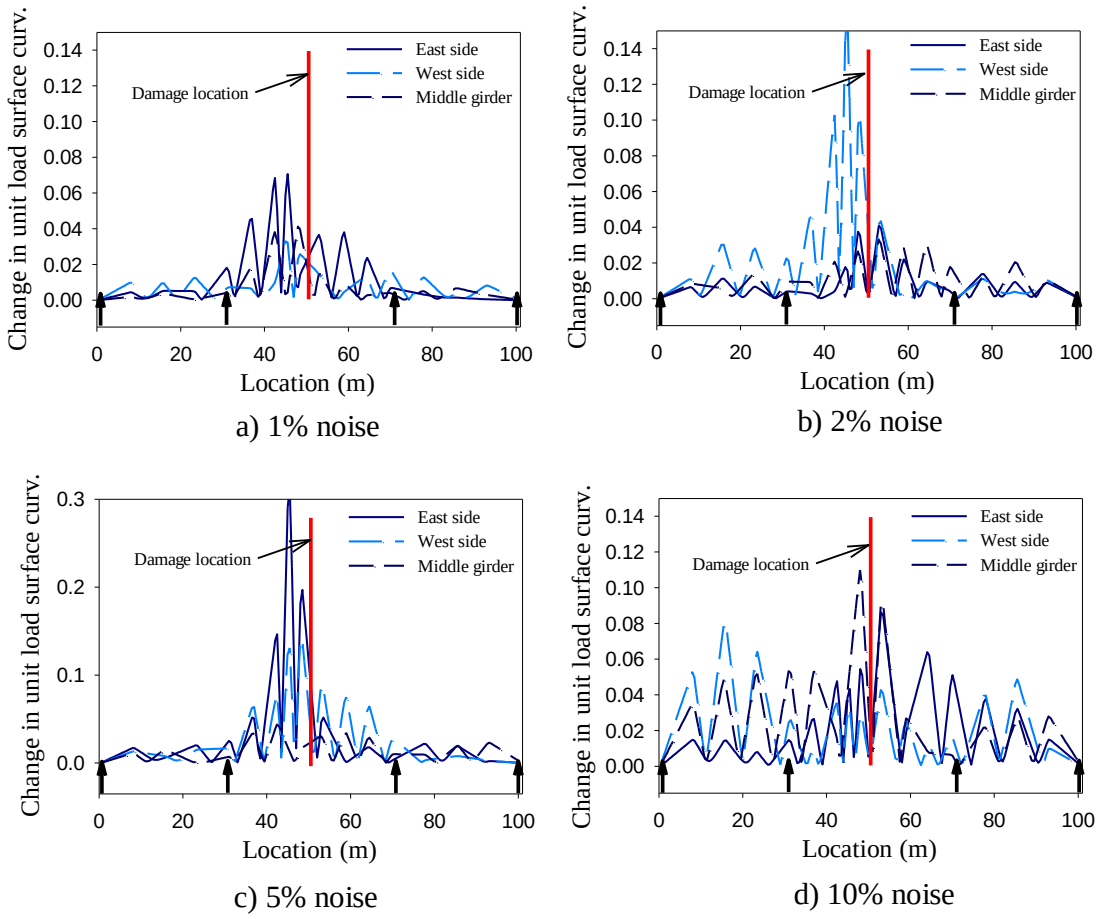

Figure G.12. Distribution of the change unit load surface curvature for the first damage scenario when harmonic excitation was used and noise was added to the output signal: a) 1% noise, b) 2% noise, c) 5% noise, d) 10% noise.

G.2.3 Impact excitation (input noise)

G.2.3.1 Change in mode shape method

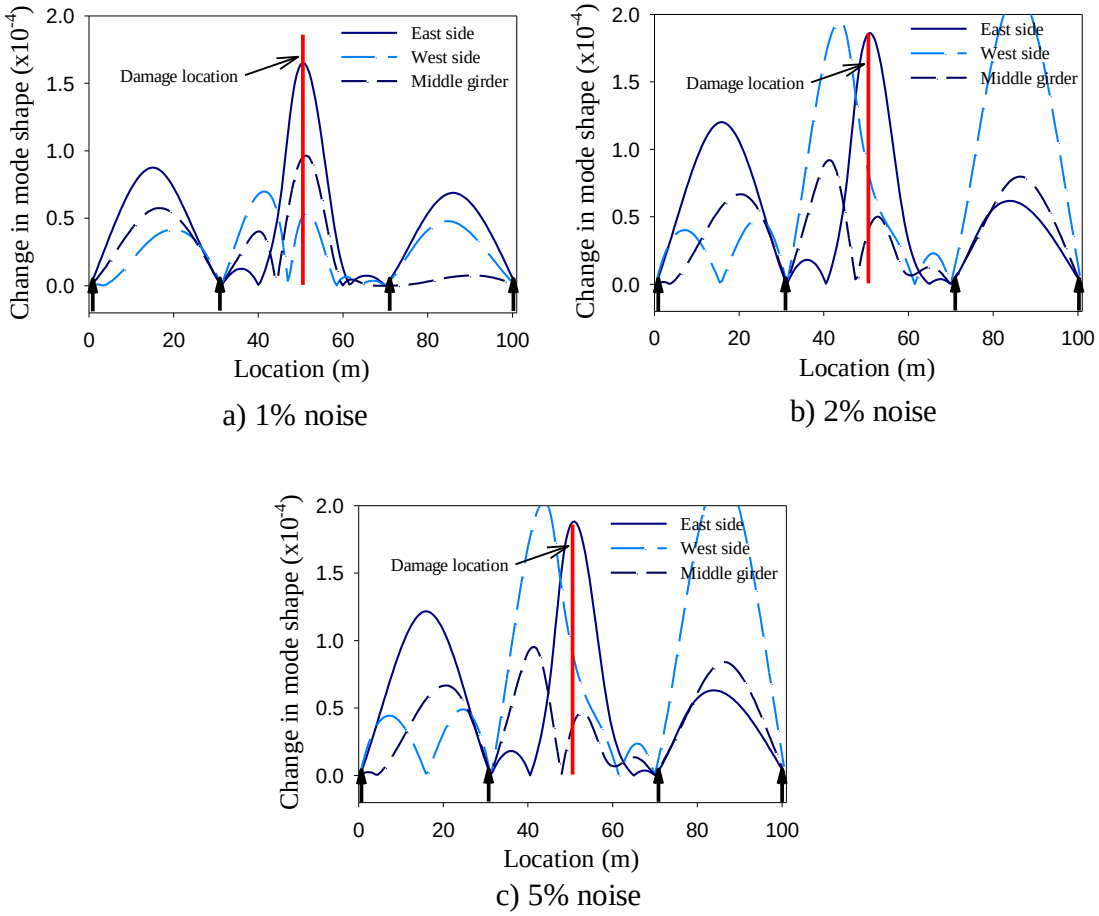

Figure G.13. Distribution of change in mode shape for the first damage scenario when impact excitation was used and noise was added to input force: a) 1% noise, b) 2% noise, c) 5% noise.

G.2.3.2 Change in mode shape curvature method

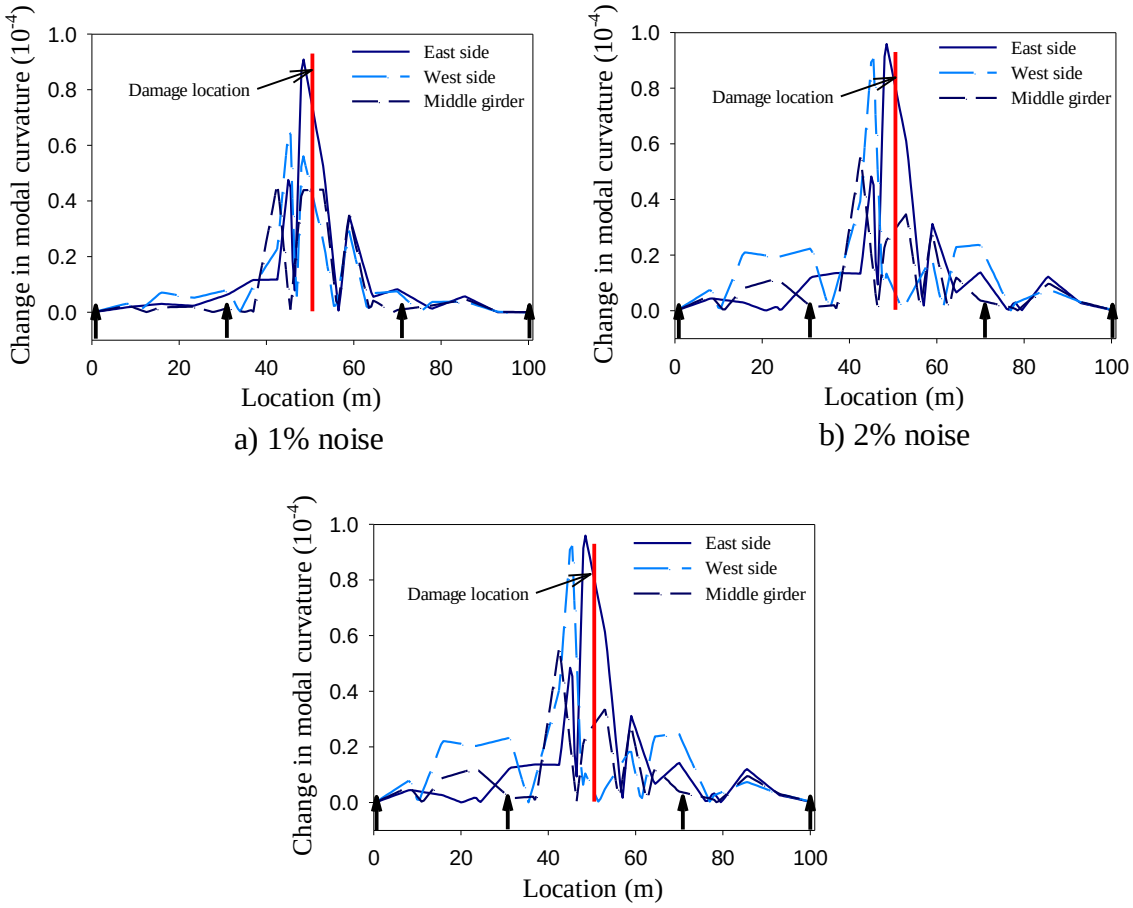

Figure G.14. Distribution of change in mode shape curvature for the first damage scenario when impact excitation was used and noise was added to input force: a) 1% noise, b) 2% noise, c) 5% noise.

G.2.3.3 Damage index method

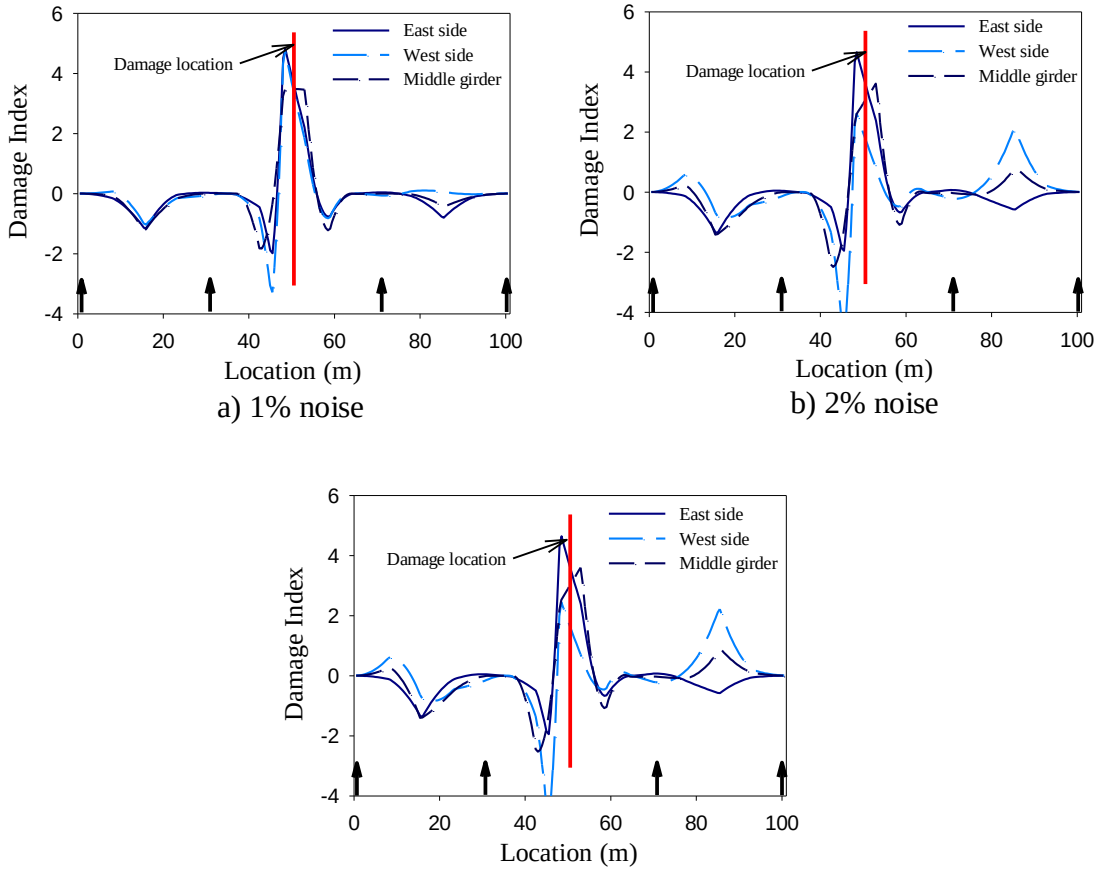

Figure G.15. Distribution of damage index for the first damage scenario when impact excitation was used and noise was added to input force: a) 1% noise, b) 2% noise, c) 5% noise.

G.2.3.4 Change in modal flexibility method

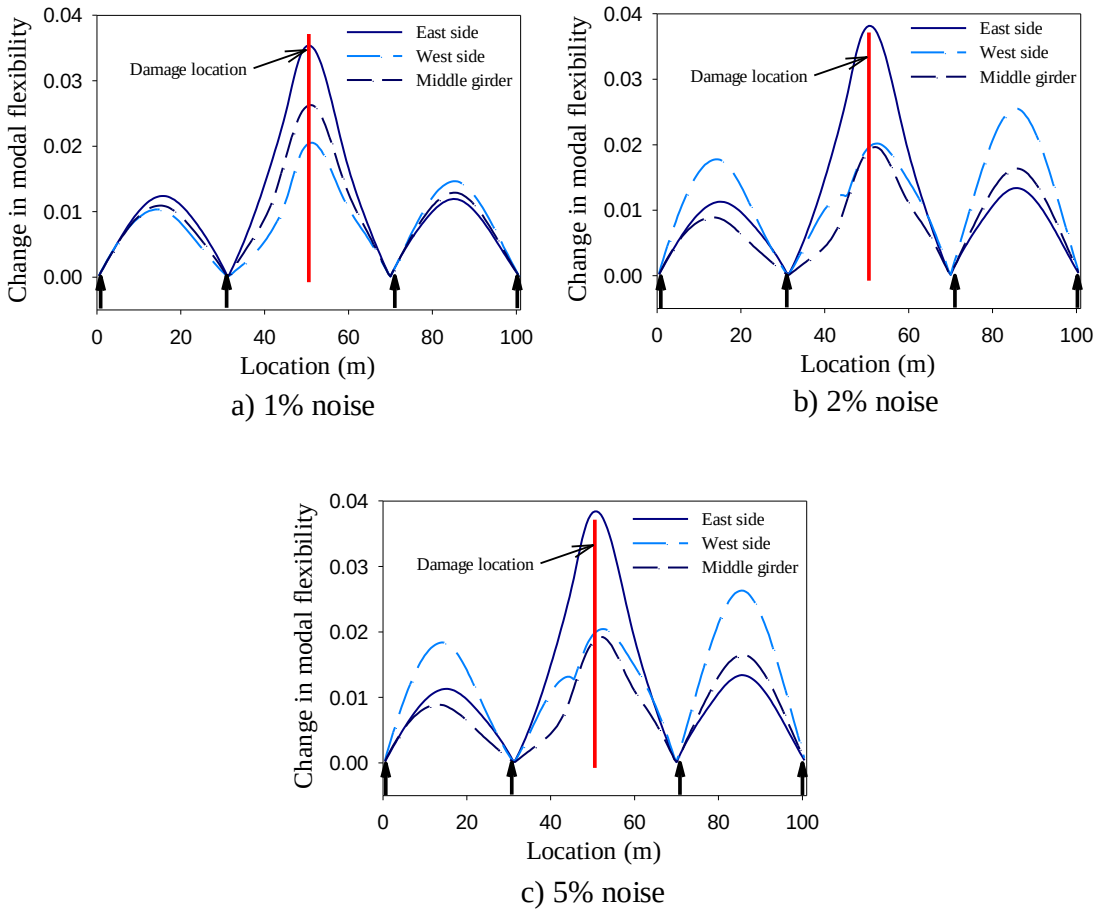

Figure G.16. Distribution of change in modal flexibility for the first damage scenario when impact excitation was used and noise was added to input force: a) 1% noise, b) 2% noise, c) 5% noise.

G.2.3.5 Change in uniform load surface curvature method

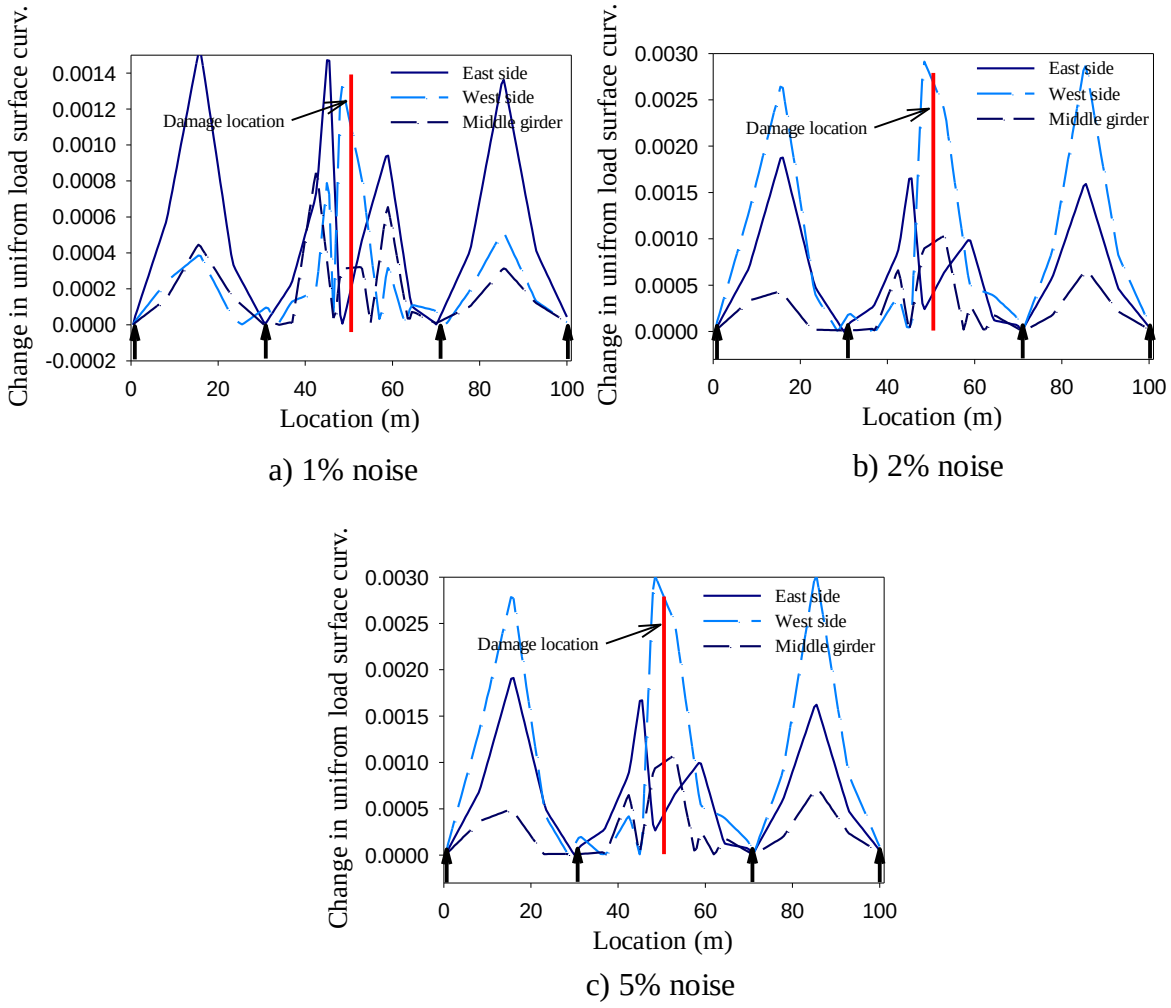

Figure G.17. Distribution of change in uniform load surface curvature for the first damage scenario when impact excitation was used and noise was added to input force: a) 1% noise, b) 2% noise, c) 5% noise.

G.2.3.6 Change in unit load surface curvature method

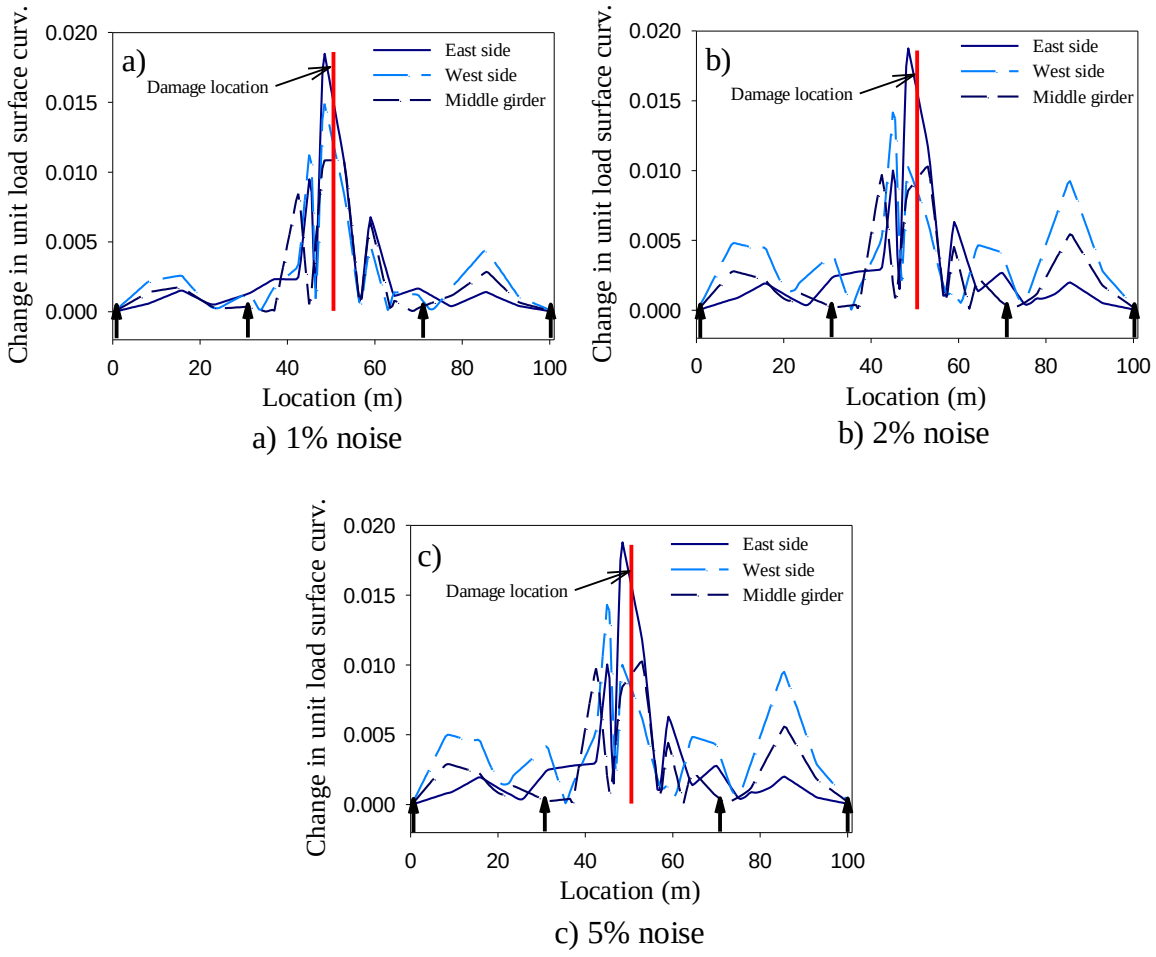

Figure G.18. Distribution of change in unit load surface curvature for the first damage scenario when impact excitation was used and noise was added to input force: a) 1% noise, b) 2% noise, c) 5% noise.

G.2.4 Impact excitation (output noise)

G.2.4.1 Change in mode shape method

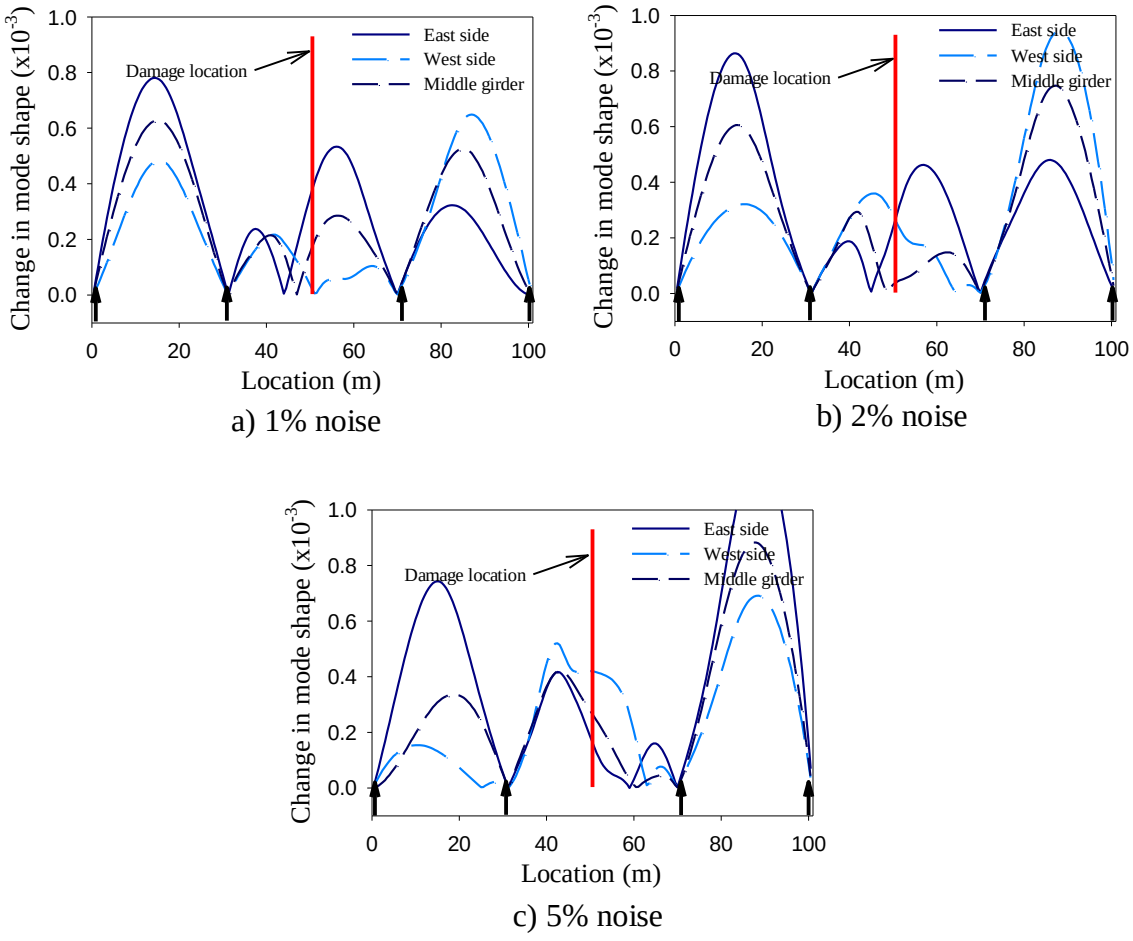

Figure G.19. Distribution of change in mode shape for the first damage scenario when impact excitation was used and noise was added to output signal: a) 1% noise, b) 2% noise, c) 5% noise.

G.2.4.2 Change in mode shape curvature method

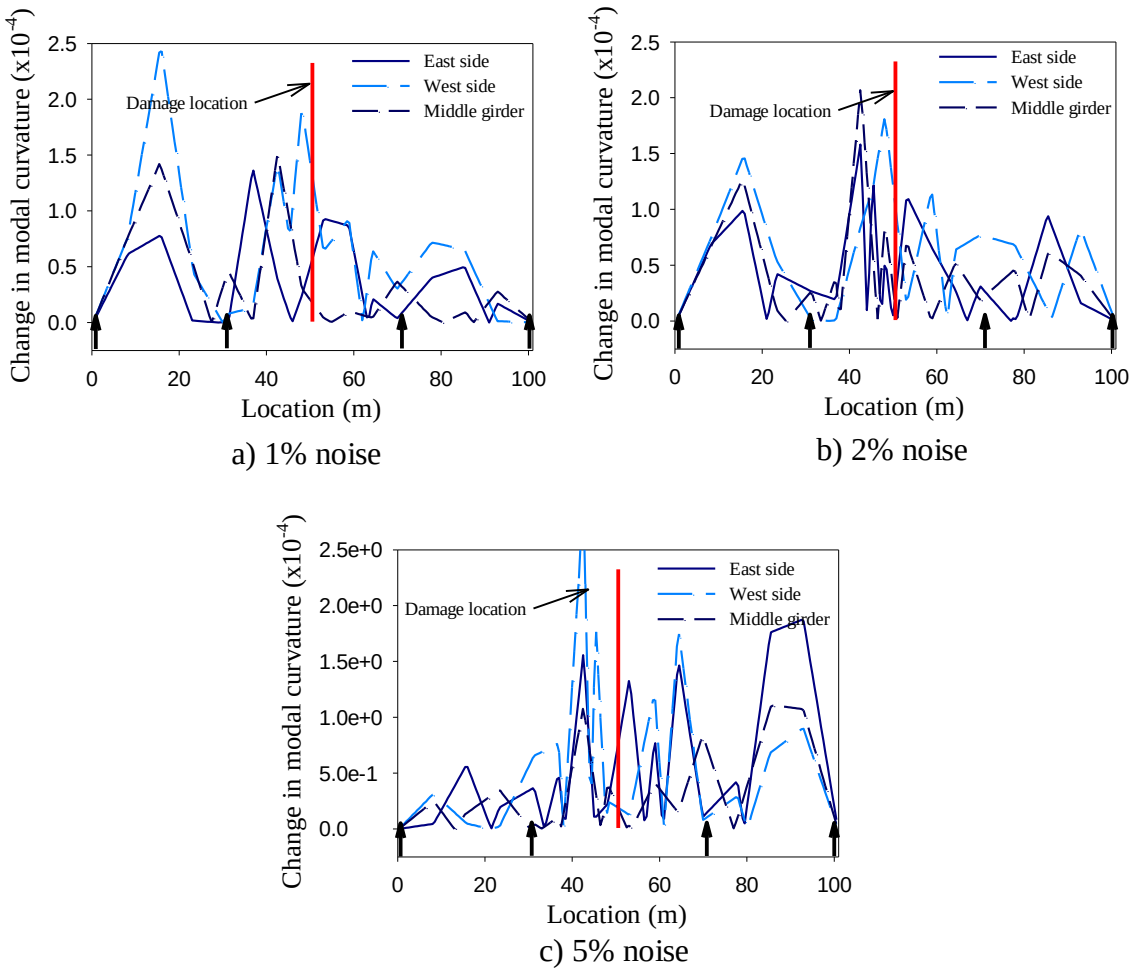

Figure G.20. Distribution of change in mode shape curvature for the first damage scenario when impact excitation was used and noise was added to output signal: a) 1% noise, b) 2% noise, c) 5% noise.

G.2.4.3 Damage index method

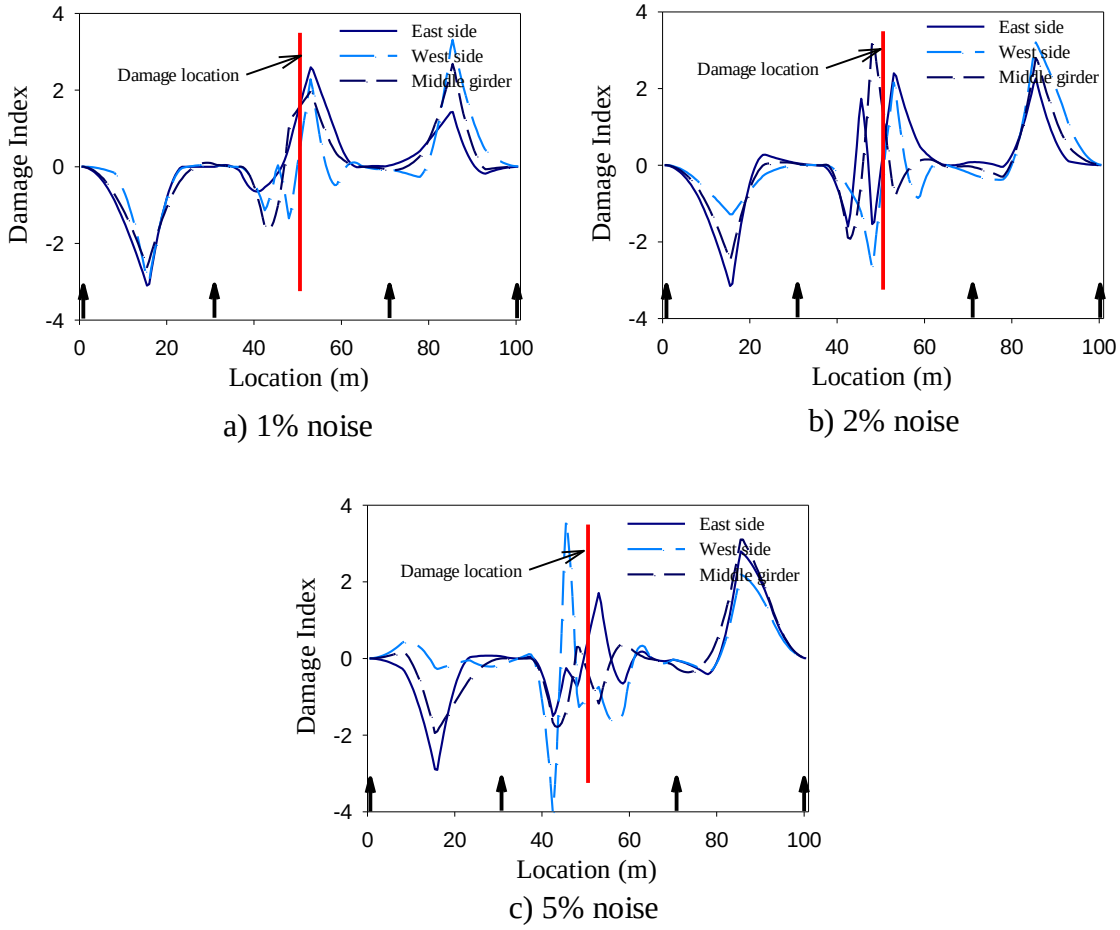

Figure G.21. Distribution of damage index for the first damage scenario when impact excitation was used and noise was added to output signal: a) 1% noise, b) 2% noise, c) 5% noise.

G.2.4.4 Change in modal flexibility method

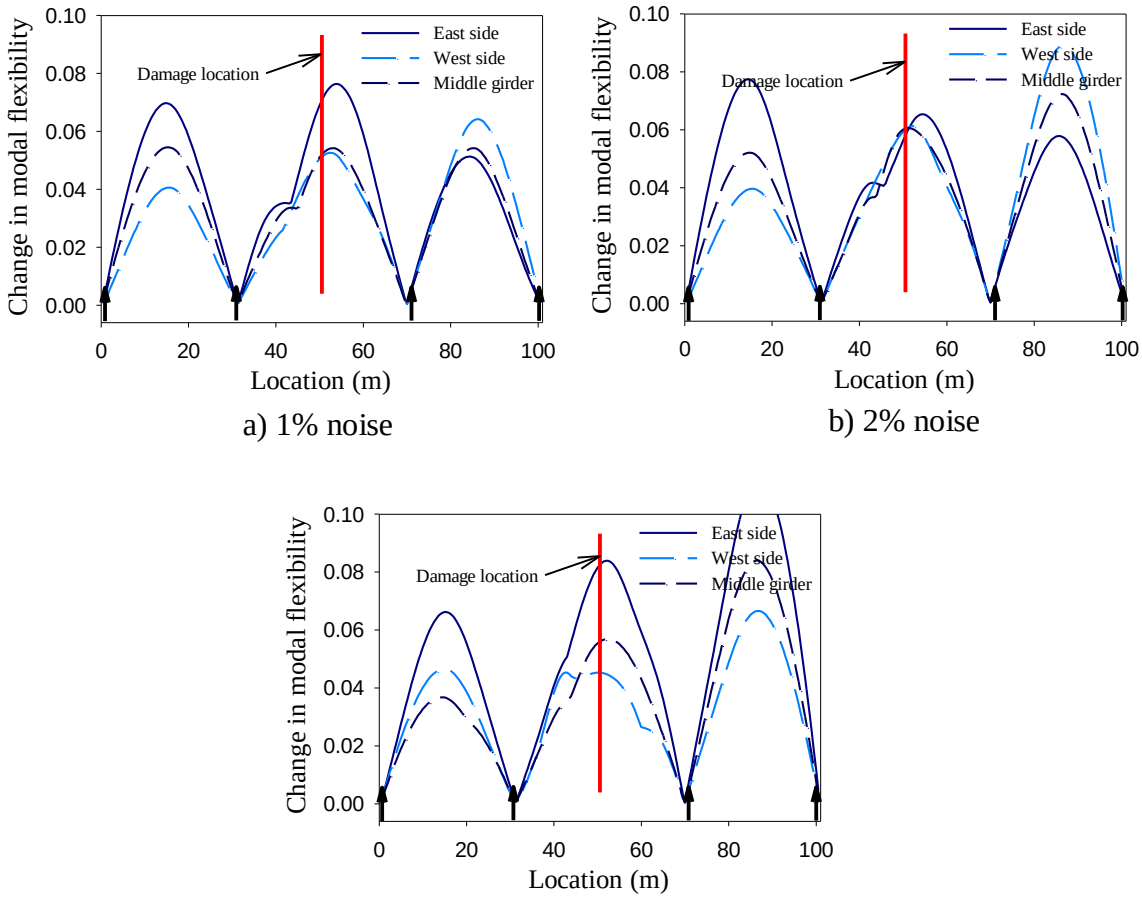

Figure G.22. Distribution of change in modal flexibility for the first damage scenario when impact excitation was used and noise was added to output signal: a) 1% noise, b) 2% noise, c) 5% noise.

G.2.4.5 Change in uniform load surface curvature method

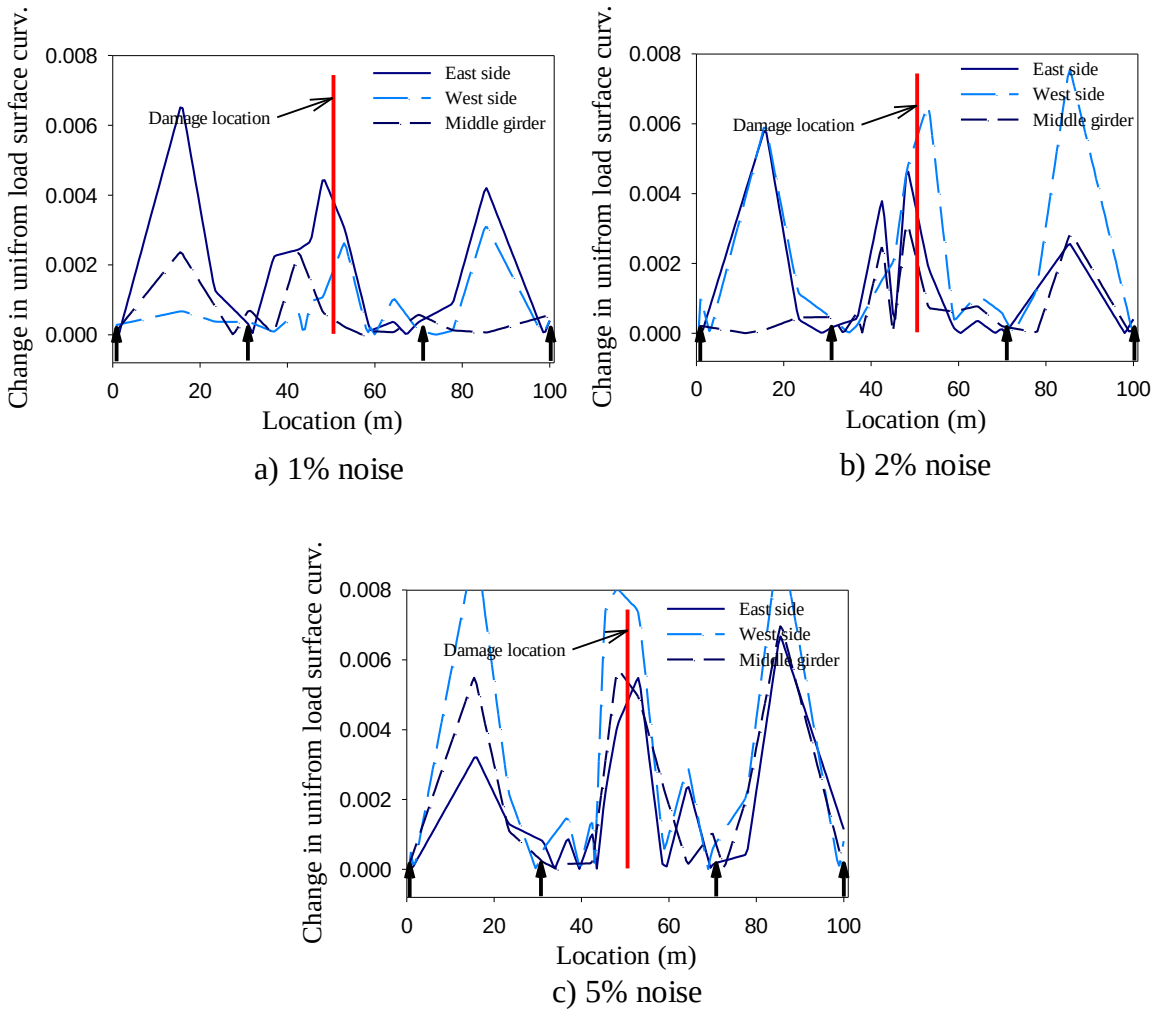

Figure G.23. Distribution of change in uniform load surface curvature for the first damage scenario when impact excitation was used and noise was added to output signal: a) 1% noise, b) 2% noise, c) 5% noise.

G.2.4.6 Change in unit load surface curvature method

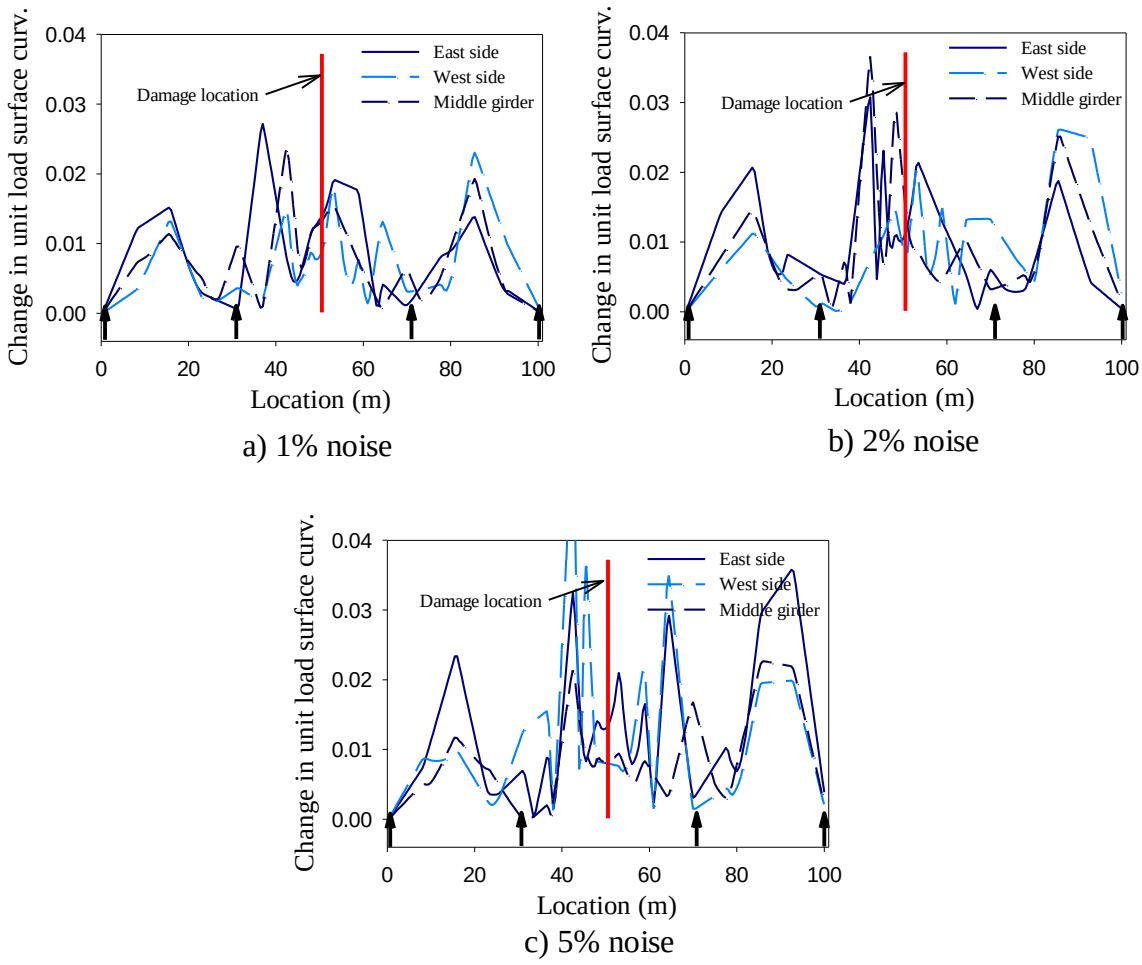

Figure G.24. Distribution of change in unit load surface curvature for the first damage scenario when impact excitation was used and noise was added to output signal: a) 1% noise, b) 2% noise, c) 5% noise.

APPENDIX H

MATLAB ROUTINES FOR VBDD

H.1 OVERVIEW

This appendix lists the MATLAB routines for the different VBDD methods that were used in this study. These VBDD methods were detailed in Chapter Two, and implemented in Chapter Five and Chapter Six. Common features of these routines are: these routines read the input files for mode shape amplitudes for the bridge before and after the simulation of damage; use cubic spline to interpolate the mode shape vectors; ortho-normalize the mode shapes so that they are scaled in a similar way; implement the different VBDD methods; and plot the curves indicating the damage for each VBDD method.

H.2 MATLAB ROUTINE FOR THE CHANGE IN MODE SHAPE METHOD, THE CHANGE IN MODE SHAPE CURVATURE METHOD, AND THE DAMAGE INDEX METHOD

This MATLAB routine implements the change in mode shape method, the change in mode shape curvature method, and the damage index method. The routine is listed below:

```
%damageID VBDD
% Determines vibration based damage detection
% reads undamaged file from MACEC .shp file, and damaged file from
MACEC .shp file

rebar = load ('disp_reduced.shp');                              % read
ANSYS modes with rebars
FRP   = load ('disp_reduced_1_short.shp');                      % read
ANSYS modes with loss of rebar

% changing the structure of rebar by removing extra rows and columns
% and changing complex modes to real
rebar(1:2,:) = []; rebar(:,5) = []; rebar(:,3) = []; rebar(:,1) = [];
```

```
nmodes = (size(rebar,2)-2)/2;                                    % number
of modes
for i = 1:nmodes
    cmodes(:,i) = rebar(:,2+i*2-1) + rebar(:,2+i*2)*sqrt(-1);
    rmodes(:,i) = abs(cmodes(:,i)).*sign(real(cmodes(:,i))); % MACEC
(GUI_shapes.m)
end
rebar(:,3:end) = []; rebar = [rebar rmodes];

cmodes =[]; rmodes=[];
% changing the structure of FRP by removing extra rows and columns
% and changing complex modes to real
FRP(1:2,:) = []; FRP(:,5) = []; FRP(:,3) = []; FRP(:,1) = [];

for i = 1:nmodes
    cmodes(:,i) = FRP(:,2+i*2-1) + FRP(:,2+i*2)*sqrt(-1);
    rmodes(:,i) = abs(cmodes(:,i)).*sign(real(cmodes(:,i))); % MACEC
(GUI_shapes.m)
    %theta = angle (cmodes(:,i));                                 % Felber
(Dvelopment of Hybrid Evaluation System p. 77)
    %if theta <= pi/4
    %    PW = 1;
    %elseif (theta > pi/4) & (theta < 3/4*pi)
    %    PW = 0;
    %elseif (theta >= 3/4*pi) & (theta <= pi)
    %    PW = -1;
    %end
    %rmodes(:,i) = PW*rmodes(:,i);
end
FRP(:,3:end) = []; FRP = [FRP rmodes];

nodesr = rebar(:,1); nodesf = FRP(:,1);                          % nodes
numbers
xr = rebar(:,2); xf = FRP(:,2);                                  % x-coord

for i = 1:nmodes                                                 %
separating the input files into seperate line modes, along east side,
west side, beam 1, beam 2, beam 3
    mode_rebar{1,i} = rebar(1:17,i+2);                           % rebar
    mode_rebar{2,i} = rebar(18:34,i+2);
    mode_rebar{3,i} = rebar(35:50,i+2);
    mode_rebar{4,i} = rebar(51:66,i+2);
    mode_rebar{5,i} = rebar(67:82,i+2);

    x{1} = xr(1:17);                                             % coord
    x{2} = xr(18:34);
    x{3} = xr(35:50);
    x{4} = xr(51:66);
    x{5} = xr(67:82);

    mode_FRP{1,i} = FRP(1:17,i+2);                               % FRP
    mode_FRP{2,i} = FRP(18:34,i+2);
    mode_FRP{3,i} = FRP(35:50,i+2);
    mode_FRP{4,i} = FRP(51:66,i+2);
    mode_FRP{5,i} = FRP(67:82,i+2);
end
```

```
% cubic spline interpolation
xx = 0.5:0.5:100.5;                                          % new
indicies for interopolation
%xx = 31.5:0.5:69.5;
xn = length (xx);                                            % number of
new indicies

% interpolating modes
for i = 1:5                                                  % loop over
number of beams
    for j = 1:nmodes                                         % loop over
number of modes
        yy_rebar_f{i,j} = spline(x{i},mode_rebar{i,j});      % rebar
spline function
        yy_FRP_f{i,j} = spline(x{i},mode_FRP{i,j});          % FRP
spline function
        yy_rebar{i,j} = ppval(yy_rebar_f{i,j},xx);           % rebar
        yy_FRP{i,j} = ppval(yy_FRP_f{i,j},xx);               % FRP
        %plot (xx,yy_rebar{i,j},xx,yy_FRP{i,j})
        %legend('rebar','frp')
        %figure
    end
end

% normalise modes by unit mass
for i = 1:5
    for j = 1:nmodes
        yy_rebar{i,j} =
yy_rebar{i,j}/sqrt(yy_rebar{i,j}*yy_rebar{i,j}');   % rebar
        yy_FRP{i,j} = yy_FRP{i,j}/sqrt(yy_FRP{i,j}*yy_FRP{i,j}');
% FRP
        yy_diff{i,j} = abs(yy_rebar{i,j} - yy_FRP{i,j});
        %plot (xx,yy_rebar{i,j},xx,yy_FRP{i,j})
        %legend('rebar','frp')
        %figure
    end
end
nmodes =1;
% damage detection routines
% difference in 1st mode
plot(xx,yy_diff{1,1},'-',xx,yy_diff{2,1},'--',...
    xx(1:end),yy_diff{3,1},':',xx,yy_diff{4,1},'-.',...
    xx,yy_diff{5,1},'o')
legend('East','West','Beam1','Beam2','Beam3')
xlabel('x')
ylabel('Mode difference method')
figure

% Curvature method
for i = 1:5                                                  %
calculating curvature
    curve_diffsum{i} = zeros(1,xn);                          %
initializing zero matrix
    for j = 1:nmodes
        %for k = 2:xn-1
```

```
        %    curve_rebar{i,j}(k) = yy_rebar{i,j}(k+1) +
yy_rebar{i,j}(k-1) - 2*yy_rebar{i,j}(k); % rebar
        %    curve_FRP{i,j}(k) = yy_FRP{i,j}(k+1) + yy_FRP{i,j}(k-1) -
2*yy_FRP{i,j}(k);         % FRP
        %end
        % caclulating curvature by differentiating the cubic spline
        coefs_rebar= []; coefs_rebar_curve = [];
        coefs_rebar= yy_rebar_f{i,j}.coefs;
        coefs_rebar_curve(:,1:2) = zeros(size(coefs_rebar,1),2);
        coefs_rebar_curve(:,3) = coefs_rebar(:,1)*6;
        coefs_rebar_curve(:,4) = coefs_rebar(:,2)*2;
        yy_rebar_curve_f{i,j} = yy_rebar_f{i,j};
        yy_rebar_curve_f{i,j}.coefs = coefs_rebar_curve;
        curve_rebar{i,j} = ppval(yy_rebar_curve_f{i,j},xx);

        coefs_FRP= []; coefs_FRP_curve = [];
        coefs_FRP= yy_FRP_f{i,j}.coefs;
        coefs_FRP_curve(:,1:2) = zeros(size(coefs_FRP,1),2);
        coefs_FRP_curve(:,3) = coefs_FRP(:,1)*6;
        coefs_FRP_curve(:,4) = coefs_FRP(:,2)*2;
        yy_FRP_curve_f{i,j} = yy_FRP_f{i,j};
        yy_FRP_curve_f{i,j}.coefs = coefs_FRP_curve;
        curve_FRP{i,j} = ppval(yy_FRP_curve_f{i,j},xx);

        % normalise modes curvature by unit mass
        curve_rebar{i,j} =
curve_rebar{i,j}/sqrt(yy_rebar{i,j}*yy_rebar{i,j}');   % rebar
        curve_FRP{i,j} = curve_FRP{i,j}/sqrt(yy_FRP{i,j}*yy_FRP{i,j}');
% FRP

        curve_diff{i,j}  = abs(curve_FRP{i,j} - curve_rebar{i,j});
        %curve_diff{i,j}  = abs(curve_FRP{i,j}) -
abs(curve_rebar{i,j});                        % calculating difference
in curvature
        curve_diffsum{i} = curve_diffsum{i} + curve_diff{i,j};
% summing up differences of all modes
        %plot
(xx(2:end),curve_rebar{i,j},xx(2:end),curve_FRP{i,j},xx(2:end),curve_di
ff{i,j})
        %legend('rebar','frp','diff')
        %figure
    end
end

plot(xx,curve_diffsum{1},'-',xx,curve_diffsum{2},'--',...
    xx,curve_diffsum{3},':',xx,curve_diffsum{4},'-.',...
    xx,curve_diffsum{5},'o')
legend('East','West','Beam1','Beam2','Beam3')
xlabel('x')
ylabel('Curvature Method')

% Damage index method
for i = 1:5
    for j = 1:nmodes
        curve_sqrsum_rebar(i,j) = sum((curve_rebar{i,j}).^2);
% sum of squares of curvatures
```

```
        curve_sqrsum_FRP(i,j) = sum((curve_FRP{i,j}).^2);
        curve_sqr_rebar{i,j} = (curve_rebar{i,j}).^2;
%squares of curvatures
        curve_sqr_FRP{i,j} = (curve_FRP{i,j}).^2;
    end
end
% Calculating damage index 'beta'
for i = 1:5
    for j = 1:nmodes
        for k = 1:xn
            aa = curve_sqr_FRP{i,j}(k) + curve_sqrsum_FRP(i,j);
            bb = curve_sqr_rebar{i,j}(k) + curve_sqrsum_rebar(i,j);
            cc = curve_sqrsum_rebar(i,j)/curve_sqrsum_FRP(i,j);
            beta{i,j}(k) = aa/bb*cc;
        end
        u(i,j) = mean(beta{i,j});
        sigma(i,j) = std(beta{i,j});
    end
end
for i = 1:5
    z_sum{i} = zeros(1,xn);
    for j = 1:nmodes
        for k = 1:xn
            z{i,j}(k) = (beta{i,j}(k)-u(i,j))/sigma(i,j);
        end
        z_sum{i} = z_sum{i} + z{i,j};
    end
end

figure
plot(xx,z_sum{1},'-',xx,z_sum{2},'--',...
    xx,z_sum{3},':',xx,z_sum{4},'-.',...
    xx,z_sum{5},'o')
legend('East','West','Beam1','Beam2','Beam3')
xlabel('x')
ylabel('Damage Index')
```

H.3 MATTLAB ROUTINE FOR THE CHANGE IN MEASURED MODAL FLEXIBILITY METHOD, AND THE CHANGE IN UNIFORM LOAD SURFACE CURVATURE METHOD

This MATLAB routine implements the change in measured modal flexibility method, and the change in uniform load surface curvature method. The routine is listed below:

```
%damageID VBDD
% Determines vibration based damage detection
% reads undamaged file from MACEC .shp file, and damaged file from
MACEC .shp file

rebar = load ('disp_reduced.shp');
FRP   = load ('disp_reduced_1_short.shp');

% changing the structure of rebar by removing extra rows and columns
% and changing complex modes to real
rebar(1:2,:) = []; rebar(:,5) = []; rebar(:,3) = []; rebar(:,1) = [];

nmodes = (size(rebar,2)-2)/2;                                  % number
of modes
for i = 1:nmodes
    cmodes(:,i) = rebar(:,2+i*2-1) + rebar(:,2+i*2)*sqrt(-1);
    rmodes(:,i) = abs(cmodes(:,i)).*sign(real(cmodes(:,i))); % MACEC
(GUI_shapes.m)
end
rebar(:,3:end) = []; rebar = [rebar rmodes];

cmodes =[]; rmodes=[];
% changing the structure of FRP by removing extra rows and columns
% and changing complex modes to real
FRP(1:2,:) = []; FRP(:,5) = []; FRP(:,3) = []; FRP(:,1) = [];

for i = 1:nmodes
    cmodes(:,i) = FRP(:,2+i*2-1) + FRP(:,2+i*2)*sqrt(-1);
    rmodes(:,i) = abs(cmodes(:,i)).*sign(real(cmodes(:,i))); % MACEC
(GUI_shapes.m)
end
FRP(:,3:end) = []; FRP = [FRP rmodes];

nodesr = rebar(:,1); nodesf = FRP(:,1);                    % nodes
numbers
xr = rebar(:,2); xf = FRP(:,2);                            % x-coord

for i = 1:nmodes                                           %
separating the input files into seperate line modes, along east side,
west side, beam 1, beam 2, beam 3
    mode_rebar{1,i} = rebar(1:17,i+2);                     % rebar
    mode_rebar{2,i} = rebar(18:34,i+2);
    mode_rebar{3,i} = rebar(35:50,i+2);
    mode_rebar{4,i} = rebar(51:66,i+2);
    mode_rebar{5,i} = rebar(67:82,i+2);

    x{1} = xr(1:17);                                       % coord
```

```
    x{2} = xr(18:34);
    x{3} = xr(35:50);
    x{4} = xr(51:66);
    x{5} = xr(67:82);

    mode_FRP{1,i} = FRP(1:17,i+2);                              % FRP
    mode_FRP{2,i} = FRP(18:34,i+2);
    mode_FRP{3,i} = FRP(35:50,i+2);
    mode_FRP{4,i} = FRP(51:66,i+2);
    mode_FRP{5,i} = FRP(67:82,i+2);
end

% cubic spline interpolation
xx = 0.5:0.5:100.5;                                             % new
indicies for interopolation
%xx = 31.5:0.5:69.5;
xn = length (xx);                                               % number of
new indicies

% interpolating modes
for i = 1:5                                                     % loop over
number of beams
    for j = 1:nmodes                                            % loop over
number of modes
        yy_rebar{i,j} = spline(x{i},mode_rebar{i,j},xx);    % rebar
        yy_FRP{i,j} = spline(x{i},mode_FRP{i,j},xx);        % FRP
    end
end

% normalise modes by unit mass
for j = 1:5
    for i = 1:nmodes
        yy_rebar{j,i} =
yy_rebar{j,i}/sqrt(yy_rebar{j,i}*yy_rebar{j,i}');   % rebar
        yy_FRP{j,i} = yy_FRP{j,i}/sqrt(yy_FRP{j,i}*yy_FRP{j,i}');
% FRP
    end
end
nmodes =1;
% damage detection routines
% Flexibility method & Change in uniform load surface curvature method
w_rebar = [2.4803];
w_FRP   = [2.4783];

for i = 1:5
    Fsum_rebar{i} = zeros(xn); Fsum_FRP{i} = zeros(xn);      %
initializing zero matrix for sum of flexibility matrices
end

for i = 1:5
    for j = 1:nmodes
        F_rebar{i,j} =
1/(w_rebar(j)*2*pi/360)^2*yy_rebar{i,j}'*yy_rebar{i,j};
        F_FRP{i,j} = 1/(w_FRP(j)*2*pi/360)^2*yy_FRP{i,j}'*yy_FRP{i,j};
        Fsum_rebar{i} = Fsum_rebar{i} + F_rebar{i,j};
%flexibility summing up contribution from different modes
```

```
        Fsum_FRP{i} = Fsum_FRP{i} + F_FRP{i,j};
%flexibility
    end
    Fcolsum_rebar{i} = sum (Fsum_rebar{i});                 %curvature
summing up the columns of the flexibility matrix
    Fcolsum_FRP{i} = sum (Fsum_FRP{i});                     %curvature
    % results of flexibility method
    F_diff{i} = Fsum_rebar{i} - Fsum_FRP{i};
    F_max{i}  = max(abs(F_diff{i}));
end

plot(xx,F_max{1},'-',xx,F_max{2},'--',xx,F_max{3},':',...
    xx,F_max{4},'-.',xx,F_max{5},'o')
legend('East','West','Beam1','Beam2','Beam3')
xlabel('x')
ylabel('Flexibility')

for i = 1:5
    for k = 2:(xn-1)
        Fcurve_rebar{i}(k) =  Fcolsum_rebar{i}(k+1) +
Fcolsum_rebar{i}(k-1) - 2*Fcolsum_rebar{i}(k);
        Fcurve_FRP{i}(k) =  Fcolsum_FRP{i}(k+1) + Fcolsum_FRP{i}(k-1) -
2*Fcolsum_FRP{i}(k);
    end
    Fcurve_diff{i} = abs(Fcurve_rebar{i})-abs(Fcurve_FRP{i});
    %Fcurve_diff{i} = abs(Fcurve_rebar{i}-Fcurve_FRP{i});
end

figure
plot(xx(2:end),Fcurve_diff{1},'-',xx(2:end),Fcurve_diff{2},'--',...
    xx(2:end),Fcurve_diff{3},':',xx(2:end),Fcurve_diff{4},'-.',...
    xx(2:end),Fcurve_diff{5},'o')
legend('East','West','Beam1','Beam2','Beam3')
xlabel('x')
ylabel('Change in Uniform Load Surface Curvature')
```

H.4 MATTLAB ROUTINE FOR THE CHANGE IN UNIT LOAD SURFACE CURVATURE METHOD

This MATLAB is similar to the routine listed in Section H.3 with the difference that the unit load surface curvature method is implemented instead of the uniform load surface curvature method. The routine is listed below:

```
%damageID VBDD
% Determines vibration based damage detection
% reads undamaged file from MACEC .shp file, and damaged file from
MACEC .shp file

rebar = load ('disp_reduced.shp');                              % read
macec modes with rebars
FRP   = load ('disp_reduced_1_short.shp');                      % read
macec modes with FRP

% changing the structure of rebar by removing extra rows and columns
% and changing complex modes to real
rebar(1:2,:) = []; rebar(:,5) = []; rebar(:,3) = []; rebar(:,1) = [];

nmodes = (size(rebar,2)-2)/2;                                    % number
of modes
for i = 1:nmodes
    cmodes(:,i) = rebar(:,2+i*2-1) + rebar(:,2+i*2)*sqrt(-1);
    rmodes(:,i) = abs(cmodes(:,i)).*sign(real(cmodes(:,i))); % MACEC
(GUI_shapes.m)
end
rebar(:,3:end) = []; rebar = [rebar rmodes];

cmodes =[]; rmodes=[];
% changing the structure of FRP by removing extra rows and columns
% and changing complex modes to real
FRP(1:2,:) = []; FRP(:,5) = []; FRP(:,3) = []; FRP(:,1) = [];

for i = 1:nmodes
    cmodes(:,i) = FRP(:,2+i*2-1) + FRP(:,2+i*2)*sqrt(-1);
    rmodes(:,i) = abs(cmodes(:,i)).*sign(real(cmodes(:,i))); % MACEC
(GUI_shapes.m)
end
FRP(:,3:end) = []; FRP = [FRP rmodes];

nodesr = rebar(:,1); nodesf = FRP(:,1);                         % nodes
numbers
xr = rebar(:,2); xf = FRP(:,2);                                 % x-coord

for i = 1:nmodes                                                %
separating the input files into seperate line modes, along east side,
west side, beam 1, beam 2, beam 3
    mode_rebar{1,i} = rebar(1:17,i+2);                          % rebar
    mode_rebar{2,i} = rebar(18:34,i+2);
    mode_rebar{3,i} = rebar(35:50,i+2);
    mode_rebar{4,i} = rebar(51:66,i+2);
```

```
    mode_rebar{5,i} = rebar(67:82,i+2);

    x{1} = xr(1:17);                                        % coord
    x{2} = xr(18:34);
    x{3} = xr(35:50);
    x{4} = xr(51:66);
    x{5} = xr(67:82);

    mode_FRP{1,i} = FRP(1:17,i+2);                          % FRP
    mode_FRP{2,i} = FRP(18:34,i+2);
    mode_FRP{3,i} = FRP(35:50,i+2);
    mode_FRP{4,i} = FRP(51:66,i+2);
    mode_FRP{5,i} = FRP(67:82,i+2);
end

% cubic spline interpolation
xx = 0.5:0.5:100.5;                                         % new
indicies for interopolation
%xx = 31.5:0.5:69.5;
xn = length (xx);                                           % number of
new indicies

% interpolating modes
for i = 1:5                                                 % loop over
number of beams
    for j = 1:nmodes                                        % loop over
number of modes
        yy_rebar{i,j} = spline(x{i},mode_rebar{i,j},xx);    % rebar
        yy_FRP{i,j} = spline(x{i},mode_FRP{i,j},xx);        % FRP
    end
end

% normalise modes by unit mass
for j = 1:5
    for i = 1:nmodes
        yy_rebar{j,i} =
yy_rebar{j,i}/sqrt(yy_rebar{j,i}*yy_rebar{j,i}');   % rebar
        yy_FRP{j,i} = yy_FRP{j,i}/sqrt(yy_FRP{j,i}*yy_FRP{j,i}');
% FRP
    end
end
nmodes =1;
% damage detection routines
% Flexibility method & Change in uniform load surface curvature method
w_rebar = [2.4803];
w_FRP   = [2.4783];

for i = 1:5
    Fsum_rebar{i} = zeros(xn); Fsum_FRP{i} = zeros(xn);      %
initializing zero matrix for sum of flexibility matrices
end

for i = 1:5
    for j = 1:nmodes
```

```
        F_rebar{i,j} =
1/(w_rebar(j)*2*pi/360)^2*yy_rebar{i,j}'*yy_rebar{i,j};
        F_FRP{i,j} = 1/(w_FRP(j)*2*pi/360)^2*yy_FRP{i,j}'*yy_FRP{i,j};
        Fsum_rebar{i} = Fsum_rebar{i} + F_rebar{i,j};
%flexibility summing up contribution from different modes
        Fsum_FRP{i} = Fsum_FRP{i} + F_FRP{i,j};
%flexibility
    end
    Fcolsum_rebar{i} = sum (Fsum_rebar{i});                 %curvature
summing up the columns of the flexibility matrix
    Fcolsum_FRP{i} = sum (Fsum_FRP{i});                     %curvature
    % results of flexibility method
    F_diff{i} = Fsum_rebar{i} - Fsum_FRP{i};
    F_max{i}  = max(abs(F_diff{i}));
end

plot(xx,F_max{1},'-',xx,F_max{2},'--',xx,F_max{3},':',...
    xx,F_max{4},'-.',xx,F_max{5},'o')
legend('East','West','Beam1','Beam2','Beam3')
xlabel('x')
ylabel('Flexibility')

for i = 1:5
    for j = 1:xn
        for k = 2:(xn-1)
            Fcurve_rebar{i}(k,j) =  Fsum_rebar{i}(k+1,j) +
Fsum_rebar{i}(k-1,j) - 2*Fsum_rebar{i}(k,j);
            Fcurve_FRP{i}(k,j) =  Fsum_FRP{i}(k+1,j) + Fsum_FRP{i}(k-
1,j) - 2*Fsum_FRP{i}(k,j);
        end
    end
    %Fcurve_diff{i} = abs(Fcurve_rebar{i})-abs(Fcurve_FRP{i});
    Fcurve_diff{i} = abs(Fcurve_rebar{i}-Fcurve_FRP{i});
    Fcurve_diff_sum{i} = sum(Fcurve_diff{i}');              % summing
up rows of vectors
end

figure
plot(xx(2:end),Fcurve_diff_sum{1},'-',xx(2:end),Fcurve_diff_sum{2},'--
',...
    xx(2:end),Fcurve_diff_sum{3},':',xx(2:end),Fcurve_diff_sum{4},'-
.',...
    xx(2:end),Fcurve_diff_sum{5},'o')
legend('East','West','Beam1','Beam2','Beam3')
xlabel('x')
ylabel('Change in Uniform Load Surface Curvature')
```

H.5 SAMPLE OF INPUT FILES

Mode shape files calculated using MACEC toolbox for MATLAB were used as input files for the various VBDD routines. Listed below are two input files for, one before damage and the other after damage, for harmonic excitation applied at the same frequency of the first natural frequency of the bridge, and using a damage scenario in which the external reinforcing bars at the middle of the centre span of the bridge were cut.

Mode shapes file before damage:

```
       NaN         NaN         NaN         NaN         NaN  2.4774079e+000  0.0000000e+000
       NaN         NaN         NaN         NaN         NaN -1.5709113e-001  0.0000000e+000
3.0000000e+000  2.0896000e+004  4.5720000e-001  3.3020000e-001  0.0000000e+000  0.0000000e+000  0.0000000e+000
3.0000000e+000  2.1022000e+004  4.5720000e-001  8.2550000e+000  0.0000000e+000 -5.3132290e-001  3.6792153e-002
3.0000000e+000  2.1401000e+004  4.5720000e-001  1.5798800e+001  0.0000000e+000 -7.6231482e-001  5.1041599e-002
3.0000000e+000  2.1596000e+004  4.5720000e-001  2.3342600e+001  0.0000000e+000 -5.0027704e-001  3.2449324e-002
3.0000000e+000  2.1876000e+004  4.5720000e-001  3.1261050e+001  0.0000000e+000  0.0000000e+000  0.0000000e+000
3.0000000e+000  2.2005000e+004  4.5720000e-001  3.6874642e+001  0.0000000e+000  3.8646007e-001 -2.7991964e-002
3.0000000e+000  2.2291000e+004  4.5720000e-001  4.2567481e+001  0.0000000e+000  7.5361337e-001 -5.6554828e-002
3.0000000e+000  2.2296000e+004  4.5720000e-001  4.5351200e+001  0.0000000e+000  8.9543481e-001 -6.8401396e-002
3.0000000e+000  2.2301000e+004  4.5720000e-001  4.8134887e+001  0.0000000e+000  9.9202898e-001 -7.7179723e-002
3.0000000e+000  2.2545000e+004  4.5720000e-001  5.3121038e+001  0.0000000e+000  9.8548111e-001 -7.8643533e-002
3.0000000e+000  2.2555000e+004  4.5720000e-001  5.8876006e+001  0.0000000e+000  7.2673548e-001 -5.8492502e-002
3.0000000e+000  2.2865000e+004  4.5720000e-001  6.4307175e+001  0.0000000e+000  3.7565879e-001 -2.9818434e-002
3.0000000e+000  2.3024000e+004  4.5720000e-001  6.9919850e+001  0.0000000e+000  0.0000000e+000  0.0000000e+000
3.0000000e+000  2.3199000e+004  4.5720000e-001  7.7838300e+001  0.0000000e+000 -4.6859802e-001  3.4344699e-002
3.0000000e+000  2.3529000e+004  4.5720000e-001  8.5382100e+001  0.0000000e+000 -6.8979353e-001  5.3209816e-002
3.0000000e+000  2.3752000e+004  4.5720000e-001  9.2925900e+001  0.0000000e+000 -4.6119939e-001  3.6500163e-002
3.0000000e+000  2.4004000e+004  4.5720000e-001  1.0085070e+002  0.0000000e+000  0.0000000e+000  0.0000000e+000
3.0000000e+000  2.0913000e+004  8.4836000e+000  3.3020000e-001  0.0000000e+000  0.0000000e+000  0.0000000e+000
3.0000000e+000  2.1141000e+004  8.4836000e+000  8.2550000e+000  0.0000000e+000 -5.3276646e-001  2.4231986e-002
3.0000000e+000  2.1418000e+004  8.4836000e+000  1.5798800e+001  0.0000000e+000 -7.6490567e-001  2.7787258e-002
3.0000000e+000  2.1613000e+004  8.4836000e+000  2.3342600e+001  0.0000000e+000 -5.0247071e-001  1.2123042e-002
3.0000000e+000  2.1893000e+004  8.4836000e+000  3.1261100e+001  0.0000000e+000  0.0000000e+000  0.0000000e+000
3.0000000e+000  2.2099000e+004  8.4836000e+000  3.6874600e+001  0.0000000e+000  3.8936013e-001 -4.5692594e-005
3.0000000e+000  2.2439000e+004  8.4836000e+000  4.2567500e+001  0.0000000e+000  7.5966631e-001  1.9552173e-003
```

3.0000000e+000 2.2434000e+004 8.4836000e+000 4.5351184e+001 0.0000000e+000 9.0269068e-001 1.8309796e-003

3.0000000e+000 2.2429000e+004 8.4836000e+000 4.8134900e+001 0.0000000e+000 1.0000000e+000 0.0000000e+000

3.0000000e+000 2.2689000e+004 8.4836000e+000 5.3121000e+001 0.0000000e+000 9.9268821e-001 -7.8499619e-003

3.0000000e+000 2.2679000e+004 8.4836000e+000 5.8876000e+001 0.0000000e+000 7.3130037e-001 -1.6392518e-002

3.0000000e+000 2.2975000e+004 8.4836000e+000 6.4307200e+001 0.0000000e+000 3.7736521e-001 -1.3951578e-002

3.0000000e+000 2.3041000e+004 8.4836000e+000 6.9919900e+001 0.0000000e+000 0.0000000e+000 0.0000000e+000

3.0000000e+000 2.3301000e+004 8.4836000e+000 7.7838300e+001 0.0000000e+000 -4.6896420e-001 3.1512547e-002

3.0000000e+000 2.3546000e+004 8.4836000e+000 8.5382100e+001 0.0000000e+000 -6.9019967e-001 5.0148263e-002

3.0000000e+000 2.3769000e+004 8.4836000e+000 9.2925900e+001 0.0000000e+000 -4.6143128e-001 3.4720926e-002

3.0000000e+000 2.4021000e+004 8.4836000e+000 1.0085070e+002 0.0000000e+000 0.0000000e+000 0.0000000e+000

3.0000000e+000 1.5019000e+004 1.7272000e+000 3.3020000e-001 0.0000000e+000 0.0000000e+000 0.0000000e+000

3.0000000e+000 1.5234000e+004 1.7272000e+000 8.2550000e+000 0.0000000e+000 -5.2946914e-001 3.4585842e-002

3.0000000e+000 1.5726000e+004 1.7272000e+000 1.5570200e+001 0.0000000e+000 -7.5239061e-001 4.6890439e-002

3.0000000e+000 1.6294000e+004 1.7272000e+000 2.3342600e+001 0.0000000e+000 -4.9800659e-001 2.9346101e-002

3.0000000e+000 1.6810000e+004 1.7272000e+000 3.1261100e+001 0.0000000e+000 0.0000000e+000 0.0000000e+000

3.0000000e+000 1.7018000e+004 1.7272000e+000 3.6874600e+001 0.0000000e+000 3.8244357e-001 -2.3370543e-002

3.0000000e+000 1.7554000e+004 1.7272000e+000 4.2567500e+001 0.0000000e+000 7.5025655e-001 -4.7314844e-002

3.0000000e+000 1.7559000e+004 1.7272000e+000 4.8134900e+001 0.0000000e+000 9.8787375e-001 -6.5212793e-002

3.0000000e+000 1.8018000e+004 1.7272000e+000 5.3121000e+001 0.0000000e+000 9.8133217e-001 -6.7529192e-002

3.0000000e+000 1.8023000e+004 1.7272000e+000 5.8876000e+001 0.0000000e+000 7.2307639e-001 -5.1420223e-002

3.0000000e+000 1.8615000e+004 1.7272000e+000 6.4307200e+001 0.0000000e+000 3.7175009e-001 -2.6430863e-002

3.0000000e+000 1.8919000e+004 1.7272000e+000 6.9919900e+001 0.0000000e+000 0.0000000e+000 0.0000000e+000

3.0000000e+000 1.9228000e+004 1.7272000e+000 7.7838300e+001 0.0000000e+000 -4.6719360e-001 3.3652550e-002

3.0000000e+000 1.9837000e+004 1.7272000e+000 8.5610700e+001 0.0000000e+000 -6.7984779e-001 5.1890755e-002

3.0000000e+000 2.0247000e+004 1.7272000e+000 9.2925900e+001 0.0000000e+000 -4.5859245e-001 3.5951662e-002

3.0000000e+000 2.0710000e+004 1.7272000e+000 1.0085070e+002 0.0000000e+000 0.0000000e+000 0.0000000e+000

3.0000000e+000 1.5031000e+004 4.4704000e+000 3.3020000e-001 0.0000000e+000 0.0000000e+000 0.0000000e+000

3.0000000e+000 1.5343000e+004 4.4704000e+000 8.2550000e+000 0.0000000e+000 -5.2836203e-001 3.0128410e-002

3.0000000e+000 1.5803000e+004 4.4704000e+000 1.5570200e+001 0.0000000e+000 -7.5024498e-001 3.8657311e-002

3.0000000e+000 1.6306000e+004 4.4704000e+000 2.3342600e+001 0.0000000e+000 -4.9662681e-001 2.1924146e-002

3.0000000e+000 1.6822000e+004 4.4704000e+000 3.1261100e+001 0.0000000e+000 0.0000000e+000 0.0000000e+000

3.0000000e+000 1.7114000e+004 4.4704000e+000 3.6874600e+001 0.0000000e+000 3.8079947e-001 -1.4071271e-002

3.0000000e+000 1.7679000e+004 4.4704000e+000 4.2567500e+001 0.0000000e+000 7.4972941e-001 -2.7402888e-002

3.0000000e+000 1.7684000e+004 4.4704000e+000 4.8134900e+001 0.0000000e+000 9.8788143e-001 -3.8605673e-002

3.0000000e+000 1.8143000e+004 4.4704000e+000 5.3121000e+001 0.0000000e+000 9.8124590e-001 -4.3345023e-002

3.0000000e+000 1.8148000e+004 4.4704000e+000 5.8876000e+001 0.0000000e+000 7.2253237e-001 -3.7440363e-002

3.0000000e+000 1.8711000e+004 4.4704000e+000 6.4307200e+001 0.0000000e+000 3.7101280e-001 -2.1734175e-002

3.0000000e+000 1.8931000e+004 4.4704000e+000 6.9919900e+001 0.0000000e+000 0.0000000e+000 0.0000000e+000

3.0000000e+000 1.9321000e+004 4.4704000e+000 7.7838300e+001 0.0000000e+000 -4.6630169e-001 3.2510999e-002

3.0000000e+000 1.9849000e+004 4.4704000e+000 8.5610700e+001 0.0000000e+000 -6.7739584e-001 5.0655172e-002

3.0000000e+000 2.0259000e+004 4.4704000e+000 9.2925900e+001 0.0000000e+000 -4.5677013e-001 3.5228344e-002

3.0000000e+000 2.0722000e+004 4.4704000e+000 1.0085070e+002 0.0000000e+000 0.0000000e+000 0.0000000e+000

3.0000000e+000 1.5043000e+004 7.2136000e+000 3.3020000e-001 0.0000000e+000 0.0000000e+000 0.0000000e+000

3.0000000e+000 1.5452000e+004 7.2136000e+000 8.2550000e+000 0.0000000e+000 -5.3046770e-001 2.5902777e-002

3.0000000e+000 1.5880000e+004 7.2136000e+000 1.5570200e+001 0.0000000e+000 -7.5417603e-001 3.0865218e-002

3.0000000e+000 1.6318000e+004 7.2136000e+000 2.3342600e+001 0.0000000e+000 -4.9957296e-001 1.4796122e-002

3.0000000e+000 1.6834000e+004 7.2136000e+000 3.1261100e+001 0.0000000e+000 0.0000000e+000 0.0000000e+000

3.0000000e+000 1.7210000e+004 7.2136000e+000 3.6874600e+001 0.0000000e+000 3.8437285e-001 -4.8406948e-003

3.0000000e+000 1.7804000e+004 7.2136000e+000 4.2567500e+001 0.0000000e+000 7.5437510e-001 -7.5479262e-003

3.0000000e+000 1.7809000e+004 7.2136000e+000 4.8134900e+001 0.0000000e+000 9.9336048e-001 -1.2079839e-002

3.0000000e+000 1.8268000e+004 7.2136000e+000 5.3121000e+001 0.0000000e+000 9.8638641e-001 -1.9066918e-002

3.0000000e+000 1.8273000e+004 7.2136000e+000 5.8876000e+001 0.0000000e+000 7.2610770e-001 -2.3392188e-002

3.0000000e+000 1.8807000e+004 7.2136000e+000 6.4307200e+001 0.0000000e+000 3.7278675e-001 -1.7014232e-002

3.0000000e+000 1.8943000e+004 7.2136000e+000 6.9919900e+001 0.0000000e+000 0.0000000e+000 0.0000000e+000

3.0000000e+000 1.9414000e+004 7.2136000e+000 7.7838300e+001 0.0000000e+000 -4.6746128e-001 3.1587163e-002

3.0000000e+000 1.9861000e+004 7.2136000e+000 8.5610700e+001 0.0000000e+000 -6.8012084e-001 4.9860187e-002

3.0000000e+000 2.0271000e+004 7.2136000e+000 9.2925900e+001 0.0000000e+000 -4.5874665e-001 3.4806124e-002

3.0000000e+000 2.0734000e+004 7.2136000e+000 1.0085070e+002 0.0000000e+000 0.0000000e+000 0.0000000e+000

Mode shapes file before damage:

NaN NaN NaN NaN NaN 2.4790233e+000 0.0000000e+000

NaN NaN NaN NaN NaN 2.2580846e+000 0.0000000e+000

3.0000000e+000 2.0896000e+004 4.5720000e-001 3.3020000e-001 0.0000000e+000 0.0000000e+000 0.0000000e+000

3.0000000e+000 2.1022000e+004 4.5720000e-001 8.2550000e+000 0.0000000e+000 -5.3391716e-001 5.4856083e-004

3.0000000e+000 2.1401000e+004 4.5720000e-001 1.5798800e+001 0.0000000e+000 -7.6587450e-001 9.9767576e-004

3.0000000e+000 2.1596000e+004 4.5720000e-001 2.3342600e+001 0.0000000e+000 -5.0256559e-001 7.8155328e-004

3.0000000e+000 2.1876000e+004 4.5720000e-001 3.1261050e+001 0.0000000e+000 0.0000000e+000 0.0000000e+000

3.0000000e+000 2.2005000e+004 4.5720000e-001 3.6874642e+001 0.0000000e+000 3.8876999e-001 -2.5024676e-004

3.0000000e+000 2.2291000e+004 4.5720000e-001 4.2567481e+001 0.0000000e+000 7.5872120e-001 -2.5026213e-004

3.0000000e+000 2.2296000e+004 4.5720000e-001 4.5351200e+001 0.0000000e+000 9.0199071e-001 -1.5293422e-004

3.0000000e+000 2.2301000e+004 4.5720000e-001 4.8134887e+001 0.0000000e+000 1.0000000e+000 0.0000000e+000

3.0000000e+000 2.2545000e+004 4.5720000e-001 5.3121038e+001 0.0000000e+000 9.9367390e-001 2.3867409e-004

3.0000000e+000 2.2555000e+004 4.5720000e-001 5.8876006e+001 0.0000000e+000 7.3222360e-001 2.3726128e-004

3.0000000e+000 2.2865000e+004 4.5720000e-001 6.4307175e+001 0.0000000e+000 3.7829371e-001 7.2894116e-005

3.0000000e+000 2.3024000e+004 4.5720000e-001 6.9919850e+001 0.0000000e+000 0.0000000e+000 0.0000000e+000

3.0000000e+000 2.3199000e+004 4.5720000e-001 7.7838300e+001 0.0000000e+000 -4.7137873e-001 2.5269678e-004

3.0000000e+000 2.3529000e+004 4.5720000e-001 8.5382100e+001 0.0000000e+000 -6.9419830e-001 5.0803403e-005

3.0000000e+000 2.3752000e+004 4.5720000e-001 9.2925900e+001 0.0000000e+000 -4.6425389e-001 -7.7892270e-005

3.0000000e+000 2.4004000e+004 4.5720000e-001 1.0085070e+002 0.0000000e+000 0.0000000e+000 0.0000000e+000

3.0000000e+000 2.0913000e+004 8.4836000e+000 3.3020000e-001 0.0000000e+000 0.0000000e+000 0.0000000e+000

3.0000000e+000 2.1141000e+004 8.4836000e+000 8.2550000e+000 0.0000000e+000 -5.3345976e-001 2.0812886e-003

3.0000000e+000 2.1418000e+004 8.4836000e+000 1.5798800e+001 0.0000000e+000 -7.6503117e-001 3.8344468e-003

3.0000000e+000 2.1613000e+004 8.4836000e+000 2.3342600e+001 0.0000000e+000 -5.0182679e-001 3.2598070e-003

3.0000000e+000 2.1893000e+004 8.4836000e+000 3.1261100e+001 0.0000000e+000 0.0000000e+000 0.0000000e+000

3.0000000e+000 2.2099000e+004 8.4836000e+000 3.6874600e+001 0.0000000e+000 3.8775718e-001 -3.6561083e-003

3.0000000e+000 2.2439000e+004 8.4836000e+000 4.2567500e+001 0.0000000e+000 7.5659623e-001 -7.3821434e-003

3.0000000e+000 2.2434000e+004 8.4836000e+000 4.5351184e+001 0.0000000e+000 8.9943978e-001 -8.7150309e-003

3.0000000e+000 2.2429000e+004 8.4836000e+000 4.8134900e+001 0.0000000e+000 9.9720080e-001 -9.4131850e-003

3.0000000e+000 2.2689000e+004 8.4836000e+000 5.3121000e+001 0.0000000e+000 9.9099976e-001 -8.3941930e-003

3.0000000e+000 2.2679000e+004 8.4836000e+000 5.8876000e+001 0.0000000e+000 7.3089968e-001 -4.8957868e-003

3.0000000e+000 2.2975000e+004 8.4836000e+000 6.4307200e+001 0.0000000e+000 3.7777250e-001 -1.8609642e-003

3.0000000e+000 2.3041000e+004 8.4836000e+000 6.9919900e+001 0.0000000e+000 0.0000000e+000 0.0000000e+000

3.0000000e+000 2.3301000e+004 8.4836000e+000 7.7838300e+001 0.0000000e+000 -4.7131698e-001 5.9864419e-004

3.0000000e+000 2.3546000e+004 8.4836000e+000 8.5382100e+001 0.0000000e+000 -6.9413569e-001 4.2501609e-004

3.0000000e+000 2.3769000e+004 8.4836000e+000 9.2925900e+001 0.0000000e+000 -4.6421224e-001 1.3959662e-004

3.0000000e+000 2.4021000e+004 8.4836000e+000 1.0085070e+002 0.0000000e+000 0.0000000e+000 0.0000000e+000

3.0000000e+000 1.5019000e+004 1.7272000e+000 3.3020000e-001 0.0000000e+000 0.0000000e+000 0.0000000e+000

3.0000000e+000 1.5234000e+004 1.7272000e+000 8.2550000e+000 0.0000000e+000 -5.3174705e-001 7.9793401e-004

3.0000000e+000 1.5726000e+004 1.7272000e+000 1.5570200e+001 0.0000000e+000 -7.5539279e-001 1.4065248e-003

3.0000000e+000 1.6294000e+004 1.7272000e+000 2.3342600e+001 0.0000000e+000 -4.9986425e-001 1.1354294e-003

3.0000000e+000 1.6810000e+004 1.7272000e+000 3.1261100e+001 0.0000000e+000 0.0000000e+000 0.0000000e+000

3.0000000e+000 1.7018000e+004 1.7272000e+000 3.6874600e+001 0.0000000e+000 3.8412153e-001 -7.7126915e-004

3.0000000e+000 1.7554000e+004 1.7272000e+000 4.2567500e+001 0.0000000e+000 7.5404813e-001 -1.3371230e-003

3.0000000e+000 1.7559000e+004 1.7272000e+000 4.8134900e+001 0.0000000e+000 9.9410897e-001 -1.4085619e-003

3.0000000e+000 1.8018000e+004 1.7272000e+000 5.3121000e+001 0.0000000e+000 9.8790574e-001 -1.0681475e-003

3.0000000e+000 1.8023000e+004 1.7272000e+000 5.8876000e+001 0.0000000e+000 7.2755178e-001 -5.8290790e-004

3.0000000e+000 1.8615000e+004 1.7272000e+000 6.4307200e+001 0.0000000e+000 3.7392378e-001 -2.9997330e-004

3.0000000e+000 1.8919000e+004 1.7272000e+000 6.9919900e+001 0.0000000e+000 0.0000000e+000 0.0000000e+000

3.0000000e+000 1.9228000e+004 1.7272000e+000 7.7838300e+001 0.0000000e+000 -4.6988214e-001 3.2319778e-004

3.0000000e+000 1.9837000e+004 1.7272000e+000 8.5610700e+001 0.0000000e+000 -6.8410722e-001 1.1681653e-004

3.0000000e+000 2.0247000e+004 1.7272000e+000 9.2925900e+001 0.0000000e+000 -4.6157943e-001 -3.6107119e-005

3.0000000e+000 2.0710000e+004 1.7272000e+000 1.0085070e+002 0.0000000e+000 0.0000000e+000 0.0000000e+000

3.0000000e+000 1.5031000e+004 4.4704000e+000 3.3020000e-001 0.0000000e+000 0.0000000e+000 0.0000000e+000

3.0000000e+000 1.5343000e+004 4.4704000e+000 8.2550000e+000 0.0000000e+000 -5.2997592e-001 1.3265232e-003

3.0000000e+000 1.5803000e+004 4.4704000e+000 1.5570200e+001 0.0000000e+000 -7.5205260e-001 2.3816609e-003

3.0000000e+000 1.6306000e+004 4.4704000e+000 2.3342600e+001 0.0000000e+000 -4.9742894e-001 2.0198023e-003

3.0000000e+000 1.6822000e+004 4.4704000e+000 3.1261100e+001 0.0000000e+000 0.0000000e+000 0.0000000e+000

3.0000000e+000 1.7114000e+004 4.4704000e+000 3.6874600e+001 0.0000000e+000 3.8117635e-001 -1.8799067e-003

3.0000000e+000 1.7679000e+004 4.4704000e+000 4.2567500e+001 0.0000000e+000 7.5070573e-001 -3.7381896e-003

3.0000000e+000 1.7684000e+004 4.4704000e+000 4.8134900e+001 0.0000000e+000 9.9036421e-001 -4.6280563e-003

3.0000000e+000 1.8143000e+004 4.4704000e+000 5.3121000e+001 0.0000000e+000 9.8440100e-001 -3.9918825e-003

3.0000000e+000 1.8148000e+004 4.4704000e+000 5.8876000e+001 0.0000000e+000 7.2501470e-001 -2.2680612e-003

3.0000000e+000 1.8711000e+004 4.4704000e+000 6.4307200e+001 0.0000000e+000 3.7252251e-001 -8.6070286e-004

3.0000000e+000 1.8931000e+004 4.4704000e+000 6.9919900e+001 0.0000000e+000 0.0000000e+000 0.0000000e+000

3.0000000e+000 1.9321000e+004 4.4704000e+000 7.7838300e+001 0.0000000e+000 -4.6882363e-001 4.5291360e-004

3.0000000e+000 1.9849000e+004 4.4704000e+000 8.5610700e+001 0.0000000e+000 -6.8147918e-001 2.4278710e-004

3.0000000e+000 2.0259000e+004 4.4704000e+000 9.2925900e+001 0.0000000e+000 -4.5965529e-001 3.4368215e-005

3.0000000e+000 2.0722000e+004 4.4704000e+000 1.0085070e+002 0.0000000e+000 0.0000000e+000 0.0000000e+000

3.0000000e+000 1.5043000e+004 7.2136000e+000 3.3020000e-001 0.0000000e+000 0.0000000e+000 0.0000000e+000

3.0000000e+000 1.5452000e+004 7.2136000e+000 8.2550000e+000 0.0000000e+000 -5.3143187e-001 1.8578375e-003

3.0000000e+000 1.5880000e+004 7.2136000e+000 1.5570200e+001 0.0000000e+000 -7.5481295e-001 3.3616487e-003

3.0000000e+000 1.6318000e+004 7.2136000e+000 2.3342600e+001 0.0000000e+000 -4.9933761e-001 2.9094562e-003

3.0000000e+000 1.6834000e+004 7.2136000e+000 3.1261100e+001 0.0000000e+000 0.0000000e+000 0.0000000e+000

3.0000000e+000 1.7210000e+004 7.2136000e+000 3.6874600e+001 0.0000000e+000 3.8345088e-001 -3.0295095e-003

3.0000000e+000 1.7804000e+004 7.2136000e+000 4.2567500e+001 0.0000000e+000 7.5260745e-001 -6.1829290e-003

3.0000000e+000 1.7809000e+004 7.2136000e+000 4.8134900e+001 0.0000000e+000 9.9217909e-001 -7.8885868e-003

3.0000000e+000 1.8268000e+004 7.2136000e+000 5.3121000e+001 0.0000000e+000 9.8619466e-001 -6.9763370e-003

3.0000000e+000 1.8273000e+004 7.2136000e+000 5.8876000e+001 0.0000000e+000 7.2665951e-001 -4.0003924e-003

3.0000000e+000 1.8807000e+004 7.2136000e+000 6.4307200e+001 0.0000000e+000 3.7363474e-001 -1.4477132e-003

3.0000000e+000 1.8943000e+004 7.2136000e+000 6.9919900e+001 0.0000000e+000 0.0000000e+000 0.0000000e+000

3.0000000e+000 1.9414000e+004 7.2136000e+000 7.7838300e+001 0.0000000e+000 -4.6983835e-001 5.7555154e-004

3.0000000e+000 1.9861000e+004 7.2136000e+000 8.5610700e+001 0.0000000e+000 -6.8406729e-001 3.6530744e-004

3.0000000e+000 2.0271000e+004 7.2136000e+000 9.2925900e+001 0.0000000e+000 -4.6155508e-001 1.0402022e-004

3.0000000e+000 2.0734000e+004 7.2136000e+000 1.0085070e+002 0.0000000e+000 0.0000000e+000 0.0000000e+000